

(NASA-CR-184505) 1992 NASA/ASEE
SUMMER FACULTY FELLOWSHIP PROGRAM
(Alabama Univ.) 307 p

N93-17279
--THRU--
N93-17340
Unclass

03

1/80 0136041

NASA CONTRACTOR REPORT

NASA CR- 184505

RESEARCH REPORTS - 1992 NASA/ASEE SUMMER FACULTY FELLOWSHIP PROGRAM

The University of Alabama
Tuscaloosa, Alabama
and
The University of Alabama in Huntsville
Huntsville, Alabama

December 1992

Final Report

Prepared for NASA, George C. Marshall Space Flight Center
Marshall Space Flight Center, Alabama 35812

RESEARCH REPORTS

1992 NASA/ASEE SUMMER FACULTY FELLOWSHIP PROGRAM

George C. Marshall Space Flight Center

The University of Alabama

and

The University of Alabama in Huntsville

EDITORS:

**Dr. L. Michael Freeman
Associate Professor of Aerospace Engineering
The University of Alabama**

**Dr. Charles R. Chappell
Associate Director for Science
Marshall Space Flight Center**

**Dr. Frank Six
University Affairs Officer
Marshall Space Flight Center**

**Dr. Gerald R. Karr
Chairman of Mechanical & Aerospace Engineering
The University of Alabama in Huntsville**

NASA CR-184505

REPORT DOCUMENTATION PAGE

Form Approved
OMB No. 0704-0188

Public reporting burden for this collection of information is estimated to average 1 hour per response, including the time for reviewing instructions, searching existing data sources, gathering and maintaining the data needed, and completing and reviewing the collection of information. Send comments regarding this burden estimate or any other aspect of this collection of information, including suggestions for reducing this burden, to Washington Headquarters Services, Directorate for Information Operations and Reports, 1215 Jefferson Davis Highway, Suite 1204, Arlington, VA 22202-4302, and to the Office of Management and Budget, Paperwork Reduction Project (0704-0188), Washington, DC 20503.

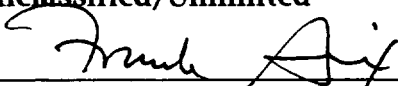
1. AGENCY USE ONLY (Leave blank)		2. REPORT DATE December 1992	3. REPORT TYPE AND DATES COVERED Contractor Report	
4. TITLE AND SUBTITLE Research Reports - 1992 NASA/ASEE Summer Faculty Fellowship Program			5. FUNDING NUMBERS G: NGT-01-002-099	
6. AUTHOR(S) M. Freeman, R. Chappell, F. Six, G. Karr, Editors				
7. PERFORMING ORGANIZATION NAME(S) AND ADDRESS(ES) The University of Alabama, Tuscaloosa, Alabama and The University of Alabama in Huntsville			8. PERFORMING ORGANIZATION REPORT NUMBER	
9. SPONSORING / MONITORING AGENCY NAME(S) AND ADDRESS(ES) National Aeronautics and Space Administration Washington, DC 20546			10. SPONSORING / MONITORING AGENCY REPORT NUMBER NASA CR- 184505	
11. SUPPLEMENTARY NOTES				
12a. DISTRIBUTION / AVAILABILITY STATEMENT Unclassified/Unlimited  Date: 12-10-92 Dr. Frank Six, University Affairs Officer			12b. DISTRIBUTION CODE	
13. ABSTRACT (Maximum 200 words) <p>For the 28th consecutive year, a NASA/ASEE Summer Faculty Fellowship Program was conducted at the Marshall Space Flight Center (MSFC). The program was conducted by the University of Alabama and MSFC during the period June 1, 1992 through August 7, 1992. Operated under the auspices of the American Society for Engineering Education, the MSFC program, as well as those at other NASA centers, was sponsored by the Office of Educational Affairs, NASA Headquarters, Washington, DC. The basic objectives of the programs, which are in the 29th year of operation nationally, are (1) to further the professional knowledge of qualified engineering and science faculty members; (2) to stimulate an exchange of ideas between participants and NASA; (3) to enrich and refresh the research and teaching activities of the participants' institutions; and (4) to contribute to the research objectives of the NASA centers.</p> <p>The Faculty Fellows spent 10 weeks at MSFC engaged in a research project compatible with their interests and background and worked in collaboration with a NASA/MSFC colleague. This document is a compilation of Fellows' reports on their research during the summer of 1992. The University of Alabama Report No. BER-575-94 presents the Co-Directors' report on the administrative operations of the program. Further information can be obtained by contacting any of the editors.</p>				
14. SUBJECT TERMS Advanced projects; information and electronic systems; materials, and processes; propulsion; space science; structures and dynamics; mission operations; systems analysis and integration; public affairs; safety and mission assurance			15. NUMBER OF PAGES 207	
			16. PRICE CODE NTIS	
17. SECURITY CLASSIFICATION OF REPORT Unclassified	18. SECURITY CLASSIFICATION OF THIS PAGE Unclassified	19. SECURITY CLASSIFICATION OF ABSTRACT Unclassified	20. LIMITATION OF ABSTRACT	

TABLE OF CONTENTS

- I. **Abdelmessih, Amanie N.**
California State Polytechnic University at Pomona
Heat Flow in Variable Polarity Plasma Arc Welds

- II. **Batson, Robert G.**
The University of Alabama
Systems Engineering Process and Organization Assessment

- III. **Blake, Jean A.**
Alabama A & M University
Updating and Expanding the Library of Materials on NASA
Spacelink Electronic Information System

- IV. **Bower, Mark V.**
The University of Alabama in Huntsville
Design and Analysis of Seals for Extended Service Life

- V. **Brewer, William V.**
Jackson State University
Shuttle Flight Experiment Preliminary Proposal: Demonstration of
Welding Applications in Space

- VI. **Brooks, Joni**
Columbia State Community College
Investigation of Rainfall Data with Regard to Low-Level Wind Flow
Regime For East Central Florida

- VII. **Bullington, Stanley F.**
Mississippi State University
Requirements for the Implementation of Schedule Repair
Technology in the Experiment Scheduling Program

- VIII. **Bykat, Alex**
Armstrong State College
A 2nd Generation Expert System for Checking and Diagnosing
AXAF's Electric Power System

- IX. **Cardelino, Beatriz H.**
Spelman College
Prediction of Nonlinear Optical Properties of Large Organic
Molecules

- X. Chyu, Mingking K.
Carnegie Mellon University
CFD Analysis on Control of Secondary Losses in STME LOX
Turbines with Endwall Fences
- XI. Cobb, Shannon S.
The University of Alabama in Huntsville
Optimal Trajectories for Orbital Transfers Using Low and Medium
Thrust Propulsion Systems
- XII. Das, Digendra K.
SUNY Institute of Technology - Utica
STME Nozzle Thermal Analysis
- XIII. Duchon, Claude E.
University of Oklahoma
A Plan for Accurate Estimation of Daily Area-Mean Rainfall During
the Cape Experiment
- XIV. Farrington, Phillip A.
The University of Alabama in Huntsville
Evaluation and Recommendations for Work Group Integration
Within the Materials and Processes Lab
- XV. Foreman, James W.
Alabama A & M University
A Study of the LUTE Metering Structure
- XVI. Frederick, Robert A.
The University of Alabama in Huntsville
Hybrid Rocket Performance
- XVII. Harrison, Harry C.
Capitol College
Guide for Object-Oriented Analysis and Design
- XVIII. Hartfield, Roy J.
Auburn University
Experimental Investigation of a Simulated LOX Injector Flow Field
and Other Nonintrusive Measurement Efforts
- XIX. Helmicki, Arthur J.
University of Cincinnati
Modeling for Health Monitoring and Control with Applications to
the Space Transportation Main Engine

- XX. Highsmith, Alton L.
The University of Alabama
Post-Impact Behavior of Composite Solid Rocket Motor Cases
- XXI. Hodel, A. Scottedward
Auburn University
Numerical Methods for the Analysis of Sampled-Data Systems and
for the Computation of System Zeros
- XXII. Jackson, Conrad N.
The University of Alabama in Huntsville
Some Effects of Time Usage Patterns on the Productivity of
Engineers
- XXIII. Jang, Bor Z.
Auburn University
Space Environmental Effects on Polymers and Composites
- XXIV. Johnson, Adriel D.
The University of Alabama in Huntsville
Ground Testing of Bioconvective Variables Such As Morphological
Characterizations and Mechanisms Which Regulate Macroscopic
Patterns
- XXV. Karimi, Majid
Indiana University of Pennsylvania
Energetics and Structural Properties of Twist Grain Boundaries in
Cu
- XXVI. Lawrence, Stella
Bronx Community College
Using Software Metrics and Software Reliability Models to Attain
Acceptable Quality Software for Flight and Ground Support
Software for Avionic Systems
- XXVII. Lebo, George
University of Florida
An Algorithm to Quantify the Performance of the JOVE Program
- XXVIII. Leland, Robert P.
The University of Alabama
Adaptive Optics for Laser Power Beaming

- XXIX. Lestrade, John Patrick
Mississippi State University
Structure in Gamma-Ray Burst Time Profiles: Statistical Analysis I
- XXX. Martin, James A.
The University of Alabama
Directions for Future Earth-to-Orbit Vehicles
- XXXI. Matson, Jack E.
The University of Alabama
Development of a Prototype Interactive Learning System Using
Multi-Media Technology for Mission Independent Training Program
- XXXII. McDonald, Malcolm W.
Berry College
Multipath Effects in a Global Positioning Satellite System Receiver
- XXXIII. McGruder, Charles H., III
Fisk University
The Ionosphere as a Gamma-Ray Burst Detector
- XXXIV. McNamara, Bernard
New Mexico State University
Correlated Optical Observations with BATSE/CGRO on SCO X-1
- XXXV. Miller, Lunelle
Northeast Mississippi Community College
Problems Involving Combined Loading
- XXXVI. Moore, Loretta A.
Auburn University
A Process for Prototyping Onboard Payload Displays for Space
Station Freedom
- XXXVII. Moynihan, Gary P.
The University of Alabama
Development of Vendor Evaluation Criteria and Post-
Implementation Considerations for MSFC Center-Wide Executive
Information System
- XXXVIII. Olsen, Richard C.
Naval Postgraduate School
On the Consequences of Bi-Maxwellian Plasma Distributions for
Parallel Electric Fields

- XXXIX. Palazzolo, Alan B.
Texas A & M University
Simulation of Cryogenic Turbopump Annular Seals
- XL. Pangia, Michael J.
Georgia Southwestern College
The Kappa Distribution as a Variational Solution for an Infinite Plasma
- XLI. Peterson, Lennart R.
University of Florida
Studies of the Charging of a Thin Dust Layer in a Plasma
- XLII. Pierson, William E.
West Virginia Institute of Technology
SEDS1 Mission Software Verification Using a Signal Simulator
- XLIII. Putcha, Chandra S.
California State University, Fullerton
Reliability Analysis of External Tank Attach Ring (ETA)
- XLIV. Ray, Paul S.
The University of Alabama
Emergency Egress Requirements for Caution and Warning, Logistics, Maintenance, and Assembly Stage MB-6 of Space Station Freedom
- XLV. Richie, James E.
Marquette University
Analysis of Waves in Space Plasma (WISP) Near Field Simulation and Experiment
- XLVI. Rosmait, Russell L.
Pittsburg State University
Industry Survey of Space System Cost Benefits from New Ways of Doing Business
- XLVII. Rule, William K.
The University of Alabama
Design of a Welded Joint for Robotic, On Orbit Assembly of Space Trusses
- XLVIII. Solakiewicz, Richard
Chicago State University
Electromagnetic Scattering in Clouds

- XLIX. Taneja, Vidya S.
Western Illinois University
Reliability Evaluation Methodology for NASA Applications**
- L. TenPas, Peter W.
The University of Kansas
Acceleration of FDNS Flow Simulations Using Initial Flowfields
Generated with a Parabolized Navier-Stokes Method**
- LI. Thompson, Roger C.
The Pennsylvania State University
Control-Structure-Thermal Interactions in Analysis of Lunar
Telescopes**
- LII. Tibbits, Patrick
Indiana Institute of Technology
Stiffnesses by (TtN) Ensemble Molecular Dynamics**
- LIII. Walsh, Daniel W.
California Polytechnic State University - San Luis Obispo
UPT Scenarios - Implications for System Reliability**
- LIV. Wang, C. Jeff
Tuskegee University
Thermostructural Responses of Carbon Phenolics in a Restrained
Thermal Growth Test**
- LV. Wang, Jai-Ching
Alabama A & M University
Nature of Fluid Flows in Differentially Heated Cylindrical Container
Filled With a Stratified Solution**
- LVI. Wdowiak, Thomas J.
The University of Alabama at Birmingham
An Experiment to Study Fullerene Formation Under Reduced
Gravity**
- LVII. Whitaker, Kevin W.
The University of Alabama
Neural Network Architectures To Analyze OPAD Data**
- LVIII. Wikstrom, Carl V.
University of Arkansas
Computerized Reduction of Elementary Reaction Sets for CFD
Combustion Modeling**

- LIX. **Wilson, Gordon R.**
 The University of Alabama in Huntsville
 The Inner Magnetospheric Imager (IMI): Instrument Heritage and
 Orbit Viewing Analysis
- LX. **Woodbury, Keith A.**
 The University of Alabama
 Analysis of Film Cooling in Rocket Nozzles
- LXI. **Yang, Yii-Ching**
 Tuskegee University
 Stress Analysis and Damage Evaluation of Flawed Composite
 Laminates by Hybrid-Numerical Methods

N 9 3 - 1 7 2 8 0

1992

NASA/ASEE SUMMER FACULTY FELLOWSHIP PROGRAM

**MARSHALL SPACE FLIGHT CENTER
THE UNIVERSITY OF ALABAMA**

HEAT FLOW IN VARIABLE POLARITY PLASMA ARC WELDS

Prepared By: Amanie N. Abdelmessih, Ph.D.
Academic Rank: Lecturer
Institution and Department: California State Polytechnic University
Chemical and Materials
Engineering Department

NASA/MSFC
Office: Materials and Processes
Division: Process Engineering
Branch: Metals Processes

MSFC Colleague: Arthur C. Nunes, Jr., Ph.D.

INTRODUCTION

The space shuttle external tank and the space station Freedom are fabricated by the variable polarity plasma arc (VPPA) welding. Heat sink effects (taper) are observed when there are irregularities in the work-piece configuration especially if these irregularities are close to the weld bead (1). These heat sinks affect the geometry of the weld bead, and in extreme cases they could cause defects such as incomplete fusion. Also, different fixtures seem to have varying heat sink effects.

The objective of the previous (1), present and consecutive research studies is to investigate the effect of irregularities in the work-piece configuration and fixture differences on the weld bead geometry with the ultimate objective to compensate automatically for the heat sink effects and achieve a perfect weld.

TAPER DURING WELDING

By taper is meant the convergence or divergence of weld diameter. In the present situation, both the crown and the root diameters, are taken to diverge or converge simultaneously.

When welding conditions are set constant, taper is particularly observed when there are irregularities close to the weld bead. Measurements of weld beads of plates with ridges, protuberances and step close to the weld beads showed decreases in weld diameters sometimes as much as 23.5% (1).

It had been thought that as welding progresses, the work piece effective ambient temperature (measurable at the edge of the plate on the same horizontal line as the power source) would rise, thus raising the temperature with respect to melting at the weld and pushing out the melting isotherm to create taper (divergence in weld bead). But taper was not observed (1) on weld beads on quarter inch flat plates, insulated except for the edges and the torch path. Taper was not detected even for the narrowest plate, where weld diameters were measured with a microscope (1). Thus, to fully understand the mechanisms of heat flow during welding, the following experiments were performed.

EXPERIMENTS

One pass, bead on plate welds were performed on two vertical plate configurations. The first configuration is flat plate 61 x 20.3 x 0.64 cm (24 x 8 x 0.25 in). A matrix

(4 rows x 6 columns) of K (k-20-TT AWG) type thermocouples were imbedded on the right side of the panel. The first and third rows were 8.928 cm (3.515 in) from the bottom and top edges of the plate, respectively. While the second and fourth rows were imbedded at the middle (30.5 cm, 12 in) of the front and back of the panel, respectively. The thermocouple columns were 1.52, 2.54, 3.81, 5.08, 7.62, and 10.16 cm (0.6, 1.0, 1.5, 2.0, 3.0, 4.0 in) from the center of the weld (plate), respectively. The last thermocouple in each row was imbedded in the center of the plate's edge.

The second configuration was similar except that the thickness of the plate was 2.54 cm (1.0 in). Also, through the length of the center there was a groove 1.95 cm (0.768 in) wide and 0.848 cm (0.334 in) deep.

The numbering of the thermocouples started as TC 1 closest to the weld at the bottom row and continued outward, then followed by TC 7 at the middle in the vicinity of the weld and the same pattern continued to TC 18 at the edge of the top row. TC 19 was reserved to measure the laminar boundary layer temperature at the far bottom end of the plate. Finally, the back row started with TC 20 through TC 24 and it shared the edge thermocouple TC 12 with the front middle row.

Imbedding of thermocouples was preferred to surface attachment for several reasons: the high temperature cement was brittle in contrast to imbedding which was very strong. Also, imbedding provided better accuracy in positioning the thermocouples. Finally, with imbedding there should be no worries of misapplication of the cement, i.e. it will not seep beneath the bead and act as an insulation between the thermocouple and the work-piece.

The shielded thermocouples were attached to a Molydacq data acquisition system.

During welding temperature fields were monitored by an Inframetrics, model 600 infrared imaging radiometer.

The power produced by the source was 4.19 kW for the first configuration, the torch speed was 0.466 cm/s (11 in/min) and the VPPA welding started 3.15 cm (1.24 in) from the bottom of the plate. While welding started at 3.32 cm (1.307 in) from the bottom of the second configuration, with a torch velocity of 0.161 cm/s (3.8 in/min) and the source power was 10.1 kW.

RESULTS AND DISCUSSION

The temperature profile in the vicinity of the torch, i.e. from the start of melting through the width of the plate is shown in Figure 1. The location of the liquidus point (643 C) and the solidus point (543 C), were determined by examining macroscopically treated specimens under the microscope.

Figure 2 a, b, c, and d shows the raw data, for the first configuration, for the bottom, middle front (facing the torch), middle back, and the top rows of data, respectively. Figure 2 represents the temperature rise from the start of welding to the end for each thermocouple, i.e. it shows the temperature rise for stationary locations as the torch moves. Examining the locations aligned parallel, close to the bead, it is observed that before the torch approaches any one of these locations there is a very small temperature rise. But as the torch becomes almost in the vicinity of that location there is a sudden sharp temperature rise which drops less abruptly as the torch moves away and levels up giving an average temperature higher than the initial plate temperature. The thermocouples were scanned once every 10 s, i.e. every 4.65 cm (1.83 in). This did not allow recording the thermocouple reading when the distance between it and the torch was the shortest. But, the bottom thermocouple (TC 1) recorded a temperature reading when the torch passed it with 0.254 cm (0.1 in), and this was the highest reading recorded for any thermocouple location as you can see comparing Figure 2 a, b, c, and d. Examining the locations parallel and farther from the weld, a gradual increase in temperature is noticed before it levels off.

As mentioned in the previous paragraph abrupt elevation in temperatures are observed only in the close proximity of the torch. This was also supported by thermography as seen in Figure 3, where the temperature isotherms have an elliptic shape.

The scatter in the power estimates made using the moving line source were within the expected order of magnitude behind and in the immediate vicinity of the torch. A power transfer efficiency of 39 % was obtained in the vicinity of the torch. Care should be exercised in estimating the power from the temperature field in front of the power source (torch) as these are very sensitive to uncertainties in physical properties and temperature measurement errors. Some of these locations ahead of the power source recorded a rise in temperature of 2.5 C, while the measurement error limit is 2.2 C. To illustrate the sensitivity to physical properties a decrease of 15 % in the thermal diffusivity at a location 1.5 cm beside the weld center and 1.4 cm. ahead of the power

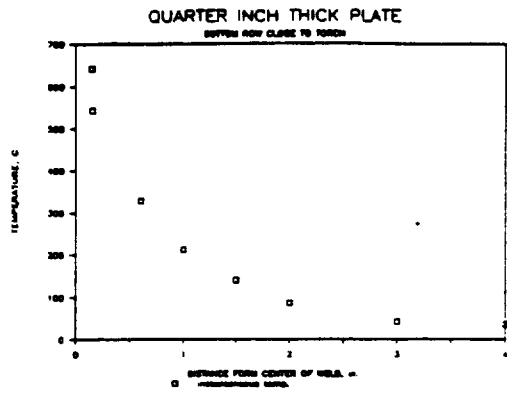


Figure 1: Temperature profile next to the power source.

Figure 2: Temperature fields at local positions as the power source moves upwards on a vertical plate. →

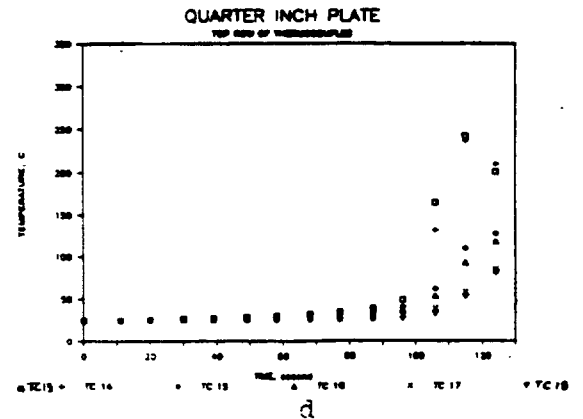
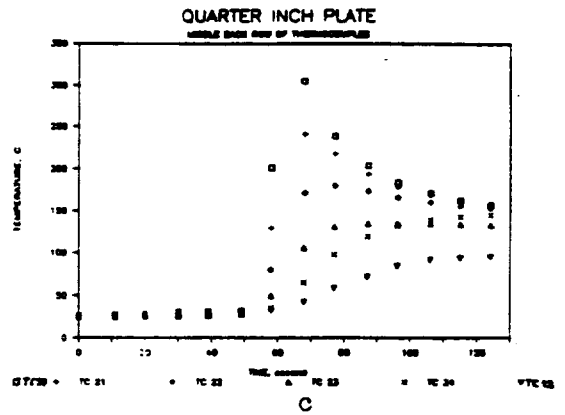
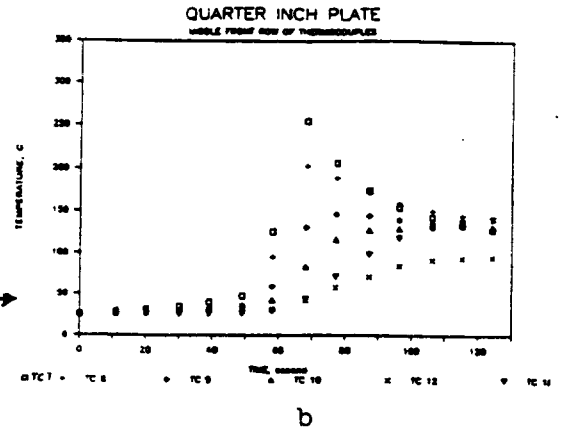
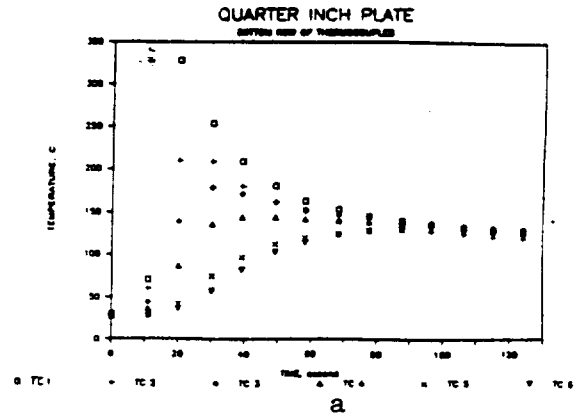


Figure 3: Isotherms during welding as shown by infrared thermography on a flat plate.

source shows an increase of 13 % in power, while for the same conditions if the distance ahead of the center of the power source was 2.8 cm. an increase of 95 % in the power calculated. But estimating the temperature field using the moving line source equation for a power absorption of 1.65 kW gave similar temperature field to that determined experimentally.

Rough estimates of natural convective losses, and thermal radiation from the plate are not large, e.g. natural convection at a constant plate temperature of 127 C is less than 10 % of the power absorbed by the work piece.

CONCLUSIONS

The average temperature rise of the work-piece was contained in the temperature hump behind the torch. The temperature field of a VPPA weld on a one pass bead on flat plate is similar to that for a moving point source on an infinite plane.

There was negligible change in the effective ambient temperature of a flat plate. Consequently, there is no measurable taper in weld width.

Power estimates made using the moving point source solution are reasonable in the vicinity of the power source, although power estimates from the temperature field in front of the power source are too sensitive to uncertainties in physical properties and temperature error to yield useful value.

Natural convection and thermal radiation losses from the work-piece outside the puddle are not large (according to rough estimates).

REFERENCES

1. Abdelmessih, A. N., "Heat Sink Effects in Variable Polarity Plasma Arc Welding," NASA CR-184253, "Research Reports - 1991 NASA/ASEE Summer Faculty Fellowship Program," pp A - A5, October 1991.
2. Rosenthal, D., "The Theory of Moving Sources of Heat and Its Application To Metal Treatments," Trans. ASME, Vol. 68, 1946, c.f. (3).
3. Schneider, P. J., "Conduction Heat Transfer," pp 284 - 290, Addison-Wesley Reading, MA, 1955.

N98-17281

1992

NASA/ASEE SUMMER FACULTY FELLOWSHIP PROGRAM

MARSHALL SPACE FLIGHT CENTER
THE UNIVERSITY OF ALABAMA

SYSTEMS ENGINEERING PROCESS AND ORGANIZATION ASSESSMENT

Prepared By:	Robert G. Batson, Ph.D.
Academic Rank:	Professor
Institution and Department:	The University of Alabama Department of Industrial Engineering
NASA/MSFC:	
Laboratory: Division:	Systems Analysis and Integration Systems Analysis Division
MSFC Colleague(s):	L. Don Woodruff Glen D. Ritter

The systems engineering (SE) process for space systems is a disciplined approach used by both NASA/MSFC and its contractors to convert mission needs into a system specification, the key technical input to NASA Phase C Detail Design activities. Although only 5% of the program effort is expended during Phase A Preliminary Analysis and Phase B Definition, 85% of the program cost is determined by the end of Phase B. The responsibility for SE work at the Center during Phases A, B, and C rests primarily with two organizations: Program Development, which manages Phase A&B; Systems Analysis and Integration Lab, whose involvement begins in Phase B and continues throughout Phase C.

The purpose of this report is to briefly summarize the results of an eight week assessment of NASA/MSFC Phase A and Phase B systems engineering processes, methodologies, and activities. Specifically, fourteen inconsistencies or weaknesses were identified and recommendations for corrective action were generated. A 1.5 hour briefing on these results was given in EL51 on 8-11-92; that documentation is available from the author or either NASA Colleague.

The first group of inconsistencies or weaknesses deals with the existing approach and organizational issues to provide SE support during Phase B:

- 1.1 Too many system development projects at MSFC, which result in:
 - Low utilization of engineering manpower to do value-adding work, because they are matrixed to too many projects (two is considered optimal);
 - SE manpower focused on Phase C/D work, not Phase B.
- 1.2 Variable documentation at the end of Phase A and Phase B, which induces rework at the start of the next phase.
- 1.3 System development times too long--in some cases 20 years from start of Phase A to operations.
- 1.4 Phase B program risk analysis capability weak-to-non-existent.
- 1.5 Trade study management procedures, associated cost and effectiveness models, and decision-structuring aids appear weak-to-non-existent.

Recommendations to resolve these problems were to:

- Control release of projects into new phases in order to reduce the number of programs "active" at NASA/MSFC to better match resources available in S&E labs.
- Realign technology R&D at the Center to meet the needs of approved programs.
- Develop standards for technical documentation that Phase A and Phase B NASA/MSFC project teams must produce, regardless of who is "customer organization."
- Consider breaking Phase B Definition into two subphases, B1 System Definition and B2 Design Definition, as does the Department of Defense (DOD). Also, appoint a Chief Systems Engineer for Phase B.
- Make a concentrated, center-wide effort to reduce development times (for cost savings) and yet meet project milestones as they were originally planned during Phase A.
- Obtain maximum benefit from development of in-house prototypes.
- Develop the capability in SE to identify and make visible to management the technical risks inherent in a technology, a design solution, or an entire design concept.
- Consider developing the expertise to convert quantified technical and programmatic risks into program risk assessments, for the purpose of early, preventive action by program managers and the chief engineers.
- Commit to becoming a world-class practitioner of system engineering methodologies that permit prediction of life-cycle cost and system effectiveness based on the technical parameters and performance characteristics of a proposed product and its associated processes.
- Establish SE's role as trade study coordinator for all Phase B projects.

The second group of inconsistencies or weaknesses deals with the approach used to plan and manage in-house SE activities:

- 2.1 NLS Definition Phase Implementation Plan, as an example, lacks necessary details on study process flow, systems analysis and control procedures, and outlines of target documents.
- 2.2 A critical task during Phase B is the preparation of a Systems Engineering Management Plan (SEMP) for Phase C, because this document is the description of the Phase C technical work will be controlled. This task was omitted from the NLS planned work.
- 2.3 RIDs prior to release of system spec into Phase C are indicative of changes needed in Phase B responsibilities, staffing, processes and documentation.
- 2.4 The MSFC SE Handbook leaves some critical SE concepts, such as traceability of a requirement, baseline control, "how to" for technical risk analysis, and others unaddressed, and must be improved.
- 2.5 In-house projects must be forced to conform to a standardized process (with project-specific variations, of course) which included periodic screening for technical leadership, documentation, and process flow.

The missing items from the NSL Implementation Plan were classified into general descriptions, Phase B tasks, and Phase B outputs. The purposes of a SEMP were described, and a comparison of SEMP outlines suggested in MIL-STD-499A and MIL-STD-499B was prepared. The need to adopt a MSFC standardized SEMP contents, and to require preparation of a SEMP by Phase C contractors (or MSFC engineers, in the case of in-house Phase C) was emphasized. It was recommended to use the record of RIDs and their source/disposition on numerous previous programs in a type of "process diagnosis" in order to discern causes embedded in the way Phase B and the preparation of the Phase C plans are conducted. Suggestions for revisions of the SE Handbook were made.

The final set of inconsistencies and weaknesses deals with PD and S&E involvement and phasing during Phases A&B. Problems identified were:

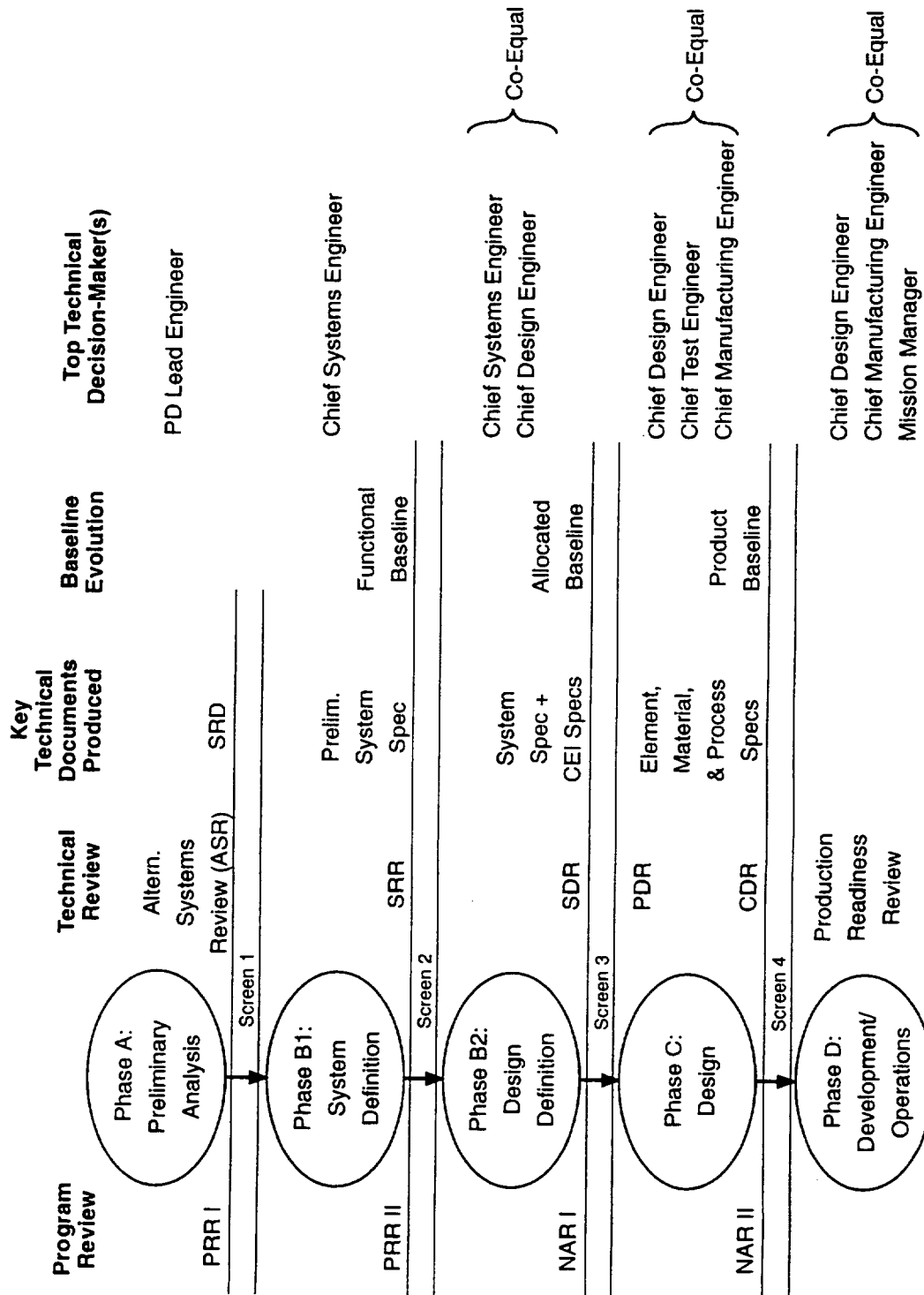
- 3.1 Phase A technical documentation not well-defined in terms of content, and there is no concept of "customer needs" for the documentation.
- 3.2 PD has little guidance in their "Lead Engineer's Handbook" on how to conduct Phase B.
- 3.3 Phase A and Phase B project teams are apparently chronically understaffed.
- 3.4 Phase B responsibilities, staffing, study processes, and target documentation are vaguely defined in both PD and SE guidance documents.

Recommendations were to adopt the System Requirements Document (SRD) as the target technical document for Phase A Study Teams. Also, Phase A Study Teams must become much more disciplined in the way they document their sources, analyses, requirements, and design concept. Also, it was recommended that a Phase B CSE from S&E be appointed to lead systems requirements work during Phase B, placing control on all Phase B technical matters within S&E. Phase B program managers under this proposal would continue to reside in PD, and the control of all Phase B programmatic matters and customer interfaces would continue under the control of PD. Finally, it was recommended that NASA/MSFC formalize the study process flow for Phase B and that the focus of each subphase be on producing the following documents:

- Phase B1: Preliminary System Spec (System Functional Baseline)
- Phase B2: System Spec and Various Item Development Specs (System Allocated Baseline)

The figure on page II-3 summarizes the reviews, key documents, baselines, and decision authority recommended for a revised NASA/MSFC development life-cycle.

Concept for Managing MSFC In-House Development Projects



5-18258

N98-17282

1992

NASA/ASEE SUMMER FACULTY FELLOWSHIP PROGRAM

MARSHALL SPACE FLIGHT CENTER
THE UNIVERSITY OF ALABAMA

UPDATING AND EXPANDING
THE LIBRARY OF MATERIALS ON
NASA SPACELINK ELECTRONIC INFORMATION SYSTEM

Prepared By:	Jean A. Blake, Ph.D.
Academic Rank:	Professor
University and Department	Alabama A & M University Department of Mathematics
NASA/MSFC:	
Division:	Public Affairs Office
Branch:	Education
MSFC Colleagues:	Jeffrey S. Ehmen William E. Anderson

INFORMATION SUMMARY

NASA Spacelink, a proven resource medium, may be accessed over telephone lines or via the Internet by teachers or anyone with a computer or modem. It is a collection of historical and current information on NASA programs and activities. Included in this library is information on a variety of NASA programs, updates on Shuttle status, news releases, aeronautics, space exploration, classroom materials, NASA Educational Services, and computer programs and graphics. The material stored in Spacelink has found widespread use by teachers and others, and is being used to stimulate students, particularly in the area of aerospace science.

To refurbish the system I assisted in updating and expanding the NASA Spacelink collection.

To accomplish this I used computer equipment in:

- Editing documents for the system.

- Modifying and testing menus for the system.

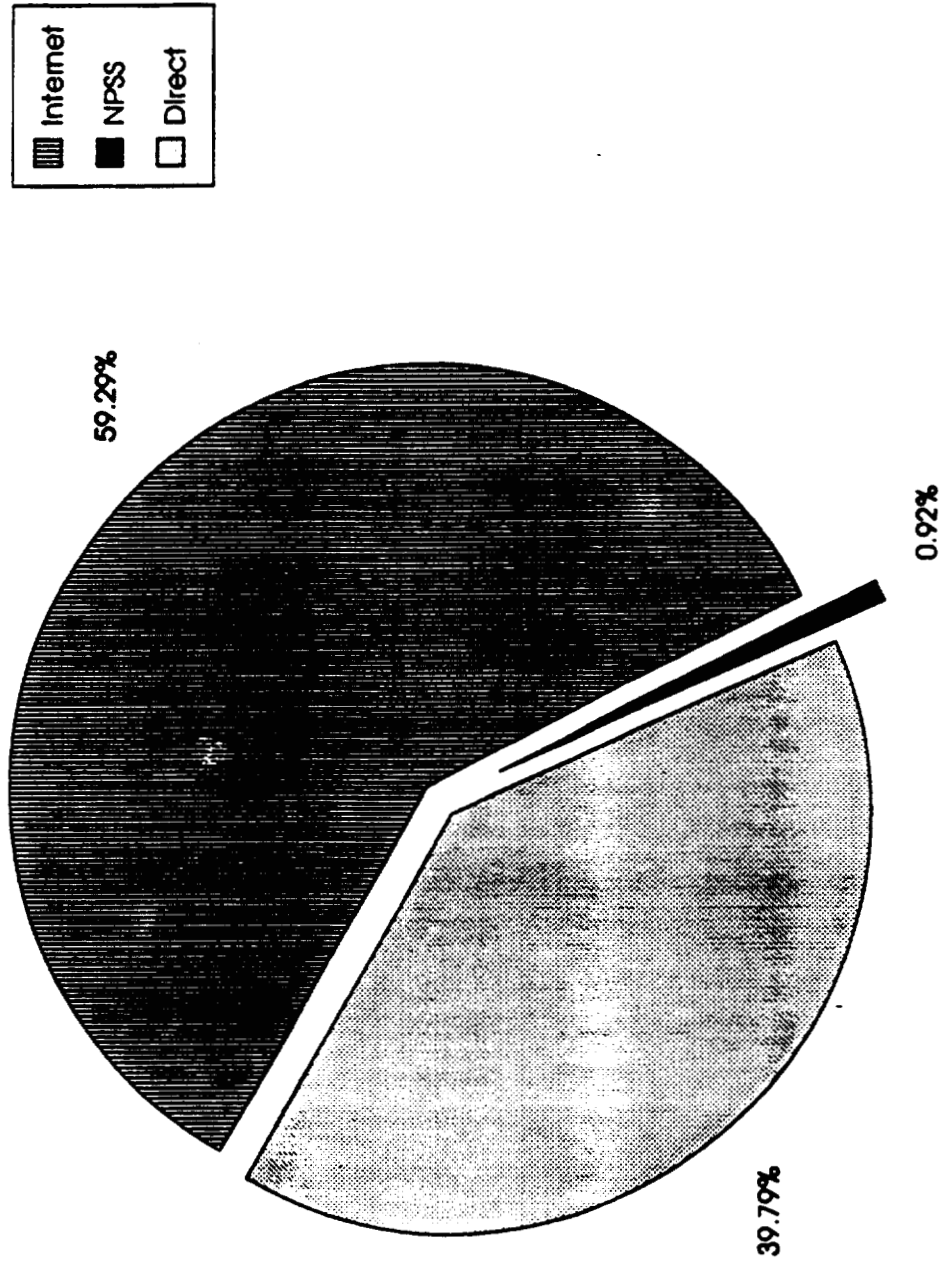
- Updating and entering information in the system.

- Rendering the available information more accessible to the Spacelink user.

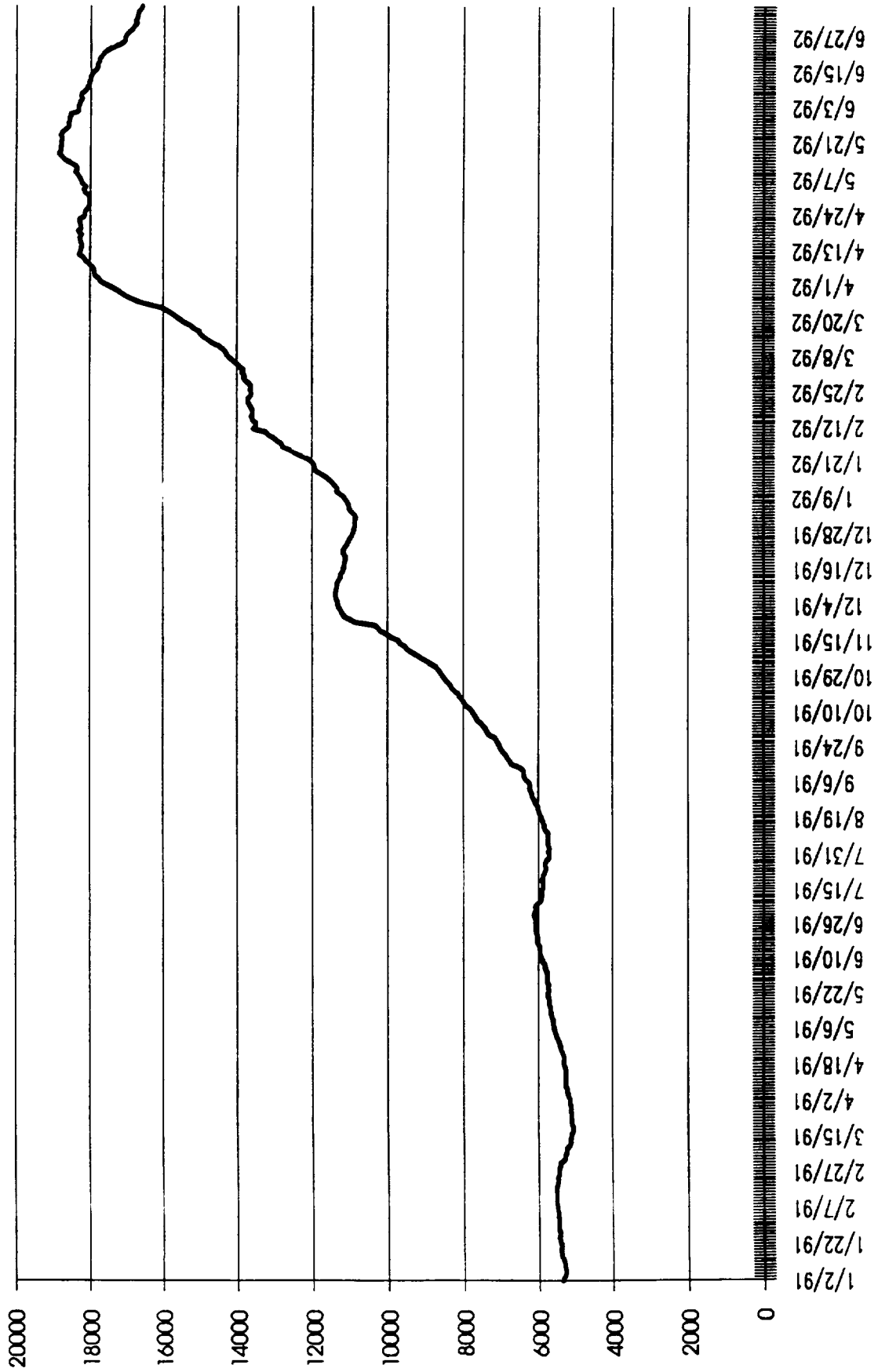
- Converting Macintosh based documents to Standard Text Form (ASCII) and uploading to system for posting.

The accompanying four charts -- NASA Spacelink Source of Callers, NASA Spacelink Registered Users, NASA Spacelink Growth by User Type, and NASA Spacelink Usage Statistics -- give a partial summary of Spacelink's usage, and attest to the fact that Spacelink is indeed a very worthwhile NASA investment.

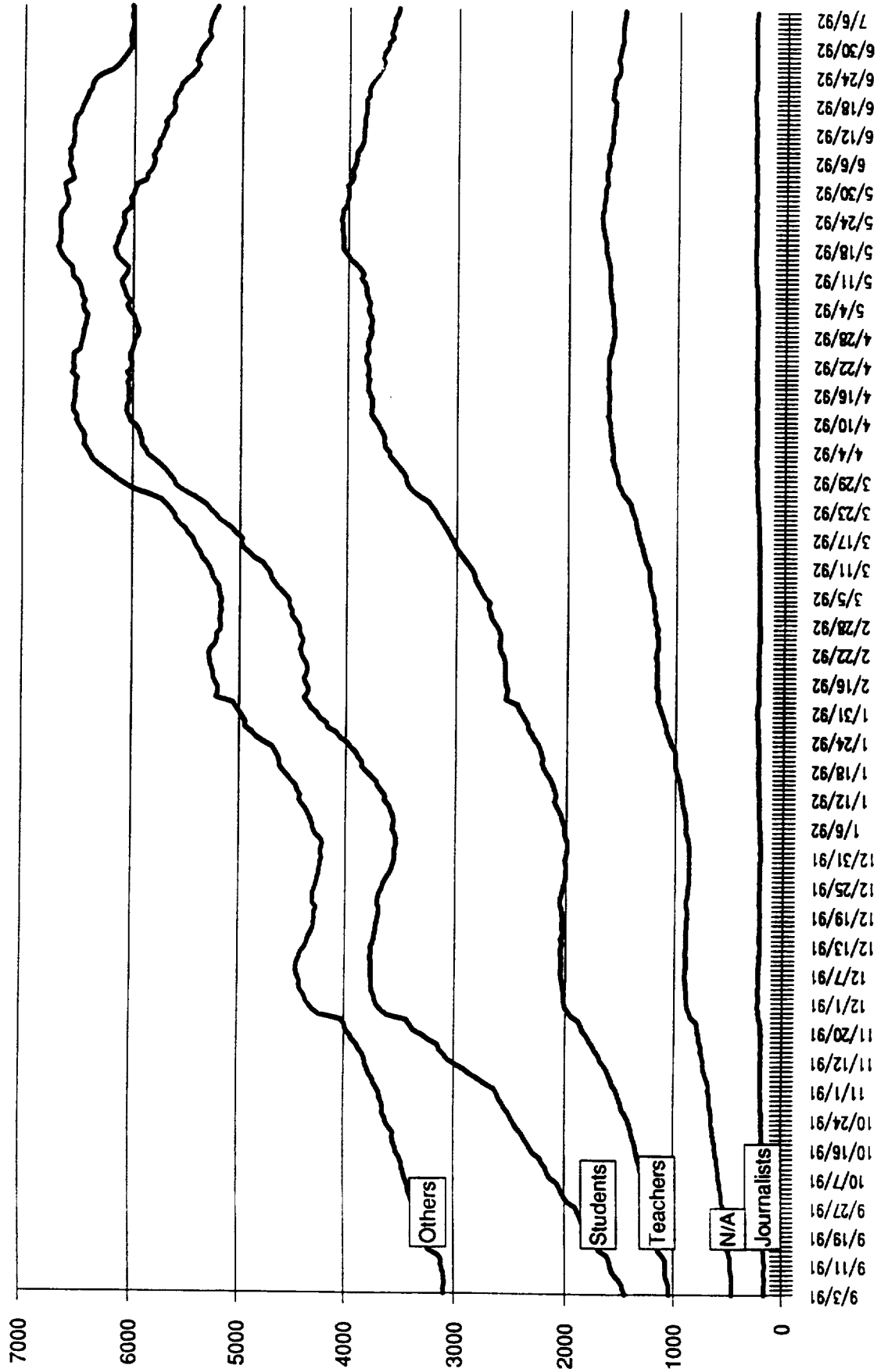
NASA Spacelink Source of Callers



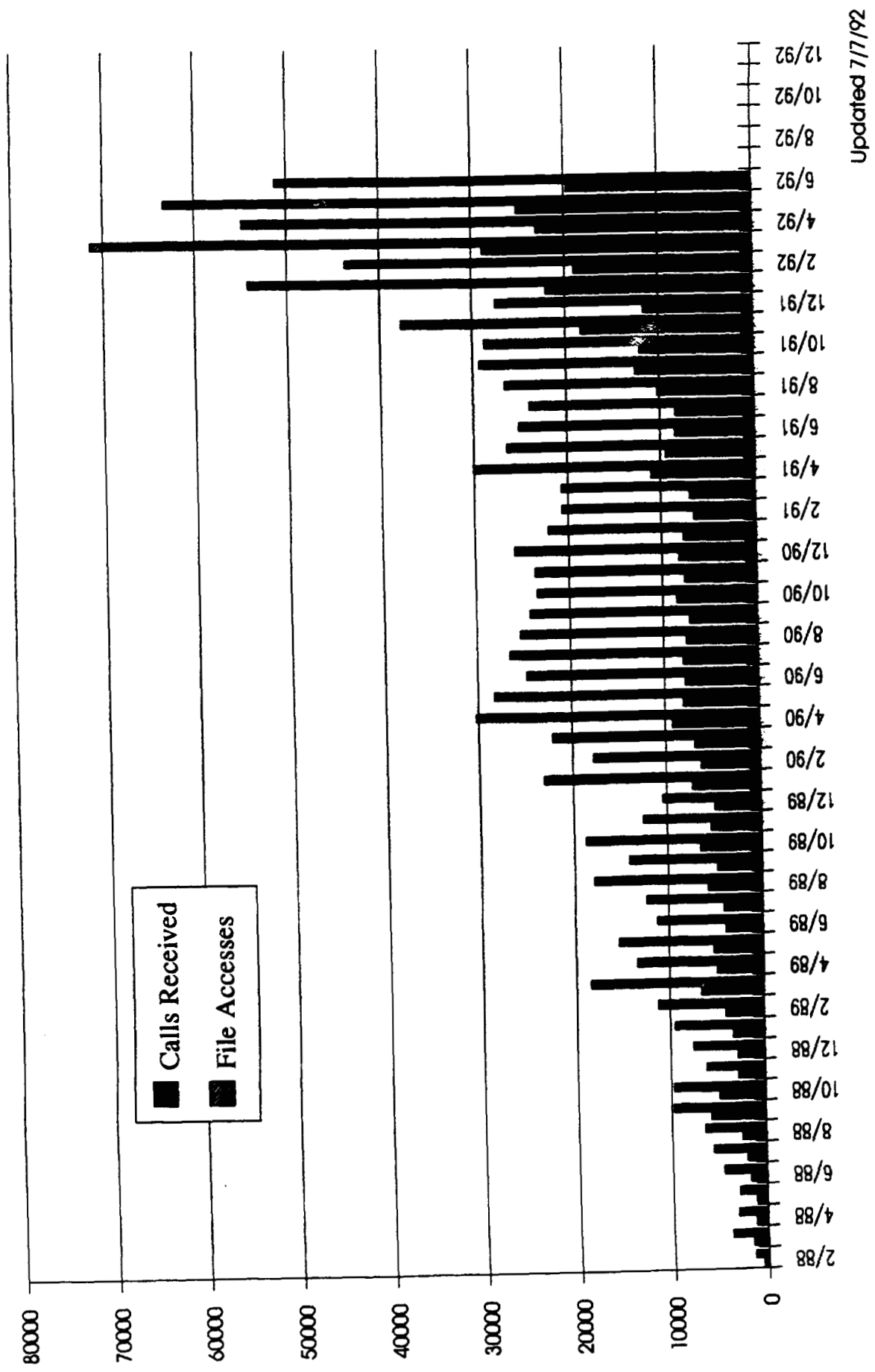
NASA Spacelink Registered Users



NASA Spacelink Growth by User Type



NASA Spacelink Usage Statistics



N 9 3 - 1 7 2 8 3

1992

NASA / ASEE SUMMER FACULTY FELLOWSHIP PROGRAM

**MARSHALL SPACE FLIGHT CENTER
THE UNIVERSITY OF ALABAMA**

DESIGN AND ANALYSIS OF SEALS FOR EXTENDED SERVICE LIFE

Prepared By: Mark V. Bower, Ph.D., P.E.

Academic Rank: Assistant Professor

Institution and Department: The University of Alabama in Huntsville
Department of Mechanical and Aerospace Engineering

NASA / MSFC:

Laboratory: Propulsion Laboratory
Division: Component Development Division
Branch: Mechanical Systems Development Branch

MSFC Colleagues: Thomas D. Bechtel
Brian K. Mitchell

Introduction

Space Station Freedom is being developed for a service life of up to thirty years. As a consequence, the design requirements for the seals to be used are unprecedented. Full scale testing to assure the selected seals can satisfy the design requirements are not feasible. As an alternative, a sub-scale test program[4] has been developed by MSFC to calibrate the analysis tools to be used to certify the proposed design. This research has been conducted in support of the MSFC Integrated Seal Test Program. The ultimate objective of this research is to correlate analysis and test results to qualify the analytical tools, which in turn, are to be used to qualify the flight hardware.

Seals are simple devices that are in widespread use. The most common type of seal is the O-ring. O-rings seals are typically rings of rubber with a circular cross section. The rings are placed between the surfaces to be sealed usually in a groove of some design. The particular designs may differ based on a number of different factors. This research is totally focused on O-rings that are compressed by perpendicular clamping forces. In this type of seal the O-ring is clamped between the sealing surfaces by loads perpendicular to the circular cross section.

In spite of the relative simplicity of the O-ring it does not lend itself to analysis. Which is why O-rings have been so frequently designed based on handbook values, without extensive analysis. O-ring analysis is complicated by the inherent nonlinearities in the problem. The O-ring problem involves nonlinear geometric effects; due to the contact, or moving boundary, problem and the large deformations. It also involves nonlinear material effects; due to the material nonlinearities at large deformations (hyperelasticity) and the viscous behavior of the material (viscoelasticity). Current advancements in computational methods have led to the development of the tools that are capable of handling the O-ring problem.

Specific Problem Addressed

There are four basic design parameters that are to be considered in the development of an O-ring seal: O-ring cross sectional diameter, groove design, O-ring squeeze, and material. In this research a single O-ring diameter was considered. Groove design is typically selected from one of four fundamental groove shapes: rectangular – no side wall contact, rectangular – side wall contact, dove tail, and half-dove tail. This research addresses both types of rectangular grooves, and the half-dove tail design. The O-ring squeeze levels range from 10% to as much as 50%. In this research three squeeze levels were considered: 15, 25, and 40%. The materials studied were selected from candidate materials for Space Station Freedom: Viton (Parker V747) and Silicone (Parker S383).

Method of Approach

The designs considered in this research were analyzed using a commercial finite element analysis code: ABAQUS by Hibbitt, Karlsson, and Sorensen, Incorporated. Preliminary model development was accomplished using EMS and IFEM by Intergraph and translation to ABAQUS and post processing using PATRAN by PDA. ABAQUS is a multipurpose finite element program developed without the classical assumptions of small displacements and rotations. It was used in this research because of its ability to analyze contact problems, nonlinear material behavior, and viscoelastic response.

Three finite element models were developed. Although O-rings present natural symmetries that may be used advantageously to reduce model size, symmetry was not used in any of the models developed. This was motivated by the desire to include axisymmetric behavior and pressure loads on internal surfaces. In the model development care was exercised to limit the number of triangular elements in the models. Further care was exercised to limit the skewness of the elements, maintain uniform element size, and maintain element aspect ratios near one. The models developed are shown in Figure 1 and the significant model characteristics listed in Table 1.

Table 1. Finite Element Model Characteristics.

Model	Number of Nodes	Total Number of Elements	Number of Triangular Elements
Coarse	202	86	4
Intermediate	633	244	8
Fine	1295	840	16

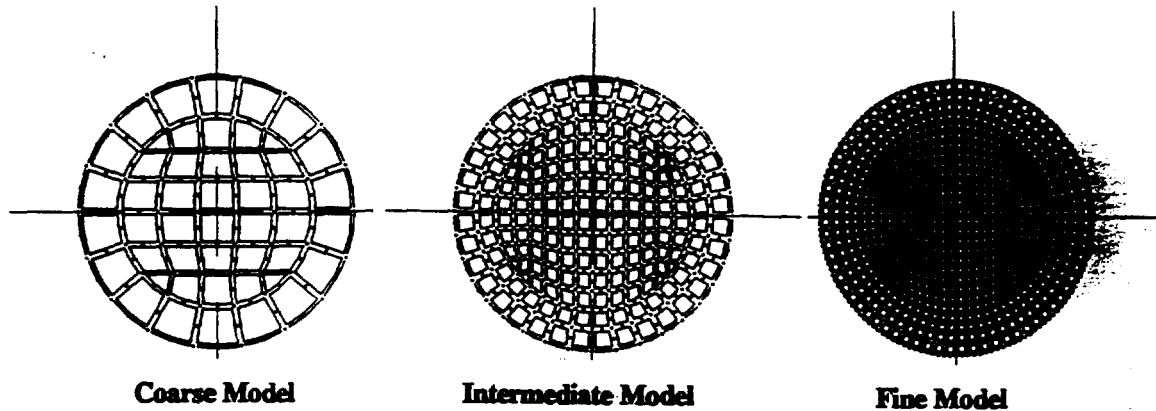


Figure 1. O-Ring Finite Element Models.

The contact problem was analyzed through use of special purpose elements within ABAQUS. These elements require definition of the rigid surfaces in the model. The side wall contact – rectangular groove and the half dove-tail groove are shown in Figure 2. Note in the figure that the groove dimension change based on the squeeze used. The rigid surfaces are defined through use of line and arc segments. The letters in the figure designate ends of the segments and the numbers indicate the centers of the arcs. The coordinates of these points are listed in Tables 2 and 3.

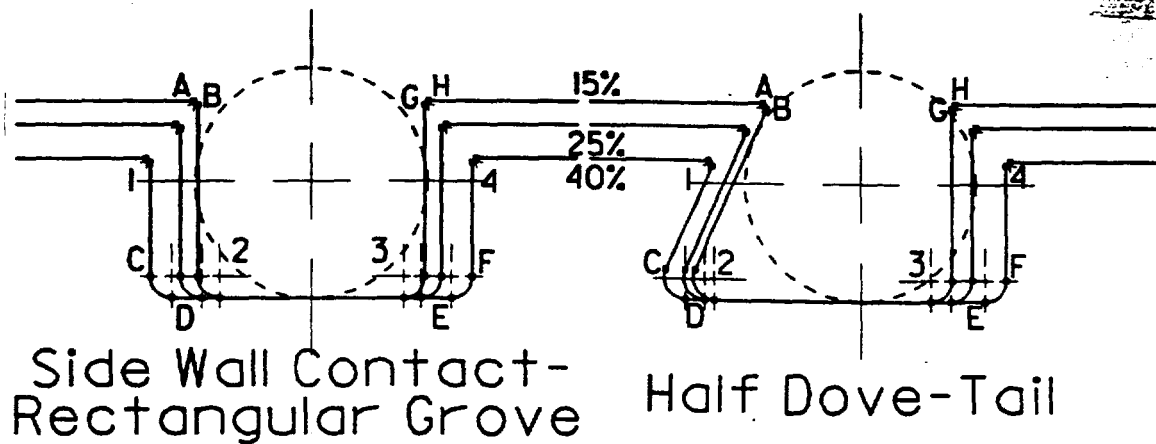


Figure 2. Candidate Groove Designs as Investigated.

Results

PATRAN and a special purpose program were used to analyze the results generated by ABAQUS. A separate translator was used to translate the results into PATRAN. This translator at this time does not support the contact element or apparently the axisymmetric elements in ABAQUS. PATRAN was used to produce plots of the deformed geometries, as shown in Figure 3, and contour plots of the stresses in the O-ring. Figure 3 shows three typical deformed geometries, 15% squeeze with no side wall contact, 15% squeeze with side wall contact, and 25% squeeze with side wall contact. Note the smaller contact areas on the horizontal surfaces for the higher squeeze. This is due to the different groove dimensions between the models.

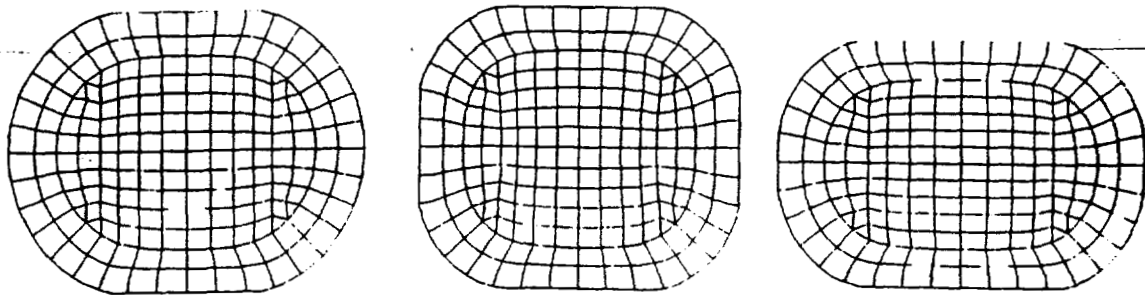
The translator files were used to calculate a von Mises stress and the strain energy at each node. These values were also plotted using PATRAN.

Table 2. Side Wall Contact - Rectangular Groove Coordinates Relative to O-Ring Center.
All units are in inches.

Position	15% Squeeze		25% Squeeze		40% Squeeze	
	x	y	x	y	x	y
A	-0.1395	0.0965	-0.1600	0.0685	-0.1960	0.0275
Center - 1	-0.1395	0.0915	-0.1600	0.0635	-0.1960	0.0225
B	-0.1345	0.0915	-0.1550	0.0635	-0.1910	0.0225
C	-0.1345	-0.1125	-0.1550	-0.1125	-0.1910	-0.1125
Center - 2	-0.1095	-0.1125	-0.1300	-0.1125	-0.1660	-0.1125
D	-0.1095	-0.1375	-0.1300	-0.1375	-0.1660	-0.1375
E	0.1095	-0.1375	0.1300	-0.1375	0.1660	-0.1375
Center - 3	0.1095	-0.1125	0.1300	-0.1125	0.1660	-0.1125
F	0.1345	-0.1125	0.1550	-0.1125	0.1910	-0.1125
G	0.1345	0.0915	0.1550	0.0635	0.1910	0.0225
Center - 4	0.1395	0.0915	0.1600	0.0635	0.1960	0.0225
H	0.1395	0.0965	0.1600	0.0685	0.1960	0.0275

Table 3. Half Dove-Tail Groove Coordinates Relative to O-Ring Center.
All units are in inches.

Position	15% Squeeze		25% Squeeze		40% Squeeze	
	x	y	x	y	x	y
A	-0.1162	0.0965	-0.1402	0.0685	-0.1810	0.0275
Center - 1	-0.1162	0.0915	-0.1402	0.0635	-0.1810	0.0225
B	-0.1116	0.0895	-0.1356	0.0615	-0.1764	0.0205
C	-0.1970	-0.1023	-0.2086	-0.1023	-0.2311	-0.1023
Center - 2	-0.1742	-0.1125	-0.1857	-0.1125	-0.2082	-0.1125
D	-0.1742	-0.1375	-0.1857	-0.1375	-0.2082	-0.1375
E	0.0835	-0.1375	0.1075	-0.1375	0.1475	-0.1375
Center - 3	0.0835	-0.1125	0.1075	-0.1125	0.1475	-0.1125
F	0.1085	-0.1125	0.1325	-0.1125	0.1725	-0.1125
G	0.1085	0.0915	0.1325	0.0635	0.1725	0.0225
Center - 4	0.1135	0.0915	0.1375	0.0635	0.1775	0.0225
H	0.1135	0.0965	0.1375	0.0685	0.1775	0.0275



15% No side wall Contact

15% Side Wall Contact

25% Side Wall Contact

Figure 3. Typical Deformed Geometries.

Conclusions

ABAQUS is an excellent tool for addressing seal performance. However, at this time the program is not capable of performing hyperelastic-viscoelastic analyses. For viscoelastic analyses the program is limited to elastic-viscoelastic analyses. This addresses the nonlinear aspect of the contact problem and the associated large deformations, but does not include the nonlinear material behavior associated with the large deformations.

A second, potentially less troublesome, limitation of the code is the limitation to a single time dependent material property. In the code the shear stress relaxation modulus and the bulk stress relaxation modulus differ only by a scale factor (which can be zero). This may not be an accurate description of the material behavior.

Acknowledgment

The author wishes to express his thanks to Mr. Brian Mitchell and Mr. Thomas Bechtel for a productive and enjoyable summer. It has truly been a pleasure to work with people who are motivated and dedicated to do their jobs, willing to go the extra mile to ensure that the job is done right. Thanks are also given to Mr. Pat Rodgers (ED24) for his support and advice. Further thanks are offered to Dr. Roy Sullivan (ED24) for his invaluable assistance. IXΘΥΣ.

References

- 1 ABAQUS Theory Manual, Version 4.8, Hibbitt, Karlsson, & Sorensen, Inc., Pawtucket, RI, 1989.
- 2 ABAQUS Users' Manual, Version 4.8, Hibbitt, Karlsson, & Sorensen, Inc., Pawtucket, RI, 1989.
- 3 Krevelen, D.W. van, Properties of Polymers: Their Correlation with Chemical Structure; Their Numerical Estimation and Prediction from Additive Group Contributions, 3rd Edition, Elsevier Scientific Publishing Company, Amsterdam, 1990.
- 4 Mitchell, B.K. and Flatt, L.W., "Design Parameter Test Plan for MSFC Integrated Seal Test Program," NASA/MSFC, 1992.
- 5 Staverman, A. J. and Schwarzl, F., "Linear Deformation Behavior of High Polymers," in Die Physik Der Hochpolymeren: Theorie und Molekulare Deutung Technologischer Eigenschaften von Hochpolymeren Werkstoffen, pp.1-121. Edited by: Stuart, H.A., Springer-Verlag, Berlin, 1956.
- 6 Staverman, A. J. and Schwarzl, F., "Non Linear Deformation Behavior of High Polymers," in Die Physik Der Hochpolymeren: Theorie und Molekulare Deutung Technologischer Eigenschaften von Hochpolymeren Werkstoffen, pp.126-158. Edited by: Stuart, H.A., Springer-Verlag, Berlin, 1956.

N 9 3 - 1 7 2 8 4

1992

NASA/ASEE SUMMER FACULTY FELLOWSHIP PROGRAM

MARSHALL SPACE FLIGHT CENTER
UNIVERSITY OF ALABAMA

SHUTTLE FLIGHT EXPERIMENT PRELIMINARY PROPOSAL:
DEMONSTRATION OF WELDING APPLICATIONS IN SPACE

Prepared by:	William V. Brewer, Ph.D.
Academic Rank:	Associate Professor
Institution and Department:	Jackson State University School of Science & Technology Technology

NASA/MSFC:

Office:	Materials & Processes Laboratory
Division:	Process Engineering
Branch:	Metals Processes

MSFC Colleagues:	Clyde S. Jones, III Carolyn K. Russell
------------------	---

INTRODUCTION

In June 1991 work was initiated at MSFC on an end-effector for "Robotic Assembly of Welded Truss Structures in Space", (1). The case for welded joint assembly on orbit was discussed in the 1991 SFFP Final Report "D", (2). Data drawn from Aerobrake studies (supported by the ISAAC program) allowed the more detailed investigations that accompany a design with relatively concrete goals. This principle guides current efforts to develop scenarios that further demonstrate the utility of welding for space construction and (or) repair.

FX MODULES

Local consensus guided the choice of representative weld joints, called FX (flight experiment) modules, that would be of general utility for space construction. These are listed in order of increasing difficulty of execution:

- I. Linear Seam Butt Weld
- II. Orbital Butt Weld
- III. " Lap "
- IV. " Elliptical Butt Weld
- V. Saddle Patch Lap Welded on a Pipe
- VI. Patch on a Large Diameter Pressure Vessel

For each module a scenario is hypothesized anticipating a need for that weld in an example application.

For each scenario simulations were then constructed ranging from the simple and inexpensive to higher fidelity and most expensive. A simulation considered:

- A. Location, Manipulation and Guidance of --
 1. component parts to be assembled;
 2. torch that performs the joining of them.
- B. Welding parameters that would optimize the joint.

Generally, the crudest simulations were prelaunch assembled parts joined on orbit by a weld torch constrained to move along a fixed path. Hard automation for on-orbit component assembly is a step toward higher fidelity. A fully robotic process represents the ultimate simulation.

INTEGRATION

Combination of the modules into a flight experiment package is the next task. Fidelity vs. cost is again a major consideration. Reliability vs. cost becomes an added concern. In the event of a critical path failure, damage to the results would be minimized if all modules were totally independent having separate utilities, motion systems, and welding torch. Such a degree of redundance, in effect six separate flight experiments, would be expensive. At the

other end of this scale, a single universal robotic end-effector capable of manipulating all component parts and performing all weld types would be ideal. It would also be expensive. End-effector complexity and its associated high developmental cost would be incurred in pursuit of reliability for the very interdependent subsystems. The best return on investment lies somewhere between these two extremes.

COMBINATIONS

Modules I. to III. are the easiest to implement.

Modules II. and III., Orbital Butt and Lap Welds respectively, represent fluid tight piping joints (the scenario). These are simulated by assuming one end of the pipe joint has been assembled previously into part of a pipe string. The other end is drawn from a supply and maneuvered into position using an axial approach path. Location must be maintained until welding is complete. Assuming robotic, telerobotic, or semirobotic methods would be the most useful for large future projects, a special purpose end-effector is required to accomplish the twin tasks of maintaining the relative position of the joint halves and guiding a weld torch. Welded truss structural joint studies reported last year (2) form a basis for the needed end-effector.

Module I., Linear Butt Weld, is not the simulation of a welding scenario but produces standard specimens for weld quality control studies. These specimens can be mounted on the surface of the same 4" diameter size of pipe selected for simulation of all cylindrical shaped modules (II. thru V.), thus it can be welded using the same end-effector as that intended for Modules II. and III.

Module IV., Orbital Elliptical Butt Weld, was inspired by the scenario: "Robotic Assembly of Welded Truss Structures In Space". In this case parts to be assembled approach each other along a path perpendicular to the strut axes which must remain parallel. This simulates placing a strut between two previously assembled nodes. The same end-effector can accomplish this task also. Modules I. thru IV. are combined.

REDUNDANCY

Module V., Saddle Patch Lap Welded on a Pipe, represents a scenario for a leak fix, mounting boss, or a tap site. Simulation involves pickup and placement of the patch for tack welding, then removal of the placement arm to finish a fluid-tight weld. The previously discussed end-effector could again be used with extensive modifications. These would be difficult to reconcile with requirements for Module IV. Modules I. to III. could be accommodated.

Two end-effectors, one specialized for Module IV. and the other for Module V. are proposed. Both could service Modules I. to III. giving a measure of redundancy while expanding the scope of the experiment. Subsystems for these end-effectors would share many design features to reduce developmental cost.

Module VI. cannot be simulated in combination with any of the other modules in such a way that a realistic scenario would be represented. Since it stands alone, development of it will be least cost effective. It will be developed later.

ASSEMBLY

Simulation of robotic maneuvering of the end-effector relative to module components being assembled is limited to a two d.o.f. motion system configured like an "x,y plotter". All displacements take place parallel to a plane of symmetry that contains the axes of the module's components. Modules are mounted on a rotating drum that presents them sequentially to the end-effector in its plane of motion. It is there that simulated assembly and welding take place.

DESCRIPTION

Figure 1 displays a central plan view with partial end views. Mounting tubes for Modules I. (there are 3 of them) and Module V. span the length of the rotating drum and give it rigidity. On the left end of the drum are mounted fixed half-tubes representing previously assembled components for Modules II. to IV. The right end simulates a "hex-close-pack" supply bundle from which unassembled parts are drawn. At the bottom is the end-effector specialized to assemble Module IV., the truss strut, shown on approach to its assembly site carrying a conjugate tube drawn from supply. The top shows the end-effector specialize for Module V., the saddle patch, with the patch positioned for tack welding.

CONCLUSIONS

Combinations of Flight Experiment Modules that share subsystems will increase simulation fidelity at a reduced developmental cost. Additional reliability can be obtained thru partially redundant end-effectors. This approach gives the most cost effective results.

REFERENCES

- (1) Jones, C. S., Thomas, F. P., Brewer, W. V., "Robotic Assembly of Welded Structures in Space", 4th Flexible Assembly Systems Conference, ASME, Phoenix AZ, 9/13/92.
- (2) Karr, G. R., et al, Research Reports, 1991 NASA/ASEE SFFP MSFC UAH UA, NASA CR-184253, 10/91.

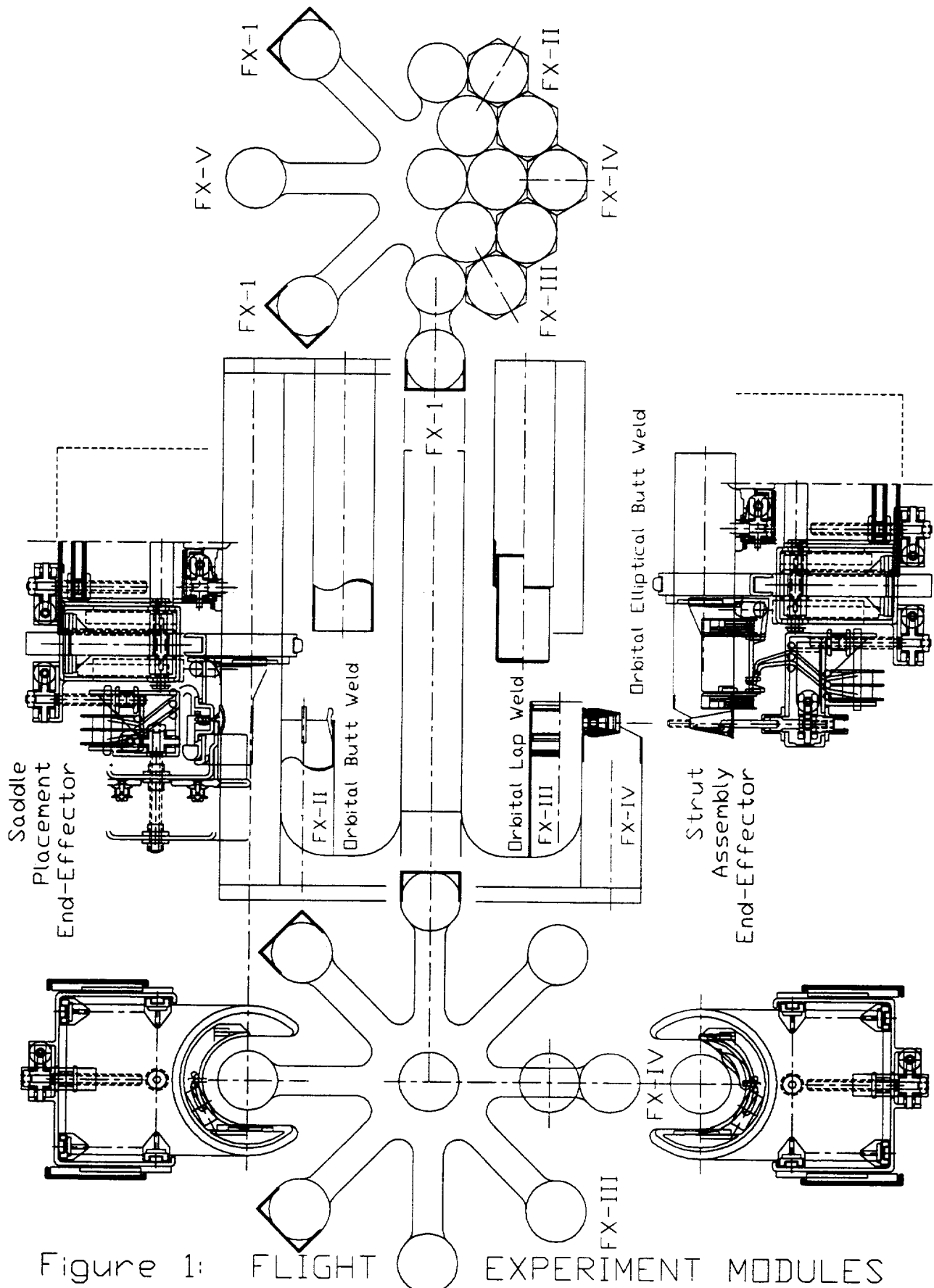


Figure 1: FLIGHT EXPERIMENT MODULES

V-4

ORIGINAL DRAWING
OF POOR QUALITY

Right End View
HEX-CLOSE-PACK
STRUT ASSEMBLY

Plan View
REVOLVING MODULE DRUM
& END-EFFECTORS

Left End View
ASSEMBLED
MODULES

N93-17285

1992

NASA/ASEE SUMMER FACULTY FELLOWSHIP PROGRAM

**MARSHALL SPACE FLIGHT CENTER
THE UNIVERSITY OF ALABAMA**

**INVESTIGATION OF RAINFALL DATA WITH REGARD TO LOW-LEVEL WIND FLOW
REGIME FOR EAST CENTRAL FLORIDA**

Prepared by: Joni Brooks

Academic Rank: Assistant Professor

Institution: Columbia State Community College
Department: Computer Information Systems

NASA/MSFC:

Office: Earth System Analysis Team
Division: Earth Science & Applications
Branch: Environmental Analysis

MSFC Colleague(s): Steve Goodman, Ph.D. - NASA
Bill Crosson, Ph.D. - USRA
Claude Duchon, Ph.D. - Univ. of Oklahoma

Previous research has been conducted to investigate the effect of the low-level wind regime on summertime convective storms in the east central Florida area (Holle et al., 1992). These effects were described by analyzing the distribution of lightning flashes within classifications based on the low-level wind regime for the months June through September of 1987 to 1990. The present research utilizes the same classification strategy to study rainfall patterns for data gathered for the CaPE (Convection and Precipitation/Electrification Experiment) field program. The CaPE field program was conducted in east central Florida from July 8, 1991 to August 18, 1991.

Each day of the study period was classified by calculating the mean wind vector, as described by Watson et al. (1987), from rawinsonde measurements from approximately 0.3 km to 3 km (1000 - 10,000 ft). These data were obtained from the Cape Canaveral sounding nearest to 1000 Greenwich Mean Time (GMT). Seven classes were defined as follows; Calm (wind speed ≤ 2.0 m/s); NE (23° - 113°); SE (113° - 158°); SO (158° - 203°); SW (203° - 293°); NW (293° - 338°); NO (338° - 023°). Fourteen days were identified as SW and will be referred to as disturbed sea breeze days. Twenty five days were classified in the remaining six categories and will be referred to as undisturbed sea breeze days. Sounding data were not available for three days during the study period.

Of the many data sets available from the CaPE field program, three precipitation data sets were utilized for this study. These surface data sets include 20 rain gages from the Kennedy Space Center (KSC) Tropical Rainfall Measuring Mission (TRMM) network, a network of 47 Portable Automated Mesonet (PAM II) sites, and 19 stations operated within the Upper St. John's River Water Management District (USJRWMD). These networks were chosen based on the availability of data collected at one minute intervals. Extensive effort was expended to convert and produce clean data sets in a common format. Some of the data sets have missing values. The problem of missing data must be considered in each step of the analysis. To allow analysis of area mean rainfall, a grid was selected which would allow a maximum number of equally spaced stations. Of the eighty six available stations, thirty six were chosen that are relatively equally spaced on a 15 km grid.

One method to study rainfall patterns is to compare the diurnal cycle on disturbed and undisturbed days. To prepare for this comparison, rainfall measurements were summed for each hour. An area mean rainfall was calculated for each hour of each day by dividing the hour sum by the number of reporting stations. The data were then segregated by day as disturbed or undisturbed. To normalize the results, the hourly means were summed and divided by the number of days in each group.

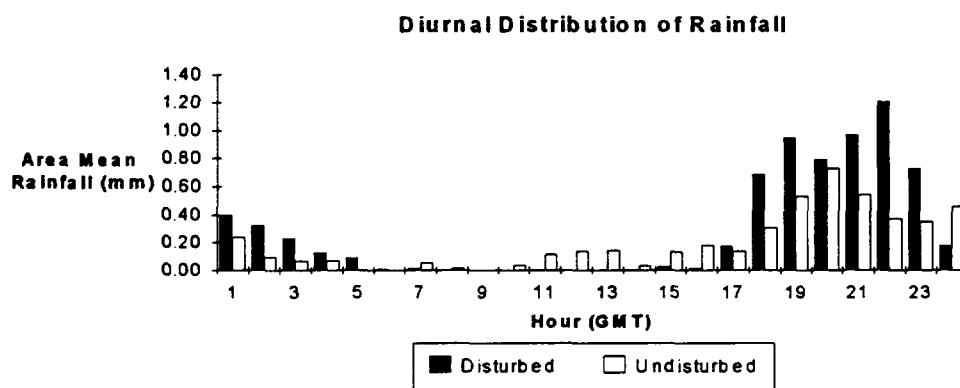


Figure 1

The results are illustrated in figure 1. The distributions are similar and show peak rainfall during the hours 18 thru 23 (GMT). The histogram indicates the area mean rainfall for disturbed days is nearly double that of the undisturbed days during these peak times. For the remainder of this paper, a day will be defined as 1300 - 0500 (GMT) corresponding to 0900 - 0100 local daylight time. This definition correspond to hours with heavier rainfall and eliminates hours with negligible rainfall.

The next approach attempts to answer the question - "Is rainfall greater on disturbed days?" In this method, rain rates (mm/hr) were categorized into twelve intervals; [0], (0,5], (5,10], (10, 15], (15, 20], (20,25], (25,30], (30,35], (35, 40], (40, 45], (45, 50], (50, +∞). (Note: In this notation a parenthesis is used to indicate an open interval; a bracket is used to indicate a closed interval.) The daily frequency of occurrence was calculated for each interval. The data were segregated by day as disturbed or undisturbed. Area means were calculated within each interval by summing the daily frequencies and dividing by the difference of the total possible reports and the number of missing values reported. The outcomes were normalized by dividing by the number of days in each group. The results are illustrated in figures 2 and 3. As one might expect, the highest percentages are found in the category with zero rainfall. The histograms show percentages for disturbed days in all remaining intervals greater than or equal to undisturbed days.

**Rainrate distribution on disturbed days
1300 - 0500 (GMT)**

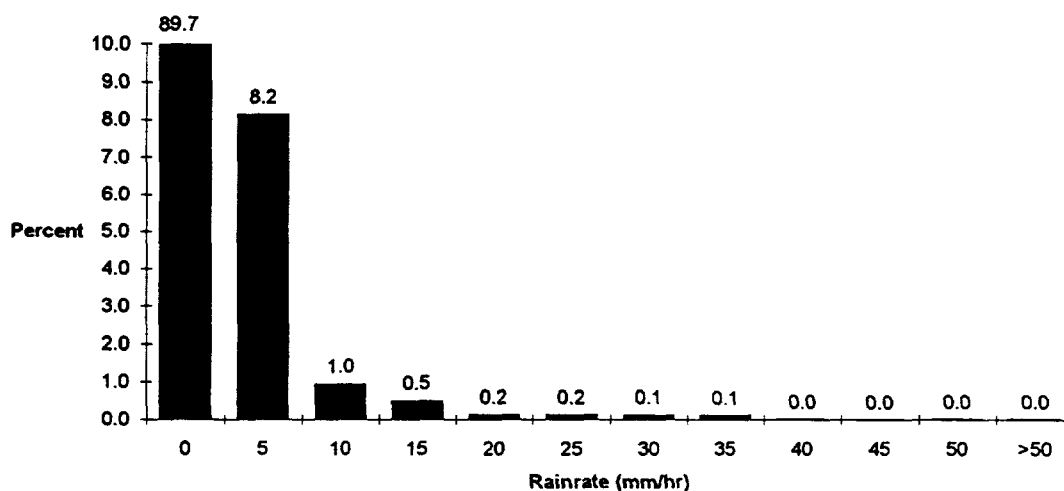


Figure 2

**Rainrate distribution on undisturbed days
1300 - 0500 (GMT)**

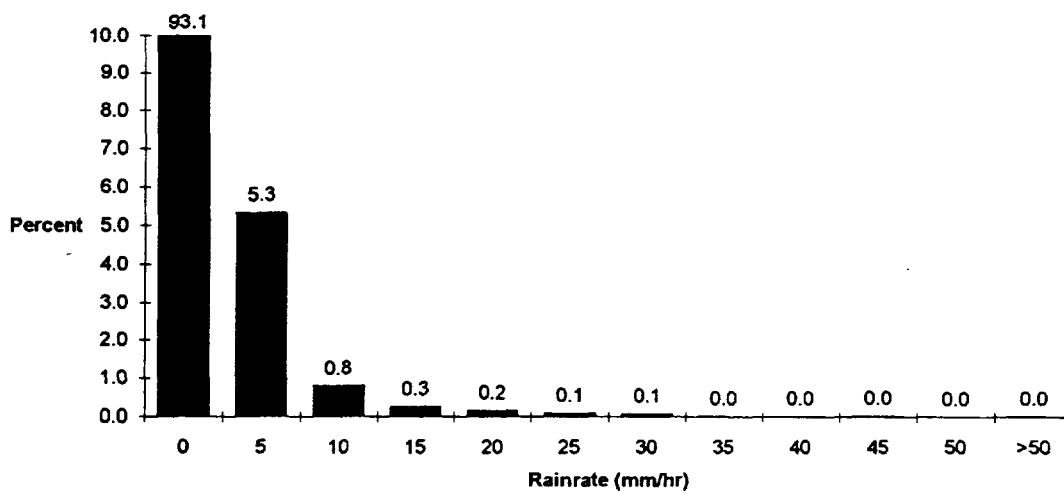


Figure 3

The final strategy attempts to compare the time frame of rain events on disturbed and undisturbed days. That is - are rain events of longer duration on disturbed days? For this analysis, six stations were eliminated from the grid. Data received from five of these sites had been adjusted using a cubic spline algorithm. It was decided that such data might effect the analysis of continuous precipitation. The sixth station was eliminated to maintain an equally spaced grid. Once the grid was finalized, a histogram was created to display the frequency of occurrence of continuous rain events during the following time intervals; 1 to 5 minutes, 6 to 10 minutes, ..., 45 to 50 minutes, and greater than 50 minutes. The histogram will vary based on the definition of a rain event. (How many consecutive minutes of zero rainfall will be allowed within a rain event?) When this definition is set to one minute, the frequency is high for rain events between 1 and 5 minutes. This may be misleading because rain may be continuous for a longer period of time but not at a rate which would be reported every minute. Figures 4-6 display the histograms for rain events defined by 1, 10, and 20 minute separations. Figures 5 and 6 show that on disturbed days the occurrence of rain events longer than forty minutes are nearly double the occurrence of similar events on undisturbed days.

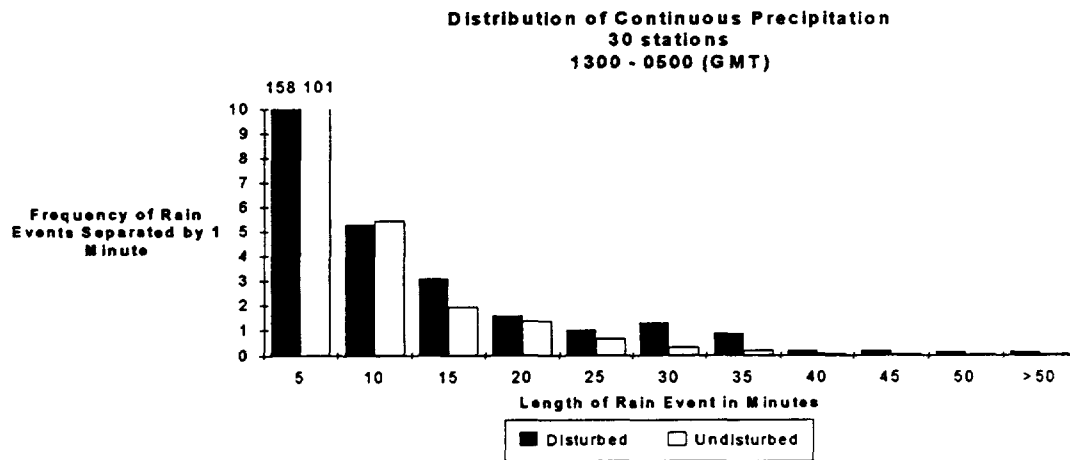


Figure 4

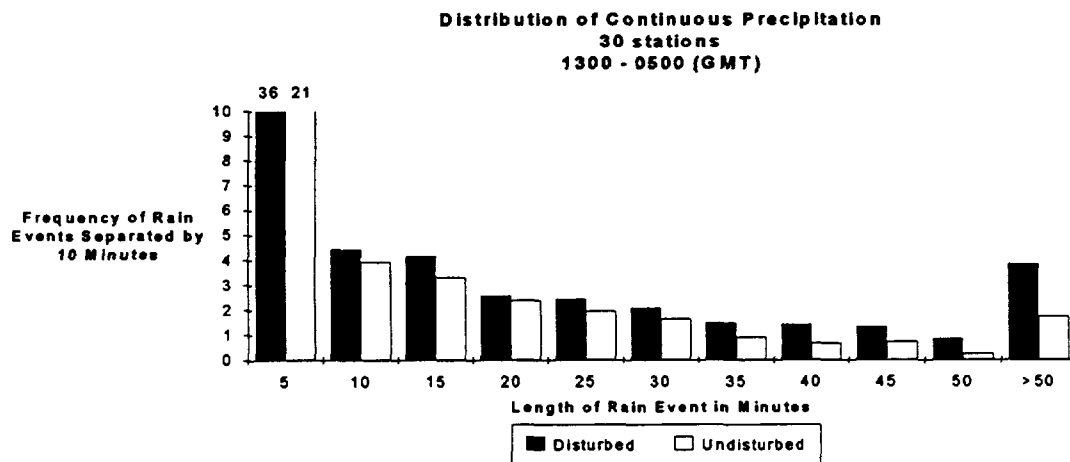


Figure 5

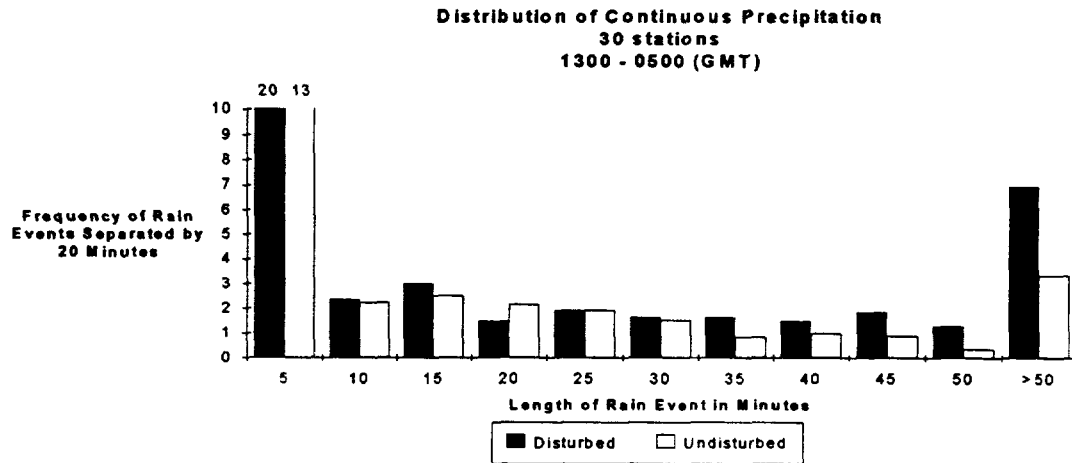


Figure 6

To determine the percent which rainfall from disturbed days contributes to the total water budget, daily totals were calculated by summing the mean area rainfall for each hour over a twenty four hour period (0-2400 GMT). From these daily totals, forty five percent of the mean area rainfall occurred on disturbed days, which comprise only thirty six percent of the study period. Due to a high variance of the daily totals of each data set, statistical T-test and F-test calculations based on a 95% confidence level indicate no significant difference between the two groups. Further study of the 7 individual classes may highlight the differences. Based upon the results of this and previous research, the effect of SW flow on rainfall and lightning could be relevant to the TRMM mission, whose objective is to measure rainfall with multiple instruments.

REFERENCES

1. Holle, R.L., Watson, A.I., Lopez, R.E., Howard, K.W., Ortiz, R. and Li, L., "Meteorological Studies to Improve Short-range Forecasting of Lightning/Thunderstorms within the Kennedy Space Area", *Final Report for Memorandum of Agreement between the Office of Space Flight, NASA and The National Severe Storms Laboratory, NOAA, Boulder, Colorado*, March 1992, 4-5.
2. Watson, A.I., Lopez, R.E., Ortiz, R., and Holle, R.L., 1987: Short-term forecasting of lightning at Kennedy Space Center based on the surface wind field. Proceedings, Symposium on Mesoscale Analysis and Forecasting incorporating "Nowcasting," August 17-19, Vancouver, British Columbia, Canada, European Space Agency, Paris, France, 401-406.
3. Scientific Overview and Operations Plan for the Convection and Precipitation/Electrification Experiment, National Center of Atmospheric Research, June 1991.

N98-17286

1992

NASA/ASEE SUMMER FACULTY FELLOWSHIP PROGRAM

MARSHALL SPACE FLIGHT CENTER
THE UNIVERSITY OF ALABAMA

REQUIREMENTS FOR THE IMPLEMENTATION
OF SCHEDULE REPAIR TECHNOLOGY IN THE
EXPERIMENT SCHEDULING PROGRAM

Prepared By: Stanley F. Bullington, Ph.D., P.E.
Academic Rank: Assistant Professor
Institution and Department: Mississippi State University
Department of Industrial Engineering
NASA/MSFC:
Office: Mission Operations Laboratory
Division: Mission Analysis
Branch: Planning Systems
MSFC Colleague: John P. Jaap

INTRODUCTION

The following list of requirements specifies the proposed revisions to the Experiment Scheduling Program (ESP2) which deal with schedule repair. These requirements are divided into those which are general in nature, those which relate to measurement and analysis functions of the software, those which relate specifically to conflict resolution, and those relating directly to the user interface. (This list is not a complete list of requirements for the user interface, but only a list of those schedule repair requirements which relate to the interface).

Some of the requirements relate only to uses of the software in real-time operations. Others are clearly for future versions of the software, beyond the upcoming revision. In either case, the fact will be clearly stated.

GENERAL REQUIREMENTS

- * The user should be able to control the level of fault tolerance by placing limits on the number of repair iterations and/or the amount of time spent searching for a repair, and by specifying the particular types of repairs to be attempted, the class of conflicts to be repaired, or the repair algorithms to be used.
- * A feasible schedule must be kept at all times, in case the schedule repair process is aborted.
- * The user should be able to define the horizon for which schedule repairs will be made.
- * The user should be able to define the horizon for which activities will be affected by a change in the schedule for a specified activity.
- * When supporting real-time operations, schedule repairs must be timely, in the sense that any changes must be implementable at the time the new schedule goes into effect, not at the time the repair process started.

MEASUREMENT AND ANALYSIS REQUIREMENTS

- * For a specified resource, the system should be able to determine the time, duration, and severity (e.g., number of activities involved, magnitude of overbooking) of all periods of overbooking.
- * For a specified target opportunity, the system should be able to determine the time, duration, and severity of all periods of unavailability of the target.

- * For a specified potential schedule change, the system should be able to quantify the effects of the change on the goodness of the schedule (e.g., change in number and severity of resource conflicts, change in schedule grade, change in crew utilization).
- * For a specified activity, the system should be able to provide both a composite measure of scheduling difficulty based upon resource usage and observation opportunities, and measures of the usage of individual resources.
- * For a specified activity, the system should be able to compute a composite measure of the importance of the activity, relative to other activities, based on a number of different user-input importance measures.
- * For a specified activity, the system should be able to provide a measure of the magnitude of the activity's relationships (e.g., concurrency, sequencing, resource generation) to other activities.
- * For a specified activity, the system should be able to present other opportunities for the placement of the activity which fall within a user-defined time horizon, and which have no conflicts or fewer conflicts than the specified activity.
- * For a specified activity, the system should keep track of the number of performances scheduled relative to the number of performances requested.
- * For a specified activity, when supporting real-time operations, the system should be able to report on whether the activity is in progress, and if so, the system should be able to respond to requests to handle stopping, and possibly restarting, the activity using any one of several available preemption modes (e.g., resume from the point where stopped, restart the activity at the beginning, abort the activity and lose the work which was already completed, stop the partially-completed activity, etc.). (This requirement is particularly applicable to possible future on-board scheduling systems).

CONFLICT RESOLUTION REQUIREMENTS

When an activity is moved, that activity (the "transient activity"), along with several others ("conflicting activities"), may combine to form a conflict. Usually, the resolution of such conflicts will consist of attempts to adjust the transient activity first, followed by attempts to adjust one or more of the conflicting activities, if needed. The requirements listed in this section exist in this context.

- * The user-specified time horizons (see "General Requirements" above) which limit the search space may be different for the transient activity than for the set of conflicting activities.
- * For a specified activity (or class of activities), the system should be able to automatically assign, recommend, or assign in response to a user request, a substitute resource(s), and to update all affected resource profiles accordingly.
- * For a specified activity, the system should be able to automatically choose, recommend, or choose in response to a user request, an alternate scenario, and to update all affected resource profiles and timelines accordingly.
- * For a specified activity (or class of activities), the system should be able to automatically adjust, recommend adjustment, or adjust in response to a user request, the duration of steps and/or delays between steps, and update all affected resource profiles and timelines accordingly.
- * The system should be able to automatically schedule, recommend, or schedule in response to a user request, the performance of an activity which generates a resource which is overbooked, if such resource generation is possible, and to update all affected resource profiles and timelines accordingly.
- * The system should be able to automatically delete (only for an autonomous on-board scheduler), recommend deletion, or delete in response to a user request, an activity, and to update all affected resource profiles and timelines accordingly.
- * For a specified resource, the system should be able to reduce or increase the capacity of the resource, based upon input from the user. The system should be able to present the effects of such resource changes, and should ask for user confirmation of the changes prior to accepting them as "permanent" changes.
- * In the case of an on-board scheduler, for activities which can be preempted while in progress, the system should be able to automatically preempt, recommend preemption, or preempt in response to a user request, and schedule the restart of the activity (in one of several possible modes, to be selected by the model subject to user definition, or defined by the user), and to update all affected resource profiles and timelines accordingly.

USER INTERFACE REQUIREMENTS

- * The system should be able, at user request, to shift between a resource-based perspective and an activity-based perspective, in terms of the displays which are presented. The choice of perspective will normally depend on whether the user is attempting to resolve a resource overbooking or to place a specific activity on the timeline.
- * The system should report to the user all changes which were actually accomplished in resolving a certain conflict, or group of conflicts.
- * For a specified user-requested schedule change, the system should be able to present the effects of making such a change, possibly through a group of graphical "before/after" illustrations. The system should then ask for confirmation before accepting the requested change. (The system could, in future versions, use "filtering heuristics" to recommend acceptance or rejection of any change request, based on the effects of the change).
- * The simpler and more-frequently-used interactive schedule repair suggestion capabilities of the system should be made more readily available for the user than more difficult features.
- * The system should be able to display specific user-requested timelines, total resource usage profiles, resource requirements for a particular activity, and periods of resource overbooking.
- * In a future revision of the system (featuring more intelligent schedule repair capabilities), for a specified user-requested schedule change, the system should query the user regarding the reason for the change (e.g., need to reduce workload on Payload Specialist #1 during the time period in question), and should be able to use this information to make intelligent schedule repairs.

CONCLUSION

A detailed review of literature relating to schedule repair and rescheduling has been performed. Based on this review, the above requirements relating to schedule repair for ESP2 have been identified. A preliminary requirements review has been held with NASA personnel, and the resulting schedule repair requirements will become part of an overall requirements document for a revised scheduling program.

1992
NASA/ASEE SUMMER FACULTY FELLOWSHIP PROGRAM

MARSHALL SPACE FLIGHT CENTER
THE UNIVERSITY OF ALABAMA

A 2nd Generation Expert System for
Checking and Diagnosing
AXAF's Electric Power System

Prepared by: Alex Bykat
Academic Rank: Professor
Institution: Armstrong State College
Department: Department of Computer Science

NASA/MSFC:

Laboratory: Information and Electronic Systems
Division: Electrical
Branch: Electrical Power Branch

MSFC Colleague: Yvette Johnson

Introduction.

AXAF - Advanced X-ray Astrophysics Facility - is a third NASA's great space observatory (HST launched in 1990 and GRO in 1991). Each of these observatories is intended to cover different part of the electromagnetic spectrum (X-rays for AXAF) and to provide high resolution (undistorted by the earth's atmosphere) images of celestial sources in our universe. AXAF is expected to be launched on an unmanned mission in second part of 1997. It will assume a high altitude, elliptical earth orbit, where it is expected to stay for at least 5 years.

Operation of AXAF is projected to require just below 1800W of peak power. To support this requirement AXAF's electric power system (EPS) will consists of a two wing six panel solar array containing 28,080 solar cells to generate power, three NiH₂ 30 Ah batteries each with 22 cells to store energy, a 22-35V bus to distribute power, and associated control electronics. The solar array will supply the spacecraft power and charge the batteries during sunlight period of the orbit. During the eclipse periods, the spacecraft will draw its power from the batteries.

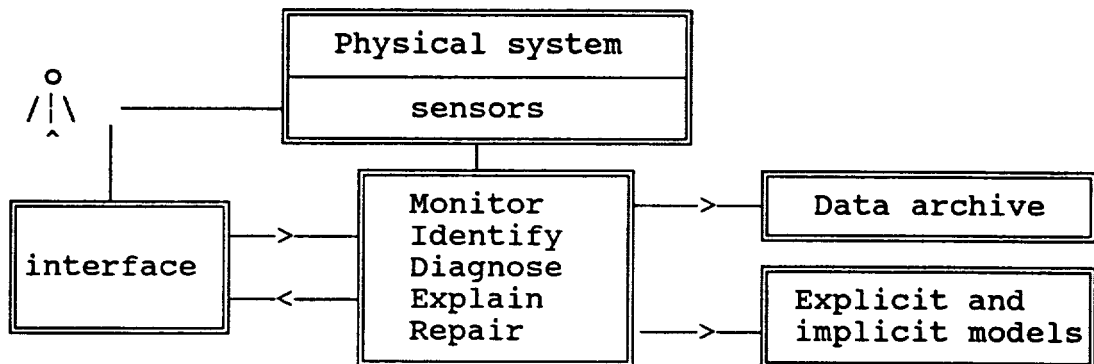
While the spacecraft is in orbit, the EPS performance is monitored via sensors measuring voltages, currents, pressures, and temperatures. The sensor data, are sent from the spacecraft to the ground station as telemetry and analyzed on arrival. When telemetry indicates possible EPS malfunctions, their causes must be dealt with immediately.

Monitoring, diagnosis and maintenance of such EPS is an arduous task which requires expertise and constant attention of the ground personnel. To help the ground crew in this task, much of it should be automated and delegated to an expert (knowledge-based) systems, which draws engineer's attention to possible malfunctions and allows him to review the telemetry to determine the source of the trouble, diagnose the suspected fault and to propose a corrective action [Bykat 1990; Bykat 1991].

Design of ESCAPADE.

First generation expert systems are based on the production systems approach. These systems are built on assumptions such as: a) domain knowledge is available and can be represented as a set of rules, b) domain knowledge is circumscribed, static, and monotonic, c) expert decision making can be emulated by a logical inference mechanism. For applications which support such assumptions, these systems perform well, but when some of the assumptions are violated they will fail, sooner or later.

AXAF's power system is still in design stage. As soon as it is firmed up, EPS test bed will be built and used to acquire the knowledge and expertise needed for managing AXAF's EPS. This scenario violates a number of the above mentioned assumptions. In particular, expertise is almost not available, knowledge is not static, and possibly non-monotonic. To cope with these problems, ESCAPADE' architecture (Figure 1) is based on that of a multi-level (2nd generation) expert system which in addition to the implicit (heuristic) model incorporates an explicit causal model of EPS paired with model-based reasoning.



ESCAPADE deals with the monitor/diagnose/repair cycle. The purpose of monitoring is to detect and describe divergence of incoming observations from expected observations. The expected observations will be elicited from a model of the correct behavior of the device components. The purpose of diagnostic module is to identify components which are responsible for that divergence. Thus, given malfunction symptoms, it uses device's structure, to identify, describe, and localize all of the manifested faults. The diagnosis is then confirmed by generating explanations which verify that the proposed diagnosis is consistent with the observed symptoms. To achieve its goals, the diagnostic module requires access to the device model which in addition to components behavior, should describe the causal and structural relationships governing the device's performance. Finally, the repair module, given the set of faults and faulty components, produces a description of procedures for repairing the device so as to assure that the symptoms identified by the monitor module, no longer manifest themselves in the subsequent data. Here again an access to the device's model is necessary. However, this time, repair knowledge such as structural descriptions and relationships is required.

In first generation expert systems the device model is present in the heuristic rules in a highly compiled ("expert digested") form. This implicit model is static and incomplete making such systems brittle. That is, while coping well with

anticipated events, they breakdown when unanticipated events/faults occur. To counter, the heuristic rules of ESCAPADE will be complemented with an explicit model of the device. The model will present structural and causal relationships governing the design and behavior principles of the physical device.

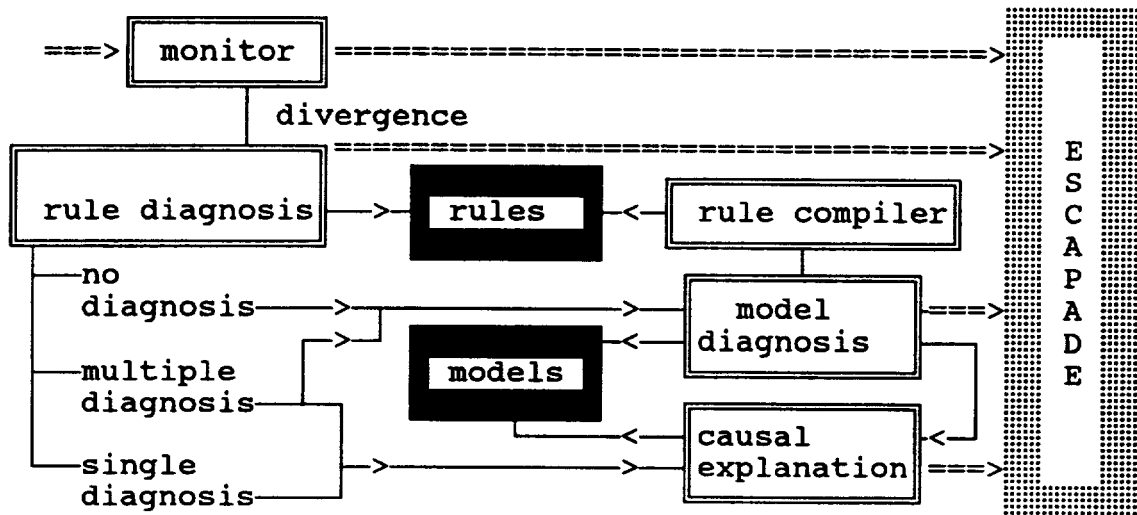
The explicit domain model will be supported by model-based reasoning and will be used to a) reduce the brittleness of the system by performing explicit model-based diagnosis when faced with unanticipated events, b) improve explanation capability by offering explanations based on causal model's description (structure, behavior...) of the device, c) provide a rule learning capability through compiling model-based inferences into new heuristic rules. The components' correct behavior model supports constraint suspension method [Davis & Hamscher 1988] for model-based diagnosis. The rule compiler can be used to offer a methodical coverage of model's search space with heuristic rules (systematic enumeration of the knowledge).

ESCAPADE: reasoning strategy

The ESCAPADE's integrated knowledge base consisting of heuristic rules and an explicit model of the device support a two-level diagnostic reasoning strategy. The adopted strategy is based on the cognitive process of a human (maintenance) expert in which past experience is used first to identify (or to focus upon) possible reasons for observed data divergence, followed by discrimination of hypotheses based on the knowledge of device's operational principles, structural relationships, etc.

Using this cognitive process as a paradigm, ESCAPADE's diagnostic strategy starts with heuristic reasoning on empirical associations of observed data about the system to generate initial hypotheses. If the heuristic reasoning results with no hypothesis, the explicit model is used for qualitative reasoning to explain the divergence. Multiple hypotheses may be dealt with using quantitative analysis to provide the final hypothesis. This strategy is further explained in Figure 2.

This strategy requires construction of an integrated model composed of structural information, functional information, and empirical associations. This knowledge will be represented via rules and frames. Rule compiler uses model-based inference chain of accepted hypotheses to formulate new rules, and to add new rules to the heuristic rule base.



Summary.

ESCAPADE is a knowledge-based system capable of supervising and managing operation of the AXAF's EPS in (semi)autonomous mode. Its main functions are to monitor AXAF's EPS telemetry and identify malfunction manifestations, diagnose suspected malfunctions and explain/verify its causes, and specify a repair procedure. The knowledge base of ESCAPE will consist of causal models of the electric power system, human expert's empirical operational knowledge, and rules derived from the system's inference chains. (It should be possible and interesting to use ESCAPE's explicit model to "verify" expert's rules through the model, and to generate rules from the model only.)

ESCAPADE is expected to offer a number of advantages including a) efficient diagnosis due to multi-level reasoning, b) effective explanation due to ability provide judgmental explanations (via heuristic rules) and ability to provide causal explanations (via functional model, structural model, logical model), c) dynamic rule learning through compilation of deep (model-based) inference chains into shallow (heuristic) rules, d) dynamic model adaptation to incorporate environment induced changes in modelled device within the explicit model.

References.

1. Bykat, A. "NICBES-2, a Nickel Cadmium Battery Expert System", IJAAI, pp.133-141, 4(3)1990
2. Bykat, A. "Intelligent monitoring and diagnostic systems: a survey", IJAAI, pp.339-352, 5(4)1991
3. Davis, R., Hamscher, W., "Model-based reasoning", in H. Shrobe (ed.) "Exploring AI", Morgan Kaufmann, 1988, pp.297-346

1992

NASA/ASEE SUMMER FACULTY FELLOWSHIP PROGRAM

**MARSHALL SPACE FLIGHT CENTER
THE UNIVERSITY OF ALABAMA**

**PREDICTION OF NONLINEAR OPTICAL
PROPERTIES OF LARGE ORGANIC MOLECULES**

Prepared By: Beatriz H. Cardelino

Academic Rank: Assistant Professor
 Research Scientist

Institution and
Department: Spelman College
 Department of Chemistry

 Atlanta University Center
 D. E. Milligan Science Research Institute

NASA/MSFC:

 Office: ES-74
 Division: Microgravity Science and Applications
 Branch: Chemistry and Polymeric Materials

MSFC Colleague: Craig E. Moore, Ph.D.



The preparation of materials with large nonlinear responses usually requires involved synthetic processes. Thus, it is very advantageous for materials scientists to have a means of predicting nonlinear optical properties. For example, correlating the strengths of the nonlinear properties of a family of compounds with different substituents at various bonding sites may be of great utility in selecting good candidates for experimentation.

The prediction of nonlinear optical properties has to be addressed first at the molecular level and then as bulk material. At the molecular level, prediction of these properties must consider both conditions of static and dynamic fields. For relatively large molecules, two types of calculations may be used: the sum-over-states (based on a perturbative expansion in terms of molecular eigenstates in the absence of an external field) and the finite-field approach (which diagonalizes a molecular Hamiltonian with a static-field dipolar perturbation). In the first case, the magnitude of the properties is obtained for a specific dynamic field, and the static field value can be extrapolated to zero frequency. In the second case, the nonlinear terms are obtained for static conditions and a correction for dispersion should be added if they are to be compared with experiments involving electromagnetic radiation.

The finite-field method was selected for this research, because this approach is better suited for larger molecules. A simplified version of the sum-over-states approach is under development to predict dispersion effects. Previously, dispersion corrections were extrapolated from experimental data on molecules similar to the ones investigated. Finally, a molecular mechanics approach is being considered to predict interatomic effects on nonlinear properties. These effects have been estimated previously from empirical data on molecules similar to the ones under study.

a) Progress in static-field calculations

During the summer of 1992, a core correction to the third-order polarizabilities was implemented. The method to calculate static nonlinear polarizabilities is a modification to the method developed by Dewar and Stewart, 1984 for calculating molecular linear polarizabilities. Dewar and Stewart include isolated point charges (or "sparkles") in the description of the molecule, with no associated electrons or atomic orbitals. An appropriate selection of these sparkles simulates the effect of a uniform electric field on a molecule, allowing for the corresponding changes in polarization to be calculated directly. The all valence-electron MNDO Hamiltonian (Dewar and Thiel, 1977) is employed to obtain molecular polarizations in the presence of various static fields. Then, polynomial regressions of polarizations versus fields data are used to calculate all tensor elements of the static second and third-order polarizabilities. Since MNDO is a valence-electron model, a correction for the atomic cores was required for third-order polarizabilities. In second-order polarizabilities, the effect of induced polarization in centrosymmetric structures cancels since they involve squares of the field strengths.

A group of substituted benzene molecules was selected to parameterize atomic core corrections for carbon, hydrogen, oxygen, and nitrogen. Experimental data for these molecules was available from third-harmonic generation (THG) measurements (Cheng et al., 1991). In order to minimize solvent effects, the molecules chosen for comparison were those measured as neat samples. Since the THG measurements were done at 0.649 eV radiation, the experimental values were corrected for dispersion effects. The correction for dispersion of the experimental values was based on the two-state anharmonic model:

$$\gamma_0 = \gamma_\omega (\omega_0^2 - \omega^2)^4 / \omega_0^8 \quad [1]$$

where γ_0 is the static third-order polarizability, γ_ω is the measured third-order polarizability, ω_0 is the resonance frequency ($\omega_0 = 6.9$ eV for benzene), and ω is the laser frequency (Zhao et al., 1989). The experimental data were also corrected for bulk effects, as follows: Two EFISH measurements on liquid and vapor benzene were used to obtain a liquid to vapor correction. The liquid-to-vapor correction was assumed to be applicable for all substituted benzene molecules.

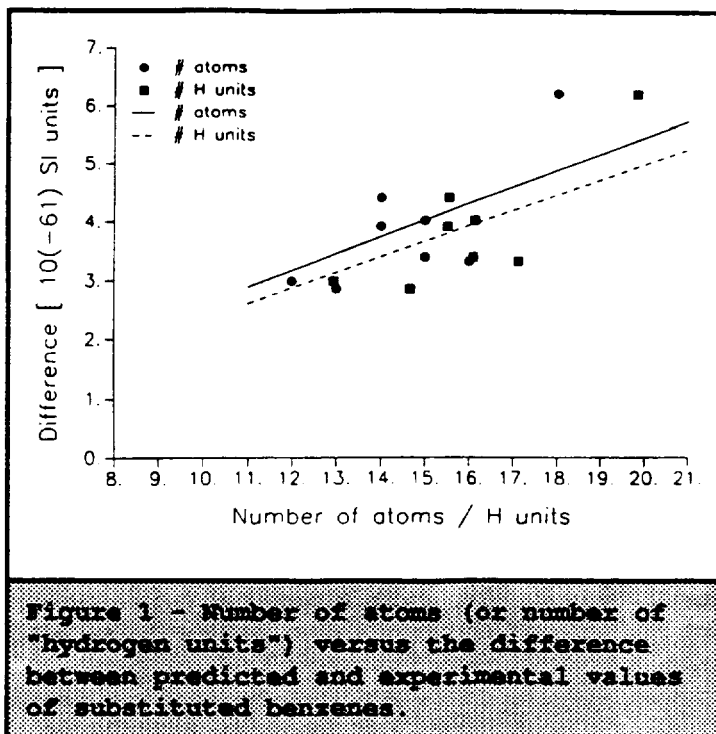
A plot of number of atoms in the molecules versus the difference between the predicted third-order polarizabilities and the corrected experimental value showed a correlation of 0.90 (Figure 1, solid line). Using as normalization factors the same non-hydrogen to hydrogen ratios from the core corrections on linear polarizabilities (Dewar and Stewart, 1984), a plot of "H units" versus the difference between predicted and experimental values showed a correlation of 0.91 (Figure 1, dotted line). Thus, the significant correlations indicate that core corrections for third-order polarizabilities were required. By performing multiple regressions with various groups of data, it was found that the core corrections for carbon and hydrogen were highly coupled. In order to overcome this problem, the same carbon to hydrogen ratio from the core correction of linear polarizabilities was used. Thus the following atomic core corrections were obtained: carbon = 0.251×10^{-61} SI, hydrogen = 0.217×10^{-61} SI, oxygen = 0.386×10^{-61} SI, and nitrogen = 0.931×10^{-61} SI. Table 1 shows the results.

Second and third-order polarizabilities have been predicted for diacetylene compounds containing pyrrol or substituted amines and a variety of functional groups. This work has been recently submitted for publication (Cardelino et al., 1992).

Second-order polarizabilities have been calculated for nitro- and amino-substituted quinolines and isoquinolines. The work was initiated from discussions with Dr. Wayne Hyde, a JOVE participant. Organic synthesis of these materials is in progress at the Northwestern State University of Louisiana. A paper on this work will shortly be submitted for publication (Moore et al., 1992).

Second-order polarizabilities have been calculated for substituted nitrobenzenes. The work was initiated from discussions with another JOVE participant, Dr. Ronald Clark. Synthesis of these materials is under way at the New Mexico Highland University.

Table 2- Third-Order Polarizabilities of Monosubstituted Benzenes		
	Predicted value 10 ⁻⁶¹ C m ⁴ V ⁻³	THG m ⁴ V ⁻³
H	3.3	3.5
CH ₃	4.2	4.1
OCH ₃	4.8	4.3
NH ₂	4.9	4.8
N(CH ₃) ₂	6.3	7.2
CN	4.7	3.8
C(O)H	4.6	4.8



b) Progress in dispersion effects

The basis for predicting the dispersion effects of nonlinear polarizabilities is time-dependent perturbation theory. At low intensities the β and γ terms are constant. In order to detect second and third harmonics, the molecules must be exposed to the intense radiation of lasers. Under these circumstances, the nonlinear polarizabilities become dependent on the frequency of the incident light.

During the summer of 1992, a method to estimate transition dipole moments was developed. To approximate the required transition dipole moments, the zero-differential-overlap method was applied to ground and excited states. Unoccupied molecular orbital wavefunctions from ground state calculations in the absence of external fields were used to construct various excited states. The dipole moments were separated into atomic point charge and hybridization contributions.

Since the goal is to design a method suitable for predicting dispersion effects on large molecules, the relative importance of the perturbative terms will be considered. Inclusion of indirect or direct summations, the number of terms in each summation, corrected expressions for the excited states and molecular orbital energies will be studied.

c) Progress on bulk effects

In our previous work, the effect of intermolecular interactions on the second and third-order polarizabilities have been estimated from experimental data fit to solvent molecular refraction or solvent dielectric

constant. In the case of neat samples, the effect on a parent compound was assumed valid for the substituted molecules.

Calculations performed on dimethylamino nitrobenzene have proven to be very sensitive to conformational isomerization. It is of great importance to know what the structure of the molecule is in the crystalline state. This problem will be examined using a molecular mechanics approach. Estimations of heats of sublimation and fusion, as well as hardness of crystals will also be done. Knowing these properties will help determine the feasibility of growing crystals of a given substance and its utility in various applications.

During the summer of 1992, the molecular mechanics program MM3 was modified to be run in a 486 personal computer.

REFERENCES

B.H. Cardelino, C.E. Moore, M.S. Paley, and D.O. Frazier; J. Phys. Chem.; submitted for publication (1992).

L.-T. Cheng, W. Tam, S.H. Stevenson, G.R. Meredith, G. Rikken, and S.R. Marder; J. Phys. Chem. 95, p.10631 (1991).

M.J.S. Dewar and J.J.P. Stewart; Chem. Phys. Lett. 111, p.416 (1984).

M.J.S. Dewar and W.Thiel; J. Am. Chem. Soc. 99, p.4899 (1977).

C.E. Moore, B.H. Cardelino, B.G. Penn, and H.W. Hayde; to be submitted (1992).

M.-T. Zhao, M. Samoc, B.P. Singh, and P.N. Prasad; J. Phys. Chem. 93, p.7916 (1989).

N98-17289

1992

NASA/ASEE SUMMER FACULTY FELLOWSHIP PROGRAM

**MARSHALL SPACE FLIGHT CENTER
THE UNIVERSITY OF ALABAMA**

**CFD ANALYSIS ON CONTROL OF SECONDARY LOSSES IN STME LOX TURBINES
WITH ENDWALL FENCES**

Prepared By: Mingking K. Chyu, Ph.D.
Academic Rank: Associate Professor
Institution and Department: Carnegie Mellon University
Dept. of Mechanical Engineering
NASA/MSFC:
Office: Structure and Dynamics Laboratory
Division: Aerophysics
Branch: Computational Fluid Dynamics
MSFC Colleague: Lisa W. Griffin

Introduction

The rotor blade in the newly designed LOx turbine for the future Space Transportation Main Engine (STME) has a severe flow turning angle, nearly 160 degrees. The estimated secondary loss in the rotor alone accounts for nearly 50% of the total loss over the entire stage. Turbine Team of CFD Consortium at MSFC has been devoting significant effort to exploring viable means to reduce such a loss. One of the potential methods is to use fences attached on the turbine endwall (hub). According to limited information available in the open literature [1], the presence of an endwall fence can alter the overall secondary flow structure in the blade passage, so the loss due to secondary flow can be alleviated. It is recognized, however, improperly arranged fences may have detrimental effects on the turbine performance, as a fence always impose additional blockage to the flow and increase the profile loss.

As a prelude to examining the effects of endwall fence with actual STME turbine configuration, the present study focuses on similar issues with a different, but more generic, geometry - a rectangular duct with a 160-degree bend. The duct cross-section has a 2-to-1 aspect (height-to-width) ratio and the radii of curvature for the inner and outer wall are 0.25 and 1.25 times the duct width, respectively. These geometric parameters simulate the mean values of those in the STME LOx turbine, thus the duct geometry preserves basic turning features of the actual blade passage. While a series of parametric studies with different fence geometries and flow conditions will be undertaken in the near future, the present emphasis lies in examining the effects of various fence-length extending along the streamwise direction. The flowfield is numerically simulated using the FDNS code developed earlier by Wang and Chen [2]. The FDNS code is a pressure based, finite-difference, Navier-Stokes equations solver.

Secondary Flows and Losses

Secondary flow is a phenomenon in which a flow motion normal to the primary flow direction prevails. In turbomachinery, aerodynamic loss due to excessive energy carried by such a flow motion is termed "secondary loss." Over the past fifty years, an extensive effort, in both theoretical and experimental aspects, has been devoted to understanding the secondary flows and losses in axial turbines. Until the recent availability of three-dimensional, Navier-Stokes equations solvers, most of the earlier developments were based on inviscid flow theories. A classical model developed by Hawthorne [3] suggests that the secondary flow in a blade passage is largely dominated by a pair of counter-rotating vortices. Such a flow pattern is typical for duct flow with a mild bend [4]. In addition, due mainly to vorticity stretching throughout the passage, vortex filaments also exists near the blade trailing edge.

Until the late 1970's [5], laboratory experiments with cascade flow visualization and/or measurements started to reveal the importance of the evolution of inlet boundary layer. The boundary layer entering the cascade separates in the blade leading edge forming a horseshoe vortex

and split into two legs wrapping around both sides of the blade. The pressure side leg of the vortex, as driven by the pressure gradient in the blade passage, migrates toward the suction side of the neighboring blade and becomes the passage vortex. This phenomenon represents one of the most dominating features in turbine secondary flow. The suction side leg of the horseshoe vortex, rotating in an opposite sense relative to the pressure side leg, grows thicker (radially outward) along the contour of the suction surface. Near the downstream portion of the surface, the suction side leg eventually meets the passage vortex forming a somewhat larger and stronger vortex. All these horseshoe vortex interactions combined account for one of the greatest sources for the secondary loss in a turbine cascade. Attaching a fence on the passage endwall may alter the overall flow patterns as previously described, so the loss associated with the secondary flow in the blade passage can be reduced.

Results and Discussion

Figure 1 shows velocity vector plots near the endwall region for three different fence (length) extensions; i.e. full, 3/4 and 1/2 of the turning arc along the center line of the duct width. For comparison, the case without fence is also included in the figure. Except for the length extension, the fence geometry and flow Reynolds number were kept the same for all the cases studied. The fence has a rectangular cross-section which occupies nearly 15% in both width and height of the channel flow area. Flow Reynolds number based on the channel width equals to 10 million. The computation uses a 75x21x32 grid and takes approximately 4000 steps for a converged solution. As shown in Figure 3, except near the vicinity of the fence, the flow pattern appears to preserve the major features of flow over a semi-circular turn. Even with such a severe turning, flow separation is non-existent throughout virtually the entire turning region (grid I from 23 to 53). A very minor separation which results in a relatively low pressure spot near the tip of the inner wall. In the post turn region, flow separates from the inner wall and forms a strong recirculation attaching to the surface. Imposing an endwall fence seems to have an effect to elongate the recirculation zone. However, this phenomenon is somewhat insensitive to the fence length.

Figure 2 displays the secondary flow near the mid-plane of the turn ($I=38$). For the case without fence, the flowfield displays a pattern consisting of two counter-rotating vortices similar to the classical model of secondary flow in a blade passage. Due to imbalance of centrifugal force and pressure gradient, the flow near the central portion of the duct moves from the inner wall toward the outer wall. The pressure gradient then forces the flow moving throughout the vortex path. Because the flow bulk inherits strong inertia for the present case, the secondary flow motion is relatively insignificant as compared to a conventional Dean-type pattern in a mild-bend duct. With the fence presence, it is clear that the secondary flow has been altered, particularly in the region close to the endwall. One important observation is that the fence diverts the low-momentum flow in the boundary layer upward and mixed with the high-momentum fluid in the mainstream. This mixing mechanism is desirable if loss reduction is

of concern. Another observation is that an additional recirculating bubble appears behind the fence.

An examination on the present results reveals that the fence extension has rather insignificant influence on the overall transport phenomena in the duct. The velocity and pressure characteristics slightly away from the endwall is virtually unaffected by the presence of the fence. This is somewhat expected, as most of the total pressure loss occurs in the post-turn region, not inside the turn. Hence the present fence may not be situated on the most effective location for restructuring the secondary flow. This finding could imply that the fence length may not be a sensitive parameter for the actual LOx turbine passage. However, it is recognized that the factor of horseshoe vortex separation ahead of a turbine blade, which is absent in the present modeling, may drastically affect this observation. Analysis with actual blade configuration is considered to be a reasonable follow-on study in the future.

Acknowledgement

The author would like to thank his NASA colleague, Ms. Lisa Griffin, for her enthusiastic support throughout the course of this research. He is also grateful for Professor Michael Freeman and Dr. Frank Six for managing a very successful summer faculty research program.

References

1. Kawai, T., Shinoki, S. and Adachi, T., "Secondary Flow Control and Loss Reduction in a Turbine Cascade Using Endwall Fences," *JSME International J.*, Ser. 2, Vol. 132, No.3 (1989) 375-387.
2. Wang, T.S. and Chen, Y.S. (1990) "A unified Navier-Stokes flowfield and performance analysis of liquid rocket engines," AIAA paper 90-2494.
3. Hawthorne, W.R., "Secondary Circulation of Fluid Flow," *Proc. Royal Society A*, 203 (1951).
4. Dean, W.R. and Hurst, J.M., "Note on the Motion of Fluid in a Curved Pipe," *Mathematika*, 6 (1959) 77-85.
5. Langston, L.S., Nice, M.L. and Hooper, R.M., "Three-Dimensional Flow in a Turbine Cascade Passage," *J. Engrg. for Power*, 99 (1977) 21-28.

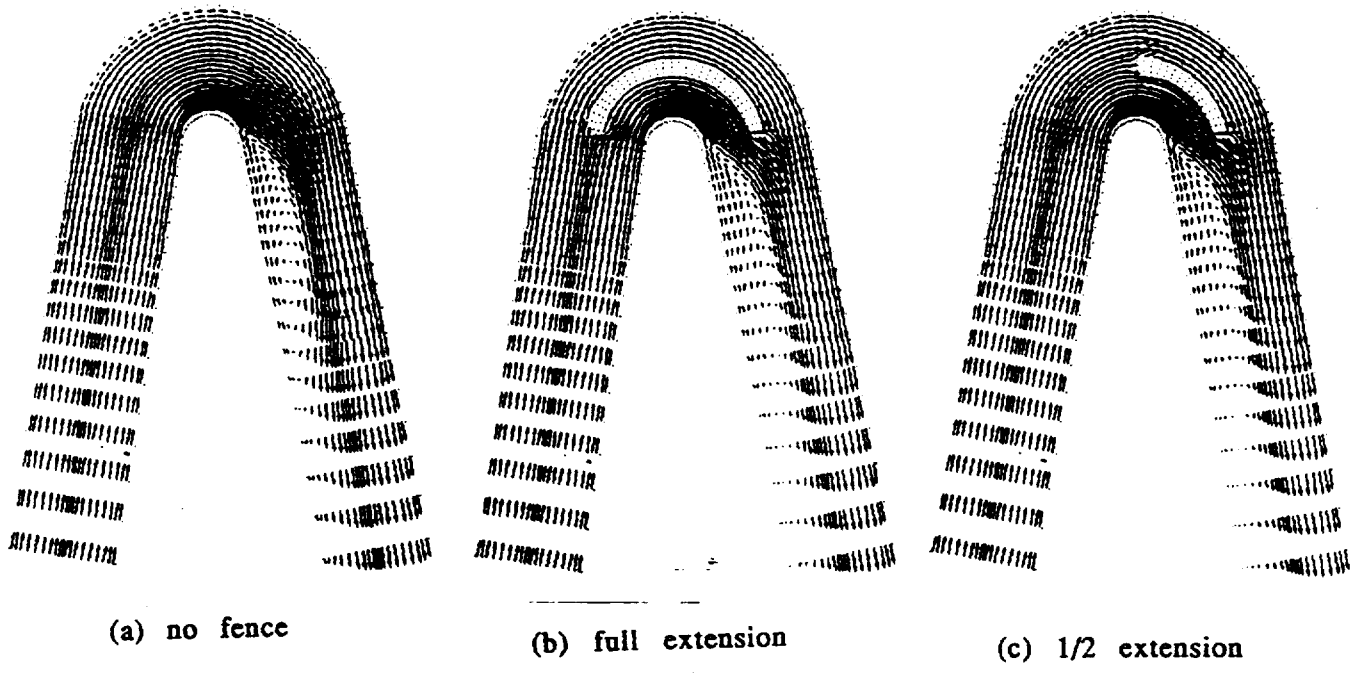


Figure 1 Velocity vector near endwall

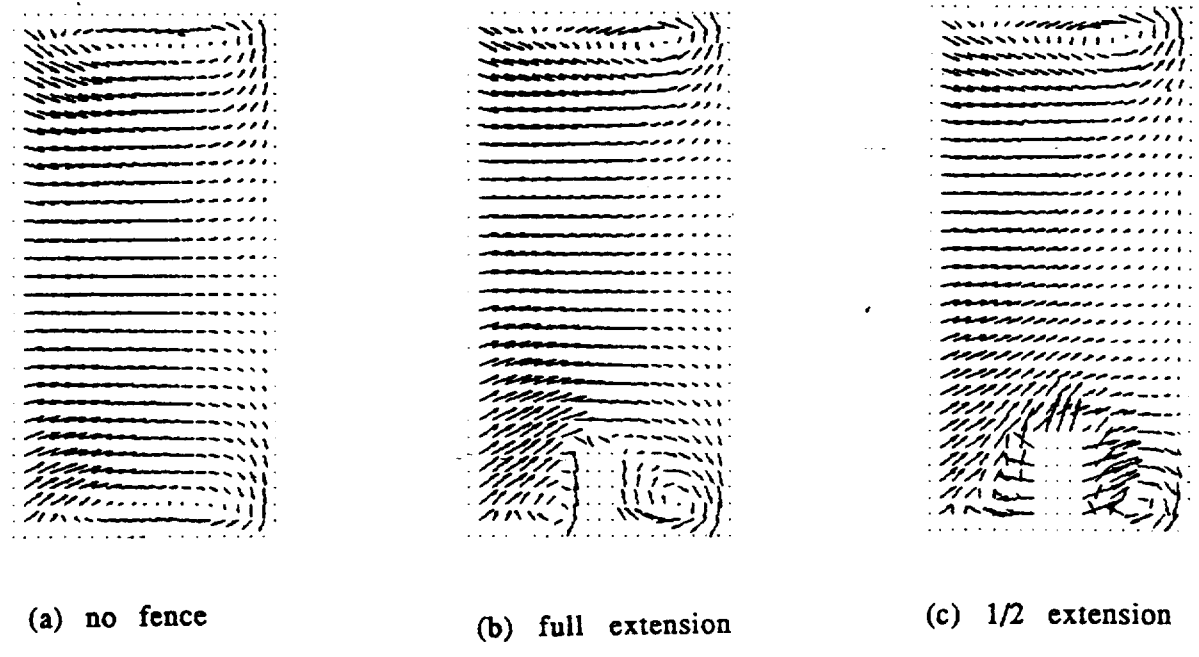


Figure 2 Secondary flow pattern in the mid-plane of bend

1992

NASA/ASEE SUMMER FACULTY FELLOWSHIP PROGRAM

MARSHALL SPACE FLIGHT CENTER
THE UNIVERSITY OF ALABAMA

OPTIMAL TRAJECTORIES FOR ORBITAL TRANSFERS USING
LOW AND MEDIUM THRUST PROPULSION SYSTEMS

Prepared By: Shannon S. Cobb, Ph.D.
Academic Rank: Assistant Professor
Institution and Department: University of Alabama
in Huntsville, Department
of Mathematical Sciences
NASA/MSFC:
Division: Systems Analysis
Branch: Flight Mechanics
MSFC Colleague: John Hanson, Ph.D.

INTRODUCTION

For many problems it is reasonable to expect that the minimum time solution is also the minimum fuel solution. However, if one allows the propulsion system to be turned off and back on, it is clear that these two solutions may differ. In general, high thrust transfers resemble the well-known impulsive transfers where the burn arcs are of very short duration. The low and medium thrust transfers differ in that their thrust acceleration levels (10^{-4} earth g's for low thrust and 10^{-2} earth g's for medium thrust accelerations) yield longer burn arcs which will require more revolutions, thus making the low thrust transfer computational intensive. Here, we consider optimal low and medium thrust orbital transfers.

APPROACH

The formulation of the problem follows that of Horsewood et. al. (1), where the state of the spacecraft is given in terms of the slowly varying equinoctial elements, which are expressed in terms of the classical elements a, e, i, ω, Ω as

$$\mathbf{z} = (a, e \sin(\omega + \Omega), e \cos(\omega + \Omega), \tan(i/2) \sin \Omega, \tan(i/2) \cos \Omega)^T.$$

The spacecraft mass, m , is also a state variable. In addition, the position of the spacecraft within an orbit is given by the eccentric longitude, $F = E + \omega + \Omega$.

The equations of motion are

$$\dot{\mathbf{z}} = \frac{2P}{mc} M \hat{\mathbf{u}}, \dot{m} = -\frac{2P}{c^2} \quad [1]$$

where $M = \frac{\partial \mathbf{z}}{\partial \mathbf{r}}$ is a 5×3 matrix calculated by treating F as an independent parameter, such that the variation of F with respect to the other state variables is zero; P is the power due to the thrusters, c is the exhaust velocity and $\hat{\mathbf{u}}$ is the unit vector in the direction of thrust.

It follows from the well-known maximum principle that the fuel optimal trajectory from a given state to some desired final state is found by thrusting at every point along the trajectory in the direction which maximizes the Hamiltonian function H . H can be written in terms of the state variables and their corresponding costate (adjoint) variables λ_z and λ_m as

$$\begin{aligned} H &= \lambda_z^T \dot{\mathbf{z}} + \lambda_m \dot{m} \\ H &= \frac{2P}{mc} \left(\lambda_z^T M \hat{\mathbf{u}} - \frac{m \lambda_m}{c} \right) \end{aligned} \quad [2]$$

where the costate variables satisfy a first order linear system of ordinary differential equations. Now, to maximize H we need only thrust in the direction given by $\hat{u} = \frac{M^T \lambda_z}{|M^T \lambda_z|}$. Note that if the quantity in parenthesis in [2], call it σ , is negative, then H is negative and hence H is maximized by letting $P = 0$, which amounts to turning the propulsion system off, i.e. "coasting"; on the other hand, if σ is positive, then H is maximized by letting P take on its maximum value, i.e. "thrusting".

Because of the many orbit revolutions of a long duration transfer, the intensive computations can be reduced by an averaging technique. We can compute an "averaged" Hamiltonian function by holding the state and costate variables constant over an orbital period of duration τ , i.e. we assume Keplerian motion, and integrating the actual Hamiltonian function as follows:

$$\begin{aligned} \tilde{H} &= \frac{1}{\tau} \int_0^{\tau} H(\bar{z}, \bar{\lambda}_z, \bar{m}, \bar{\lambda}_m, F) dt \\ &= \int_0^{2\pi} H(\bar{z}, \bar{\lambda}_z, \bar{m}, \bar{\lambda}_m, F) s(\bar{z}, F) dF \end{aligned}$$

where $s(\bar{z}, F) = \frac{1}{\tau} \frac{dt}{dF}$. The "averaged" equations of motion can now be computed using this "averaged" Hamiltonian, and since the Hamiltonian and its derivatives are zero during coast phases, we need only integrate these equations over the predetermined thrust intervals.

NUMERICAL APPROACH

A FORTRAN program MINFUEL has been written to compute this minimum-fuel solution. The basic algorithm is:

(1) start iteration of the unknown initial costate values by making a first guess—for the simplified problem of a circle-to-circle coplanar transfer, an initial costate guess can be found by using the fact that it is fuel-optimal to thrust in the direction of motion, or tangential direction. This known direction can be used to help guess the initial costate values since $\hat{u} = \frac{M^T \lambda_z}{|M^T \lambda_z|}$. Given any state, this optimal thrust direction can be calculated in terms of the costate values by running the program XFORM to compute the transpose of the matrix M and the velocity vector.

(2) compute a trajectory corresponding to an initial costate guess—one calls the Runge-Kutta routine to integrate the averaged equations of motion; the

switch function can be expressed in terms of the fast variable F around an orbit and the zeroes of the switch function $\sigma = \left[\lambda_z^T M M^T \lambda_z \right]^{\frac{1}{2}} - \frac{m \lambda_m}{c}$ are found, which defines the thrusting subintervals of $[0, 2\pi]$ for integration. Again for the circle-to-circle transfer we know that initially the switch function should be positive.

(3) compare the computed final state with the specified final state and the proper transversality conditions, such as $\lambda_{m_f} = 1$. The Newton method used for this iteration is very sensitive to the initial costate guess.

The medium thrust problem was investigated through the use of the Flight Mechanics Branch's program SCOOT (Simplex Computation of Optimal Orbital Transfers). SCOOT was known to converge to a quasi-optimum solution for high thrust levels and short burn times. Although low thrust transfers require long burn times, SCOOT was thought to be a viable option for guessing optimal low thrust trajectories by using the final output from the converged higher thrust cases as input to MINFUEL. After many runs of SCOOT, the fact that it calculates only a local optimal and is thus sensitive to coast and burn times guessed, makes it very difficult for comparisons of medium and low thrust transfers.

CONCLUSIONS

The results of SCOOT have indicated that lowering the thrust level "can" increase the amount of final propellant; increasing the ISP can increase the final propellant as well. The output of SCOOT, in particular the optimal thrust directions, from medium thrust level solutions can be used to help calculate an initial guess for low thrust transfers. The program MINFUEL, once properly debugged, should prove very capable of handling minimum-fuel low thrust transfers.

REFERENCES

- (1) Horsewood, J.L., Suskin, M.A., Pines, S., Moon Trajectory Computational Capability Development. Technical Report 90-51, NASA Lewis Research Center, July 1990.
- (2) Jasper, T.P., Low-Thrust Trajectory Analysis for the Geosynchronous Mission. AIAA 10th Electric Propulsion Conference, 1973.
- (3) Sackett, L.L., Malchow, H.L., Edelbaum, T.N., Solar Electric Geocentric Transfer with Attitude Constraints: Analysis. Technical Report NASA CR-134927, The Charles Stark Draper Laboratory, Inc. August 1975.

1992

NASA/ASEE SUMMER FACULTY FELLOWSHIP PROGRAM

**MARSHALL SPACE FLIGHT CENTER
THE UNIVERSITY OF ALABAMA**

STME NOZZLE THERMLA ANALYSIS

Prepared By: Digendra K. Das, Ph.D.
Academic Rank: Associate Professor
Institution and Department: SUNY Institute of Technology
Department of Mechanical Engineering Technology
NASA/MSFC:
Office: Structures & Dynamics Laboratory
Division: Thermal Engineering & Life Support
Branch: Thermal Analysis
MSFC Colleague(s): Brian K. Goode
James W. Owen

→

|

The National Launch System (NLS), previously known as the Advanced Launch System (ALS), is a joint program of the DoD and NASA. After being initiated in July 1987, the phase I of the program was completed in 1988 in collaboration with seven contractors. Work is now in progress on phase II, based on the concepts developed in phase I. The NLS program is anticipated to acquire launch and operational capabilities by the beginning of the next century. A common cryogenic (liquid oxygen and hydrogen) core engine called Space Transportation Main Engine (STME) provides the common core for a variety of reference vehicle concepts developed in phase I.

A review of the current technology, relevant to the design and development of the STME, was undertaken by the author in the Summer of 1991 as a NASA/ASEE Summer Faculty Fellow at MSFC. The review involved an extensive literature search relevant to the development of the following major components of the STME:

- 1) Gas Generator
- 2) Hydrostatic/Fluid Bearings
- 3) Seals/Clearances
- 4) Heat Exchangers
- 5) Nozzle
- 6) Nozzle/Main Combustion Chamber Joint
- 7) Main Injector Face Plate
- 8) Rocket Engines-General

The details of this investigation are given in Ref. 1.

The current summer project which is a continuation of last year's summer project, has the objective of carrying out a detailed thermal analysis of the STME nozzle.

The design and development of the STME nozzle has been undertaken by Pratt & Whitney in collaboration with NASA/MSFC and DoD. The nozzle design has adopted film/convective cooling techniques. The turbine exhaust has been utilized as the coolant in the nozzle cooling system. The coolant is injected into the nozzle wall at a section about 21 inches downstream of the throat. At the inlet, the coolant is divided into three different streams: (1) convective, (2) primary film, and (3) secondary film coolant as shown in figure 1.

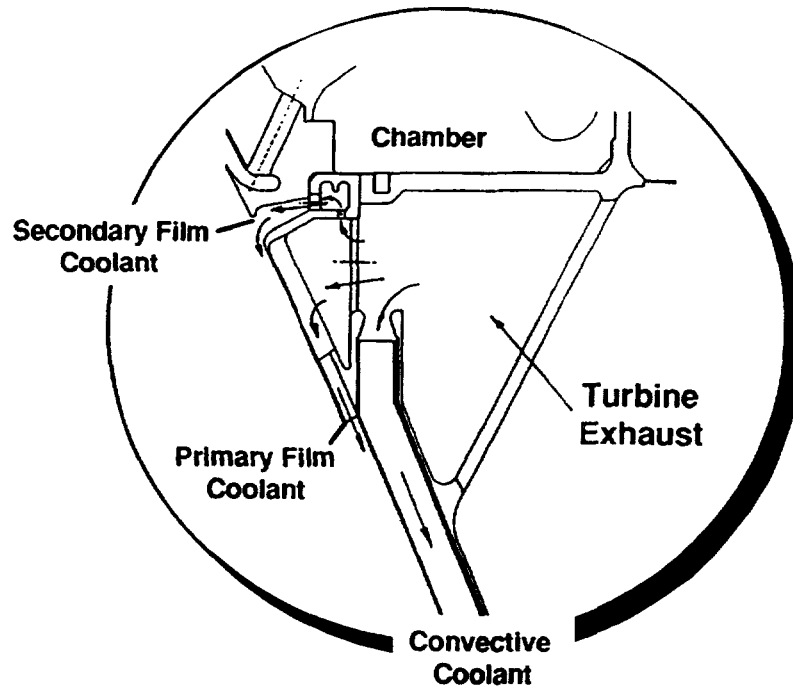


Figure 1

Some of the important parameters are shown in table 1.

TABLE 1

<u>Coolant Parameters</u>	<u>Value</u>
Inlet pressure	268.90 psia
Exit pressure	71.00 psia
Inlet temperature	1168.06°R
Exit temperature	1504.00°R
Flow:	66.72 lbm/sec
- Convective	55%
- Primary Film	38%
- Secondary Film	7%

An attempt is being made to develop a coupled (conjugate) fluid/thermal analysis model for the nozzle cooling system using the software Systems Improved Numerical Differencing Analyzer (SINDA) 1987/ANSI (Gaski Version). Owing to the limited time available for the summer project (ten weeks), it was decided that initially, the model should be developed for the convective coolant flow only. Further development of the model to include the primary and secondary coolant flows will be undertaken as a continuation project.

The Convective Flow/Thermal Analysis Model

The one-dimensional conjugate model has been developed according to the standard SINDA 1987/ANSI (Ref. 2) procedure. The geometric input data were obtained from the engineering drawings made available by Pratt & Whitney and the gas properties were derived from the archives of Rocketdyne. The model consists of 44 flow nodes and 43 thermal nodes and utilizes the standard SINDA subroutine SNHOSS. The solution procedure follows the four steps outlined below:

- (1) The solution is initiated by solving a set of linear incompressible, but physically unrealistic network equations.
- (2) This solution is used as a starting point for the linearized incompressible flow equations.
- (3) The model then calculates the steady state solution of the linearized compressible flow equations.
- (4) The final solutions are then obtained with the density corrected for the static pressure.

Further details on the solution procedure can be obtained from (Ref. 3). The flow chart of the model presented in Fig. 2.

As indicated earlier, the model in its present form deals only with one-dimensional convective coolant flow. Extension of the model to include the primary and secondary coolant flows will be undertaken as a continuation project.

REFERENCES

1. Das, D.K., "An Overview of the Current Technology Relevant to the Design and Development of the Space Transportation Main Engine (STME)," NASA/MSFC Report, Thermal Analysis Branch, ED64. August 1991
2. Gaski, J.D., "SINDA 1987/ANSI," User's Manual, Network Analysis Associates, Inc., Fountain Valley, CA
3. Owen, J.W., "Thermal Analysis Workbook," NASA Technical Memorandum, NASA TM-103568, January 1992

1992

NASA/ASEE SUMMER FACULTY FELLOWSHIP PROGRAM

MARSHALL SPACE FLIGHT CENTER
THE UNIVERSITY OF ALABAMA

A PLAN FOR ACCURATE ESTIMATION OF DAILY
AREA-MEAN RAINFALL DURING THE CAPE EXPERIMENT

Prepared by: Claude E. Duchon

Academic Rank: Professor

Institution: University of Oklahoma
Department: School of Meteorology

NASA/MSFC:

Laboratory: Space Sciences
Division: Earth Science and Applications
Branch: Environmental Analysis

MSFC Colleague: Steven J. Goodman, Ph.D.- NASA

I. Introduction

The Convection and Precipitation/Electrification (CaPE) experiment took place in east central Florida from 8 July to 18 August, 1991. There were five research themes associated with CaPE. In broad terms they are: investigation of the evolution of the electric field in convective clouds, determination of meteorological and electrical conditions associated with lightning, development of mesoscale numerical forecasts (2-12 hr) and nowcasts (<2 hr) of convective initiation and remote estimation of rainfall. It is the last theme coupled with numerous raingage and streamgage measurements, satellite and aircraft remote sensing, radiosondes and other meteorological measurements in the atmospheric boundary layer that provide the basis for determining the hydrologic cycle for the CaPE experiment area. The largest component of the hydrologic cycle in this region is rainfall. An accurate determination of daily area-mean rainfall is important in correctly modeling its apportionment into runoff, infiltration and evapotranspiration. In order to achieve this goal a research plan was devised and initial analysis begun. The overall research plan is discussed with special emphasis placed on the adjustment of radar rainfall estimates to raingage rainfall.

II. Research Plan

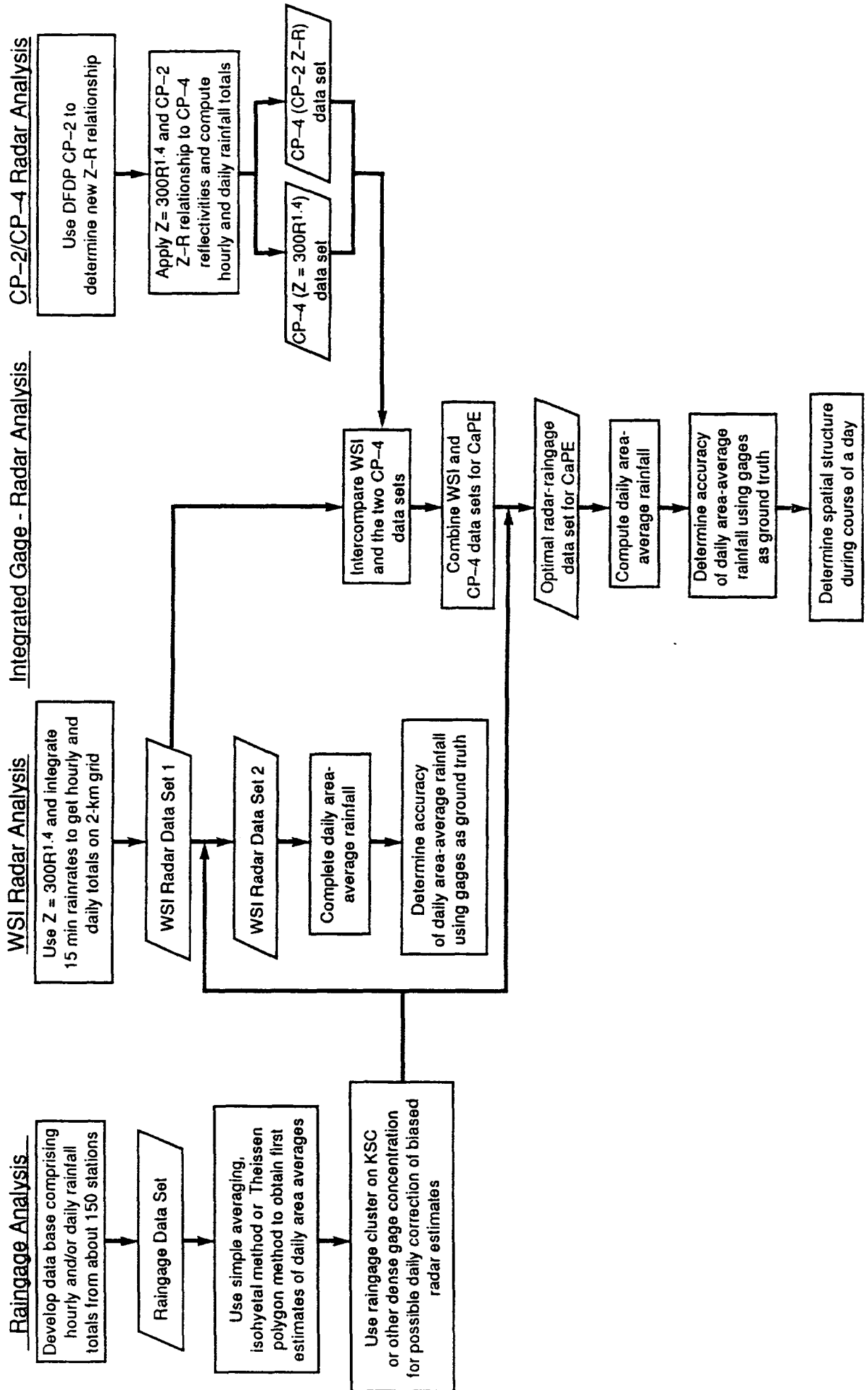
Fig. 1 show the Precipitation Analysis Work Plan. It comprises four channels of analysis: raingage, WSI radar, integrated gage-radar and CP-2/CP-4 radar. The purpose of the raingage analysis is to develop a high quality data set that can be used to estimate daily area-mean rainfall over two areas of CaPE: one relatively small area within which there is a dense concentration (a cluster) of gages and a much larger area where the concentration ranges from moderate to dense. The daily area-mean rainfall from analysis of the former area will be used to correct corresponding rainfall estimates derived from WSI radar. This is indicated in Fig. 1 by the connection from raingage analysis to WSI radar analysis.

In general, raingages provide a quite accurate measurement of rainfall at a point but comparatively inaccurate assesment over a large area. On the other hand radar provides good areal coverage but may require adjustment of the rainrates determined from the assumed Z-R relationship. A dense concentration of gages can yield rainfall data that can be used to determine a potential radar correction.

In a paper by Woodley et al. (1975), dealing with raingage-radar comparisons of convective rainfall in the Miami, FL area, a number of results were presented that are relevant to correcting the radar. It should be noted that similar types of raingages (tipping-bucket) and radars (WSR-57) were employed in both the Miami experiment and the CaPE experiment.

One of the results they found was a systematic 2% underestimate of point rainfall by the tipping-bucket gages when compared to dipstick gages. Since the latter are considered the standard for measuring point rainfall and the precipitation regimes in both experiments are similar, it may be necessary to upwardly adjust daily tipping-bucket rainfall amounts. There

Fig. 1 Precipitation Analysis Work Plan



are some locations in the CaPE experimental area that have both tipping-bucket and dipstick gages so that new intercomparisons can be made.

Based on measurements from collocated raingages they found that it was unreasonable to expect rainfall observations at a point to be accurate to better than 5 to 10%. The cause for these differences was apparently due to different gages and small differences in gage exposure. This result must be taken into consideration in comparing radar estimates to raingage observations in which the latter are considered the standard.

Comparisons between radar and raingages in clusters were performed using the "factor of difference" or FD, where FD is defined as G_i/G_F when $G_i \geq G_F$, or G_F/G_i when $G_i < G_F$. Thus $FD \geq 1$. G_F is the daily rainfall derived from radar and G_i is that from raingages. From clusters of gages ranging in size from 21 to 78 km² and gage density from 3 to 8 km²/gage, they found that the average FD is 2.02 for rain volumes $< 10^5$ m³ and 1.50 for rain volumes $\geq 10^5$ m³. The equivalent water depth for the rain volume criterion varies from about 0.8 mm to 1.2 mm over the range of cluster areas. These results show that the greater the rainfall the smaller the differences. This would be expected because greater rainfall is associated with larger storms which, in turn, encompass more raingages within a fixed array of gages.

In order to improve the estimation of rainfall by radar, daily radar-derived rainfall was multiplied by the ratio of the summed gage to summed radar rainfall from the 5 clusters, the total area of which was 340 km². (For CaPE there is one cluster of approximately 13 gages over about 80 km², corresponding to about 6 km²/gage, a figure comparable to the gage density noted above.) When this adjustment was applied to a 655 km² mesonet containing 229 gages the FD was reduced from 1.53 to 1.38. This is equivalent to reducing the gage density from 60 km²/gage to 25 km²/gage.

It was found that when the size of the area increases from 655 km² to 1.3×10^4 km², about the area of CaPE, a gage density of 73 km²/gage in the larger area should provide the same accuracy in daily areal estimates of rainfall as a gage density of 8 km²/gage in the mesonet. If there were 73 km²/gage in the CaPE area the FD would be within 1.2 90% of the time. While, ultimately, this gage density may be possible for the CaPE area, the gages are not uniformly distributed. Because of this it will be important to employ radar in order to obtain acceptable estimates of daily area-mean rainfall for CaPE.

The second column in Fig. 1 indicates that an adjustment derived from the cluster of raingages in CaPE will be applied to the radar estimates in a manner similar to that described by Woodley et al. (1975). Daily area-mean rainfall will be computed from this improved data set (WSI Radar Data Set 2). In addition, the accuracy (or inaccuracy) will be determined. Analysis of the dual-frequency dual-polarization CP-2 radar data, shown in the fourth column, may lead to an improved Z-R relationship for central Florida in summer. Because the CP-4 was used in the PPI mode and was located within the CaPE experiment area, it should be extremely useful to compare simultaneous reflectivities from this radar and the WSI composite radars which are located well outside CaPE.

This comparison is shown as the first step in the third column in Fig. 1. Continuing in this column, after adjusting the radar data using a daily correction derived from the gages, as previously discussed, an optimal daily area-mean rainfall data set is produced that includes estimation of its accuracy.

III. Summary

In moist tropical and subtropical climates the largest component of the hydrologic cycle is precipitation. The CaPE area is located in the latter climate. A plan for analyzing precipitation for the CaPE experimental area has been presented. The available measurements include well over 100 raingages of different types, composite radar reflectivities from NWS WSR-57 radars and two onsite high quality research radars. The principal objective of the analysis is to compute daily area-average rainfall for CaPE using an optimal radar-raingage data set and assess its accuracy.

Acknowledgments

The production of Fig. 1 was accomplished through many discussions with a number of individuals; among them are Bill Crosson, Steve Goodman and Chip Laymon. Their contributions are very much appreciated.

Reference

Woodley, W. L., A. R. Olsen, A. Herndon and V. Wiggert, "Comparison of gage and radar methods of convective rain measurement. J. Appl. Meteor., 14 (1975) 909-928

1992

NASA/ASEE SUMMER FACULTY FELLOWSHIP PROGRAM

**MARSHALL SPACE FLIGHT CENTER
THE UNIVERSITY OF ALABAMA**

**EVALUATION AND RECOMMENDATIONS FOR
WORK GROUP INTEGRATION WITHIN THE MATERIALS AND PROCESSES LAB**

Prepared By: Phillip A. Farrington, Ph.D.
Academic Rank: Assistant Professor
**Institution and
Department:** The University of Alabama in Huntsville
Department of Industrial and Systems Engineering
NASA/MSFC:
Office: Materials and Processes Lab
Division: Process Engineering
Branch: Chemical & Non-Metals Processes
MSFC Colleague: Eutiquio Martinez

The goal of this study was to evaluate and make recommendations for improving the level of integration of several work groups within the Materials and Processes Lab at the Marshall Space Flight Center. This evaluation has uncovered a variety of projects that could improve the efficiency and operation of the work groups as well as the overall integration of the system. In addition, this study provides the foundation for specification of a computer integrated manufacturing test bed environment in the Materials and Processes Lab.

A total of six branches were included in this investigation: EH13 - Non-destructive Evaluation; EH42 - Metals Processes; EH43 - Chemical and Non-Metals Processes; EH44 - Tooling Applications; EH52 - Planning and Control; and EH53 - Fixture Design. The latter two branches fall under the auspices of EH51 - The Fabrication Division. These six branches and their associated systems reside in all or part of buildings 4702, 4705, 4707, 4708, and 4711. The primary mode of investigation was to conduct interviews with key NASA and contractor personnel familiar with the projects and systems within each of the six branches. A total of 45 NASA and contractor personnel were interviewed over the course of six weeks. The purpose of these interviews was to gain an understanding of current projects, assess the current level of automation and integration, and to identify projects that would improve the overall system.

Three aspects of the system were considered in this evaluation: the physical system, the information/communication system, and the managerial/control system. Evaluation of the physical system in an integration study typically considers the level of process automation, the relationship between the various processes (i.e., how material flows through the system), as well as the material handling system. Because the primary focus of the M&P lab is on process optimization the movement of material/items from process to process appears to be minimal. Most items remain within the confines of a particular work area with the primary modes of material handling being forklifts, and overhead cranes (buildings 4705 and 4707). This investigation, therefore, focused on the processes involved, the equipment utilized and how it fits within the overall system.

Evaluation of the information system considered the underlying communications system, the computer systems being utilized, how data is passed from one function to another, the number and types of local area networks in place, what devices are hooked to the LAN, and the information needs of the various work groups. Because of the relatively high level of process automation this became the primary focus of this study. The majority of recommendations made within this document are concerned with improvements to the information/communication system.

Finally, evaluation of the managerial/control aspects of the system included consideration of how well various functions are communicating, which functions interact frequently and how well cross functional projects are being coordinated between functions. Integration of the managerial/control system requires that an organization breakdown barriers between functions. A few recommendations will be made regarding this aspect of the system but time did not permit large scale investigation of the managerial/control structure of the M&P lab.

Assessment of EH13 - Non-Destructive Evaluation: The NDE branch's systems and personnel are housed in building 4702 with the exception of the Computed Tomography Lab in 4707 and the Radiography Lab in 4711. The majority of systems and computers are stand-alone. While there has been some discussion regarding installation of an Ethernet backbone in 4702 none of the engineer's personal computers (PC's) are, at this time, linked to the NASA Ethernet or to the LAN. There is, in fact, only one connection to the Ethernet LAN the Branch Chief's secretary's terminal. Review of the NDE test equipment indicates that a mix of computer controlled and manual systems are currently being utilized. Again, the computer-controlled systems are not networked making them inaccessible from remote sites. As for test records, some areas are still utilizing paper based systems (e.g., the Radiography Lab).

Recommendations to EH13: This branch's primary need is a networking arrangement that allows each of the engineers within the branch to communicate electronically with each other and with personnel outside EH13. Two possible options that should be considered are: 1) installation of a personal computer (PC) based network within 4702 with a link to NASA's Ethernet, and 2) installation of Ethernet cards in all of the computer systems in 4702 allowing them to be directly connected to the

network. The advantage of the PC network is that it would allow the branch to utilize network versions of software and have a common set of software tools (i.e., word processor, spreadsheet, etc.). Either option would be an improvement over the current situation and should increase data sharing and provide a more efficient means of communication with other groups. One concern that must be addressed, regardless of the networking option chosen, is to how to provide access to NDE data while ensuring that good data is released. Also, the network should provide NDE personnel with access to MAPTIS. In addition, investigation should be done to determine how to link the TABS system to the NDE network so that branch personnel can access the information from the personal computer at their desk.

In addition to the installation of a network the NDE branch also needs to utilize database technology for maintaining test records. In particular, a database system should be developed to track test results in the Radiography Lab. Any other areas currently using paper based record keeping systems should also seriously consider converting to a computerized database system. The current paper based system(s) hinder retrieval and analysis of the data. Development of a computer based system should provide a more efficient and effective means for retrieving and analyzing the data.

Assessment of EH42 - Metals Processes: The systems utilized by the Metals Processes Branch are housed in portions of buildings 4705, 4707, and 4711. Overall, these systems exhibit a high level of process automation. A number of robotic and computer controlled welding systems are in place, however, the majority of these are stand-alone. Only two systems are currently linked to NASA's Ethernet, the old Cincinnati Milacron robot welding system in 4705 and the Vacuum Plasma Spray Cell in 4707. With the acquisition of some new systems there are 3 or 4 different controllers being utilized, limiting the transportability of weld schedule data. The oldest controller, the taper weld controller, was developed in the 1970's and is technologically dated. The newest system, the Motoman K-10 robot, utilizes a VME based, Ethernet compatible, controller. Plans are being developed to eventually replace the existing controllers with VME based, Ethernet compatible, controllers similar to the one on the Motoman K-10 robot.

In addition to the welding systems, the Vacuum Plasma Spray Facility, in 4707, exhibits a high level of process automation. The process is entirely computer controlled. It is also directly linked to the NASA's Ethernet backbone, allowing programs to be developed off-line and downloaded to the controller directly. This system is also setup to log data during operation.

This study also revealed that historical documentation of the R&D work going on in this branch is predominantly paper based. There is, at present, no common database of weld schedule information that NASA and contractor personnel can access to see the types of setups run in the past. Information sharing is done on an informal basis. A paper based system is currently being developed to keep track of weld schedule information and the resultant test results. While such a system is a good start an electronic database would make the retrieval and sorting tasks easier as the database becomes larger. It should be noted that some initial work was done with Intergraph to develop such a system but it was never fully implemented and is not currently being utilized.

Recommendations to EH42: This branches has two primary needs. First, they should continue to upgrade the welding controllers to VME based Ethernet compatible systems. Ultimately these systems can be linked to the Ethernet backbone, providing engineers with remote access to programs and information on the controllers. It should be noted that these new controllers should be GOSIP compliant if possible. GOSIP (Government Open System Interconnect Protocol) is a coming requirement for all government systems. This new standard is directed at the installation of open systems and promotes interoperability, which should be beneficial to the M&P lab because of the wide variety of computers and systems being used. After upgrading the controllers the most pressing need within this branch is the development of electronic databases to track and capture the R&D work under way. As has been mentioned, there is currently no central repository for weld schedule information it is presently scattered among several engineers log books. Three areas that could benefit by the development of a database system are Welding (i.e., weld schedule information and test results), the Vacuum Plasma Spray Cell (i.e., system settings and results), and the Materials test lab in 4711.

Assessment of EH43 - Chemical & Non-Metals Processes & EH44 - Tooling Applications: The areas supervised by these branches contain a wide variety of computers, controllers, and systems. In general there is a high level of process automation with a few manual processes. Most of the systems are, however, stand-alone with no link to NASA's Ethernet LAN. The most common means of passing programs to the controller is a serial connection between the controller and a remote PC or workstation.

As for the communication system, it was discovered that there are two separate, unconnected, Ethernet segments within Buildings 4711 and 4705, a NASA segment and an Intergraph segment. Data can be passed between the two systems by setting the files on a VAX that is accessible by both systems and pulling the file to the desired system. While passing data is possible it is cumbersome for most operators and may, in the long run, limit data sharing. In addition to the Ethernet LAN's a Novell network has recently been established to link PC's within building 4711. At present there are 50 users on the system and plans to expand to ~250 users in the future. This system should ultimately provide an efficient means of communication and data sharing within this facility.

Recommendations to EH43 and EH44: These branches should consider upgrading the controllers that see the greatest use of off-line programming. Again, any upgrades should be Ethernet compatible and GOSIP compliant. The greatest difficulty with making this recommendation is the fact that current activity levels make this cost prohibitive. Thus, it is suggested that three strategies be considered: 1) Establish a direct serial connection between the machine controller and a remote PC/workstation. This is essential what has been done to date. 2) Use a PC, hooked to the Ethernet LAN, with a serial connection to one or more controllers, as a remote storage device accessible over the network. This strategy will provide wider access to programs and data via the network. 3) Upgrade to Ethernet compatible and GOSIP compliant controllers. This is the most comprehensive strategy giving remote users full access to the controller. It is, however, the most expensive solution and, given the current level of activity in many areas, the most difficult to justify.

With regard to the communication system, eventually the NASA and Intergraph Ethernet segments should be integrated. The present configuration maintains redundant systems unnecessarily and limits data sharing. Technologically, there are no reasons that they cannot be integrated or at least linked together to provide a more efficient means of passing data. As for the Novell network in 4711, there is a need to establish an effective means of linking engineers on the PC LAN to the larger Ethernet LAN. This investigation indicated that, at present, not all engineers have access to the LAN. Also, there is a need to establish a set of procedures for passing documents/reports from commonly used PC based word processors to the CEO systems used by other divisions of NASA. While these procedures may already be in place there is a need to make sure that all users are aware of them. Passing data between the two systems should eliminate the need to recreate reports in CEO for wider distribution. Finally, as with the Metals Processes branch EH43 and EH44 could benefit from the use of database technology to maintain records of machine settings and experimental test results within in the various R&D areas (i.e., composites, MSA, etc.).

Assessment of EH52 - Planning and Control: The Planning and Control Branch of the M&P lab and is concerned with the manufacture of a wide variety of items, including everything from experimental fixtures and devices to flight hardware. They supervise the manufacturing facilities housed in 4705. The current manufacturing system contains a mix of computer controlled and manual systems. Some off-line programming is being done using Intergraph's I/NC package, however, some programs are still being developed manually. At present four machines are linked to this CAD/CAM system via a serial connection. Three or four recently installed machines could also be connected. The primary purpose of the direct connection is pass programs to the controller.

The production planning task utilizes the Integrated Manufacturing Planning and Control System (IMPACS) a scheduling system developed with the assistance of Boeing Computer Services. This system appears to be good for a job shop type environment such as EH52. Unfortunately, not all of VerVal's planners have access to the system. The system has evolved to its current configuration over the last seven years. Several initiatives are presently underway to enhance the IMPACS system and further integrate it with other NASA systems. Another system, the Manufacturing Inventory

Management System (MIMS) is used to maintain and track the material and parts inventory in 4705.

This branch also has a producibility group which checks drawings for correctness and provides feedback to designers on manufacturing considerations. This group appears to be a good start toward concurrent engineering.

Recommendations to EH52: The most pressing need of this group is improved communication and cooperation with other groups. Serious consideration should be given to forming a TQM/CI team to evaluate the design process and identify ways to improve communication and cooperation with the fabrication personnel. While the CAD/CAM system appears to be working adequately programming efficiency could be improved through increased communication between the programmers and the designers. At present a large proportion of the drawings are sent on paper. Thus, the programmers must recreate the drawings on the Intergraph system, often a time consuming process. Unfortunately, even when CAD files are sent they may not be Intergraph compatible or, when they are, they may not be in a format usable by the programmers. In these instances, the programmers must recreate the drawings on Intergraph or manually develop the NC program. Three things are needed to alleviate the problem of redundant drawing entry. First, designers need to be educated on the needs of the NC programmers. In particular, it would be useful to establish some basic guidelines for CAD drawings to ensure that the NC programmers will not have to modify them. Second, Intergraph compatible files should be sent when possible. If this is not possible then translators should be purchased for the most common file formats. Reviewing the CAD/CAM system also highlighted the need for increased communication between the fabrication personnel and the designers. While the producibility group is a good start toward concurrent engineering there is still a need to get fabrication involved as early in the design process as possible. In addition, to giving designers feedback on the producibility of their designs early involvement of fabrication makes designers aware of current shop capacity and expected lead times. It also allows the planner to begin early consideration of the make/buy decision.

With regard to the planning and control system the branch should continue their efforts to improve and expand the capabilities of the scheduling and inventory systems. Specifically, the IMPACS scheduling system and the Procurement Management Information System (PROMIS) should be linked. At present planners can access some information from PROMIS but there is a need to expand the screens available to allow the planner to monitor the status of outstanding purchase orders. Also, the Inventory system (MIMS) and the Automated Procurement Request System (APRS) should be modified to allow users to copy inventory information directly into APRS thereby reducing data entry time when creating long lists of purchased items. Finally, long term, the planning and control branch needs a real time scheduling system that would allow schedulers to assess the scheduling impact of new orders and the changing priorities of existing orders.

Assessment of EH52 - Fixture Design: This is the design branch of the M&P Labs Fabrication Division. The personnel and systems in this branch are housed in 4708. The development of designs is predominantly CAD based, utilizing a VAX based version of Intergraph's Engineering Modeling System [EMS]. This CAD system is linked to Intergraph's Ethernet and is used for drawing development and design analysis. Two or three Intergraph workstations are being used also, primarily for analysis. Also, while of the engineers have PC's in their offices they are not, at present, on a local area network or linked to either of the Ethernet systems or the IAN.

Recommendations to EH53: The present CAD system appears to fulfill the present needs of this group. In the future consideration should be given to moving toward networked workstations, given the current trend in the CAD/CAM industry toward distributed systems. A more important need in this area is an emphasis on increased communication between EH52 and EH53 early and often during design development. It appeared from talking to personnel from both branches that increased communication would benefit both groups. The designers need to be aware of the documentation needs of the fabrication people, particularly for items that will be run on NC equipment so as to reduce the need to recreate drawings just for program development. Fabrication needs to be aware of the jobs coming in so that the make/buy decision can be made early so the final customer can be given a good estimate of the expected delivery date. In addition, early involvement of the fabrication personnel will help to reduce the instances of designs that are difficult or impossible to produce. One

hindrance to communication is the fact that the EH52 and EH53 are located in separate buildings. Serious consideration should be given to locating the branches in the same building and, if possible, having the designers and planners share office space. Co-locating personnel from different functions would encourage informal communication and is one way to begin to breakdown functional barriers. Both branches need to gain an appreciation for the needs and concerns of the other.

Recommendations regarding Managerial/Control System: In addition, to the many branch specific recommendations a few managerial/control issues should also be addressed. While some of these recommendations echo those made earlier there is a need to reiterate and address them in the larger organization. The M&P lab and NASA in general, are in the midst of a large scale cultural change. From this investigation it was evident that the greatest need within the M&P lab is improved communication between divisions, between branches, and even in a few instances within branches. The personnel within the branches need to gain an appreciation for the needs and concerns of the other branches that they interact with, thereby breaking down functional barriers. The current emphasis on TQM and Continuous Improvement should continue to be strongly supported and encouraged by M&P lab administrators. TQM/CI is an important means for improving communication and helping personnel to gain an understanding of the processes that they are involved with and support.

More specifically, an evaluation of the R&D process needs to be undertaken. This evaluation should focus on ways to improve coordination among all groups involved in experimentation within the M&P lab. The current process seems to lack firm procedures for setting up and conducting experiments that involve several groups within the lab. Consideration should also be given to increasing the use of experimental design/Taguchi methods for setting up and conducting experiments. These techniques promote experimental efficiency and maximize the learning process. There is also a strong need for utilizing database technology to maintain historical records of research setups and results. In several cases, there appears to be no formal mechanism for capturing this information and making it available to NASA and contractor personnel. Ultimately, analysis and interpretation of these records could provide the foundation for establishment of knowledge bases to support future experimentation and investigation. Finally, in the area of systems management, there is a need to promote communication between groups involved in the specification and purchase of new equipment. They must communicate their needs to current system administrators to ensure that the equipment they are specifying is compatible and can be easily integrated into the existing system. As has been mentioned previously, there is a need to purchase systems that are GOSIP compliant which, if the promises hold true, should improve the integration of the overall system.

The facilities and systems that comprise the Materials and Processes Lab are quite impressive. Overall, the greatest need in the M&P Lab is better communication and cooperation between branches and functions. While the TQM/CI initiatives promote and support this, individuals are the ones that make it happen. NASA and contractor personnel at all levels, must buy into the idea that cooperation will take everyone farther than competition ever could. Because many of the projects and initiatives currently underway in this lab involve several different groups there is a strong need for communication to ensure that the goals of the program(s) are achieved in an effective and efficient manner. A second need that must be addressed is for individual project leaders to take a systems viewpoint when specifying, purchasing, and installing new equipment and systems. New systems must be specified with an understanding of how they fit into and support the overall system. The future must see a renewed emphasis on the integration of existing systems into the larger communications system. The benefits associated with these two fundamental suggestions, as well as the more specific recommendations mentioned previously, are a breaking down of functional barriers, increased efficiency, and a better foundation for knowledge development and retention.

1992

NASA/ASEE SUMMER FACULTY FELLOWSHIP PROGRAM

**MARSHALL SPACE FLIGHT CENTER
THE UNIVERSITY OF ALABAMA**

A STUDY OF THE LUTE METERING STRUCTURE

Prepared By: James W. Foreman
Academic Rank: Assistant Professor
Institution and Department: Alabama A & M University
Civil Engineering Department

NASA/MSFC

Office: Space Science and Applications
Division: Program Development Group
Branch: Payload and Orbital Systems

MSFC Colleague(s): Max Nein
Robert Porter



Two Metering Structure configurations were investigated. The first case was the traditional style metering structure which is larger than the outside diameter of the primary mirror. The second case investigated was the center support concept in which the outside diameter of the structure is less than the inside diameter of the primary mirror. Beryllium was used as the baseline material for this study. Four other materials were considered as candidates for the metering structure. These materials are:

Graphite Epoxy

Aluminum

Titanium

Invar

The loading conditions used for this study were estimated to be:

Quasi Static: 6.0 G (all three directions)

Random Vibration: 30.0 G (applied 1 axis at a time)

Taking advantage of symmetry, it was necessary to apply the lateral loading to only one axis. These loads were applied to both concepts and to all material configurations. The loadings as described above were based on the best available information and is felt to be adequate for this study since it was consistently used for all configurations. A load factor 2.00 was applied to both quasi static and random vibration loads. The allowable stresses are conservatively based yield strength of the material, except for the struts which are controlled by elastic stability. The stresses determined from each individual loading direction were conservatively combined by the absolute sum method.

A frequency determination was made treating the secondary mirror and metering structure as a two degree -of-freedom system.

Conclusions and Recommendations:

The results of the study as summarized in Table I indicate that the more favorable materials using weight as the criterion are beryllium and graphite epoxy. Either of these materials give a stiff lightweight structure. Graphite epoxy appears to be more favorable because of its low coefficient of thermal expansion. It is recommended that a study be made to determine the advantages and disadvantages of these two materials. Also, further study is needed to determine if there are other candidate materials which might be favored over beryllium or graphite epoxy. Additionally, a more comprehensive dynamic analysis and a stability analysis is recommended.

TABLE I
SUMMARY OF RESULTS
ACCEL/THERM LOADS*

MATERIAL	WEIGHT (LBS)	FREQUENCY (HZ)	DISPLACEMENT		
			X	Z	ROT(Y)
BERYLLIUM	6.93	177	.0183 .00087	.0002 .00014	.0067 .0015
GRAPHITE EPOXY	6.67	167	.0198	.0002	.0072
ALUMINUM	26.52	68	.100 .0021	.001 .00035	.037 .0036
TITANIUM	40.0	77	.0815 .00172	.0092 .0029	.0026 .0030
INVAR	80.0	71	.091	.001	.036

*1 DEGREE K DIFFERENTIAL ON 1/3 OF STRUCTURE

1992

NASA/ASEE SUMMER FACULTY FELLOWSHIP PROGRAM

MARSHALL SPACE FLIGHT CENTER
THE UNIVERSITY OF ALABAMA

HYBRID ROCKET PERFORMANCE

Prepared by: Robert A. Frederick, Jr., Ph.D.

Academic Rank: Assistant Professor

Institution and
Department: University of Alabama in Huntsville
College of Engineering
School of Mechanical and Aerospace
Engineering

NASA/MSFC:

Office: Propulsion Laboratory
Division: Propulsion Systems Division
Branch: Solid Propulsion Branch

MSFC Colleague: Benjamin Goldberg

A hybrid rocket is a system consisting of a solid fuel grain and a gaseous/or liquid oxidizer. Figure 1 shows three popular hybrid propulsion cycles that are under current consideration. NASA MSFC has teamed with industry to test two hybrid propulsion systems that will allow scaling to motors of potential interest for Titan and Atlas systems, as well as encompassing the range of interest for SEI lunar ascent stages and National Launch System Cargo Transfer Vehicle (NLS CTV) and NLS deorbit systems (1). Hybrid systems also offer advantages as moderate-cost, environmentally acceptable propulsion system.

The objective of this work was to recommend a performance prediction methodology for hybrid rocket motors. The scope included completion of: a literature review, a general methodology, and a simplified performance model.

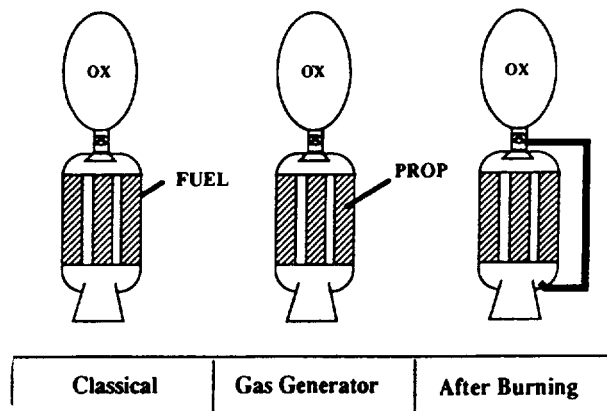


Figure 1. Hybrid Rocket Propulsion Cycles

A literature review team was established with three Master's students in conjunction with the University of Alabama in Huntsville. The literature review produced 450 citations on hybrid rocket motors and related technologies. From these, the team selected 120 papers for closer evaluation. The papers were catalogued and referenced. The following topics were examined in detail: Hybrid Rocket Performance, Hybrid Rocket Flight Vehicles - History, Hybrid Rocket Combustion Modeling, and Hybrid Rocket Testing Methodology. The results of the review are being developed into a lecture series that will be delivered at MSFC this fall entitled "Rediscovering Hybrids".

Hybrid rockets look like a combination of a liquid and a solid rocket. The hybrid rocket can borrow oxidizer tank, feed system, and injector technology from the liquid rocket. They also can use propellant grain, case, and nozzle hardware technologies from solid rockets.

However, when considering the internal combustion phenomena; liquids, solids, and hybrids are very different. Figure 2 compares the internal combustion phenomena of a liquid, solid, and hybrid rocket, and a solid fuel ramjet. In a liquid rocket, the fuel and oxidizer are essentially "completely" burned before they reach the entrance to the nozzle. In a

solid rocket the gas phase combustion occurs within a millimeter of the propellant surface with only active metal droplet combustion occurring in the port or nozzle. For the hybrid rocket, the active combustion region is in the boundary layer above the fuel surface. The details of the combustion processes are important in the hybrid because they control the fuel production rate. The hybrid rocket really looks like a solid fuel ramjet when considering the internal combustion processes.

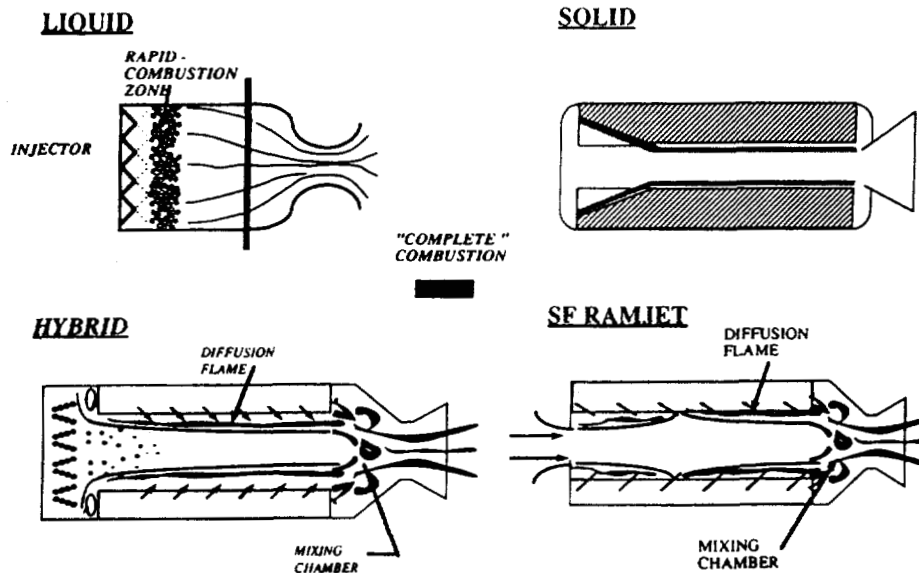


Figure 2. System Comparisons - Combustion Phenomena

The key performance analysis areas for a hybrid rocket are injector analysis, fuel regression rate analysis, grain evolution, mixing efficiency, and nozzle erosion rate. For a complete analysis, each of these areas must be coupled to an internal flowfield analysis. In simplified solutions, they are assumed to be uncoupled.

A general methodology for hybrid rocket performance would consist of three areas: a performance predictor, CFD analyses, and testing. An efficient performance program is required to make design trade studies and for the evaluation of test results. This predictive capability should embody, in a simplified form, the results of CFD analyses and testing. The performance predictor should be efficient enough that trade studies on particular parameters could be performed in a matter of hours. This would allow the designer to gain understanding of the underlying principles that are controlling the motor operation. CFD analyses and testing must be designed to provide essential global parameters to be used in the performance predictor.

Based on these premises, a very simple performance analysis code was developed for hybrid motors. The analysis had the

following assumptions: 1) uniform gaseous oxygen injection, 2) fuel regression controlled by oxidizer mass flux, 3) multiple circular ports, 4) constant nozzle erosion rate, 5) a combustion efficiency of 0.95, and 6) one-dimensional equilibrium in the chamber and nozzle.

A PC version of the One Dimensional Equilibrium Code with Transport Properties (ODETRAN) (2) was modified to perform the thermochemical calculations. A sensitivity study was performed on product species to reduce the thermal property data deck by 171 species so that ODETRAN can now run practical problems on a personal computer. This effort also produced a TM applications document entitled "Running ODETRAN for Rocket applications."

This simple analysis method was programmed on a spreadsheet. The spreadsheet allowed input of the number of ports, port length, characteristic velocity as a function of oxidizer-to-fuel ratio, and a transient oxygen flow rate. Once the program was checked out, a concept study for the National Launch System (NLS) was performed.

Figure 3 shows the concept that was investigated. The hybrid motor would be mounted on top of the NLS stage-and-a-half booster. Residual oxygen from the booster tank would be "blown down" through a multi-port hybrid rocket motor. This low-cost concept could fulfill the total impulse requirements of 585,000 lb_fsec to deorbit the stage. Using the spreadsheet and the results of the ODETRAN analysis, a concept was developed that has 30 ports, 750 pounds of fuel, a 36-in. length, and 517,000 lb_fsec of total impulse. Figure 4 show results of the analysis. A graph of the oxidizer mass flow, motor oxidizer-to-fuel ratio, and thrust as a function of time are plotted. Also, the characteristic velocity as a function of oxidizer-to-fuel ratio is shown.

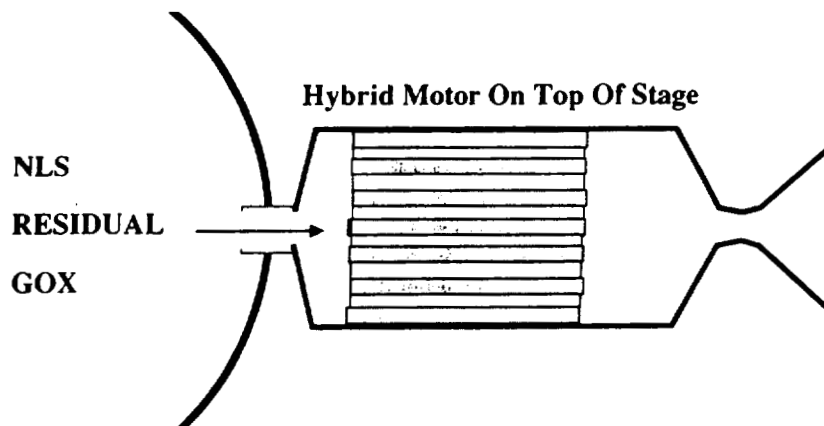
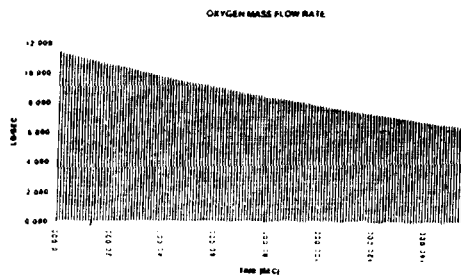
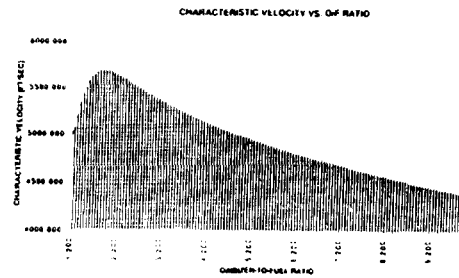


Figure 3. Hybrid Rocket Design for NLS Deorbit Application

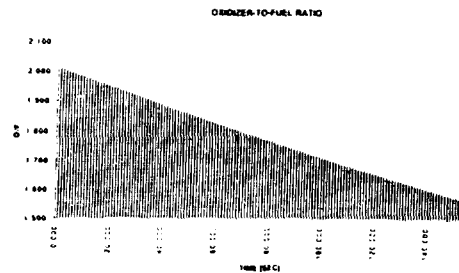
Oxygen Mass Flow Rate



C* vs. O/F/Ratio



Oxidizer-to-Fuel Ratio



Thrust

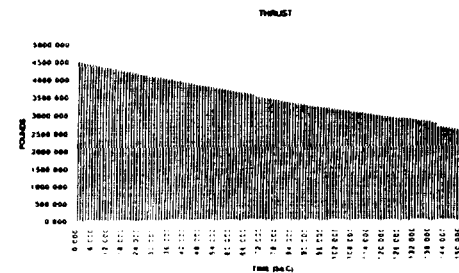


Figure 4. Results of Analysis of NLS Hybrid Deorbit Motor

The conclusions of this work are as follows: 1) the literature indicates moderate existing capability in hybrid ballistics, 2) thinking must be expanded to include performance tools from solid fuel ramjets, 3) component ballistic analyses must be coupled to the internal flowfield analyses, 4) mixing efficiency and nozzle/insulator erosion analyses for hybrids are slightly beyond existing practice, 5) a general performance methodology should embody results of CFD analyses, test data, and general ballistic analysis, and 6) concept studies can be performed with a simple spreadsheet program.

1. Goldberg, B. and Cook, J., "Preliminary Results of NASA/Industry Hybrid Propulsion Program," AIAA 92-3299, AIAA/SAE/ASME/ASEE 28th Joint Propulsion Conference, Nashville, TN July 6-8, 1992.
2. Maser, K., "ODETRAN-One-Dimensional Equilibrium and Transport Properties Program, Ver. 2.0," NASA MSFC, Users Document, Prepared for K.Gross/EP53/MSFC.
3. Greiner, B and Frederick, R.A., Jr., "Results of Labscale Hybrid Rocket Motor Investigation," AIAA 92-3301, AIAA/SAE/ASME/ASEE 28th Joint Propulsion Conference, Nashville, TN July 6-8, 1992.

1992

**NASA/ASEE SUMMER FACULTY FELLOWSHIP
PROGRAM**

MARSHALL SPACE FLIGHT CENTER

THE UNIVERSITY OF ALABAMA

GUIDE TO OBJECT-ORIENTED ANALYSIS AND DESIGN

Prepared by: Harry C. Harrison
Academic Rank: Associate Professor
Institution and Department: Capitol College
Department of Mathematics and
Computer Engineering

NASA/MSFC:

Office: Information Systems Office
Division: Systems Development and Implementation Office
Branch: Data Systems Branch

MSFC Colleague: Marcellus Graham

Introduction

Purpose

The purpose of this guide is to provide Marshall Space Flight Center personnel with guidelines for the use of object-oriented analysis and design and to describe how it can be accomplished within the framework of existing development directives, including the **Software Development Plan**. It is not intended as a detailed tutorial. The reader is referred to the Coad and Yourdon texts[1,2] in the References.

Overview

The term **object-oriented** has become a popular buzz word in the computer world today. Many say that it will be the dominant form of software development in the future. It is characterized by reusability of code, resulting in faster development and significantly lower development costs. In today's budget constrained world, it is critical to use the most cost-effective tool to develop software. NASA should be at the leading edge of this development.

While the object-oriented approach has great potential, it has been misused. Some vendors use this paradigm:

**Object-oriented is good.
My Product is object-oriented.
Therefore my product is good.**

Additionally, object-oriented analysis and design is still young. Standards are still not firm.

The object-oriented approach is not a panacea. It is not always the best choice. And when it is selected, the transition maybe difficult for many organizations. The object-oriented approach will require a radically new way of thinking about software development. Analysts will have to deal with a whole new language involving classes, inheritance, encapsulation, polymorphism, virtual functions, overloading, and a whole new model of programming.

Simplistically, in the object-oriented approach, the world is modeled in terms of objects that pass messages back and forth. The user does not need to know the details of how an object implements a message(data abstraction), but only what goes in and what comes back. He or she simply creates objects from a class and passes them messages.

The object-oriented analysis and design approach presented here is based on the Yourdon/Coad textbooks[1] and [2]. Their approach appears to be the most widely accepted and is very clearly explained in these texts. These texts are highly recommended to any developer who plans to utilize OOA/OOD.

Terminology

attribute - a characteristic of an object, such as a name, size, part number, etc.

class - An abstract description of the data and behavior of a collection of similar objects.

data abstraction - defining high-level data types that provide a complete description of the system without a great amount of detail.

encapsulation - the tying together of data and functions into a single entity.

inheritance - the property of objects that gives them access to data and functions contained in a previously defined class.

polymorphism - literally, "many shapes". The exact way of implementing a service or function depends on the class that an object is in. You may have the same function name implemented differently in different classes.

service - a behavior that an object performs.

The Object-Oriented Approach

The object-oriented approach began with the programming language Simula. It then spread with other languages such as SmallTalk, and C++. The need for analysis and design approaches to support these languages led to object-oriented analysis(OOA), object-oriented design(OOD), and object-oriented programming(OOP). A language that supports object-oriented programming is known as an OOL. OOD is very closely related to OOA. OOD basically refines the model that was built in the OOA analysis. Both can be done without necessarily building the system with a language that supports object-oriented programming(OOP). There are still benefits to be gained from such an approach.

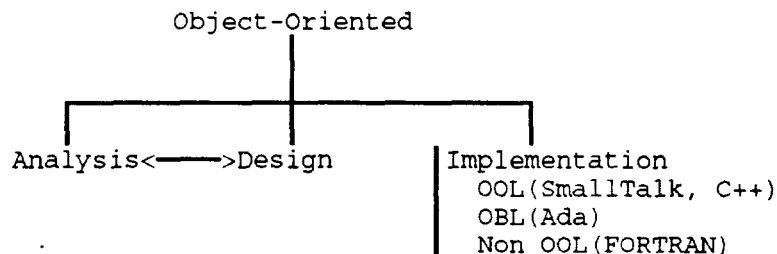


Figure 1 The Object-Oriented Approach

Object Diagrams

The heart of OOA/OOD is the object diagram. It consists of objects(rectangles with the object/class name, attributes, and services it provides listed inside. These objects have inheritance relations with classes, component relations when they are part of a larger system, and instance relationship when a certain number of the these objects are required for a system to perform. An object can pass message to other objects. These are the arrows. Objects can be grouped into subject areas to make the system easier to understand. Below is an object diagram that illustrates all of the symbols used.

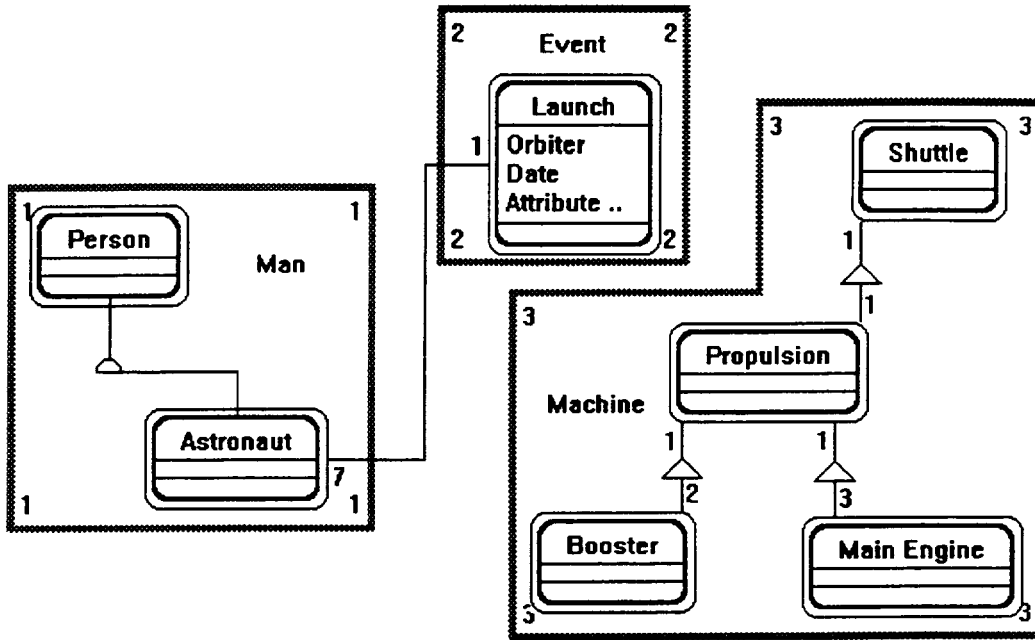


Figure 2 Object Diagram

The subject areas are Man, Machine, and Event. Inside Man is the class Person. A specialization of Person is Astronaut. The Astronaut class inherits information from person. Only the unique aspects of Astronaut need to be described, due to inheritance. There are 7 Astronauts required for a Shuttle mission. This is shown by an instance line. An event consists of a Shuttle Launch. A launch has an orbiter, a launch date, an STS number, etc. associated with it. The propulsion system consists of 3 main engines, 2 boosters, and a refueling tank. This is the component relationship.

Guidance for MFSC Software does not specify any particular development methodology. This report shows how charts such as the object diagram can be used in the development process.

Conclusions

Object-oriented analysis and design enable the developer to model the problem using objects, classes, attributes, and functions as the components. The combining of data and processing into a single entity (data encapsulation) protects the data and aids in making the software more reusable.

This approach is based on a model that is closer to reality. This facilitates communications with the user.

Although the approach is different from the classical waterfall approach used with structured techniques, the process can be adapted to fit within the guidelines of the SDP.

References

1. Peter Coad and Edward Yourdon, Object-Oriented Analysis, Yourdon Press, 1991.
2. Peter Coad and Edward Yourdon, Object-Oriented Design, Yourdon Press, 1991.

1992

NASA/ASEE SUMMER FACULTY FELLOWSHIP PROGRAM

**MARSHAL SPACE FLIGHT CENTER
THE UNIVERSITY OF ALABAMA**

**EXPERIMENTAL INVESTIGATION OF A SIMULATED
LOX INJECTOR FLOW FIELD AND OTHER
NONINTRUSIVE MEASUREMENT EFFORTS**

Prepared By: Roy J. Hartfield, Jr.

Academic Rank: Assistant Professor

Institution and
Department: Auburn University
Aerospace Engineering Department

NASA/MSFC:

Office: Science and Engineering
Division: Propulsion Laboratory
Branch: Performance Analysis

MSFC Colleague: Charles Schafer

Introduction

Efforts to improve the characteristics of fuel-oxidizer mixing in liquid rocket combustors have led to a swirl element design for a liquid oxygen injector which is being considered for use on the STME. For the design which is the subject of this investigation, the oxygen enters the injector element perpendicular to the injector axis and nearly tangent to the circular injector wall. This swirl element is at one end of a tube and the injector exit is at the other. This geometric configuration creates a plume in the shape of a conical sheet. This sheet is either primarily contiguous liquid or droplets depending on the pressure drop in the injector and the distance from the injector exit.

Probe-based devices such as two-dimensional grid patternators have been used to investigate simulated LOX injector flow fields (Hulka). The primary work described herein is an effort to use optical techniques to investigate the plume of a swirl injector element. For this investigation, a high pressure (500 psig) cold flow test facility was constructed. Water was used as the LOX simulate and air pressure was used to drive the injector flow field. Laser-induced fluorescence (LIF) from dye seeded into the water was used to obtain quantitative measurements of the time-averaged water concentration distribution in the plume. Scattered laser light and LIF were used for time averaged plume visualization and scattered light from a strobe with a 1 microsecond pulse was used for time-resolved plume visualization.

During the Summer Faculty Fellowship for which this report was developed, an additional effort, unrelated to the swirl injector investigation, was made to resolve fluctuations in the combustion product composition in the exhaust of a hybrid rocket motor. A brief description of this effort is included herein.

Hybrid Motor Investigation

Instabilities in the chamber pressure of a laboratory scale hybrid rocket motor have been observed and are possibly due to combustion instabilities induced by vortex shedding in the motor. To detect the combustion instabilities, a nonintrusive method for tracking the concentration of combustion products is needed. One fuel used in the motor is HTPB and a minor product of HTPB-oxygen combustion is NO_2 . LIF from NO_2 has been used successfully to track number densities (Barnes, Gulati, Agarwal) and the potential for observing fluctuations in laser-induced NO_2 fluorescence signal in the exhaust plume of the hybrid motor appeared to be an attractive instrument for correlating combustion instabilities to observed pressure fluctuations. A system to observe NO_2 fluorescence was assembled and operated briefly. This system uses an argon ion laser tuned to the 488 nm line as an excitation source and a photomultiplier tube as the detector. To discriminate against the chemiluminescence of the plume and other backgrounds, an optical chopper and a lockin amplifier were used in the data collection.

Efforts to observe NO_2 fluorescence signals were unsuccessful for a small number of rocket firings and the effort was abandoned so that the swirl injector project could proceed. However, in the effort to use NO_2 fluorescence as a diagnostic tool, an approximate calculation of the equilibrium mole fraction of NO_2 in an HTPB-oxygen flame was conducted for a range of oxygen to fuel mole fraction ratios known to exist in the motor. A plot of the calculated mole fractions and the corresponding equilibrium temperatures is given in Figure 1. The chemical equilibrium code known as STANJAN was used for this calculation and the calculation is approximate in that the bond energy for the HTPB fuel was neglected. NO_2 has been observed using the basic LIF technique described above for mole fractions of 5×10^{-4} which is approximately two orders of magnitude higher than the maximum

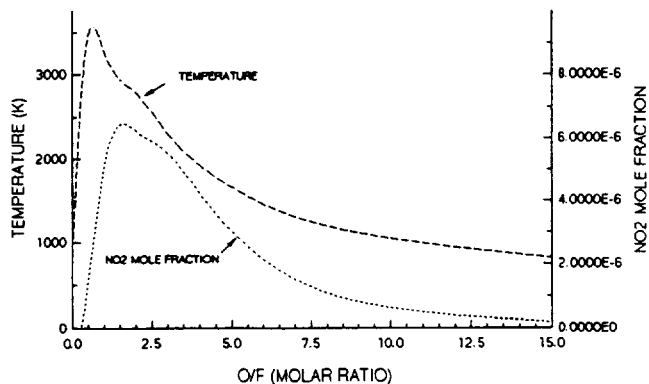


Figure 1: Approximate Equilibrium Calculation for HTPB - Oxygen Combustion

concentration found in Figure 1. This does not necessarily preclude the use of NO_2 as a detection molecule in the hybrid rocket flow field; however, signal to noise ratios will clearly be limited.

Swirl Element Injector Investigation

To begin an experimental investigation of a swirl element injector plume, a test rig was constructed. In this rig, high pressure (up to 500 psig) water is supplied to the injector using a network of stainless steel plumbing. An air bottle connected to the plumbing network is used to supply the high pressure. The plume from the injector empties into a stainless steel accumulator vessel. A centrifugal water pump is connected to this vessel and is used to fill the plumbing. Solenoid valves are used to isolate the air bottle, the injector, the water pump and a vent line. The injector is constructed with three axisymmetric rows of three ports each exhausting into the head end of a 9.3 mm diameter tube. The liquid travels for 13 cm at this diameter before encountering a forward-facing step cut at 60° to the axial direction. The tube diameter downstream of the step is 5.3 mm and this section extends 3 cm to the injector exit.

This investigation is composed of both efforts to understand the fluid mechanics of the swirl element injector and efforts to develop additional quantitative optical techniques for use in two-phase flows. In two-phase flows, strong signals from optical scattering are to be expected and are useful for visualization studies of phase boundaries and the plume structure. In the case of particulates or discrete liquid drops in a gas flow, highly developed scattering techniques such as Laser-Doppler-Velocimetry can be used to measure time dependent velocity components and particle sizes. However, for a dense liquid spray in which droplets are in the process of being formed from a liquid jet, the complicated directional dependence of the scattered light severely limits its use as a quantitative diagnostic tool. Signal levels from LIF are much lower than from scattered light; however, LIF is more attractive for quantitative measurements because the emission is isotropic. Intense scatter found in dense sprays can cause significant power reductions and spatial nonuniformities in a laser beam or sheet used as an excitation source thereby complicating the interpretation of the fluorescence signal. However, for the particular injector configuration investigated herein, a LIF technique for resolving the average radial liquid distribution in the plume has been implemented. This technique is based on the uniform illumination of the axisymmetric plume and a subsequent inversion of the measured fluorescence.

For the time-averaged measurements and visualization work, a Spectra Physics Model 2016 argon ion laser tuned to the 514.5 nm line was used as a light or excitation source. A 35mm SLR film camera was used for the visualization photographs and a Xibion Electronic Systems intensified CID camera (model ISG-205-DUHMQ-2) was used for the quantitative measurements. To obtain fluorescence measurements in the plume, 3 mg of R6G dye were added to the approximately 40 liters of water in the accumulator. For the argon ion laser, the 514 line is one of the strongest and is spectrally closest to the strongest part of the R6G absorption spectrum. The time-averaged visualization work was completed with a laser sheet formed using a 1 cm diameter glass rod to fan out the beam and a 35 cm focal length spherical lens to recollimate and focus the sheet. For uniform illumination, a microscope objective was used to expand the laser beam and a pin hole at the focus was used to spatially filter the expanding beam. For the time resolved photography, a 1 microsecond light flash was generated with a Stroboscope from Pioneer Electric and Research Corporation.

Figures 2, 3 and 4 are representative examples of the photographic visualization effort. Figure 2 is a photograph of the light scattered by a laser sheet passing through the center of the plume with an injector pressure drop of approximately 50 psi. Figure 3 is a photograph of the LIF for the same conditions and Figure 4 is photograph using the strobe with a 300 psi injector pressure drop. Because of the pressure difference for these particular photos, no detailed analyses will be given here; however, it should be noted that for all of the time averaged visualization photographs, the plume boundary in the vicinity of the injector exit was significantly curved but was very nearly straight in this region in the time resolved photographs. Visualization photographs such as those presented herein were taken for pressure drops of 100 psi, 300 psi and 500 psi. These photographs will be analyzed in detail in the future.

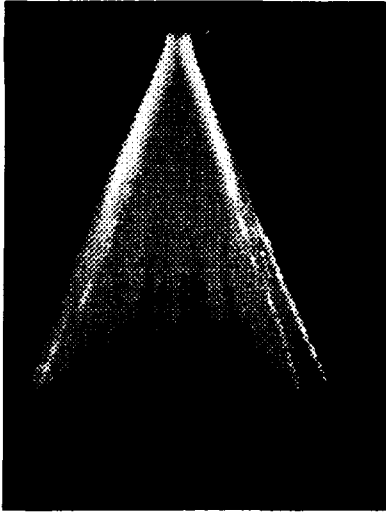


Figure 2: Photograph of Scattered Light From a Laser Sheet in Swirl Element Injector Plume

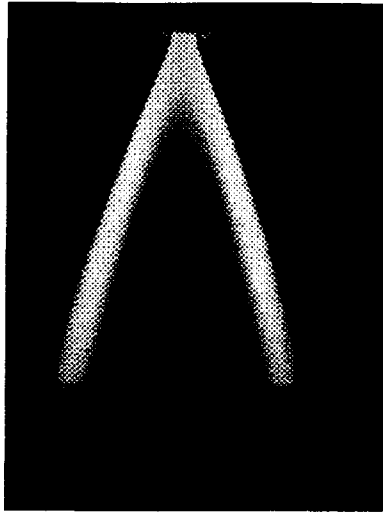


Figure 3: Photograph of Laser-Induced Fluorescence in Swirl Element Injector Plume

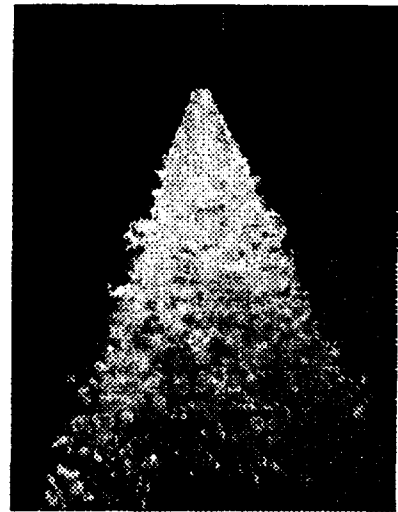


Figure 4: Photograph of Swirl Element Injector Plume Using a 1 Microsecond Strobe

The radial distribution of the liquid injectant was derived from fluorescence data collected using uniform illumination of the injectant plume. The plume data for a pressure drop of 105 psi was selected for this analysis. A three dimensional plot of normalized fluorescence intensity as a function of radial and axial position is shown in Figure 5. The general shape of the injectant plume is known to be a conical sheet

(because of centrifugal forces associated with the swirl). As mentioned above, the interface between the two fluid phases results in scatter and, ultimately, nonuniformities in the excitation source; however, since the bulk of liquid injectant is concentrated in a sheet at the exit of the plume, the half of the plume which the beam enters first is illuminated uniformly. For this reason, the right half of the data shown in Figure 5 was selected for the axisymmetric inversion process. The Abel inversion procedure (Shelby) was used to convert the spatially integrated axisymmetric signal distributions into radial intensity (or time averaged liquid mass fraction) distributions. This integral inversion is dependent on both the value of the data and the derivative of the data. For this reason, it is necessary to

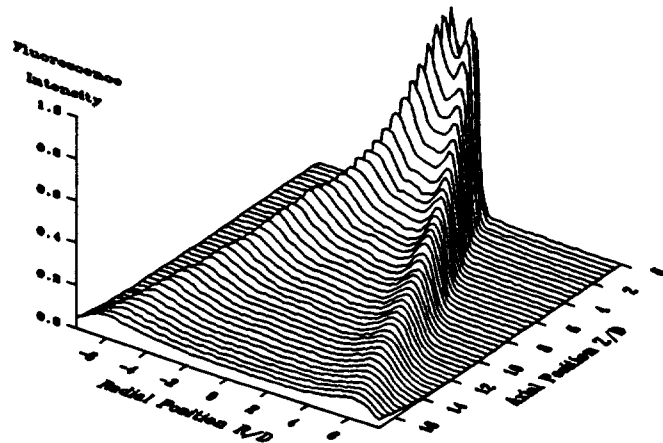


Figure 5: Fluorescence Data Collected at 105 psi With Uniform Illumination.

fit a smooth curve to the data before it is inverted. To illustrate the inversion process, the data at the nozzle exit and its curve fit are shown in Figure 6 and the inversion of this data is shown in Figure 7. The uncertainty in this inversion is highest at the center because of the nature of the mathematics. Additionally, at the jet exit, interference from the nozzle affects signal quality; nevertheless, with the exception of the nonzero concentration along the centerline, the inverted signal reflects the expected liquid distribution in the plume. The Abel inversions of the data at 0.29 injector diameters away from the injector and at 1.14 injector diameters away from the injector exit are shown in Figures 8 and 9. Although there is no data collected using classical techniques readily available to compare with these measurements, at these locations where there is little interference, the inversions represent a mass distribution expected for this plume with most of the injectant concentrated at the edge of the plume and negligible amounts of liquid at the plume core. It should be noted that an additional source of error is the scattering of the fluorescence signal by the plume. Some proposed future work will address this issue.

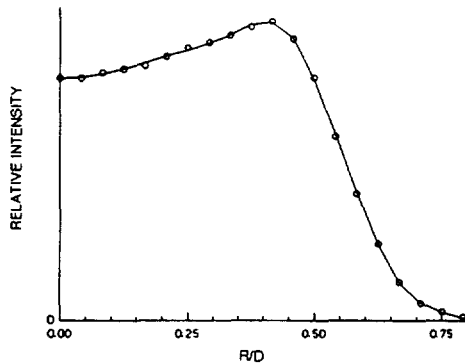


Figure 6: Data For Abel Inversion at Nozzle Exit

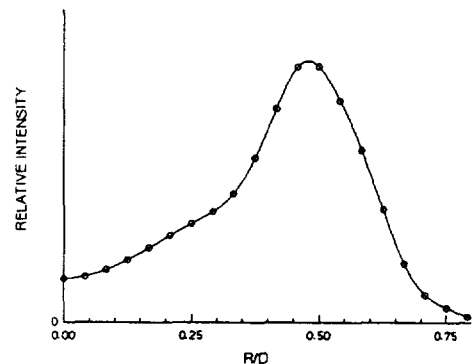


Figure 7: Abel Inversion at Nozzle Exit

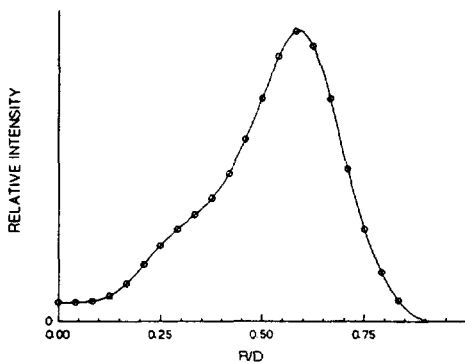


Figure 8: Abel Inversion at $Z/D = 0.29$

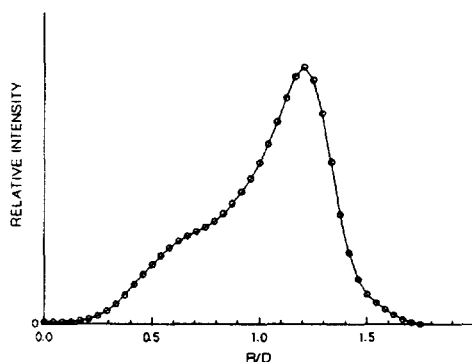


Figure 9: Abel Inversion at $Z/D = 1.14$

Conclusions

A swirl element injector flow field has been investigated using both visualization techniques and a new LIF technique for the quantitative measurement of the mass distribution of liquid in the plume. This work included the construction of a suitable spray rig, some film photography and the development of an appropriate quantitative measurement approach.

Acknowledgement

The work presented herein has been supported by Richard Eskridge, Chris Dobson and Tony Robertson. Their efforts have been invaluable to the completion of this project.

References

1. Agarwal, Y., T. Hadeishi and Robben, F., "Measurement of NO_2 Concentration in Combustion using Fluorescence Excited by an Argon-Ion Laser," AIAA Paper 76-136, presented at the Fourteenth Aerospace Sciences Meeting, Washington, D.C., 1976.
2. Barnes, Russell H., Boiarski, Anthony A., and Kircher, John F., "Laser Spectroscopy For Continuous Combustion Applications," U. S. Department of Energy Report For Work Performed Under Contract No. W-7405-ENG-92-088.
3. Gulati, A. and Warren, R. E., Jr., " NO_2 -Based Laser-Induced Fluorescence (LIF) Technique to Measure Cold-Flow Mixing," AIAA 92-0511, Presented at the AIAA Thirtieth Aerospace Sciences Meeting, Reno, NV (January 1992).
4. Hulka, J., Schneider, J. A., and Davis, J., "Single Element Injector Testing For STME Injector Technology," AIAA 92-3281, Presented at the Twenty-Eighth AIAA/SAE/ASME/ASEE Joint Propulsion Conference and Exhibit, Nashville, TN (July 1992).
5. Shelby, R. T., "Abel Inversion Error Propagation Analysis," Master of Science Thesis, The University of Tennessee, June 1976.

N93-17298

1992

NASA/ASEE Summer Faculty Fellowship

Marshall Space Flight Center
The University of Alabama

**Modeling for Health Monitoring and Control
with Applications to the Space Transportation Main Engine**

Prepared By:	Arthur J. Helmicki
Academic Rank:	Assistant Professor
Institution:	University of Cincinnati Department of Electrical and Computer Engineering
NASA/MSFC:	
Office:	Structures and Dynamics Laboratory
Division:	Control Systems Division
Branch:	Mechanical Control Systems Branch
MSFC Colleagues:	D. Pat Valley Fred Kuo Tom Fox

1 Introduction

The work reported herein represents a continuation of work begun at MSFC during the 1991 NASA/ASEE Summer Faculty Fellowship Program [5, 7]. During this period the author proposed and studied a paradigm for the analysis and synthesis of Integrated Health Monitoring and Control Systems (IHMCS) for rocket engines. This work was motivated by NASA's desire to develop advanced propulsion systems which could operate with increased reliability at decreased cost. The Space Transportation Main Engine (STME) whose function it is to provide primary thrust for the National Launch System (NLS) family of vehicles is a primary example of this trend [2, 9].

The need for an *integrated* approach to health monitoring and controls was established by the author who has identified significant interaction effects which exist between control and health monitoring functions [5, 7]. The nature of these interaction effects is such that unless they are taken into account during the design phase, significant performance degradation may occur in overall the system operation.

The specific approach proposed allows the designer to embed the IHMCS into a general system architecture wherein the wide array system analysis and design tools can be brought to bear. Within the this approach off-nominal conditions are modeled as indicated in Figure 1. Here p denotes some nominal component or subsystem within the rocket engine. In the first case (Figure 1(a)), off-nominal conditions are represented by exogenous signals f injected at either the component input or output. When off-nominal conditions of this sort are incorporated into the overall engine model, the IHMCS analysis and design tasks can be reduced to problems in tracking and disturbance rejection [5, 7]. In the second case (Figure 1(b)), off-nominal conditions are represented by exogenous component dynamics Δ which may augment the nominal component dynamics. When off-nominal conditions of this sort are incorporated into the overall engine model, the IHMCS analysis and design tasks can be reduced to problems in uncertainty accommodation and robustness [5, 7].

In either case, it is clear that the approach discussed above is model-based. Thus, in order to apply these results it necessary to have access dynamical models for both the nominal rocket engine system and all off-nominal conditions of interest. Alternatively, and perhaps more favorably, would be to have a method for obtaining such models in a systematic manner. It is the task of this report to present just such a method.

This methodology is based on the application and manipulation of the fundamental laws of conservation in order to derive dynamical models for thermo-fluid systems such as those contained in chemical propulsion systems. It has a number of significant features which make it well suited for use addressing the problems encountered in IHMCS design: First, it allows the assembly of dynamical nominal and off-nominal engine models of low order by indicating the significant dynamics. Second, it allows us to distinguish between those off-nominal conditions which are likely to be modeled as signal type (Figure 1(a)), and those likely to be modeled as uncertainty type (Figure 1(b)). Third, it allows for the easy incorporation of various sensor and actuator types. Finally, it provides models in a format suitable for direct computer simulation.

Due to space constraints, the development here is necessarily brief and the interested reader is referred to [6] for a more detailed treatment.

2 Development of Thermo-fluid Modeling Principles

Chemical propulsion systems such as the STME are basically thermo-fluid systems whose dynamics are governed by the laws of conservation of mass, momentum, and energy. Discussion of these basic laws of physics can readily be found in the literature (e.g., [3, 8]). Here we will apply these laws in order to develop a set of principles for model development by studying the dynamical behavior of the fluid in a generic engine component represented by the variable area control volume given in Figure 2. The results given here are motivated by treatments given in [8, 4].

The basic assumptions which are made for the purposes of the development below are given as follows: (i) Fluid is allowed to cross the boundary only at the inlet ($x = x_1$) and the outlet ($x = x_2$). (ii) We assume that the fluid flows in the component are quasi-one-dimensional, i.e., flow properties are axisymmetric and uniform in any plane normal to the direction of flow. (iii) Where the working fluid (i.e., the propellants, combustion products, etc.) are in gaseous state, they behave as ideal gases. Specifically, $p = \rho RT$, $e = c_v T$, and $h = c_p T$. (iv) Body forces are negligible. (v) The flow is inviscid.

Given these assumptions we can now develop dynamical expressions characterizing the behavior of the fluid in the generic engine component of Figure 2.¹ The behavior of this fluid can be completely characterized in terms of 4 state variables: $V(x, t)$ - flow velocity, $p(x, t)$ - pressure, $T(x, t)$ - temperature, and $\rho(x, t)$ - density. These 4 variables are constrained to obey the laws of conservation of mass, momentum, and energy which can be expressed for the control volume of Figure 2 as follows:

Conservation of Mass:

$$\frac{\partial}{\partial t} \iiint_{\mathcal{V}} \rho dV = - \iint_S \rho \mathbf{V} \cdot d\mathbf{S} \quad (1)$$

Here the terms, from left-to-right, can be interpreted as follows: the rate of increase of mass in \mathcal{V} , and the mass flow out of S .

Conservation of Momentum:

$$\frac{\partial}{\partial t} \iiint_{\mathcal{V}} \rho \mathbf{V} dV + \iint_S (\rho \mathbf{V} \cdot d\mathbf{S}) \mathbf{V} = - \iint_S p d\mathbf{S} \quad (2)$$

Here the terms, from left-to-right, can be interpreted as follows: the rate of increase of momentum in \mathcal{V} , the momentum flow across S , the total body force in \mathcal{V} , and the total pressure force on S .

Conservation of Energy:

$$\dot{Q} + \dot{W}_{\text{shaft}} - \iint_S p \mathbf{V} \cdot d\mathbf{S} = \frac{\partial}{\partial t} \iiint_{\mathcal{V}} \rho \left(e + \frac{V^2}{2} \right) dV + \iint_S \rho \left(e + \frac{V^2}{2} \right) \mathbf{V} \cdot d\mathbf{S} \quad (3)$$

Here the terms, from left-to-right, can be interpreted as follows: the rate of heat added across S , the rate of shaft work done in \mathcal{V} , the rate of work done on S by pressure forces, the rate of change of energy in \mathcal{V} , and the rate of flow of energy across S .

Compressible Flow: We begin with the case where the fluid flow is considered compressible. The assumption of compressibility is necessary in the rear stages of a rocket engine system where the propellants/combustion products are in gas phase. Under these conditions equation 1 can be simplified to yield:

$$\frac{\partial \rho}{\partial t} = \frac{A}{V} \left(\rho_1 V_1 \frac{A_1}{A} - \rho_2 V_2 \frac{A_2}{A} \right)$$

where A denotes the mean area between inlet, x_1 , and outlet, x_2 .

It is clear from this expression that if the ratio A/V is large, then the dynamics corresponding to the mass equation for the component tend to equilibrium quickly. In such cases, the dynamic mass equation can be replaced by the algebraic equation $\rho_1 V_1 A_1 = \rho_2 V_2 A_2$ for that component, and the mass equation does not contribute to the system's dynamic order.

In a similar manner, equation 2 can be simplified yielding the expression

$$\frac{\partial(\rho V)}{\partial t} = \frac{1}{x_2 - x_1} \left(\rho_1 V_1^2 \frac{A_1}{A} - \rho_2 V_2^2 \frac{A_2}{A} + p_1 \frac{A_1}{A} - p_2 \frac{A_2}{A} \right)$$

From this expression it is clear that if $1/(x_2 - x_1)$ is large, then the dynamics corresponding to the momentum equation for the component tend to equilibrium quickly. In such cases, the dynamic momentum equation can be replaced by the algebraic equation $\rho_1 V_1^2 A_1 + p_1 A_1 = \rho_2 V_2^2 A_2 + p_2 A_2$ for that component, and the momentum equation does not contribute to the system's dynamic order.

Finally, equation 3 can be simplified yielding the expression

$$\frac{\partial}{\partial t} \left[\rho \left(e + \frac{V^2}{2} \right) \right] = \frac{1}{V} (\rho_1 A_1 V_1 c_p T_1 - \rho_2 A_2 V_2 c_p T_2 + \dot{W}_{\text{shaft}} + \dot{Q})$$

From this expression it is clear that if V is small, then the dynamics corresponding to the energy equation for the component tend to equilibrium quickly. In such cases, the dynamic energy equation can be replaced by the algebraic equation $\rho_1 A_1 V_1 c_p T_1 + \dot{W}_{\text{shaft}} + \dot{Q} = \rho_2 A_2 V_2 c_p T_2$ for that component, and the energy equation does not contribute to the system's dynamic order.

¹Table 1 provides a catalog of the symbols used here.

Incompressible Flow Dynamics: Next, we consider the case where the fluid flow is incompressible. The assumption of incompressibility is especially reasonable in the front stages of a rocket engine system where the propellants are still in liquid phase. In this case $\rho(x, t)$ is constant and so not a dynamic state variable, and the energy equation is not needed. The equations for conservation of mass and momentum given above can be simplified to yield

$$V_1 = V_2 \quad , \quad \frac{dV}{dt} = \frac{A}{\rho(x_2 - x_1)}(p_2 - p_1) .$$

Summary: Based on the analysis given here, the relative sizes for

$$\frac{A}{V} , \frac{1}{x_2 - x_1} , \frac{1}{V} , \frac{A}{\rho(x_2 - x_1)}$$

for a given engine component can be used to decide which dynamics are required to model that component, and which dynamics can be replaced by algebraic relationships.

3 Application to the STME

The results outlined above were applied to develop preliminary models of the STME for the purposes of studying the health monitoring and control functions.

Figure 4 provides a schematic diagram of the engine [2]. As it indicates the STME will employ a gas generator cycle with liquid hydrogen and oxygen propellants. Figure 3 provides a preliminary indication of the physical layout of the STME roughly to scale thereby providing of the relative dimensions of the various components [2].

Based on the information contained in Figure 4 the STME is modelled using the concepts from Section 2 by first breaking it up into four major assemblies: Main Combustion Chamber, Fuel Turbo-pump, Oxidizer Turbo-pump, and Gas Generator. Next, the relative dimension information given in Figure 3 is used to characterize the behavior of each subassembly using the appropriate combination of dynamic and algebraic equations. This resulted in a 17th order dynamical engine model. Finally, the overall model was encoded into MARSYAS [1] and used for simulation studies.

References

- [1] *MARSYAS User's Manual: Marshall System for Aerospace Simulation*, July 1992.
- [2] STME technical information document. Technical report, The Space Transportation Propulsion Team, June 1992.
- [3] J. D. Anderson. *Modern Compressible Flow With Historical Perspective*. McGraw-Hill, 2nd edition, 1990.
- [4] K. M. Eveker and C. N. Nett. Model development for active surge control/rotating stall avoidance in aircraft gas turbine engines. In *Proc. 1991 Amer. Cont. Conf.*, 1991.
- [5] A. J. Helmicki. Rocket engine health monitoring: A system's perspective. Technical report, NASA Marshall Space Flight Center, August 1991. Detailed report for NASA/ASEE Summer Faculty Fellowship Program.
- [6] A. J. Helmicki. Health monitoring and control for the STME: A case study. Technical report, NASA Marshall Space Flight Center, September 1992. Detailed report for NASA/ASEE Summer Faculty Fellowship Program.
- [7] A. J. Helmicki, F. Kuo, and D. P. Valley. Rocket engine health monitoring and control: Some connection and their implications. In *Proc. 3rd Annual Health Monitoring Conf. for Sp. Prop. Sys.*, Cincinnati, OH, November 1991.
- [8] C. C. Lin and L. A. Segel. *Mathematics Applied to Deterministic Problems in the Natural Sciences*. Macmillan, 1974.

[9] J. W. Smelser and M. T. Constantine. STME: Streamlining the engine of change. *Aerospace America*, pages 22-25, July 1992.

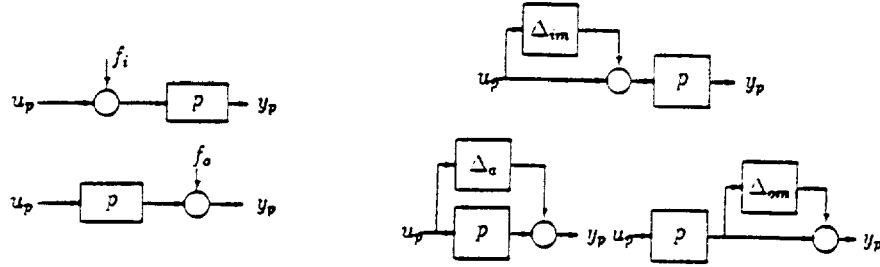


Figure 1: (a) Signal type and (b) Uncertainty type off-nominal conditions.

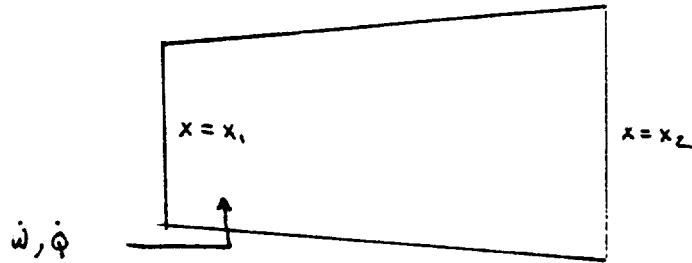


Figure 2: Generic engine component control volume.

Symbol	Variable
p	pressure
e	internal energy
h	enthalpy
ρ	density
T	temperature
V	flow velocity
A, S	area, surface area
V	volume
Q	heat

Table 1: General variable definitions.

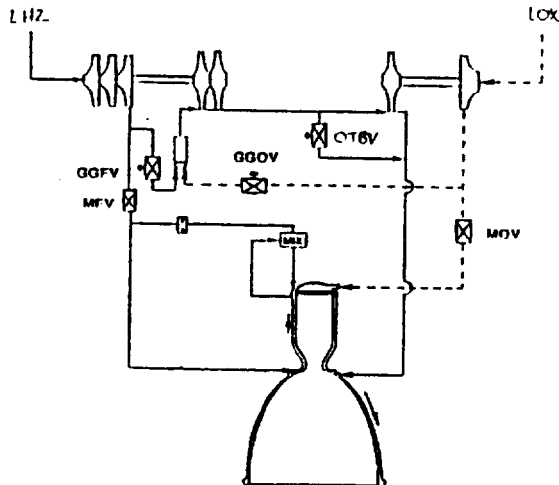


Figure 4: STME flow schematic.

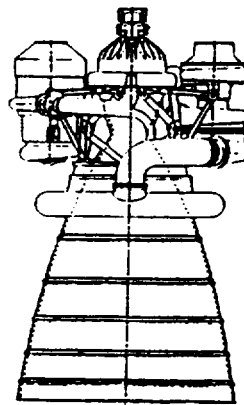


Figure 3: STME physical layout.

N93-17899

1992

NASA/ASEE SUMMER FACULTY FELLOWSHIP PROGRAM

**MARSHALL SPACE FLIGHT CENTER
THE UNIVERSITY OF ALABAMA**

**POST-IMPACT BEHAVIOR OF
COMPOSITE SOLID ROCKET MOTOR CASES**

Prepared By: Alton L. Highsmith
Academic Rank: Assistant Professor
Institution and Department: University of Alabama
Department of Aerospace Engineering
NASA/MSFC:
Office: Materials and Processes Laboratory
Division: Non-Metallic Materials Division
Branch: Polymeric Materials Branch
MSFC Colleague(s): Alan Nettles

In recent years, composite materials have seen increasing use in advanced structural applications because of the significant weight savings they offer when compared to more traditional engineering materials. The higher cost of composites must be offset by the increased performance that results from reduced structural weight if these new materials are to be used effectively. At present, there is considerable interest in fabricating solid rocket motor cases out of composite materials, and capitalizing on the reduced structural weight to increase rocket performance. However, one of the difficulties that arises when composite materials are used is that composites can develop significant amounts of internal damage during low velocity impacts. Such low velocity impacts may be encountered in routine handling of a structural component like a rocket motor case. The ability to assess the reduction in structural integrity of composite motor cases that experience accidental impacts is essential if composite rocket motor cases are to be certified for manned flight. While experimental studies of the post-impact performance of filament wound composite motor cases have been performed (1,2), scaling impact data from small specimens to full scale structures has proven difficult. If such a scaling methodology is to be achieved, an increased understanding of the damage processes which influence residual strength is required. The study described herein was an initial investigation of damage development and reduction of tensile strength in an idealized composite subjected to low velocity impacts.

Composite rocket motor cases are cylindrical structures which are fabricated using a filament winding process. When in service, these cylinders are subjected to internal pressures which give rise to tensile stresses in the longitudinal and hoop directions, with the stress in the hoop direction being dominant. The filament wound structure typically contains some combination of helical layers, hoop direction layers, and longitudinal layers. For the present study, it was not practical to fabricate filament wound specimens. Instead, 12 in. by 12 in. flat plate laminates fabricated from Fiberite T300/934 graphite epoxy prepreg tape were used to model the filament wound structure. A repeating pattern of layers similar to that found in filament wound cases was used. However, to reduce the complexity of the damage in this initial study, no counterparts to the longitudinal layers were included in the model structure. The stacking sequence chosen was $[0_2/(+70)_2/0_2/(+70)_2/0_2]_n$, where the 0° plies represent the hoop direction layers in the filament wound structure, and the 70° plies represent the helical layers in the filament wound structure.

A drop tower-type impact testing machine was used to impact the specimens. The specimens were 10 in. long by 3 in. wide, and were held in place by a pneumatic clamping fixture. The clamping plates contained 2.5 in. diameter holes which allowed the specimen to move out of plane during the impact. Impact energy was controlled by adjusting the height from which the crosshead assembly was dropped. Dynamic impact data was collected from the 0.25 in. diameter instrumented impact tup during impact. One important factor influencing the impact response of a solid rocket motor case is whether or not the case has been filled with propellant (3). It was expected that filled cases will develop less damage, since the propellant increases the overall rigidity of the structure. However, impact of the propellant-backed case may in fact be the most critical scenario since the propellant backing impedes the use of non-destructive techniques for damage assessment. For this reason, some specimens were impacted while backed with a 1.0 in. thick layer of inert propellant, and others were impacted without any backing. A solid steel clamping plate was used on the bottom (backing) side of the propellant-backed specimens.

The test matrix used to plan the experimental program in the present study is shown in Table 1. Based on some preliminary impact tests, three impact energies -- low (3.0 in.-lb.), intermediate (7.5 in.-lb.) and high (12.0 in.-lb.) were used. For each combination of impact energy and propellant backing, six specimens were impacted. Three of these specimens were loaded to failure in a tension testing machine in order to determine

Table 1. Test matrix used in designing the present study.

Propellant Backing	Low Impact Energy		Intermediate Impact Energy		High Impact Energy	
	Residual Strength	X-Ray Inspection	Residual Strength	X-Ray Inspection	Residual Strength	X-Ray Inspection
Backed	3	3	3	3	3	3
Unbacked	3	3	3	3	3	3

the residual tensile strength after impact. The other three specimens were treated with an x-ray dye penetrant, and then radiographed in order to determine what damage had been induced by the impact event.

Uniaxial tension tests were performed to assess strength reduction resulting from impact. The load was applied in the 0° (hoop) direction. Gripping tabs were applied to those specimens which were tested for tensile residual strength. The tabs were approximately 3.25 in. long by 3 in. wide. Some specimens were equipped with 0.1875 in. thick glass/epoxy composite tabs, while others were equipped with 0.25 in. thick aluminum tabs. The tabs were bonded to the specimens using a fast-acting cyanoacrylate adhesive. Generally, the glass/epoxy tabs and the aluminum tabs worked equally well. It was found that specimens that were tested shortly after the tabs were bonded failed at relatively low loads, and failure was associated almost entirely with the gripped region. A cure time of 16 hours or more was found to circumvent these premature failures.

As mentioned previously, some of the specimens were inspected via dye-penetrant enhanced x-ray radiography (4) after being impacted. The dye penetrant used was a zinc iodide solution (60 g zinc iodide, 10 ml. water, 10 ml. isopropyl alcohol, 10 ml. Kodak "Photo-Flo 200"). A small dam encircling the impact site was made using plumbers putty. This dam was filled with the zinc iodide solution, which was allowed to seep into the specimen for at least one hour. The dye penetrant filled those damage events (matrix cracks, delaminations) which it could flow into. The zinc iodide thus rendered these areas more opaque to x-rays than the surrounding undamaged regions. Three radiographs were taken of each specimen using different angles of incidence of the x-ray beam -- one with an angle of incidence of 82.5°, one with an angle of incidence of 90°, and one with an angle of incidence of 97.5°. The 90°, or normal incidence x-ray provided a planform view of damage in the specimen. The other two x-rays formed a stereo pair and, when viewed using a stereo viewer, provided a three dimensional view of damage in the specimen (4). Using such a stereo imaging process, it was possible to resolve the location of damage through the thickness of the specimen.

It is appropriate to note that the test matrix shown in Table 1 does not reference specimens that are tested for residual strength after x-ray inspection. There was some concern that the x-ray dye penetrant might affect the residual strength, and therefore the original plan required that specimens tested for residual strength should not be treated with x-ray dye penetrant. However, as mentioned previously, there were some premature failures attributed to an inadequate cure of the adhesive used to bond the gripping tabs to the specimens. Specimens used for damage inspection via radiography were used to provide residual strength data for the case of unbacked specimens subjected to low impact energy. Residual strengths obtained from these specimens were consistent with other residual strengths obtained in this study. Certainly this study was too limited to resolve the question of whether or not the dye penetrant affects residual strength. The original plan specimens tested for residual were not to be radiographed. However, resolution of this issue should be considered as part of some future study. If the dye penetrant were found not to affect the residual strength, the dye-penetrant enhanced x-ray technique could be safely used to inspect actual structural components.

Figure 1 shows residual strength versus impact energy for both backed and unbacked materials. All of the individual test results are presented in the figure. In order to obtain reference strength data, two specimens were tested for tensile strength without being subjected to any impact loading. The tensile strengths for these specimens correspond to the two solid circles plotted at zero impact energy. There is significant scatter in the tensile strength data. Some of this scatter can be attributed to the inherent variability of the composites, and some of this scatter has been attributed to the influence of the grips on failure. While all of the specimens represented in Fig. 1 exhibited significant damage development and growth within the test section during the tensile test, in many of the specimens, the final fracture occurred within the gripped regions. The use of longer test specimens with a streamlined (dogboned) test section would help reduce this data scatter.

The average residual strength data for each of the impact levels, indicated by the lines in Fig. 1, reveal some interesting trends. Neither the backed nor the unbacked specimens exhibit appreciable changes in residual strength resulting from the low and intermediate energy impacts. The backed specimens might show a slight reduction in residual strength after the high energy impact. On the other hand, the unbacked specimens exhibit a 10 percent reduction in tensile strength after the high energy impact. As expected, the unbacked specimens are more susceptible to tensile strength reduction after impact than the backed specimens.

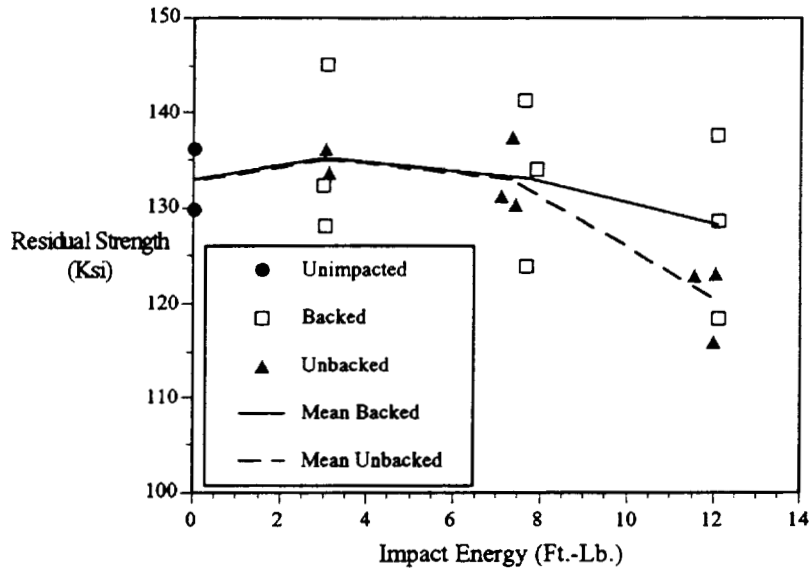


Figure 1. Plot of residual tensile strength versus impact energy for backed and unbacked specimens.

The inert propellant does provide sufficient reinforcement to limit the deflection of the composite, and hence reduce the effect of the impact.

Normal incidence x-ray radiographs taken from backed and unbacked specimens subjected to high energy impacts are presented in Fig. 2. The sharp lines that appear in the radiographs correspond to matrix ply cracks that were decorated with dye penetrant. Careful inspection of the radiographs reveals ply cracks in three different directions corresponding to the three different ply orientations. The most obvious ply cracks are

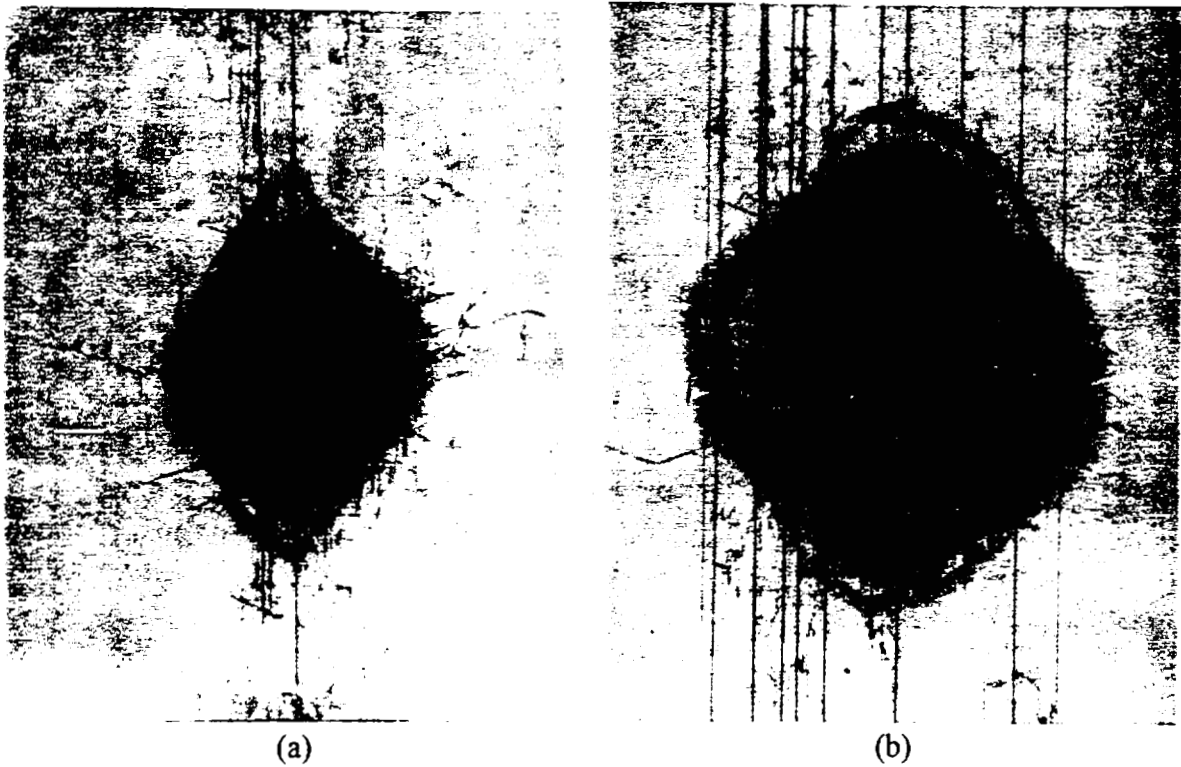


Figure 2. X-ray radiographs of (a) backed and (b) unbacked specimens subjected to high energy impacts.

the long vertical cracks, or longitudinal splits, in the 0° layers. All of the 0° layers exhibit some splitting. Most of the damage is concentrated in the center of the specimen, around the impact site. The various shaded regions that form elliptical or "cloverleaf" shapes correspond to delaminations that were decorated with dye penetrant. Stereo imaging shows that damage near the impact site is distributed in a conical region radiating from the impact site through the specimen thickness.

As seen in Fig. 2, more extensive damage developed in unbacked specimens than in backed specimens for a given impact energy. Unbacked specimens showed significant damage development at all three impact energy levels. In contrast, specimens that were backed with inert propellant exhibited an impact energy threshold for damage development. None of the backed specimens showed damage development when subjected to the low energy impact. Of the three specimens which were subjected to the intermediate energy impact and then x-rayed, one specimen showed no damage development, one specimen showed very slight damage development, and one specimen showed significant damage development. All of the unbacked specimens developed damage patterns similar to that seen in Fig. 2a when subjected to the high energy impact.

What is most intriguing about the experimental results obtained in the present study is that some specimens that exhibited significant damage after impact showed little reduction in tensile residual strength. Radiographic inspection of unbacked specimens subjected to low and intermediate energy impacts, and backed specimens subjected to high energy impacts, indicated that significant damage was produced by the impact event. Although this damage was present, there was virtually no loss of tensile strength. What distinguishes the unbacked, high impact energy case, which did show a loss of tensile strength, from these other cases, is the presence of significant 0° fiber fracture at the impact site. In these specimens, a microscopic examination of the radiographs reveals lines of fiber fracture in the 0° layers, typically within the circular region of contact between the impacting tup and the specimen, which is at the center of the region of concentrated damage in the radiographs. Since the 0° fibers are the primary load carriers, it is not surprising that the tensile strength would decrease if a sufficient number of these fibers were fractured during impact. The ply cracks and delaminations which comprise most of the damage seen in the radiographs have little effect on tensile strength. In fact, some of this matrix damage develops during the failure process of initially undamaged material. It is important to note that stability issues make this matrix damage much more significant for residual compression response after impact.

As expected, composite specimens which were backed with inert propellant developed less damage during impact than specimens which were unbacked. Further, backed specimens showed a distinct impact energy threshold for damage development. Finally, as far as residual tensile response is concerned, the composite was found to be quite tolerant of matrix damage. Specimens with extensive ply cracking and delamination but little or no fiber fracture exhibited little or no reduction in tensile strength, while specimens with more extensive fiber fracture showed more pronounced reductions in tensile strength.

REFERENCES

1. Madsen, C.B., Morgan, M.E., and Nusimer, R.J., "Scaling Impact Response and Damage in Composites. Damage Assessment for Composites - Phase I Final Report," AL-TR-90-037, Hercules Aerospace Co. for Astronautics Laboratory, AFSC, Edwards AFB, CA, August 1990.
2. Morgan, M.E., Madsen, C.B., and Watson, J.O., "Damage Screening Methodology for Design of Composite Rocket Motor Cases," JANNAF Propulsion Meeting, Indianapolis, Feb. 1992.
3. Dombrowski, D.C. and Knight, G.K., "Residual Strength of Carbon/Epoxy Pressure Vessels Subjected to Low Velocity Impacts," Morton Thiokol, Inc./Strategic Operations, Brigham City, Utah.
4. Jamison, R.D., "Advanced Fatigue Damage Development in Graphite Epoxy Laminates," Ph.D. dissertation, Virginia Polytechnic Institute and State University, Aug. 1982.

N93-13300

1992

NASA/ASEE SUMMER FACULTY FELLOWSHIP PROGRAM

Numerical Methods for the Analysis of Sampled-Data Systems and for the Computation of System Zeros

Prepared by:
Academic Rank:
Institution

A. Scottedward Hodel, Ph. D.
Assistant Professor
Department of Electrical Engineering
Auburn University

NASA/MSFC:

Office:
Division:
Branch:
MSFC Colleague:
Contract No:

Structures and Dynamics Laboratory
Control System Division
Mechanical Systems Control Branch
D. P. Valley
NGT-01-008-021
The University of Alabama at Huntsville

1 Introduction

MARSYAS is a computer-aided control system design package for the simulation and analysis of dynamic systems. In the summer of 1991 MARSYAS was updated to allow for the analysis of sampled-data systems in terms of frequency response, stability, etc. This update was continued during the summer of 1992 in order to extend further MARSYAS commands to the study of sampled-data systems. Further work was done to examine the computation of OPENAT transfer functions, root-locii and w -plane frequency response plots.

2 Sampled-data systems with feed-forward coefficients

Consider a sampled data system whose state-space equations are

$$\dot{x}_c(t) = A_c x_c(t) + B_{cd} y_d(kT) + B_c u(t) \quad (2.1)$$

$$y(t) = C_c x_c(t) + D_{cd} y_d(kT) + D_c u(t) \quad (2.2)$$

$$u_d(t) = C_{dc} x_c(t) + D_{dd} y_d(kT) + D_{dc} u(t) \quad (2.3)$$

with corresponding discrete time subsystem

$$x_d(kT + T) = A_d x_d(kT) + B_d u_d(kT) \quad (2.4)$$

$$y_d(kT) = C_d x_d(kT) + D_d u_d(kT). \quad (2.5)$$

(Purely discrete time inputs $r_d(kT)$ to the discrete time system may be incorporated into the above equations by augmenting the input vector $u(t)$ and the feed-forward matrix D_{dc} .) The feed-forward coefficient D_d causes the states $x_c(t)$ to depend not only on their continuous values through the coefficient matrix A_c , but also on their sampled values through the coefficient matrix $B_{cd} D_d C_{dc}$. As of MARSYAS version 6.0.5, this dependence is dealt with by creating a matrix $ZX = B_{cd} D_d C_{dc}$ in the linearized continuous time dynamics.

Unfortunately, MARSYAS version 6.0.5 does not correctly treat the case where there are feed-forward coefficients in both the continuous time and discrete time blocks (i.e. $D_{dd} \neq 0$ and $D_d \neq 0$). In this case, MARSYAS infers an algebraic loop where there is none. For example, consider the sampled-data system with continuous time block

$$y(t) = y_d(kT) \quad u_d(t) = u(t)/2 - y_d(kT)$$

and discrete time block

$$y_d(kT) = k_d u_d(kT).$$

The code has no (explicit) states, yet because of the direct feed-forward gains (i.e., the "D" matrices) in the discrete and continuous time blocks of the linear system, a "hidden state" associated with the A/D converters in the system manifests itself at sampling times. The MARSYAS-6.0.5-generated system equations are

$$W [1] = (2.500000E-01) * U [1]$$

while the simulated output values display "spikes" at sampling times and the values between sampling times incorrect. There is a specific order in which the simulation updates must occur at each "scheduled" run of the discrete time systems: (1) Evaluate the continuous time system states and algebraic outputs. (2) Update the discrete time system states and algebraic outputs. (3) the algebraic outputs of the continuous time system to reflect the discrete time system changes. Once these three steps are completed, the simulation may proceed with the next integration step. Similarly, the analysis of discrete time systems must be modified as follows.

Lemma 2.6 *Let a sampled data system be defined by the equations (2.1)-(2.5) with sampling time T given. Then*

$$u_d(kT) = C_{dc} x_c(kT) + D_{dc} u(kT) + D_{dd} y_d(kT - T);$$

that is, the discrete-time output y_d becomes a system state when $D_{dd} \neq 0$.

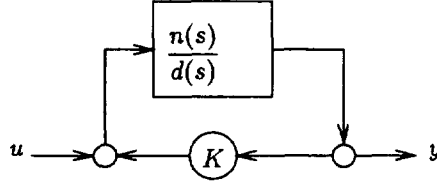


Figure 1: OPENAT linearized system

Based on the above operation, the vector $y_d(t)$ can be used as a vector state that replaces the “ZX” input used in MARSYAS version 6.0.5 as follows. Let $x_{dy}(kT) = y_d(kT - T)$. Then the overall system simplifies to

$$\begin{aligned}
 \dot{x}_c(t) &= A_c x_c(t) + B_{cd} y_d(kT) + B_c u(t) \\
 y(t) &= C_c x_c(t) + D_{cd} y_d(kT) + D_c u(t) \\
 u_d(t) &= C_{dc} x_c(t) + D_{dc} u(t) \\
 x_d(kT + T) &= A_d x_d(kT) + B_d u_d(kT) + B_d D_{dd} x_{dy}(kT) \\
 x_{dy}(kT + T) &= C_{dc} x_d(kT) + D_d D_{dd} x_{dy}(kT) + D_d u_d(kT) \\
 y_d(kT) &= C_d x_d(kT) + D_d D_{dd} x_{dy}(kT) + D_d u_d(kT).
 \end{aligned}$$

3 OPENAT analysis: options and an example

The **OPENAT** command allows MARSYAS users to examine system robustness with respect to an individual parameter by breaking a specified signal path in a closed-loop system model and examining the poles/zeros of the newly created open loop system.

The current MARSYAS implementation (and the original MARSYAS implementation) treat the **OPENAT** command as a special case of the **INOUT** command. The manual for the original MARSYAS implementation describes an alternate technique for computing the **OPENAT** transfer function; this alternate technique forms the basis of the root locus calculation, and is thus of interest in both of these calculations. The two techniques are described below. A simple numerical example is given that indicates that algebraic loops (i.e., a non-zero D matrix in a linearized **OPENAT** system) can render the alternate algorithm inaccurate; it is advised that the **INOUT** approach be used in both **OPENAT** and root locus calculations.

The **OPENAT** command can be summarized as follows. Given a closed loop continuous time system $\dot{x} = f(x, w)$ with algebraic constraint $0 = g(x, w)$, **OPENAT** k selects a gain value in the system and linearizes about an operating point in order to obtain the SISO system shown in Figure 1. The **OPENAT** command identifies the poles and zeros of the transfer function $n(s)/d(s)$. The **INOUT** algorithm computes the poles and zeros by computing the matrices (A, B, C, D) that characterized a state-space realization of $n(s)/d(s)$ and then computing the (finite) generalized eigenvalues of the matrix pencil $\left(\begin{bmatrix} -A & -B \\ C & D \end{bmatrix} - \lambda \begin{bmatrix} I & 0 \\ 0 & 0 \end{bmatrix} \right)$.

The alternate *closed-loop matrix method* is as follows For a fixed linearization, let $A(k)$ be the system Jacobian matrix evaluated with $K = k$; i.e. $A(k) = (A + k/(1 - Dk)BC)$. Then $\det(sI - A(k)) = a(k)(d(s) - kn(s))$ where $a(k)^{-1}$ is the leading coefficient of $(d(s) - kn(s))$. Clearly, the poles of the **OPENAT** system are the eigenvalues of $A(0)$, since $\det(sI - A(0)) = a(0)(d(s) - 0 \cdot n(s)) = d(s)$.

In order to obtain the zeros of the system, it is required to compute the algebraic gain D and the closed loop matrix $A(1) = (A(0) + 1/(1 - D)BC)$. Let \hat{B}, \hat{C} be a column and row vector, respectively, such that $\hat{B}\hat{C} = (D - 1)(A(1) - A(0))$; then the zeros of the **OPENAT** transfer function may be obtained by computing

INOUT method			Closed-loop matrix method		
ϵ	$ \lambda - \hat{\lambda} $	$ \hat{D} - D $	ϵ	$ \lambda - \hat{\lambda} $	$ \hat{D}_2 - \hat{D}_1 $
1	$\approx 1.0\text{e-}13$	$1.9984\text{e-}14$	1	$1.0\text{e-}13$	$2*1.9984\text{e-}14$
0.1000	$\approx 1.0\text{e-}14$	$1.1102\text{e-}14$	0.1000	$\approx 1.0\text{e-}12$	$2*1.1102\text{e-}14$
0.0100	$\approx 1.0\text{e-}12$	$9.9920\text{e-}15$	0.0100	$\approx 1.0\text{e-}10$	$2*9.9920\text{e-}15$
$1.0000\text{e-}03$	$\approx 1.0\text{e-}12$	$9.9920\text{e-}15$	$1.0000\text{e-}03$	$\approx 1.0\text{e-}09$	$2*9.9920\text{e-}15$
$1.0000\text{e-}04$	$\approx 1.0\text{e-}11$	$9.9920\text{e-}15$	$1.0000\text{e-}04$	$\approx 1.0\text{e-}07$	$2*9.9920\text{e-}15$
$1.0000\text{e-}05$	$\approx 1.0\text{e-}11$	$9.9920\text{e-}15$	$1.0000\text{e-}05$	$\approx 1.0\text{e-}06$	$2*9.9920\text{e-}15$
$1.0000\text{e-}06$	$\approx 1.0\text{e-}10$	$9.9920\text{e-}15$	$1.0000\text{e-}06$	$\approx 1.0\text{e-}04$	$2*9.9920\text{e-}15$
$1.0000\text{e-}07$	$\approx 1.0\text{e-}09$	$9.9920\text{e-}15$	$1.0000\text{e-}07$	$\approx 1.0\text{e-}03$	$2*9.9920\text{e-}15$

Figure 2: Results of tests of openat algorithms

the finite generalized eigenvalues of the matrix pencil $\left(\begin{bmatrix} -A & -\hat{B} \\ \hat{C} & D \end{bmatrix} - \lambda \begin{bmatrix} I & 0 \\ 0 & 0 \end{bmatrix} \right)$. This is the *closed-loop matrix method* discussed in the manual for the original MARSYAS implementation.

The discussion of the closed-loop matrix method in the original MARSYAS manual did not correctly treat the case of $D \neq 0$. If $D \neq 0$, in particular, if $D \approx 1$, then the **INOUT** method is clearly superior to the closed-loop matrix method, as shown in the following example.

Example 3.1 Let the **OPENAT** linearized system have coefficient matrices $A = \begin{bmatrix} -1 & 1 \\ -1 & -1 \end{bmatrix}$, $B = \begin{bmatrix} 1 \\ 2 \end{bmatrix}$, $C = \begin{bmatrix} 2 & 1 \end{bmatrix}$, and $D = 1 + \epsilon$. The exact system zeros can be found to be

$$\lambda = \left(1 + \frac{2}{1 + \epsilon} \right) \pm \sqrt{\left(1 + \frac{2}{1 + \epsilon} \right)^2 - \left(2 + \frac{7}{1 + \epsilon} \right)}.$$

Observe that as $\epsilon \rightarrow 0$, the zeros coincide at $\lambda = 3$.

A computed linearization $(\hat{A}, \hat{B}, \hat{C}, \hat{D}) = (A, B, C, D)$ will typically have roundoff noise in each matrix in proportion to the matrix norm; i.e., $\|\hat{A} - A\| \leq \mu \|A\|$ where μ is a function of machine precision and the algorithm condition. The example was selected so that matrix entries were “balanced;” that is, the matrix entries were of approximately the same magnitude so that round-off effects on problem condition would be reduced. For the purposes of a numerical experiment, small error ($\approx 10^{-14}$) was deliberately introduced into the problem in order to examine algorithm sensitivity. Since the computed value of \mathbf{Ab} is near to the correct computed value, this method yields good results.

The closed-loop matrix method involves computing $A(0)$, $A(1)$, and the open-loop D -matrix. It was *not* assumed that the gain D involved in computing $A(1) = A - 1/(D - 1)BC$ is exactly the same as that gained from an **INOUT** linearization; i.e., **INOUT** computes $(\hat{A}, \hat{B}, \hat{C}, \hat{D}_1) = (A, B, C, \hat{D})$, while $A(1)$ was computed as $A(1) = \hat{A} + 1/(\hat{D}_2 - 1)\hat{B}\hat{C}$. The respective results are shown in Figure 2. It is clear that the **INOUT** method yields superior accuracy; it is important to recognize that the difference in these two methods is a result of the difference between $1/(\hat{D}_1 - 1)$ and $1/(\hat{D}_2 - 1)$; since the estimated values of \hat{B} and \hat{C} in the closed loop matrix method will be scaled by the ratio $(\hat{D}_1 - 1)/(\hat{D}_2 - 1)$ from their “correct” values, it is to be expected that the closed-loop matrix method will yield poor results when $D \approx 1$.

□

On the basis of the above example and analysis, it is recommended that both **OPENAT** and root locus calculations be performed on the basis of the matrices (A, B, C, D) obtained from an **INOUT** linearization of the appropriate system. FORTRAN code for the **mvzero** routine and the associated numerical balancing procedure [2] have been delivered to John Tiller, BCSS, this summer for use in MARSYAS.

The calculation of OPENAT transfer functions and root locus data become much more complicated in a sampled-data system. If the OPENAT operation is performed on a gain k in the discrete time portion of the system, then the OPENAT function may be executed in the normal fashion on the equivalent discrete time system. However, if the OPENAT is performed on a gain k in the continuous time part of the system, then the OPENAT function ceases to have a clear meaning. If an artificial *continuous time* input u and output y are placed around the gain, then there is no rational transfer function from u to y because of the time-varying dependence on the discrete time subsystem. Instead, *discrete time* input-output pair is inserted about the *continuous time* gain element K .

This system is not amenable to an OPENAT style analysis, since the transfer function varies in a transcendental (non-algebraic) fashion with the gain value K ; closed form perturbation analysis of the equivalent discrete time system is intractable since the matrices A and BC do not commute in general. ($e^{ABC} = e^A e^{BC} = e^{BC} e^A \iff A(BC) = (BC)A$.) Hence a single "open-loop" OPENAT transfer function calculated with $K = 0$ is not meaningful to the user. However, a "transcendental root-locus" from u to y may be computed by computing the poles and zeros of an equivalent discrete-time plant for various values of k .

Closed-form analysis of transcendental root-locii is hindered by the property that $e^{(A_c + KB_c D_c)t}$ cannot be computed from $e^{A_c t}$ and $e^{(B_c C_c)t}$ except when A_c commutes with $B_c C_c$; this is clearly not the case in practice. It may be possible to gain some norm-bounds on the closed-loop eigenvalues of the overall discrete-time system in terms of the feedback gain K , but this is an open question.

4 W-plane analysis

MARSYAS currently provides z -plane frequency response plots of discrete-time systems. w -plane analysis is often used in practice to allow designers to employ continuous time design techniques to discrete-time systems; see, e.g., [1]. $G(z) \rightarrow G(w)$ by $w = \frac{2}{T} \left(\frac{z-1}{z+1} \right)$. s -plane, z -plane, and w -plane frequency response plots are related by $z = e^{sT}$ and $w = \frac{2}{T} \frac{e^{sT} - 1}{e^{sT} + 1} = \frac{2}{T} \tanh\left(\frac{sT}{2}\right)$. So as $s = j\omega$ follows the imaginary axis, $z = e^{j\omega T}$ follows the unit circle (periodic with period $2\pi/T$), and

$$w = \frac{2}{T} \tanh\left(\frac{j\omega T}{2}\right) = \frac{2j}{T} \tan\left(\frac{\omega T}{2}\right)$$

follows the entire imaginary axis each time $z = e^{j\omega T}$ rotates about the unit circle. The inverse bilinear transform from w to z is $z = \frac{1 + wT/2}{1 - wT/2}$; hence the Nyquist plots in the z and w plane will be identical. Magnitude and phase information in the z and w -planes will be the same except for a "warping" of the w -plane frequency variable $\nu \triangleq \tan(\omega T/2)$.

References

- [1] G. F. Franklin, J. D. Powell, and M. L. Workman. *Digital Control of Dynamic Systems*. Addison-Wesley, 2nd edition, 1990.
- [2] A. Scottedward Hodel and John Tiller. Computation of system zeros with balancing. In *Proceedings of the 29th Allerton Conference on Comm., Contr., and Computing*, Monticello, Il., Oct 2-4 1991.

N93-17301

1992

NASA/ASEE SUMMER FACULTY FELLOWSHIP PROGRAM

**MARSHALL SPACE FLIGHT CENTER
THE UNIVERSITY OF ALABAMA**

**SOME EFFECTS OF TIME USAGE PATTERNS
ON THE PRODUCTIVITY OF ENGINEERS**

Prepared By: Conrad N. Jackson, Ph.D.
Academic Rank: Associate Professor of Management
Institution and Department: The University of Alabama in Huntsville
Marketing Department of Management and
Marketing

NASA/MSFC:
Directorate: Science and Engineering
MSFC Colleague: Leonard W. Howell, Ph.D.

INTRODUCTION The performance of the 1500+ engineers at MSFC is critical to the Center's mission. Worker's performance, however, is a variable affected by ability, motivation, role understanding, and other factors. Managing subordinates' performance is a great challenges to managers. Special challenges confront the managers of engineers because engineers often work with general goals, long deadlines, and considerable autonomy (1).

Budget challenges should make all managers concerned about their workgroup's efficiency as well as its effectiveness(2). One measure of efficiency is productivity -- the amount of useful output which is obtained per unit input. Productivity is easy to measure when the output is easy to count, the time required to produce each unit is relatively short, and the standards for acceptable quality are apparent and routine. For example, a manufacturing plant might produce 200 cars per day, or a license bureau might process 20 applications per hour. Productivity of the typical S&E branch at MSFC is not as easy to measure. However, some examples of productivity improvements include completing more critical tests per month, finishing analyses more quickly, or serving the branch's customers well with fewer engineers.

The productivity of a team or branch is a function of the productivity of each of its members. While many managers have personal theories about how to run their work group, surprisingly little systematic scientific knowledge exists about the effects of various factors on engineers' productivity. This study is intended to help lay the foundation for such a program of research.

METHOD The primary goals of the present study have been to familiarize the principal investigator (PI) with the work environment and the nature of the tasks faced by MSFC engineers, to gain insights into how productivity might be measured for engineering tasks, and to formulate models and hypotheses which suggest relationships among these issues. The PI thus spent fifty days at MSFC observing numerous engineers from three S&E labs and two Chief Engineers' offices as they went about their daily work, and interviewing them regarding their work. These observations included attending numerous meetings and teleconferences with engineers. Several managers from various levels of the S&E organization were also interviewed. Particularly valuable insights were gained from in depth interviews of 40 MSFC engineers using a structured set of open-ended questions (summary of questions below).

Interview Questions For Engineers' Time And Work Study

1. Job title, brief job description, projects you work on
2. Education history and career path; why you became an engineer, why you joined NASA

3. Present top priority tasks and deadlines
4. Activities in a typical week; time in meetings, on phone, on computer
5. How your work tasks/projects are initiated; by whom
6. Extent to which you like your job
7. How you feel about your work performance; indicators of success in your work
8. How one might judge productivity in a job like yours
9. Things that block you from being more productive
10. How many hours you work each week, day
11. Percent of your time you typically feel to be productive
12. How you would describe yourself as a worker; self discipline, perfectionist, time manager, confidence
13. What the most productive engineers you have observed do differently from average engineers
14. What you need from NASA/your boss to be more effective
15. Advice for a new employee to be successful in your job
16. How you feel about NASA's current mission and direction

OBSERVATIONS AND DISCUSSION **Measuring Productivity** In order to manage an outcome one generally must be able to measure it(2). Most interviewees initially expressed uncertainty about how to measure productivity, but then went on to speculate usefully on possible methods or criteria for such measurement. Many expressed a belief that supervisors who stay in touch daily with what their engineers are working on can make a reasonably accurate subjective estimate of engineers' productivity. Factors which should be integrated into this judgement include the difficulty of the task (including the development stage of the required tools or methodology), comparison of progress rates among engineers doing similar types of tasks (or past experiences with people doing similar types of tasks), and comparison of progress against a mutually-agreed-upon time line (when posing a design or analysis question to an engineer, it helps to specify whether one wants a one-day answer, a one-week answer, a one-month answer, etc.)

Work output measurements for estimating productivity could include specific observations of work methods or outcomes. For example, track the number of analyses an engineer produces in a period of time, the number of papers they publish or present, the number of phone calls made or received, the number of action items completed, or even the number of action items not completed by the requested date. Or poll customers for feedback on an engineer's work, including their general satisfaction with work quality or pace, estimates of work impact on a program or at least the thinking of others, the degree to which an engineer is consulted by others for an opinion, or the general accuracy of one's models, tests, and designs. Finally, productivity might

be reflected in system-level indications such as whether one's work has held up a flight or test schedule, a new motor flew tested without problems, or a meeting was productive.

Ideally, engineers and their supervisors should collaborate to find the best method for monitoring their productivity. Where colleagues or customers are in the best position to judge an engineer's productivity, a formal or informal system could be set up to gather their feedback. While some engineers may be sufficiently defensive about their work to make them uncomfortable with such a feedback program, most appear to be justly proud of their work and of the world-renown accomplishments of the Center, and many expressed great interest in learning from any available feedback.

Being Busy Versus Being Productive One's work effort can be viewed as a vector. The length of the Effort Vector might indicate the degree to which one is busy during the work day. However, that work effort can be factored into a Productive Work component (i.e., work which is directed toward accomplishment of the specified job goal) and a perpendicular "Wasted Motion" component (e.g., work effort which is directed toward simply satisfying one's curiosity, looking busy, or fulfilling a perfunctory obligation). Thus, one engineer might be seen as putting forth less work effort than another (e.g., attending fewer meetings, writing shorter memos, taking a longer lunch break), yet might actually accomplish more than the latter with respect to job goals. Both continuous clarification of organizational and departmental goals and honest feedback to engineers by supervisors or co-workers can affect powerfully the direction of work effort toward productive ends. Many engineers feel that they need more goal clarification or feedback than their supervisors now give.

Some engineers seem to find it difficult to prioritize their work activities. For example, some are inclined to study a problem forever in search of an optimal answer, though the organization needs a sufficient answer quickly to meet a project deadline. Indeed, some engineers in the labs see "getting smart" on an issue being as important in their job as is applying their knowledge to a specific project. However, an overly compulsive or extremely cautious personality in such a person might result in a great deal of wasted motion. Others believe that learning directed toward specific project questions is most efficient in the long run. In any event, it is natural for workers to spend as much time as possible on the activities they find intrinsically interesting. Thus, to optimize productivity, engineers must be placed in jobs which require the work they intrinsically enjoy.

Career Issues Five career types were observed in interviews. 1) The Center has a lot of "New Kids" who are in the early phases of their NASA careers. Most do not yet know for what job they are best suited, and their work habits and

standards are still extremely malleable. They need a good view of the types of work available at MSFC, and close supervision to ensure task success until their competence and confidence grows. Young engineers typically aspire to high levels of technical competence. Highly experienced engineers from project offices who would spend a year or two back in the labs before retirement might make excellent mentors and role models for New Kids. 2) Some engineers mature into "Techo-Wizards", carving out an area of great technical expertise from which they greatly influence design, analysis, or test methodology decisions. They work with maximum autonomy. 3) A few engineers find that they enjoy questioning and helping define departmental/ organizational priorities and strategic direction even more than developing greater technical expertise. Those with good interpersonal skills may become "Movers and Shakers", seeking management track careers. 4) Many engineers, perhaps due to differing interests, have not developed the technical proficiency of Techno-Wizards nor the leadership qualities of Movers and Shakers, but instead specialize in attending to details of information and data management, tasks often critical to project success. These "Worker Bees" seem satisfied with a modest level of technical challenge in their jobs. 5) However, a few engineers never found appealing career tracks, or somehow run out of steam. These "Lost Souls" often eventually were relegated to tasks which are least critical to the organizational mission. They seem to have low expectations of the prospects for whatever years remain in their career. Perhaps a "PIP Program" for veteran engineers could help place these Lost Souls into more productive work.

Future Research Clearly research on engineers' productivity is in a preliminary stage. A questionnaire survey of 300 randomly-selected MSFC engineers, sponsored by Dr. George McDonough, Head of S&E, is now gathering information from a wider sample about many issues related to engineers' effectiveness and use of time. It builds on previous research by the PI(3) plus insights from the present study.

ACKNOWLEDGMENTS Special thanks for support and cooperation go to Dr. George McDonough, Lab Directors Bill Chubb, Jim Blair and John McCartey, Chief Engineers Dennis Gosdin and Len Worlund, interviewees, and many managers and helpful others too numerous to list here.

REFERENCES

- 1 Pelz, D.C. and Andrews, F.M., Scientists in Organizations, New York: Wiley, 1966.
- 2 Administrator Daniel Goldin's Memorandum For All NASA and JPL Employees dated July 9, 1992.
- 3 Jackson, C., "Some effects of time management styles on the personal productivity of knowledge workers", CAS Research Report Number 90-11-02, Center for Management and Economic Research, University of Alabama in Huntsville, 1990.

1992

NASA/ASEE SUMMER FACULTY FELLOWSHIP PROGRAM

MARSHALL SPACE FLIGHT CENTER
THE UNIVERSITY OF ALABAMA

SPACE ENVIRONMENTAL EFFECTS ON POLYMERS AND COMPOSITES

Prepared By:	Bor Z. Jang, Ph.D.
Academic Rank:	Associate Professor
Institution and Department and Engineering	Auburn University Materials Engineering Program Department of Mechanical
NASA/MSFC: Office: Division: Branch:	Materials and Processes Lab Engineering Physics Physical Science
MSFC Colleague:	Roger Linton

INTRODUCTION

The response of polymers and polymer-based composites to the space environment is being investigated. A wide range of materials are covered in this study, including elastomer seals for Space Station Freedom, polymer films for thermal control, and composites for space structural elements. Space environmental agents of concern include atomic oxygen, thermal cycling, space debris impacts, UV, charged particles and other forms of high-energy radiation. This ambitious project is potentially a multi-year research effort and the success of such a project could be expected to have a profound impact on the design of future space-based structures. The research goal of this first Summer is to identify the priority areas of research and to carry out the initial phase task so that a collaborative research can proceed smoothly and fruitfully in the near future.

PROJECT 1: SERVICE LIFE PREDICTIONS FOR SEAL ELASTOMERS

Accomplishments:

1. The most commonly used technique for studying the long-term performance of an elastomer seal--the compression set test--has been critically reviewed. A model has been developed to predict the compression set of an elastomer as a function of time and to provide insight into the molecular origins of compression set.
2. A simple standard linear solid model was utilized to derive constitutive equations that relate the compression set data to the corresponding stress relaxation and creep data for a given elastomer.
3. Effective techniques for studying elastomer degradation kinetics and mechanisms have been identified and the corresponding theoretical foundation has been established.
4. It is recommended that an extensive stress relaxation (or creep) test program be planned and carried out to cover a wide range of temperatures and radiation dose rates so that a master curve may be constructed to predict the service lifetime of an elastomer for space applications.
5. It is further recommended that an in-depth study be performed to understand the ageing mechanisms, at the molecular level, of select elastomers (e.g., S383 silicone and V747 fluorocompound rubber) over a wide range of temperatures. Proper thermal shift factors cannot be evaluated and the master curves cannot be constructed without the knowledge of degradation mechanisms for each elastomer. It is of particular significance to differentiate between physical and chemical stress relaxation, so that correct equations can be used to estimate the thermal shift factors.

For simulations of short-term deterioration of polymers, real-time measurements can be used by duplicating the expected real time space environment. For polymers exposed for many years to the space environment, the generation of real-time data is practically impossible. Predictions must be based on accelerated aging experiments completed in a shorter time-frame in a ground-based laboratory. Such lab work invariably involves increasing the environmental stress levels above those appropriate to the real exposures. This would likely mean higher than ambient UV dose rates, atomic oxygen fluence, higher temperatures, and higher mechanical stresses. Thus, developing predictive methods based on ground experiments necessitates understanding and modeling of space environment dose-rate effects.

The dose rate effects of polymers exposed to high energy radiation, such as in a nuclear environment, have been studied extensively [1-7]. A common assumption in these studies is that the total dose alone determines the damage under inert atmosphere situations and that long-term predictions for low dose-rate conditions can be made by using an equal dose, equal damage basis. It is now well known that, in the presence of air (oxygen), dose rate effects are frequently observed and can be very significant [8,9]. This observation could be extended to predict that, in the presence of atomic oxygen which is even more reactive than molecular oxygen, dose rate effects may be significant in the space environment. This has yet to be verified experimentally.

Temperature is an important factor to consider when discussing the space environmental effects on polymers. Stress relaxation of elastomers can occur as a result of chemical reactions inducing the breakdown of the network structure. Several network degradation theories have been developed and chemical stress relaxation studies have been carried out on a wide range of elastomers in order to study their thermal degradation mechanisms. During this Summer, these theories were critically reviewed, along with the chemical stress relaxation technique and other methods for investigating cross-linking and chain scission of polymers.

PROJECT 2: THERMAL CYCLING OF POLYMER COMPOSITES

Accomplishments:

1. Thermal cycle induced micro-cracking phenomena were observed on carbon fiber reinforced polymer matrix composites. One or two minute intraply cracks were observed on thermoplastic matrix composites after a single thermal cycle between -45°C and $+85^{\circ}$. Microcracks appear to initiate at the fiber-matrix interface, preferentially in fiber-rich (or resin-deficient) zones. Microcracking appears more severe in

PPS than in PEEK composites. Microcracking was not observed in epoxy composites for the first twenty cycles. Judging from the fact that thermoplastic composites tend to have weak fiber-matrix interfacial bonding, these observations appear to suggest that interfacial bond plays a critical role in initiating microcracks in carbon fiber reinforced polymer composites. Intraply cracks are known to be the precursors to the delamination cracks, the most serious life-limiting failure mode in laminated composites.

2. Thermal cycle cracks obviously are caused by the hygrothermal stresses present in a laminate. The residual thermal stresses in a fibrous composite may be analyzed at different levels of complexity. First, the differential thermal stresses established between a single fiber and the matrix may be estimated either analytically or numerically. Second, the residual stress fields developed within a group of regularly arrayed fibers may also be determined either theoretically or experimentally. Third, the thermal stresses that occur between laminae with different effective thermal expansion coefficients (e.g., due to different fiber orientations) may also be calculated using, for example, the classical lamination theory. In each level of study certain assumptions have to be made to render the problem more tractable.

As a first approach (levels 1 and 2), a "thick cylinder model" was developed to simulate the thermo-mechanical behavior near a fiber in a group of fibers with a given fiber volume fraction. In this model, the stress and the strain fields in a thick cylinder under uniform pressure were derived based on the classical elasticity theory. Using such a thick cylinder model, the residual stresses established in a model single fiber-matrix system representing various polymer composites were calculated.

In practically all cases the matrix has a greater CTE than the fiber, which subjects the fiber to compressive stress. For most practical volume fractions of fibers, the matrix will generally be subjected to a radial compression at the fiber-matrix interface and a tangential tensile stress. Even in the absence of a good chemical bond, this radial compression against the interface provides friction forces to assist in the load transfer process between the fiber and the matrix. The magnitudes of such residual thermal stresses at the microscopic level have been calculated for the composite systems being considered for space applications.

A change in temperature (ΔT) or moisture content of a composite structure causes a variation in its dimensions proportional to the change in temperature (ΔT) or moisture content (ΔC) and its initial dimensions. This leads to the

development of a thermal strain (ϵ^T) or hygroscopic strain (ϵ^H). However, thermal deformation of a lamina is constrained by its neighboring laminae, leading to the development of residual stresses. The magnitudes of these macroscopic residual stresses in each layer of a composite for several composite systems have been estimated using the classical lamination theory. These data, in combination with the interface thermal stress data mentioned earlier, may be used to explain the thermal cycle induced micro-cracking phenomena in composites.

PROJECT 3: RESIDUAL STRENGTH PREDICTION OF ATOMIC OXYGEN ERODED MATERIALS

A statistical fracture mechanics approach is being developed for predicting the residual strength of engineering polymers and composites as a function of surface morphology, which varies with atomic oxygen exposure conditions. This project is just now getting started. Literature review on the subject *Surface Cracks* has been conducted. Theoretical equations are being derived while the mechanical test samples are being prepared.

REFERENCES

1. O. Sisman and C.D. Bopp, Physical Properties of Irradiated Plastics, USAEC Report ORNL-928, Oak Ridge National Laboratory, 1951.
2. C.D. Bopp and O. Sisman, Radiation Stability of Plastics and Elastomers, USAEC Report ORNL-1373, Oak Ridge National Laboratory, 1953.
3. C.G. Collins and V.P. Calkins, Radiation Damage to Elastomers, Plastics and Organic Liquids, Report APEX-261, General Electric Co., Aircraft Nuclear Propulsion Dept., NTIS, 1956.
4. R.W. King, N.J. Broadway and S. Palinchak, The Effect of Nuclear Radiation on Elastomeric and Plastic Components and Materials, REIC Report No. 21, 1961.
5. W.W. Parkinson and O. Sisman, Nucl. Eng. and Design, 1971, 17, 247.
6. W.E. Skeins, Radiat. Phys. Chem., 1980, 15, 47.
7. P. Beynell, P. Maier and H. Schonbacher, Compilation of Radiation Damage Test Data-Part III: Materials Used Around High-Energy Accelerators, CERN 82-10, Geneva, 1982.
8. K.T. Gillen, R.L. Clough and N.J. Dhooge, Polymer, 1986, 27, 225.
9. R.L. Clough and K.T. Gillen, in Radiation Effects at the SSC, M. G. D. Gilchriese (ED.), SSC-SR-1035, Lawrence Berkeley Lab., June 1988.

1992

NASA/ASEE SUMMER FACULTY FELLOWSHIP PROGRAM

MARSHALL SPACE FLIGHT CENTER
THE UNIVERSITY OF ALABAMA

GROUND TESTING OF BIOCONVECTIVE VARIABLES SUCH AS MORPHOLOGICAL
CHARACTERIZATIONS AND MECHANISMS WHICH REGULATE MACROSCOPIC
PATTERNS.

Prepared By: Adriel D. Johnson, Ph.D.
Academic Rank: Assistant Professor
Institution and Department: University of Alabama in Huntsville
Department of Biological Sciences
NASA/MSFC:
Office: Space Sciences Laboratory
Division: Microgravity Sciences & Applications
Branch: Biophysics
MSFC Colleagues: Helen C. Matsos
David A. Noever, Ph.D.

Conditions simulating low- and high-gravity, reveal changes in macroscopic pattern formation in selected microorganisms, but whether these structures are gravity dependent is not clear. Two theories have been identified in the fluid dynamics community which support macroscopic pattern formation. The first one is gravity dependent (fluid density models) where small concentrated regions of organisms sink unstably, and the second is gravity independent (wave reinforcement theory) where organisms align their movements in concert, such that either their swimming strokes beat in phase or their vortices entrain neighbors to follow parallel paths (3). Movement or locomotion of microorganisms such as paramecium, algae, protozoa, and spermatozoa, form macroscopic patterns analogous to thermally driven convection cells. Gravitational test have shown bioconvective pattern for both the flagellated algae, *Polytomella parva* and the ciliated non-gyrotaxic protozoa, *Tetrahymena pyriformis* to show similar polygonal morphology, changes in the inter-nodal distances, and decreases in pattern wavenumber and fineness (3). In addition, macroscopic patterns of caprine spermatozoa continue during conditons of variable gravity (1). Studies have shown that macroscopic pattern formation is consistent with the fluid density models for protozoa and algae and wave reinforcement hypothesis for caprine spermatozoa (1,3).

Nearly every eukaryotic cell contains microtubules including algae, protozoa, and spermatozoa. Microtubules are important cellular components essential for movement of the cytoskeleton, spindle fibers, cilia, and flagella. In cilia and flagella, microtubules are in a characteristic array of nine outer doublets of microtubules and two central single microtubules. All microtubules have a common ultrastructure composed of tubulin, a dimeric globular protein capable of generating various dissipative structures when combined with guanosine triphosphate in solution. These structures include traveling waves of microtubule assembly and disassembly and the formation of polygonal networks, suggesting dynamic spatial pattern formation of microtubule components in the absence of cellular organizing centers (2). Thus the microtubule assembly and disassembly process in vitro could serve as a ground base model by examining regulatory mechanisms for comparing pattern formation by selected organisms under microgravity conditions.

As a part of Marshall Space Flight Centers' Summer Faculty Fellowship Program within the Biophysics Branch, the objectives of the summer faculty fellow were to provide a procedure to isolate bovine tubulin, to assist with determining whether the microtubule assembly and disassembly system could be quantitated using spectrophotometric techniques for ground based studies, and to assist with the development of a technique to examine the microtubule assembly and disassembly system for future studies under the simulated microgravity conditions of the KC-135 experimental aircraft.

The brain tubulin preparation procedure was as follows: bovine brains were obtained from a local slaughter house, put on ice, meninges removed, and the cortex minced. Brains were washed with cold calcium free phosphate buffered saline solution and suspended in cold Hanks physiological buffer. The tissue was homogenized with a polytron and centrifuged at 14,000 rpm for 20 minutes at 5°C. The supernatant was collected and ultracentrifuged at 40,000 rpm for 1 hour at 5°C. Guanosine triphosphate (GTP) was added, incubated at 37°C for 45 minutes and centrifuged at 14,000 rpm for 40 minutes at 28°C. The pellet was resuspended with cold Hanks buffer, GTP added, homogenized with a Teflon-glass homogenizer, and centrifuged at 18,000 rpm for 30 minutes at 5°C. The mixture was allowed to polymerize at 37°C for 15-20 minutes, and the pellet can then be used for phosphocellulose purification of the tubulin.

Microtubules are the only biopolymers which can simultaneously polymerize and depolymerize (2). The tubulin preparation procedure described above provides a source of tubulin which can facilitate the study of the assembly and disassembly process of the microtubule system. Further understanding of the microtubule system would provide a data base for both ground base and microgravity studies on this regulatory mechanism associated to pattern formations in organisms.

References

1. Johnson, J.U. Biological patterns: Novel indicators for pharmacological assays. NASA Contractor Report - 184253, Research Reports - 1991 NASA/ASEE Summer Faculty Fellowship Program. R-R2. October 1991.
2. Mandelkow, E., Mandelkow, E.-M., Hotani, H., Hess, B. and Muller, S.C. Spatial patterns from oscillating microtubules. Science. 246:1291-1293. December 1989.
3. Noever, D.A., Matsos, H.C., Johnson, J.U., and Cronise, R.J. A gravitational test of bioconvective patterns: Wave reinforcement versus fluid density models (Submitted and personal communication) 1992.

1992

NASA/ASEE SUMMER FACULTY FELLOWSHIP PROGRAM
MARSHALL SPACE FLIGHT CENTER
THE UNIVERSITY OF ALABAMA

ENERGETICS AND STRUCTURAL PROPERTIES OF TWIST GRAIN BOUNDARIES
IN Cu

Prepared By: Majid Karimi, Ph.D.
Academic Rank: Assistant Professor
Institution: Indiana University of
Pennsylvania
Department: Department of Physics

NASA/MSFC

Office: EH22
division: Metallic Materials
Branch: Metallurgical & Failure
Analysis
MSFC Colleague: Ilmars Dalins, Ph.D.

Introduction

Structural and energetics properties of atoms near a grain boundary are of great importance from theoretical and experimental standpoints. From various experimental work it is concluded that diffusion at low temperatures at polycrystalline materials take place near grain boundary. Experimental and theoretical results also indicate changes of up to 70% in physical properties near a grain boundary. The Embedded Atom Method (EAM) (1) calculations on structural properties of Au twist grain boundaries (2) are in quite good agreement with their experimental counterparts. The EAM is believed to predict reliable values for the single vacancy formation energy as well as migration energy. However, it is not clear whether the EAM functions which are fitted to the bulk properties of a perfect crystalline solid can produce reliable results on grain boundaries.

One of the objectives of this work is to construct the EAM functions for Cu and use them in conjunction with the molecular static simulation to study structures and energetics of atoms near twist grain boundaries $\Sigma 5$ and $\Sigma 13$ in Cu. This provide test of the EAM functions near a grain boundary. In particular, we determine structure, single vacancy formation energy, migration energy, single vacancy activation energy, and interlayer spacing as a function of distance from grain boundary. Our results are compared with the available experimental and theoretical results from grain boundaries and bulk.

Methodology

Interatomic pair potentials suffer from two major problems, zero Cauchy pressure, i.e., $C_{11}-C_{12}=0$, and equality of single vacancy formation energy E_{1v} and cohesive energy E_c . In practice, for most crystals $C_{11} \neq C_{12}$ and $E_{1v} \neq E_c$. To overcome these and other shortcomings of pair potentials the EAM potentials are developed. In the EAM, the major contribution to energy of each atom is due to the embedding energy which is supplemented by a two body potential. The embedding energy of an atom can be interpreted as the energy that is required to embed that atom in the electronic charge produced by the other atoms in the crystal. The two body potential ϕ can also be interpreted as the electrostatic interaction between cores of embedding atom and atoms of crystal. Energy of atom i in the EAM formalism can then be written as,

$$E_i = F_i(\rho_i) + 0.5 \sum_{j \neq i} \phi_{ij}(r_{ij})$$

where E_i is the energy of atom i , F_i is the embedding energy of atom i , ϕ_{ij} is the two body potential between atoms i and j , r_{ij} is the

interatomic distance between atoms i and j , and ρ_i is the charge density at site i due to atoms in other sites. One of the assumptions in the EAM approach is that ρ_i is superposition of atomic charge densities from all the other sites,

$$\rho_i = \sum_{j \neq i} \rho_j^a$$

where ρ^a is the atomic charge density.

F and ϕ are determined by considering for them functional forms and finding their parameters by fitting to the bulk properties of crystalline solid (3).

In our calculations, we have employed the EAM functions of Cu along with the molecular static routine to study structures and energetics of twist grain boundaries. In a molecular static simulation, total energy of the system is minimized with respect to positions of atoms. In any energy minimization approach extreme caution should be taken that final state of the system has the lowest energy (i.e., global minimum).

Results

a) single vacancy formation energy

Our $\Sigma 5(\theta=36.87)$ and $\Sigma 13(\theta=22.62)$ twist grain boundaries are comprised of 14 fcc(001) atomic layers, 80 atoms per layer, and with half of the layers rotated with respect to the (001) axis by an angle θ . A vacancy is created in a desired site and the single vacancy formation energy E_{1v}^f is calculated using,

$$E_{1v}^f = E(N-1, 1) - E(N, 0)$$

where $E(N-1, 1)$ is the total energy of a system of N atomic sites with $N-1$ sites filled and 1 site vacant and $E(N, 0)$ is the energy with all N sites filled. Our results for E_{1v}^f are plotted in Fig.(2).

b) Migration and activation energies

Various migration paths for vacancy is considered (look at Fig. 1) by moving the atom through the desired path and allowing it to relax in the plane perpendicular to the path. All the other atoms are allowed to relax without any constraint. Total potential energy of the system is then calculated as a function of migrating

distance. Our results for migration energies are reported below and plotted in Fig.(2):

$\Sigma 5$		$\Sigma 13$	
$E_{1m} = 0.018$	ev, path 1	$E_{1m} = 0.037$	ev, path 1
$E_{1m} = 0.050$	ev, path 2	$E_{1m} = 0.018$	ev, path 2
$E_{1m} = 0.087$	ev, path 3	$E_{1m} = 0.016$	ev, path 3
$E_{1m} = 0.7$	ev, path 4 (bulk)	$E_{1m} = 0.7$	ev, path 4 (bulk)

Single vacancy activation energy $Q = E_{1v}^f + E_{1m}$ is calculated and plotted in Fig.(2).

c) Interlayer spacing across a $\Sigma 5$ grain boundary

Total energy of the grain boundary lattice described in part (a) is minimized using our molecular static code and interlayer spacing is calculated and plotted in Fig.(3).

Summary and conclusion

Our work can be summarized as follows:

- Vacancy formation energy is shown to be directly correlated to the degree of coincidence.
- Single vacancy activation energy near the grain boundary is about 60% lower than its corresponding value in the bulk.
- Vacancy migration energy near a $\Sigma 5$ or $\Sigma 13$ grain boundaries is about 0.1 ev which is much smaller than its corresponding bulk value of ~ 0.7 ev.
- Interlayer spacing at a $\Sigma 5$ grain boundary is enhanced by a factor of about 17% as compared to its bulk value.

References

- M. S. Daw and M. I. Baskes, Phys. Rev. B29, 6443 (1984).
- I. Majid, P. D. Bristowe, and R. W. Baluffi, Phys. Rev. B40, 2779 (1989).
- M. Karimi and M. Mostoller, Phys. Rev. B45, 6289 (1992).

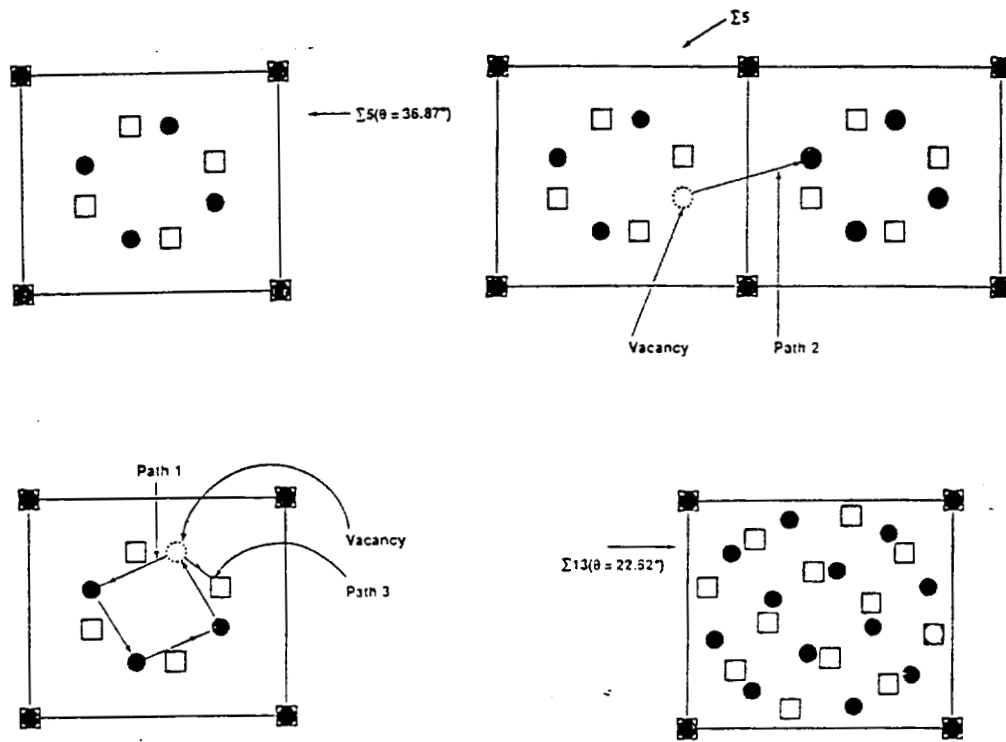
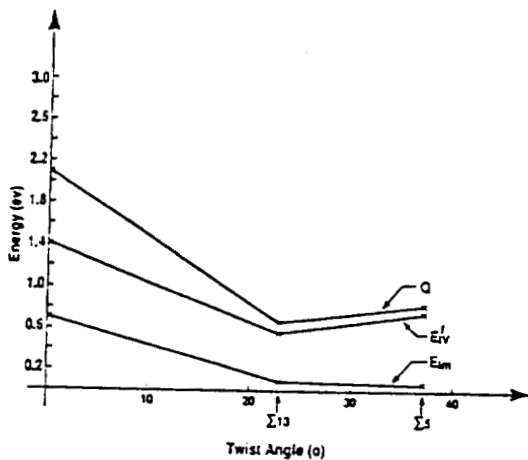


Fig. (1)



E_V , E_m , and Q as a Function of Twist Angle θ for $\Sigma 5$ and $\Sigma 13$

Fig. (2)

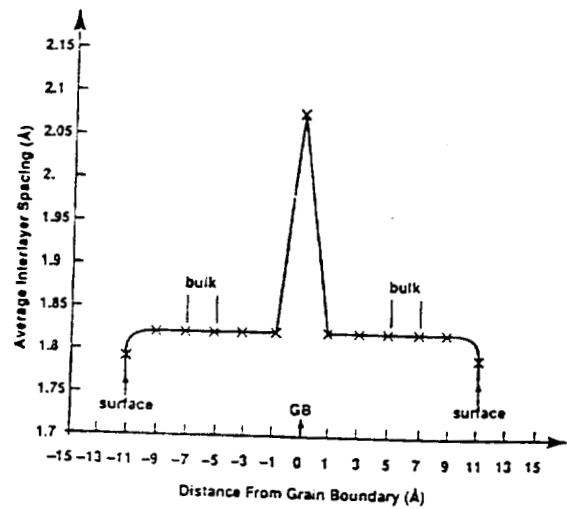


Fig. (3)

1992

NASA/ASEE SUMMER FACULTY FELLOWSHIP PROGRAM

MARSHALL SPACE FLIGHT CENTER
THE UNIVERSITY OF ALABAMAUSING SOFTWARE METRICS AND SOFTWARE RELIABILITY MODELS
TO ATTAIN ACCEPTABLE QUALITY SOFTWARE FOR
FLIGHT AND GROUND SUPPORT SOFTWARE
FOR AVIONIC SYSTEMS

Prepared By: Stella Lawrence

Academic Rank: Professor

Institution: Bronx Community College,
Department of Engineering Technologies

NASA/MSFC:

Office: Information & Electronic Systems Lab.
Division: Software & Data Management
Branch: Systems Software

MSFC Colleague(s): Kenneth Williamson
Charles Cozelos



This paper is concerned with methods of measuring and developing quality software. Reliable flight and ground support software is a highly important factor in the successful operation of the space shuttle program. Reliability is probably the most important of the characteristics inherent in the concept of "software quality." It is the probability of failure free operation of a computer program for a specified time and environment.

There has been an increased awareness in recent years of the critical problems that have been encountered in the development of large scale software systems. These problems not only include the cost and schedule overruns typical of development efforts, and the poor performance of the systems once they are delivered, but also include the high cost to maintain the systems, the lack of portability and the high degree the systems can be sensitive requirement changes.

The efforts related to the development of a standard programming language, and of software development tools and aids, all provide partial solution to the above problems by encouraging disciplined development of software and therefore a controlled development process.

Recently there has been a great deal of research in the area of software metrics. A number of metrics which measure various attributes of software and relate them to different aspects of software quality have been developed and evaluated. The program manager responsible for the development of the software can establish specific software product quality goals and measure the progress towards these goals during development. Metrics can also provide the means to assess the difficulty in modifying a software product.

A validated metric is one whose values have been statistically associated with corresponding quality factor values or attributes of software that contribute to the quality of the software. The critical value of a validated metric is that value which is used to identify software which has unacceptable quality. The major benefit of validation is that it increases the probability that the metric will be a good indicator of quality. The six criteria that a metric must satisfy to be validated are associativity, consistency, discriminative power, tracking, predictability and repeatability.

The quality factor reliability has been associated with various subfactors. These include completeness, accuracy, consistency, error tolerance, simplicity, availability, non-deficiency and anomaly management.

The measurement of software complexity is receiving increased attention since software accounts for a growing proportion of total computer system costs. Besides the

above mentioned complexity measures, the following basic and conceptually simple measures are also considered: the total number of lines encountered in the main body of the program, the number of lines of code, the total number of characters, the number of code characters, then number of comments and the number of comment characters in a program.

Parsers have been developed and used to compute the various metrics for Pascal and Fortran programs, and recently for Ada programs. The Dynamics Research Corporation has developed a Measurement and Analysis Tool called AdaMat. AdaMat is a specific source code quality analysis tool. Its metrics hierarchy is based on the RADC (Rome Air Development Center) metrics framework. It measures adherence to over 240 quality principles which impact the reliability, maintainability and portability of Ada source code. Its principles are based on the most effective use of Ada language features and adherence to long standing software engineering principles. In the AdaMat system the quality factor, Reliability, has two subfactors, Anomaly Management and Simplicity. Anomaly Management has three subfactors: Prevention, Detection and Recovery. Simplicity has three subfactors: Coding Simplicity, Design Simplicity and Flow Simplicity. AdaMat reports contain concise information on each metric's level of adherence, the ranking option allows worst case Ada units to be isolated rapidly, and AdaMat Documentation clearly explains what is being counted by each metric. It also explains why it is important to quality, provides a suggested method of improvement and gives a source code example of adherence to the metric principle and non-adherence to the principle.

AdaMat provides a user friendly interface which makes reporting simplified and straightforward, it provides maintenance cost savings resulting from the use of a disciplined development process. In addition there are substantial early error detection cost benefits. Lastly it provides an automated code review and inspection process. In particular, formal source code inspections can use such a tool to locate potential problem areas for the inspectors.

The second part of this project dealt with the development and calibration of quantitative models for predicting the quality of software. A software reliability model specifies the general form of the dependence of the failure process on the principal factors that affect it: fault introduction, fault removal, and the environment. Software reliability models are generally formulated in terms of random processes. Analytic expressions can be derived for the average number of failures experienced at any point in time, the average number of failures in a time interval, the failure intensity at any point in time, and the probability distribution of failure interval models. A good software reliability model gives good predictions of future failure

behavior, estimates MTTF, estimates time to test completion, is simple, widely applicable, and based on sound assumptions. Prediction of future failure behavior assumes that the values of the model parameters will not change for the period of prediction.

The models used in the present study consisted of:

1. SMERFS (Statistical Modeling and Estimation of Reliability Functions for Software). There are ten models in SMERFS: error count models (generalized Poisson model, NHPP model, Brooks and Motley, Schneidewind model, S-shaped reliability growth model) and time-between-error models (Littlewood and Verrall Bayesian model, Musa execution time model, geometric model, NHPP model for time between error occurrence, Musa logarithmic Poisson execution time model).

2. Kenneth Williamson's NHPP Binomial type software reliability model

3. Goel-Okumoto NHPP model.

The software utilized consisted of the IMCE (Image Motion Compensation Electronics) software flight data, BATSE (Burst Transient Source Experiment, Gamma Ray Observatory) software, and a further program will also utilize POCC (Payload Operations Control Center for the Space Shuttle), Payload Checkout Unit Software for the Space Shuttle and HIT's Software (Space Shuttle Telemetry Systems).

Before discussing the results obtained with the models used in the present study, it must be kept in mind that software reliability modeling is just one of many tools. It cannot provide all the answers to the problems managers and developers must face. It must be taken as a bit of information, which along with others, is helpful in making a realistic judgment concerning a program's status.

For a first run, the results obtained in modeling the cumulative number of failures versus execution time showed fairly good results for the data. Plots of cumulative software failures versus calendar weeks were made and the model results were compared with the historical data on the same graph. If the model agrees with actual historical behavior for a set of data then there is confidence in future predictions for this data.

Considering the quality of the data, the models have given some significant results, even at this early stage. With better care in data collection, data analysis, recording of the fixing of failures and CPU execution times, the models should prove valuable in making predictions regarding the future pattern of failures, including an estimate of the number of errors remaining in the software and the addition-

al testing time required for the software failure rate to reach a chosen target level. In addition, conditions occurring during V&V are not always covered by the models. A Center Director's Discretionary Fund proposal is planned to address these conditions.

It appears that there is no one "best" model for all cases. It is for this reason that the aim of this project was to test several models. One of the recommendations resulting from this study is that great care must be taken in the collection of data. When using a model, the data should satisfy the model assumptions.

As previously stated, the data has to have the ability to correctly identify and measure what is desired. The data provided must satisfy the following:

1. It should be correctly recorded.
2. It should consist of samples that are random in nature.
3. It should be stated in CPU hours between failures or error counts per interval.
4. All error failure data should be accurate.

Reliability will improve if the field software is corrected as failures occur. What about repeated failures due to the same fault? Fixing of faults leading to failures has to be properly recorded and properly attended to. The record of failures must be obtained for a sufficient length of time. Recent theory indicates that the failure intensity function probably decreases exponentially with time, i.e. a plot of the rate of occurrence of failures versus the number of faults found decreased asymptotically to zero.

There are also several recommendations regarding the use of the models:

1. The models require the insertion of various parameters. The models should be run with various values of these parameters, which should be carefully chosen for optimum results.
2. The data should be modeled piecewise, in addition to running the models for the total data.
3. Various forms of data input are provided including time between failure data and error count data and the model may yield different results for different types of data input.
4. The length of the trial should be a proportion of the expected life of the system; predictions made from a very small set of data tend to be poor.

5. The rate of manifestation of errors varies greatly from fault to fault, models which treat all faults as having the same rate may lead to optimistic bias estimates. Perhaps some type of analysis should be performed to classify failures by severity, what kind of failure is it and is it critical or not?

To sum up the preliminary trials indicate that the models tested show much promise and that with their proper use and tailoring they are expected to yield an accurate reliability prediction for the flight and supporting ground software of embedded avionic systems.

REFERENCES

1. Musa, John S., Iannino, A., and Okumoto, Kazuhira, Software Reliability Measurement, Prediction, Application, McGraw-Hill Book Company, New York, 1987.
2. Schneidewind, Norman F., Validating Software Metrics Naval Surface Warfare Center, Dahlgren, VA 22448, Sept. 1990.
3. Dynamics Research Corporation, AdaMat, Measurement and Analysis Tool, 60 Frontage Road, Andover, MA 01810, Oct. 1991
4. Farr, William H., Strategic Systems Department, Naval Systems Warfare Center, Dahlgren, VA 22448, Sponsored by Strategic Systems Programs, Washington, DC 203765-5002, Statistical Modeling and Estimation of Reliability Functions for Software (SMERFS), Report No. NSWC TR 84-373, Revision No. 2, March, 1991.
5. Williamson, Kenneth, Non-Homogeneous Poisson Process Binomial Type Software Reliability Model, Preliminary Edition, EB41/Software & Data Management Division, EB42/Systems Software Branch, Marshall Space Flight Center, Huntsville, AL 35812, July, 1991.

1992

NASA/ASEE SUMMER FACULTY FELLOWSHIP PROGRAM

MARSHALL SPACE FLIGHT CENTER

THE UNIVERSITY OF ALABAMA

AN ALGORITHM TO QUANTIFY THE PERFORMANCE OF THE JOVE PROGRAM

PREPARED BY:	GEORGE LEBO, Ph.D.
ACADEMIC RANK	ASSOCIATE PROFESSOR
INSTITUTION:	UNIVERSITY OF FLORIDA DEPARTMENT OF ASTRONOMY
NASA/MSFC	
OFFICE:	OFFICE OF THE ASSOCIATE DIRECTOR FOR SCIENCE
MSFC COLLEAGUE:	N.F. SIX, Ph.D.

THE ALGORITHM

Just after he was appointed NASA Administrator earlier this year, Dan Goldin made it clear that each person and program at NASA would be evaluated using quantifiable criteria. He instructed each person to define the standards by which he/she and his/her programs will be graded. My assignment was to define criteria by which the JOVE program could be graded and to develop an algorithm that would quantify the evaluation.

The JOVE program is a JOint VEnture between small four-year colleges and NASA in which select faculty members work with scientists and engineers (mentors at the NASA centers and major universities.) NASA and the colleges share expenses of the program approximately equally.

Dr. N.F. Six, Director of the JOVE program, suggested that JOVE be evaluated in the areas of research, education, and outreach; areas specified in JOVE's charter. The author prepared a sample algorithm which was presented for discussion to the JOVE faculty at their summer retreat in Fredericksburg, Virginia July 22-25, 1992.

A small discussion group comprised of six JOVE faculty members suggested that, starting with the algorithm developed by the author, various evaluation scenarios be circulated among a committee made up of members from the oldest JOVE schools.

It was decided that the algorithm should address and/or include the following features:

1. Research should be the most important parameter as the JOVE initiative is aimed at improving NASA related research capabilities at the JOVE school.
2. A given JOVE institution should, within limits, be allowed to determine the relative importance of research, education, and outreach, subject to number one above.
3. Care should be taken to "normalize" or otherwise shape the algorithm so that a given term does not get too large if a JOVE school performs unusually well in any one area.

Once the algorithm is chosen, the report forms which are filled out annually by the JOVE schools will be modified so that the data required by the algorithm will be provided. The results of subsequent evaluations will be provided to each JOVE school so it can continually upgrade its performance.

It was the hope of the working group that, through closely monitored upgrading, the algorithm would become a reliable measure of how a given school (or the JOVE program as a whole) was really performing.

CORRELATING JUPITER'S AURORAL ACTIVITY AND
ITS DECAMETRIC RADIO EMISSION

A proposal to the Hubble Space Institute from Hunter Waite, Southwest Research Institute, James Green, GSFC, and the author will be written to examine potential correlations between the Jovian auroral activity as recently discovered by the Hubble Space Telescope UV imaging experiment and Jupiter's decametric radio waves as recorded by two ground-based radio observatories; one at The University of Florida, the other in Japan.

The experiment will use the location of the Jovian auroral hot spots as shown by HST UV images to pinpoint the source of Jupiter's decametric radio waves. The ground-based radio observatories will run two spectrographs: one, sweeping at very high speed, will indicate how fast the radiating region is moving and the other, a slower instrument will generate the large spectral arcs that were discovered by the Voyager PRA experiment. Inspection of the large arcs will show how the location of the radio source is related to the auroral hot spot and Jupiter's magnetic field and will indicate whether Jupiter's moon IO or its torus plays a role in creating the radio waves.

The UF will upgrade its radiometers to present data in a format which will show the large spectral arcs that were discovered by the Voyager PRA experiment. Several new commercially available crossed log-periodic antennas will be installed and the radio spectrograph will be updated using a new acousto-optical Bragg cell.

1992

NASA/ASEE SUMMER FACULTY FELLOWSHIP PROGRAM

MARSHALL SPACE FLIGHT CENTER

THE UNIVERSITY OF ALABAMA

ADAPTIVE OPTICS FOR LASER POWER BEAMING

Prepared By: Robert P. Leland, Ph.D.
 Academic Rank: Assistant Professor
 Institution and Department: The University of Alabama
 Department of Electrical Engineering

NASA/MSFC:

Division: Guidance, Control, and Optical Systems
 Branch: Optical Systems
 MSFC Colleague: James Bilbro

It has been proposed to use a high energy pulsed laser to beam power into space for satellites or a lunar base. The effects of atmospheric transmission are critical to such a system. Thermal blooming in the atmosphere can cause the beam to spread rapidly. Atmospheric turbulence can cause beam bending or beam spreading, resulting in the loss of transmitted energy that fails to hit the target receiver.

If the laser beam is expanded to a width of 12 m using a Cassegrain beam expander, and the beam is collimated, thermal blooming will be minimized. An adaptive optics system has been proposed to compensate for the effects of turbulence. The primary mirror is made up of hexagonal segments which can each be moved in a piston or two axis tilt manner. A Hartmann Shack sensor is used to measure the wavefront of radiation from a distant source, called a beacon. In our case, the beacon is a "spot" formed by the reflection of a laser beam by atmospheric aerosols, referred to as an artificial guide star. A laser pulse is transmitted into the atmosphere, and the wavefront of the radiation reflected by aerosols at a desired altitude is measured and used to impose a wavefront correction on the shape of the primary mirror. The next laser pulse is transmitted with this correction, which compensates for the effects of turbulence. The system is shown in Figure 1 below.

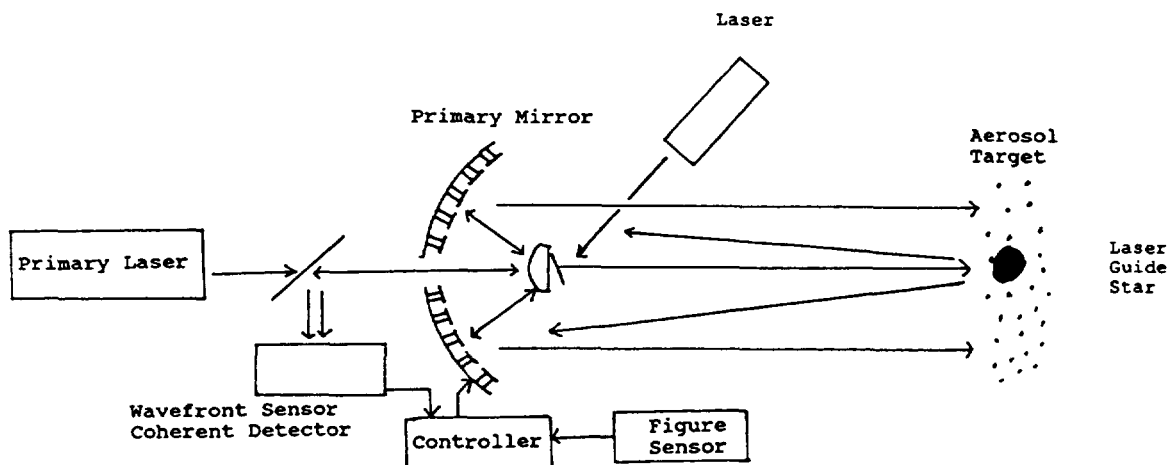


Figure 1.

The goal of the adaptive optics system is to obtain a diffraction limited 12 meter collimated beam at a given altitude. We consider three schemes for creating beacons using artificial guide stars, and the resulting system performance.

Case 1. Entire 12 m Beam Used as Guide Star.

Suppose the reflection from the 12 meter beam itself is used as a beacon. This idea is attractive, since we will be getting a return signal from all points of the 12 m beam at the chosen altitude. However the beacon occupies an area larger than the isoplanatic patch. To calculate the isoplanatic patch, we assume the mean turbulence profile of the Hufnagel-Valley-Boundary model:

$$C_h^2(h) = .374 * (2.2E-53 h^{10} \exp(-h/1000) + 1.E-16 \exp(-h/1500) + 1.7E-14 \exp(-h/100)) m^{-2/3}$$

This turbulence profile corresponds to a value of the Fried coherence length of $r_0 = 23$ cm for a 1μ wavelength, which would be 10 cm for visible light. The isoplanatic angle θ_{IP} and isoplanatic patch D_{IP} are shown in Table 1 for several guide star altitudes.

Altitude km	θ_{IP} arc sec	D_{IP} m
7	29.3	1.99
12	12.2	1.42
30	8.2	2.38
60	8.2	4.76
90	8.2	7.13

Table 1. Isoplanatic angle θ_{IP} and patch diameter D_{IP}

The data in Figure 2 assumes the laser is pointed vertically, and that there is no significant turbulence layer at tropopause (about 12 - 15 km). A significant turbulence layer at tropopause would greatly reduce the isoplanatic angle for guide stars above 15 km, as would deflection of the beam from vertical. At 90 km the guide star is assumed to be formed by exciting the sodium layer. At 60 km the concentration of aerosols is extremely low.

Since the beam diameter is larger than the isoplanatic patch, we cannot use the return from the entire beam for wavefront correction. Since the Hartmann wavefront sensor will use coherent detection, the signal to noise ratio in the wavefront measurement will be decreased due to speckle from the 12 m beacon. Hence use of the entire 12 m beam for wavefront correction appears infeasible.

Case 2. Single Guide Star with Small Radius.

An alternative approach is to produce a smaller guide star with a second laser. This avoids the problems of signal loss due to speckle. Anisoplanatism is still a problem, however, since the primary mirror aperture is larger than the isoplanatic patch at any of the altitudes under consideration. Hence a single guide star cannot be used to correct the effects of turbulence over a 12 m aperture.

Case 3. Multiple Guide Stars.

For ground based large aperture telescopes it has been proposed to use multiple guide stars, and to correct the wavefront on the subaperture of the mirror directly below a guide star based on the return from that star. In this manner, the effects of anisoplanatism are greatly reduced. This technique could be used for the laser power beaming problem. Each guide star would be used to correct the part of the beam expander mirror within an area that is a fraction of the the isoplanatic patch around the guide star. In this way the part of the beam in the isoplanatic patch around the guide star will be corrected for turbulence effects, relative to the position of the guide star. The number of guide stars needed depends on the diameter of the primary mirror aperture and the size of the isoplanatic patch. For wavefront correction with rms error of $\lambda/10$, it is required that

$$N_{gs} = (1.25 D/D_{IP})^2$$

where N_{gs} is the number of guide stars, and D is the mirror aperture, 12 m in this case. The number of guide stars required at several altitudes is given in Table 2 below.

Altitude km	Number of Guide Stars (N_{gs})
7	57
12	112
30	40
60	10
90	5

Table 2. Multiple Guide Star Requirements

Power Considerations:

Each guide star at a given altitude requires sufficient brightness, or laser power, in order to provide enough photons for each cell of the Hartmann sensor to produce a wavefront slope measurement. If the guide stars are created at higher altitudes, we require more power per star, since the density of aerosols is lower, however we need fewer stars. Hence the amount of power needed to produce 57 guide stars at 7 km is less than that needed to produce 40 guide stars at 30 km. However, guide stars at 30 km could be used to correct for turbulence at tropopause, whereas wavefront correction based on a star at 7 km would be limited to turbulence in the boundary layer and a few kilometers above. Since the most intense turbulence is in the boundary layer, a guide star at 7 km may yield good performance. In addition, it is easier to precisely position the guide stars at the lower altitude, since the angular separation between them is greater.

Referencing and Positioning of Multiple Guide Stars

Since our beacon is in the atmosphere, and not on the target, no correction can be made for pointing errors, or overall tilt of the wavefront. When using multiple guide stars, the average tilt of the wavefront over the subaperture around each guide star cannot be corrected. If the guide stars are positioned correctly with respect to each other, this does not present a problem. However if the guide stars spread out, then the corrected beam will also spread. Hence it is required that the guide stars be positioned accurately with respect to each other. In an experiment on Mt. Haleakala, Maui, Hawaii [2], two guide stars were produced about 30 cm apart at an altitude of 6 km. A second telescope was used to verify the position of two guide stars.

Production and Sensing of Multiple Guide Stars

In the Mt. Haleakala experiment, the guide stars were produced by two staggered pulsed lasers, and a switching tip-tilt mirror. In this manner, by gating the returns from the guide stars, the returns from each star could be separated and associated with the corresponding primary mirror subaperture. This approach is not practical for larger numbers of guide stars, since the delay time between sensing the wavefront and transmitting the corrected laser pulse must be less than about 10 ms. In the multidither approach the wavelength of each guide star is shifted about $\lambda/15$ so that each star has its own frequency, and can be discriminated using coherent detection. A third approach is to produce an array of guide stars, and use appropriate stopping and vignetting in the optical path so that each cell in the Hartmann sensor sees a single guide star through an appropriate subaperture of the primary mirror. The wavefront sensor would be located behind the primary mirror in the optical path and a beam splitter would be required in the path of the primary laser. Wavefront sensors could not be integrated into the primary mirror segments, as is currently being discussed. The multidither approach would allow the wavefront sensors to be integrated into the mirror segments.

Conclusions

Turbulence compensation for a 12 m laser beam will require multiple guide stars produced by a second laser. The number of guide stars required at various altitudes was calculated. The potential costs and benefits of using low or high altitude guide stars were discussed in terms of power requirements, positioning and wavefront correction.

References

1. Gardner, C.S., Welsh, B.M., "Design and Performance Analysis of Adaptive Optical Telescopes Using Laser Guide Stars", IEEE Proceedings, Vol. 78, No. 11, Nov. 1990.
2. Murphy, D., Primmerman, C., Zollars, B., Barclay, H., "Experimental Demonstration of Atmospheric Compensation Using Multiple Synthetic Beacons", submitted for publication.

493-17308

1992

NASA/ASEE SUMMER FACULTY FELLOWSHIP PROGRAM

**MARSHALL SPACE FLIGHT CENTER
The University of Alabama**

**Structure in Gamma-Ray Burst Time Profiles:
Statistical Analysis I**

Prepared by:	John Patrick Lestrade
Academic Rank:	Associate Professor
Institution and Department:	Mississippi State University Department of Physics and Astronomy
NASA/MSFC:	
Laboratory:	Space Science
Division:	Astrophysics
Branch:	High-Energy Astrophysics
MSFC Colleague:	G. J. Fishman

1. Introduction:

Since its launch on April 5, 1991, the Burst And Transient Source Experiment (BATSE) has observed and recorded over 500 gamma-ray bursts (GRB). The analysis of the time profiles of these bursts has proven to be difficult. An example profile is shown in Figure 1. Attempts to find periodicities through Fourier analysis have been fruitless except in one celebrated case (Mazets et al., 1979). The only meaningful results that have been derived are some general rise and fall times of the pulses. However, even these studies fail to show any significant trends or consistent classifications (Barat et al., 1984). The only definitive, agreed-upon, statement is that the positions and heights of the pulses in a gamma-ray burst time history appear to be completely stochastic in nature.

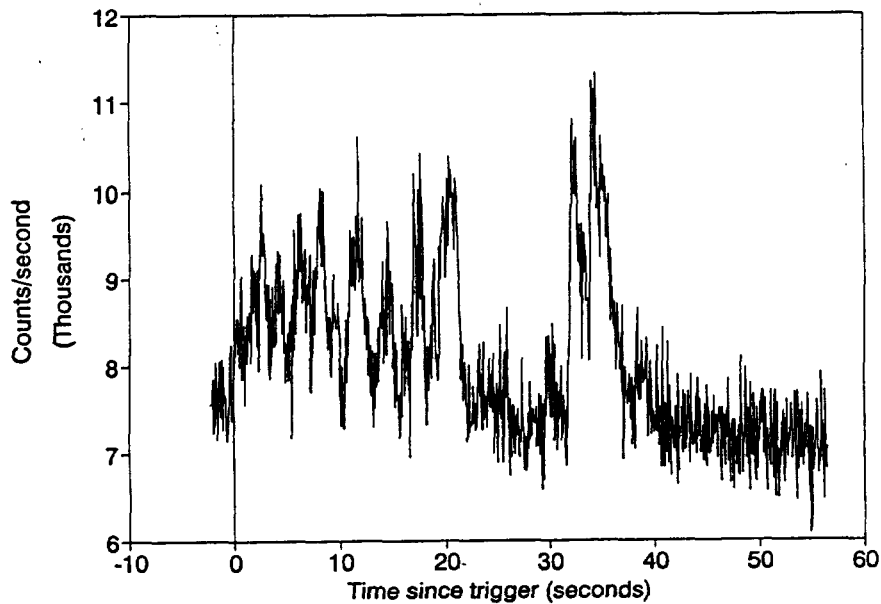


Figure 1. Time Profile of GRB #404

In a recent paper (Lestrade et al., 1991), we showed that a robust quantitative measure of a profile's structure is given by a count of the number of occurrences of monotonic "runs", similar to the standard "run test" (Eadie et al., 1971). This parameter (S_p) has several properties that make it attractive as a statistic: linearity with changing structure, independence from background fluctuations, independence from trigger time, and most importantly it is based upon a well-defined numerical recipe. The nominal recipe is 1) smooth the profile with a 5-point moving average, 2) choose a spike "size" $a|b$, and 3) scan through the profile counting "spikes". A

spike is defined as $b + 1$ successive bins with the first $a + 1$ counts monotonically increasing and the following $b - a$ monotonically decreasing.

Our goal is to be able to quantify the observed time-profile structure. Before applying this formalism to bursts, we have tested it on profiles composed of random poissonian noise. This paper is a report of those preliminary results.

2. Spikiness:

The probability of observing x counts in a BATSE 64-msec bin is given by the normal p.d.f., viz,

$$P(x) = \frac{1}{\sigma\sqrt{2\pi}} e^{-(x-\mu)^2/2\sigma^2}, \quad [1]$$

where μ is the mean (about 600 counts for BATSE discsc data) and σ is the standard deviation ($\approx \sqrt{\mu}$). The probability of finding n monotonically increasing bins is

$$P_n = \int_{-\infty}^{\infty} P(x_1) \int_{x_1}^{\infty} P(x_2) \dots \int_{x_{n-1}}^{\infty} P(x) dx dx_{n-1} \dots dx_1. \quad [2]$$

Fortunately, we can avoid the integral in Equation [2] and use the algebra of permutations and combinations to calculate P_n .

As a test, we generated 10 artificial profiles of 3900 bins each from normal deviates (Press, 1986). Table 1 presents the observed number of spikes in these profiles as a function of spike duration. It should be kept in mind that a spike is recorded, if the *minimum* criterion is met. For example, an observed rising slope of 7 consecutive bins followed by 3 monotonically decreasing bins, would be counted as a spike for all criteria of sizes $a|b$ where $a \leq 6$ and $b - a \leq 3$.

**Table 1: Number of Spikes in Random Profile
As a function of Spike Size.**

Size (ab)	12	24	36	47	57	67	77	88	99
$N_s/39k$ pts.	9545	2462	787	514	516	259	98	34	8

Figure 2 shows the distribution of spikes binned by their position in the profile. Since the possibility of a spike occurrence is equally likely in any of the ten intervals, any observed fluctuation is statistical (e.g., compare the 1|2 curve ($\mu = 1000$) and the 9|9 curve ($\mu = 0.8$)).

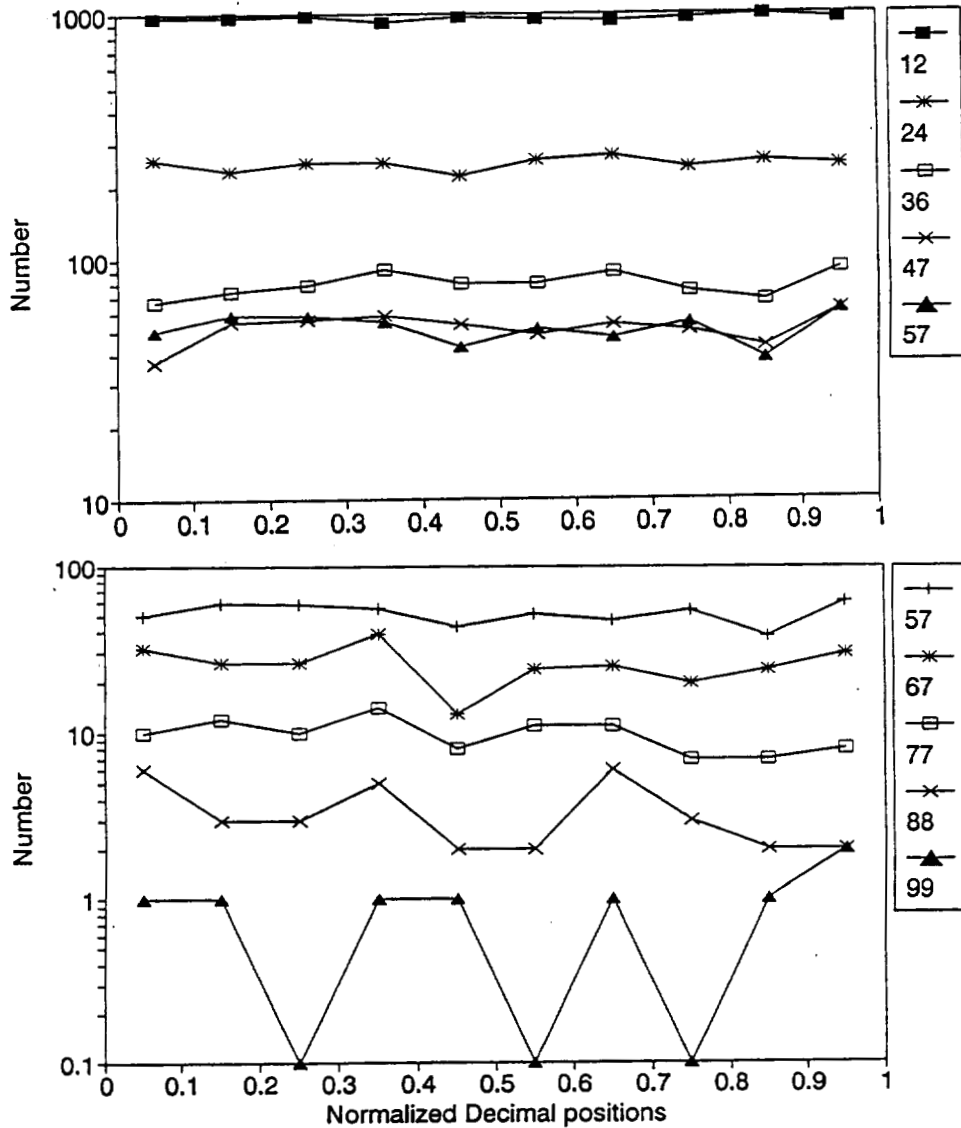


Figure 2. Distribution of Spikes in Normalized Duration.

Figure 3 presents a comparison of the total number of spikes versus spike size for the random data as well as for several real background profiles taken from BATSE data.

3. Conclusions:

We next plan to apply this program to the BATSE GRB profiles. At first, we will limit the analysis to long bursts which show a lot of structure. In addition, we have given the program the flexibility to include 1) a threshold, so that we count only spikes whose heights are greater than some number of sigma, 2) negative slopes, so that a peak criterion of $6|8$, in addition to the normal spikes, would count 7

monotonically *decreasing* bins followed by two *increasing* bins as a spike, and 3) different smoothing criterion.

Furthermore, we will eventually look at higher resolution data, especially for the short bursts. We can apply these same criterion to the TTE data for those GRB's which show no structure on the 64-msec time scale.

In this way, we may find a characteristic of bursts that allows us to determine classes. This then could lead to a better understanding of the underlying physics.

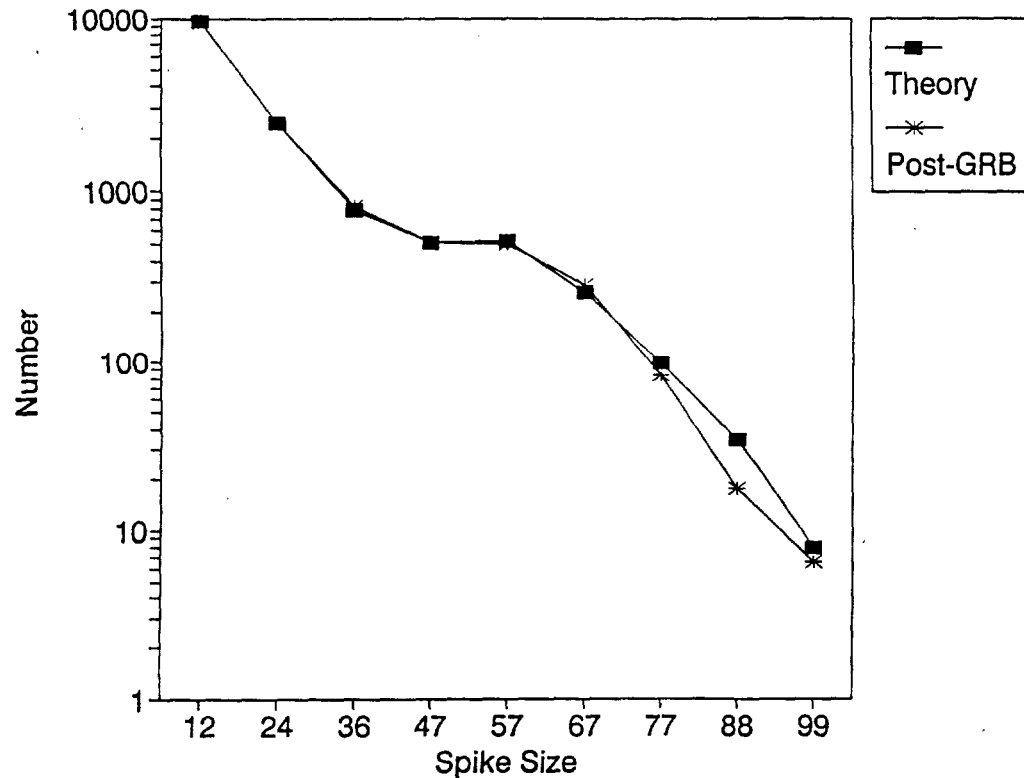


Figure 3. Number of Spikes versus Spike Size.

4. References:

1. C. Barat, R. I. Hayles, K. Hurley, and G. Vedrenne, *Ap. J.* **285**, 791 (1984).
2. W. T. Eadie, D. Drijard, F. E. James, M. Roos, and B. Sadoulet, *Statistical Methods in Experimental Physics* (No. Holland Publ., N. Y., 1971), p. 263.
3. J. P. Lestrade, G. J. Fishman, J. M. Horack, C. A. Meegan, and P. Moore, *A.I.P. Proc. of the Gamma-Ray Burst Workshop, A Quantitative Measure of the Structure of Gamma-Ray Burst Time Profiles*, October, 1991.
4. E. P. Mazets, S. V. Golenetskii, V. N. Ilinskii, *et. al.*, *Nature* **282**, 587 (1979).
5. W. H. Press, B. P. Flannery, S. A. Teukolsky, W. T. Vetterling, *Numerical Recipes: The Art of Scientific Computing* (Cambridge University Press, 1986).

N93-17309

1992

NASA/ASEE SUMMER FACULTY FELLOWSHIP PROGRAM

MARSHALL SPACE FLIGHT CENTER
THE UNIVERSITY OF ALABAMA

DIRECTIONS FOR FUTURE EARTH-TO-ORBIT VEHICLES

Prepared By: James A. Martin
Academic Rank: Associate Professor
Institution and Department: The University of Alabama
Dept. of Aerospace Engineering
NASA/MSFC:
Office: Space Transportation and Expl.
Group: Upper Stages
Office: Preliminary Design
Division: Subsystem Design
Branch: Propulsion Systems
MSFC Colleague(s): Robert F. Nixon
James F. Thompson

XXX

INTRODUCTION

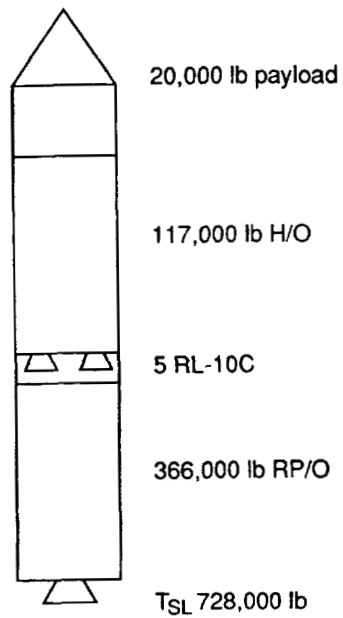
NASA is currently assessing several programmatic possibilities. The desire is to maintain the current capability for transportation to orbit provided by the Space Shuttle and the existing fleet of commercial vehicles, develop the Space Station Freedom, and initiate a new program of exploration of the moon and Mars, called the Space Exploration Initiative (SEI). At the same time, the NASA budget is likely to be held to current levels. Cost estimates indicate that it will not be possible to satisfy all the goals without cost reductions.

One of the concepts being considered for cost reduction is to replace the Space Shuttle and existing commercial vehicles with a new set of vehicles called the National Launch System (NLS). Several concepts have been studied, but none of the concepts studied to date provides the desired combination of cost/flight reduction, acceptable development cost, and technology readiness. An additional goal is to provide a path to grow the NLS capability into a heavy-lift capability for SEI missions.

PRESSURE-FED BOOSTERS

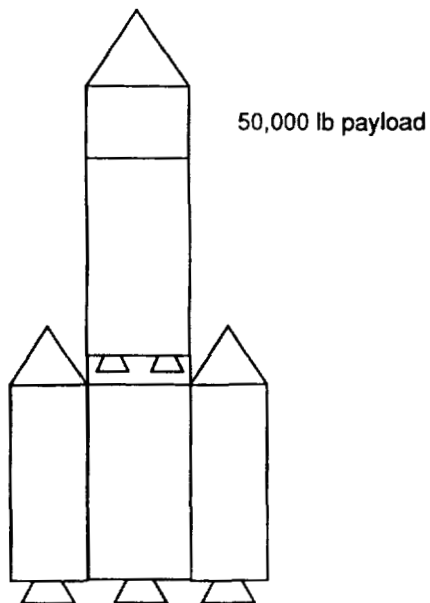
One concept that has not been considered for NLS is the reusable pressure-fed booster. This concept uses propellants stored in tanks on the vehicle at high pressure, such as 600 psi, to eliminate the need for turbopumps on the rocket engine. The result is a heavy but simple vehicle that is well suited to recovery and reuse after an ocean landing.

An initial design for the smaller NLS-3 vehicle is shown in Fig. 1. A reusable pressure-fed booster is used with an expendable hydrogen and oxygen upper stage. In Fig. 2, the larger NLS-2 capability is provided by a first stage with 4 of the same reusable boosters, a second stage with an expendable version of the same pressure-fed design, and the same hydrogen and oxygen stage.



- FASTPASS trajectory and sizing
- No cost estimates
- No split optimization
- Booster weight needs refined

Figure 1. NLS-3 Design with Reusable Pressure-Fed Booster.



- Same H/O stage as NLS-3
- Same pressure-fed stage as NLS-3
- 4 reusable pressure-fed boosters for stage 1
- 1 expendable stage 2 pressure-fed booster

Figure 2. NLS-2 Design with Reusable Pressure-Fed Boosters.

BUILDING CONFIDENCE

Estimating the cost of Earth-to-orbit vehicles is difficult. The technical design is subject to some uncertainty, and the performance requirement is quite stringent. Cost/flight estimates are particularly uncertain because much of the cost is related to people who are responsible for assuring the success of the mission. Because an especially large number of people are involved with the operation of the Space Shuttle, it has not proven that reusable hardware reduces cost/flight.

While estimates of the cost/flight of reusable pressure-fed boosters have indicated a cost advantage, it will probably be necessary to build confidence that the cost advantage can be achieved before selecting this concept for NLS. The confidence can be built by developing pressure-fed boosters at a smaller scale and applying them to an existing vehicle. A study was conducted that indicated that 2 reusable pressure-fed boosters could be used to replace the 9 expendable solid rocket motors used by the Delta-II commercial vehicle. By using the reusable boosters on the Delta-II, real data on the cost advantage of reusable hardware could be accumulated.

PULSED DETONATION ENGINES

A survey of the literature and discussions with experts was conducted to determine the status of pulsed detonation engines. Figure 3 shows how such engine operate. A charge of air is mixed with fuel and flows into the main combustion chamber. A detonation wave is started which travels forward through the chamber and reflects off of the thrust wall as a shock wave. The shock wave travels out the aft end of the chamber and takes the combusted mixture with it.

The survey indicated that there is great potential for the pulsed detonation engine. It might provide high specific impulse, high thrust-to-weight, and simple, low-cost engines. It might provide thrust at flight speeds from zero to hypersonic.

The survey also indicated that there is much work that needs to be done before the potential of the pulsed detonation engine can be realized. Some experimental work has been completed, and some computation analyses have been done, but no experimental work has been done that verifies the performance potential of the engine. An experimental aircraft that has been sighted over the western U. S. leaves a contrail that could be created by a pulsed engine. No information was found to verify what propulsion this aircraft uses.

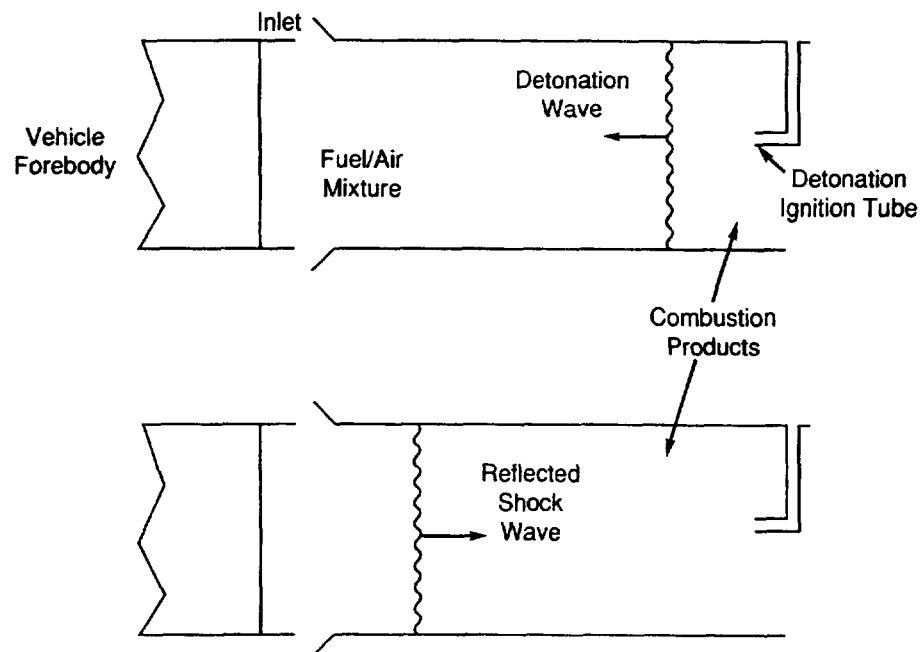


Figure 3.- Operation of Pulsed Detonation Engine.

CONCLUDING REMARKS

Pressure-fed boosters have potential to reduce the cost of Earth-to-orbit transportation. Reduced-scale demonstrations could determine the value of this potential and lead to development of an economical National Launch System.

N 9 3 - 1 7 3 1 0

1992

NASA/ASEE SUMMER FACULTY FELLOWSHIP PROGRAM

MARSHALL SPACE FLIGHT CENTER
THE UNIVERSITY OF ALABAMA

DEVELOPMENT OF A PROTOTYPE INTERACTIVE LEARNING
SYSTEM USING MULTI-MEDIA TECHNOLOGY
FOR MISSION INDEPENDENT TRAINING PROGRAM

Prepared by:	Jack E. Matson, Ph.D.
Academic Rank:	Assistant Professor
Institution and Department:	The University of Alabama Department of Industrial
Engineering	
NASA/MSFC:	
Office:	Mission Operations Lab
Division:	Mission Engineering
Branch:	Training and Crew Support
MSFC Colleague:	Ken Smith

INTRODUCTION

The Spacelab Mission Independent Training Program provides an overview of payload operations. Most of the training material is currently presented in workbook form with some lecture sessions to supplement selected topics. The goal of this project was to develop a prototype interactive learning system for one of the Mission Independent Training topics to demonstrate how the learning process can be improved by incorporating multi-media technology into an interactive system. This report documents the development process and some of the problems encountered during the analysis, design, and production phases of this system.

OBJECTIVES OF THE SYSTEM

The following objectives were identified:

1. Present the course material in an a manner that maintains the interest of the student. Using an interactive system will keep the student involved in the learning process and emphasizing visual and audio presentation of the course topics should keep his attention.
2. Provide consistent training from learner to learner. Using an interactive learning system, the course material will be presented in the same manner and at the same level of detail each time a student takes the course. The result should be more consistent training.
3. Make the training accessible. It is planned to make the system available on a network where any Mac computer can have access to the system.
4. Assess the student's comprehension of the course material. The system will have a testing capability and will provide immediate feedback as to whether or not the student answered a question correctly. At the end of the course, the system will provide a summary of how the student performed on the test and some suggested prescriptive measures that the student can take to correct the deficiencies.
5. Make the process of learning more effective. Incorporating multi-media effects, such as animation, graphics, narratives, sound effects, and video segments, will make the presentation more interesting and should help maintain the attention of the student. It should also some personality into the system as it interacts with the student.

INSTRUCTIONAL SYSTEM DEVELOPMENT PHASES

The development of this prototype system went through an Analysis Phase, a Design Phase, and a Production Phase. The following paragraphs describe the activities performed in each development phase.

ANALYSIS PHASE ACTIVITIES

The first activity in the Analysis Phase was to define the training requirements. These were divided into identifying the training tasks that any interactive learning system would perform and identifying the topics that would be covered by this particular system.

Four training tasks were identified. The system needs to provide direct instruction. The traditional educational approach (Teach it, Test it, Assess it, Re-teach it) was adopted as the presentation method for this interactive system. Another requirement that was identified is to keep the student involved in the learning system and to provide positive feedback. To keep the student's attention, the course material needs to emphasize the visual and audio presentation of the course material and limit the amount of text material that the student needs to read.

The second training task involves the assessment of the student's comprehension of the course material. The system needs to provide immediate feedback after each test question and provide a summary of the student's performance with some prescriptive actions for the student to take following the completion of the course.

The third training task should give the student a view of the course content. The student should be able to see all of the topics contained in the course. As the student progresses through the courses, the student should be able to see the topics already covered, the current topic, and remaining topics to be covered. This gives the student a view of where he has been and where he needs to go to complete the course. This type of information gives the student a feel for what is required to complete the course.

The fourth training task is the capability to backtrack or go back to topics already covered by the student. As a student progresses through a course, many times it is necessary to return to a topic to get a better understanding of the material.

The second part of defining the system requirements involved selecting a topic from the Mission Independent Training Program. The subject selected was the Command and

Data Management System (CDMS) Overview course. This topic is covered in two workbooks containing approximately 300 pages of information. To determine course content, interviews with two subject matter experts -- one who had written the CDMS Overview Workbooks and the other an instructor with knowledge of the CDMS subject. It was decided that the orientation of the course needed to reflect the interests and needs of Principal Investigators and Cadre members. The course topics that were identified include identification of CDMS components and their functions, review the flow of command transactions, review the flow of experiment data, and a "What happens when a CDMS device fails?".

Once the system requirements were defined, the next step involved assembling reference materials related to the CDMS subject. There were volumes of information available, in addition to pictures, diagrams, video presentations, that were obtained. The method of organizing, selecting the best materials to use, etc. was the use of a storyboard.

The storyboard technique allows a person to visualize how best to present the available materials. Under the CDMS topics, all information including text, diagrams, pictures, and any other relevant information were assembled. This involved cutting and pasting. The materials under each topic were then condensed and it was fairly easy to identify the diagrams and other visual materials that best described the CDMS topic. The storyboard helped define a functional path for presenting the material and develop information to be used for scripting the presentation of the material. This concluded the Analysis Phase.

DESIGN PHASE

Some method for organizing the CDMS topics and information identified during the Analysis Phase was needed. The system needs to be designed around some structure. The structure selected was a hierarchy of nodes, where each node represents a CDMS topic. It was fairly easy to transition from the storyboard to the hierarchal organization. Each node was assigned a topic name along with the related information that was made up of text information and graphics. Based on the information, nodes were added to the hierarchy to better define sub-topic under the major CDMS topics. Folders were used to represent the nodes in the hierarchy, which kept all the information related to a sub-topic together.

From the information available in each of the sub-topic folders (or nodes in the hierarchy), the program specifications were developed. These specifications include screen formats, scripts for narrations, test questions and prescriptive instructions, menus, and diagrams.

PRODUCTION PHASE

This phase consists of developing the system, verifying the system, and validating the system. The first step involved selecting the software to develop the learning system. The first consideration was to re-use some of the software developed as part of the MacCIC system. It still would involve developing a SuperCard User Interface, developing a Nexpert Object rule base, developing some multi-media interfaces, and developing a link between the SuperCard interface and the Nexpert Object rule base. This was viewed as too involved an approach for a 10 week project. Also, because of Nexpert Object licensing costs, this approach was viewed as not being cost effective for the CDMS Overview prototype system. It was decided to review other software available in the Lab.

The second alternative considered was MacVideo Interactive authoring system. It supports multi-media functions including the playing of video clips. After selecting this software and working with it for about a week, it was found to be not usable in its current version. The version available in the Lab is a beta test version, which means that the system was released so that software bugs can be identified and corrected. The current version had enough bugs that the software was deemed unusable for the CDMS Overview Prototype system.

A third alternative was an authoring system called LessonCard. The CDMS Overview prototype system was programmed using LessonCard. The result was an interactive learning system with a point and click user interface that generally satisfies the system requirements and meets the objectives defined for the system. However, this was accomplished with limited multi-media capabilities. LessonCard supports HyperCard Graphics which does not include color. Therefore, the capability of displaying color photographs was lost. Video is supported by LessonCard, but only when played from a videodisc player to a television monitor. This capability was also lost. The CDMS prototype system is able to display black and white diagrams and play narrations. While these are limited capabilities, the CDMS system is still effective.

The verification of the CDMS prototype system was done by one of the subject matter experts interviewed early in the system development. He reviewed the system two different times. He concluded that the course content was correct and that the proper level of detail was presented. He made some suggestions on how to present some material and these suggestions are being incorporated in to the system.

The system is currently being validated. Other Branch members are reviewing the system and their comments and suggestions are being reviewed.

SUMMARY

The CDMS Overview prototype system is limited in multi-media capabilities, but it met its objectives. Some of the limitations may be overcome when a new version of LessonCard is released in the Fall. It demonstrates the effectiveness of an interactive learning system that involves the student in the learning process and emphasizes the visual and audio presentation of the course topics. It was also completed within a ten week window, even with the difficulties and lost time when using the Mac Video Interactive software.

However, a problem does exist with the LessonCard version of the CDMS Overview course. After including the diagrams and recording the scripts, the system grew to over 14 megabytes, and is probably too large to really be portable or accessible. This points to a major problem when attempting to use personal computer platforms for an application with even limited multi-media capabilities. The storage requirements are too large. An external storage device and a television monitor are needed to display any kind of color photographs or video clips. This is probably the major shortcoming of the CDMS Overview prototype system.

N 9 8 - 1 7 3 1 1

1992

NASA/ASEE SUMMER FACULTY FELLOWSHIP PROGRAM

MARSHALL SPACE FLIGHT CENTER
THE UNIVERSITY OF ALABAMA

MULTIPATH EFFECTS IN A GLOBAL POSITIONING SATELLITE
SYSTEM RECEIVER

Prepared By:

Malcolm W. McDonald, Ph.D.

Academic Rank

Associate Professor

Institution and
Department

Berry College
Department of Physics

NASA/MSFC

Laboratory:
Division:
Branch:

Information & Electronic Systems
Computers and Communications
Communications Systems

MSFC Colleagues:

Mr. William Hopkins, EB33
Mr. Todd Freestone, EB33

Multipath Effects in a Global Positioning Satellite System Receiver

I. Introduction

The Global Positioning Satellite (GPS) system consists of eighteen satellites orbiting earth in six well-defined orbits. The orbits are inclined 55 degrees with respect to the equator, and the orbital planes are uniformly spaced to provide widespread satellite coverage over most of the earth's surface. Generally speaking, four or more GPS satellites are visible at any populated location on the earth's surface at almost any time. The view of GPS satellites is even better from the vantage point of space vehicles orbiting a few hundred kilometers above the earth's surface.

The GPS satellites orbit at an average height above the earth's surface slightly in excess of 20,000 kilometers with an orbital period of one-half a sidereal day (a sidereal day is the time required for the earth to rotate once on its axis, relative to a distant star. It is about four minutes shorter than the synodic "ordinary" day, which is defined using the sun as a reference). Thus the GPS satellites orbit the earth approximately twice a "day".

Each GPS satellite broadcasts a unique pseudorandom number (PRN)-encoded spread-spectrum signal on a carrier frequency of 1.57542 gigahertz. The PRN code rate ("chip rate", as it is known) is 1.023 megahertz. The method for spreading the spectrum is bi-phase shift key (BPSK) modulation. The signal is further modulated with a 50 bit-per-second data code. The data includes satellite ephemerides, satellite clock correction offsets, ionospheric transmission characteristics, etc. This description pertains to the C/A ("clear access", or "coarse acquisition"; interpretations vary) encoded signal. There is simultaneously a second encoding scheme (known as P-code) and another carrier frequency broadcast by the GPS satellites which has no bearing on this study.

The GPS system consists of three "segments": a) the Control Segment, b) the Space Segment, and c) the User Segment. The Control Segment is a master station and a system of ground stations which rigorously monitor the orbits and the health of the GPS satellites and strictly maintain an accurate system time reference. The Space Segment refers to the eighteen GPS satellite vehicles (SV's) which receive and re-broadcast the data sent up to them by the Control Segment. Each satellite broadcasts data about itself as well as the other satellites in the Space Segment. The User Segment consists of users who operate GPS receivers capable of receiving and decoding the GPS satellite signals.

The purpose of the GPS system is to enable accurate determination of user position (on earth, or in the space above it). In principle the method of determining position is quite straightforward, assuming that the user and all the GPS SV's have perfectly synchronized clocks and the satellites' positions are accurately known at all times. Then, by knowing the exact location of each of the SV's, the exact time a signal was broadcast by a given SV, and the exact time each SV signal was received by the user (GPS receiver) after having traversed the SV-to-user distance at the constant "speed of light", it is a trivial problem to compute how far the user is from each of the SV's. Observation of four SV signals determines a unique fix of user location. In actual practice several small corrections have to be applied in order to produce precise user location.

This study, as a part of a larger continuing investigation being conducted by the Communications Systems Branch of the Information and Electronic Systems Laboratory at the Marshall Space Flight

Center, was undertaken to explore the multipath response characteristics of a particular GPS receiver which was available in the laboratory at the beginning and throughout the entirety of the study, and to develop a suitable regime of experimental procedure which can be applied to other state-of-the-art GPS receivers in the larger investigation.

The underlying question which drives this research is: how much user position uncertainty can be anticipated when a GPS receiver is being operated in a space vehicle that is subjected to varying levels of multipath reflections of a particular SV signal which is being relied upon for the user's position fix. In other words, should one expect a multipath problem in GPS receiver operation, say in the environs of a large reflective space structure, such as the Space Station Freedom, for example, and, if so, how serious might that problem be?

II. Experimental Procedures

The measurements of multipath effects were performed with instrumentation and equipment available in the laboratory at MSFC. The principal instruments were: a) a GPS Satellite Signal Simulator (SSS) (manufactured by Stanford Telecommunications, Model 7200 NAVSTAR) and b) a GPS receiver (manufactured by Trimble, Model 4000-AX). In addition, radio frequency (RF) amplifiers, power meters, signal attenuators, signal splitters and combiners, a carrier-wave phase shifter, various lengths of RG-214/U coaxial signal transmission cable, two computers, and a spectrum analyzer were configured in the experimental circuit illustrated by the block diagram in Figure 1.

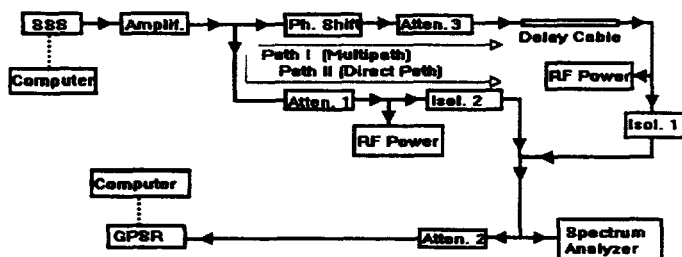


Fig. 1. Block Diagram of Experimental Circuit

The SSS generates a "constellation" of up to five fully encoded GPS satellite signals appropriate for a specified user location and time. The SSS further permits simulation of the satellite signals appropriate for a user presumed to be undergoing motion along a programmed trajectory. This latter capability provided an opportunity to establish a GPS satellite simulation scenario wherein the GPS receiver platform was assumed to be moving along a trajectory near the earth's surface in such a manner as to maintain a near-constant pseudorange (defined as the detected satellite-to-user distance) from one of the satellites (identified as SV01, for satellite vehicle number 1) for a protracted period of time. During this time interval in the simulated scenario the Doppler shifts of the SV01 signal were quite small, advancing through a zero Doppler value.

While the SV01 was standing still (relative to the GPS receiver) in the simulated scenario pseudorange and time data, as detected by the GPS receiver (GPSR) were recorded. The SSS signal for

the SV01 satellite was split into two components, a "direct" component and a "multipath" component, as indicated in Figure 1, and recombined as an input to the GPSR. Provisions in the circuit allowed the multipath component to be time-delayed (by insertion of various lengths of transmission cable), phase-shifted by up to three-fourths of a carrier cycle, and attenuated, as needed, to allow control of the relative power level of the multipath component.

The simulated scenario was repeated in successive runs with different cable lengths inserted in the multipath line. On each run, a somewhat systematic pattern of inserting and removing the multipath component while its phase was being swept by the phase shifter was undertaken. Raw pseudorange and time information was sampled at the GPSR.

III. Results and Conclusions

Graphical plots of the raw pseudorange versus time data for SV01 demonstrated the GPSR's response to the various injected multipath conditions. Data were recorded for cable lengths of approximately 15 meters, 32 meters, and 61 meters. These delays were the equivalents of space path differences of approximately 23 meters, 48 meters, and 92 meters, respectively. In each of the delays, the power levels of the multipath component was adjusted on successive runs to being a) equal to the direct component, b) down by 3 dB, c) down by 6 dB, and d) down by 10 dB.

Preliminary observations of the graphs demonstrate that: 1) the longer time delays (cable lengths) produce larger pseudorange excursion from the nominal, and 2) for any given delay, stronger multipath signals (relative to the direct signal) produce larger pseudorange excursions. The maximum observed pseudorange excursions (occurring with 92 meter (space equivalent) multipath delay and relatively strong multipath signal power) were on the order of 240 meters. When the multipath signal traveled an additional path length of 23 meters equivalent and was at a power level ten dB below that of the direct signal the pseudorange excursions were on the order of ten meters.

It should be noted that the worst pseudorange excursions for each delay accompanied the carrier wave phasing conditions where the nearest-to-a-null spectrum analyzer power display was observed. It happens that near-total nulling occurs for the very short time delays (yet those led to the smallest pseudorange changes) and the apparent severity of the nulling diminishes as the multipath component is delayed a larger portion of a "chip". The longest delay (92 meter space equivalent) is equal to approximately one-third of a chip.

It should be noted further that the effects observed and reported here concern raw pseudorange for a single satellite, not actual position. Also, these data represent no attempts to "smooth" or condition.

1992

NASA/ASEE SUMMER FACULTY FELLOWSHIP PROGRAM

MARSHALL SPACE FLIGHT CENTER
THE UNIVERSITY OF ALABAMA

The Ionosphere as a Gamma-Ray Burst Detector

Prepared by:	Charles H. McGruder III, Ph.D.
Academic Rank:	Full Professor
Institution:	Fisk University Physics Department
NASA/MSFC:	
Office:	Space Science Laboratory
Division:	Astrophysics
Branch:	High Energy Astrophysics
MSFC Colleague:	Jerry Fishman, Ph.D.

Unlike all man made detectors, which are only sensitive to relative narrow regions of the electromagnetic spectrum, the ionosphere is practically a perfect detector for high energy radiation because it absorbs all radiation from the far-ultraviolet to the highest energy gamma-rays ($\lambda \leq 1350 \text{ \AA}$ or $E \geq 9.2 \text{ eV}$). Therefore, it may be possible to employ the terrestrial atmosphere as a detector of high energy celestial photons.

This is an old idea. As early as the 1940's solar flares were detected by the disturbance they cause to the ionosphere. The VLF (3 - 30 kHz) approach for detecting ionospheric disturbances is based on the following physical circumstance: celestial high energy radiation ionizes the atoms of the earth's ionosphere leading to the production of free electrons. These free electrons influence the propagation of electromagnetic waves. By studying the phase and amplitude changes of VLF radio waves propagating in the earth-ionosphere waveguide we can hope to ascertain the electron density in these regions and draw conclusions about the celestial radiation which caused them.

This method has been and still is used to detect solar flares. The basic question of this research project is: Can the method be employed to detect gamma-ray bursts?

The method is based on the detection of free electrons. The maximum value of electron production rate created by a gamma-ray burst occurs at altitudes of 25-70 km (Brown 1973, Baird 1974, Kasturirangan et al 1975; 1976, O'Mongain & Baird 1976, Weekes 1976). The exact altitude for each burst depends upon the spectrum and zenith angle of the burst. There is a principle problem in detecting free electrons created in this altitude range. Because the recombination coefficient here is order of magnitudes higher than that at 85 km (the nighttime reflection height of VLF radio waves), the electrons created are immediately lost. This is the reason why the detection of only one ionospheric disturbance caused by a gamma-ray burst has been reported so far (Fishman and Inan, 1988) despite a number of attempts (Drever et.al, 1973; Kasturirangan, 1975; and Flickinger. 1990).

We must improve our VLF methods of detection so that significant numbers of gamma-ray bursts can be detected. Because of high recombination rates at lower altitudes, we are forced to look for gamma-ray bursts at the 85 km altitude of VLF nighttime reflection. The question is how?

Our situation is characterized by a meager number of detected gamma-ray bursts. Why have so few been detected? Because the peak in electron production occurs at an altitude where the recombination coefficient is prohibitively large. So we see, somehow we must observe the peak intensity not at lower altitudes where the recombination coefficient is large but at higher

altitudes, where it is lower. But, how are we going to observe the peak at higher altitudes? The answer is: We must observe a burst at a large zenith angle. Brown (1973) has shown that at large zenith angles the altitude of peak energy deposition shifts by a significant amount (more than 10 km) to higher altitudes.

Unfortunately, as a celestial source is detected at ever larger zenith angles in order to observe the peak at higher altitudes, where the recombination coefficient is sufficiently small, the amount of energy in the peak is declines dramatically (Brown 1973). So when we get up to a zenith angle or altitude, where we may be able to see the burst, the energy per unit volume is much too low. So we have another problem. How are we going to solve this problem?

We must observe the burst in such a way that it is aligned along the propagation path. This means the azimuth of the burst at all points along the burst must be the same. If this is the case most of the energy of the burst will be deposited in the plane formed by the propagation path and the transmitter and receiver.

We now have two conditions for the optimal detection of a gamma-ray burst.

1. large zenith angle
2. alignment of burst and propagation path (same azimuth of burst along propagation path).

In the VLF databank at Stanford University we looked for gamma-ray burst, 1B910503, one of the strongest bursts seen by the gamma-ray burst detector (BATSE) of the Gamma-Ray Observatory. It occurred on 3 May 1991. The figure shows the amplitude vs. time plot of two completely different propagation paths. For the first path the transmitter (NLK) is located at Jim Creek in Washington State and the receiver at Houston, Texas. For the second path the transmitter (NAA) is at Cutler, Maine and the receiver at Arecibo, Puerto Rico. The black arrows above and below denote the start time (7:4:14.72 UT) of the gamma-ray burst according to BATSE.

The ionospheric disturbance begins simultaneously along both propagation paths. This time is 7:5:15 one minute after the burst begin according to BATSE. Because of the ionospheric response time it is not expected for the ionospheric disturbance to begin at the same time as the initial gamma-ray impulse. It is well known that this is generally true for solar flares too. Recently Blair (1992) confirmed this delay for solar flares. He finds that the average time delay between the GOES satellite and VLF is 2 to 3 minutes.

The following table presents data on the zenith angle and azimuth of 1B910503 as seen from both the transmitters (48.5, NAA, NAU, NLK, NPM, NSS) and receivers (Arecibo and Houston). The last two columns contain the azimuth values relative to the azimuth values of the two receivers.

Azimuth and Zenith Angle

Location	Azimuth	Zenith Angle	Arecibo	Houston
NPM(Hawaii)	309°14'	67°25'	-42°14'	-23°23'
NAA(Maine)	352°20'	91°42'	20'	19°43'
48.5(Nebraska)	331°28'	87°43'	-20°32'	-1° 9'
NLK(Washington)	315°56'	72°12'	-36° 4'	-16°41'
NAU(Aquadilla)	351°27'	117°42'	33'	18°50'
NSS(Annapolis)	345°41'	95°57'	-6° 19'	13° 4'
Arecibo	352° 0'	117°56'		
Houston	332°37'	99°19'		

There is only a 20' difference between the azimuth values of the burst seen at Arecibo (receiver) and Cutler, Maine (transmitter). Thus, the burst is aligned almost exactly along the propagation path and it is here that we see the maximum amplitude change of 0.3 dB. The other values are significantly greater except for NAU but it is also on Puerto Rico and Arecibo is receiving only the ground wave.

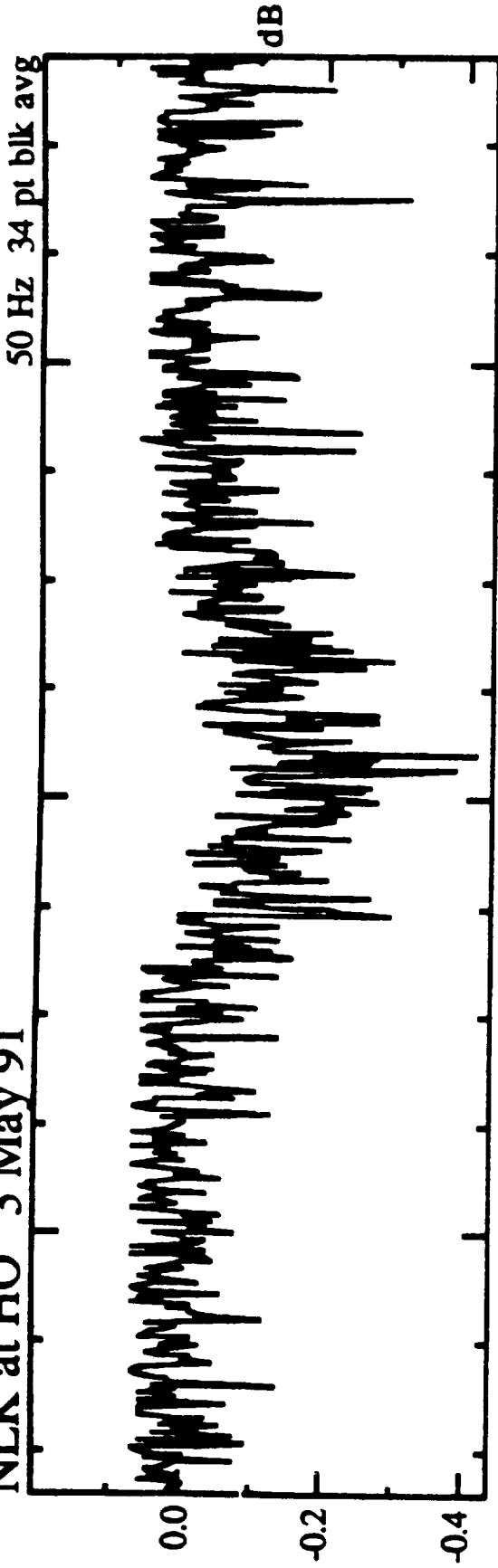
The situation along the propagation paths to Houston is not quite so clear. There are two paths with lower azimuth differences - Nebraska and Annapolis. Nebraska, however, is an LF (long wave) transmitter and the reflection height is higher than the 85 km for VLF, so it is not expected to see the burst. Annapolis - Houston also is closer aligned with the burst than NLK, but the burst is always below the horizon and never less than 6° from the horizon. So NLK appears to be the most likely path to see the burst and indeed we find a 0.2 dB amplitude change.

References

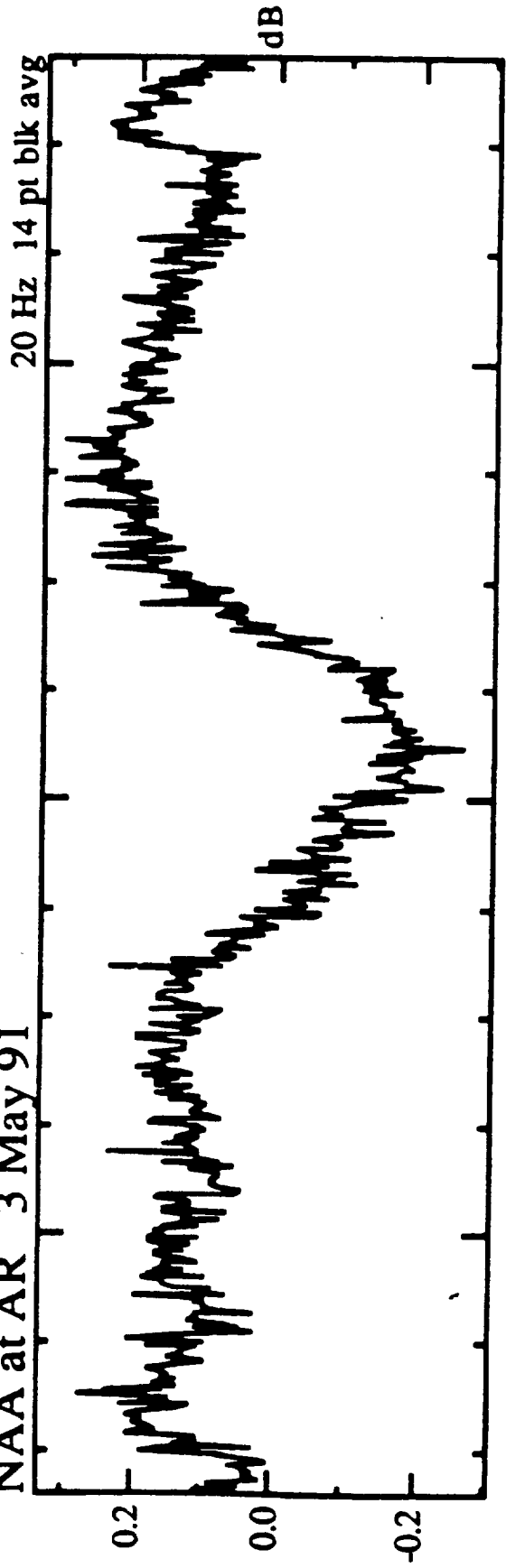
- Baird, G. A., 1974. J. atmos. terr. Phys. **36**, 1565
 Blair, J. , 1992. private communication
 Drever, R. W. P., et al. 1974. Proc. L.A. Conf. on Transient
 Fishman, G. J., Inan, U. S., 1988. Nature **331**, 418
 Flickinger, M. D., 1990. private communication
 Kasturirangan, U. R., et al 1975. Indian J. Rad. Space Phys. **4**, 203
 Kasturirangan, U. R. et al. 1976. Astrophys. Space Sci. **42**, 57
 O'Mongain, E., Baird, A., 1976. Astrophys. Space Sci. **42**, 63
 Weekes, T. C., 1976. J. terr. atmos. Phys. **38**, 1021



NLK at HO 3 May 91



NAA at AR 3 May 91



1992

NASA/ASEE SUMMER FACULTY FELLOWSHIP PROGRAM

MARSHALL SPACE FLIGHT CENTER
THE UNIVERSITY OF ALABAMA

CORRELATED OPTICAL OBSERVATIONS
WITH BATSE/CGRO ON SCO X-1

Prepared by:	Bernard McNamara
Academic Rank:	Professor
Institution and Department:	New Mexico State University Astronomy Department
NASA/MSFC Office:	Space Sciences Laboratory
Division:	High Energy Astrophysics
Branch:	Gamma-Ray and Cosmic Ray
MSFC Colleague	B.A. Harmon

Introduction

The Burst and Transient Source Experiment (BATSE) instrument on the Compton Gamma-Ray Observatory consists of two banks of eight instruments referred to as the Large Area Detectors (LADs) and the Spectroscopic Detectors (SDs). Each LAD crystal is 50.8 cm in diameter by 1.27 cm thick while for a SD these values are 12.7 cm in diameter by 7.62 cm in diameter. Both the LADs and SDs are NaI(Tl) scintillation detectors. The LADs and SDs are situated on the CGRO spacecraft so as to provide all sky coverage for both sets of detectors. The SDs have the ability to measure energies in the 8-16 keV range whereas the minimum energy at which the LADs operate is near 20 keV.

Sco X-1 is the brightest continuous X-ray source in the sky. It is believed to consist of a low mass star orbiting and transferring mass onto a neutron star. It is representative of a class of similar objects referred to as low mass X-ray binaries (LMXB). Because Sco X-1 serves as the proto-type of this class of X-ray emitters and since its detectable emission is so large, it warrants extended study.

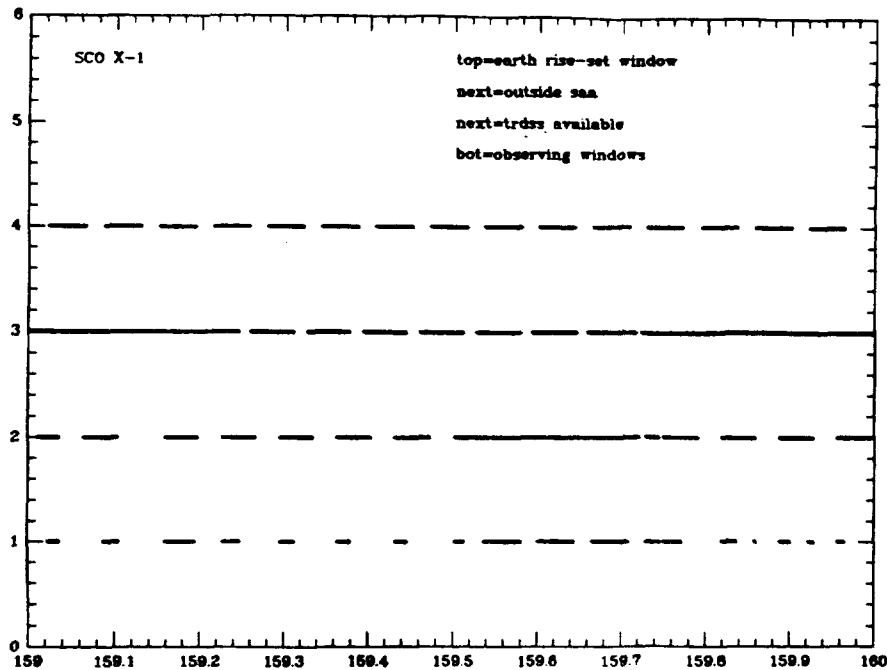
One of the most fruitful techniques of studying a LMXB system is by simultaneously monitoring its emission at a variety of different wavelengths. These correlated datasets can be used to probe the source environment, investigate emission mechanisms, and examine the mass transfer process itself. In principle, the BATSE SDs have the capability of providing a nearly continuous 8-16 keV record of Sco X-1 activity. The aim of this study was to investigate the feasibility of using the BATSE SDs along with simultaneous optical measurements to study this source.

Observational Considerations

In order to obtain simultaneous ground-based optical data with BATSE, three satellite related constraints must be considered. Satellite observations are only possible (1) when Sco X-1 is unobscured by the earth, (2) when the satellite is outside the South Atlantic Anomaly (SAA), and (3) when TDRSS is available to transmit data to ground-based facilities. Each of these constraints influences the extent of the joint optical/high energy observational windows. An example of this is shown in figure 1. From top to bottom, the solid lines indicate when Sco X-1 is observable by CGRO, when the

satellite is outside of the SAA, when TDRSS communication is available, and finally the extent of the simultaneous optical and 8-16 keV windows. Typically, notification of guaranteed TDRSS availability proceed the actual observational dates by a only few days. SAA passage times are available for up to two week intervals and earth rise, set times can be predicted to an accuracy of about 30 seconds one week prior to a desired date of joint observations. The ability to plan joint observations is thus limited to a few days prior to the actual observational date by the TDRSS notification time.

Figure 1



Measuring the 8-16 keV Sco X-1 Signal Strength

Because of space limitations this section will deal only with the acquisition of the Sco X-1 8-16 keV data. This can be measured in two different fashions. The most straight forward procedure involves measuring the step in the received signal as Sco X-1 rises and sets over the Earth's limb. This is the procedure used by the BATSE team to measure the flux detected by the LADs for a number of astronomically interesting sources. An extension of this procedure to a SD is fairly straight forward. We have written a number of software programs that measure the Sco X-1 step size in the SD flux data. In addition to these values, the flux during the interval between earth

rise and earth set can be approximately measured. In order for this information to be obtained, one must subtract the 8-16 keV background signal from the observed flux. Two techniques were developed for this purpose. The first technique models the background using a 3rd order polynomial fit in terms of the cosine of the angle between the detector normal and the center of the earth. In principle this procedure should work quite well because the cosmic 8-16 keV radiation is highly modulated by earth blockage and is the major background contributor. If flux measurements are available over a significant portion of the orbit prior to the rise of Sco X-1, this procedure indeed allows one to estimate and thus subtract the background contribution during those times when Sco X-1 is in the field of view of a SD.

The second technique for subtracting the background is less model sensitive but relies upon the assumption that over the course of a few hours, the cosmic background 8-16 keV radiation remains constant within orbital position. This assumption essentially states that one can use a past orbit to predict the background contribution in a subsequent orbit. If the time span is only a few hours, this assumption appears to be valid. A second, more dangerous, assumption must also be made as part of this technique. That is, that during some orbits the 8-16 keV emission from Sco X-1 is constant. This latter assumption has been tested using BATSE SD data and appears to be valid. Background subtraction is then accomplished by using an orbit which shows no Sco X-1 activity as a reference and subtracting it from a nearby orbit in which Sco X-1 is active. The flux level of the subtracted signal can then be adjusted using the measured Sco X-1 step size from the reference orbit.

Results and Conclusions

Figures 2 and 3 show the correlated optical and BATSE 8-16 keV SD signal for the days TDJ 8791 and 8811. The optical data (top portion of each figure) shows that during these periods Sco X-1 was in a flaring state. The BATSE 8-16 keV light curve (bottom portion of each figure) closely tracks the optical data. There appears to be a slight time delay (seconds) between the two light curves in the sense that the optical activity follows the higher energy signal. This is what one would expect if the optical signal represents reprocessed high energy photons, presumably from an accretion disk surrounding the neutron star. If the optical signal indeed arises from an accretion disk, then one might also expect the optical signal to be smeared (of longer time duration)

than the high energy signal. At this point data analysis is not sufficiently advanced to state whether this smearing is present or not. A second interesting feature seen in both figures is that the optical and high energy continuum radiations are not correlated. This may be due to inadequacies in the background subtraction model which veil this correlation or it may be due to the fact that optical continuum variations reflect a longer term response to the high energy variations.

Figure 2

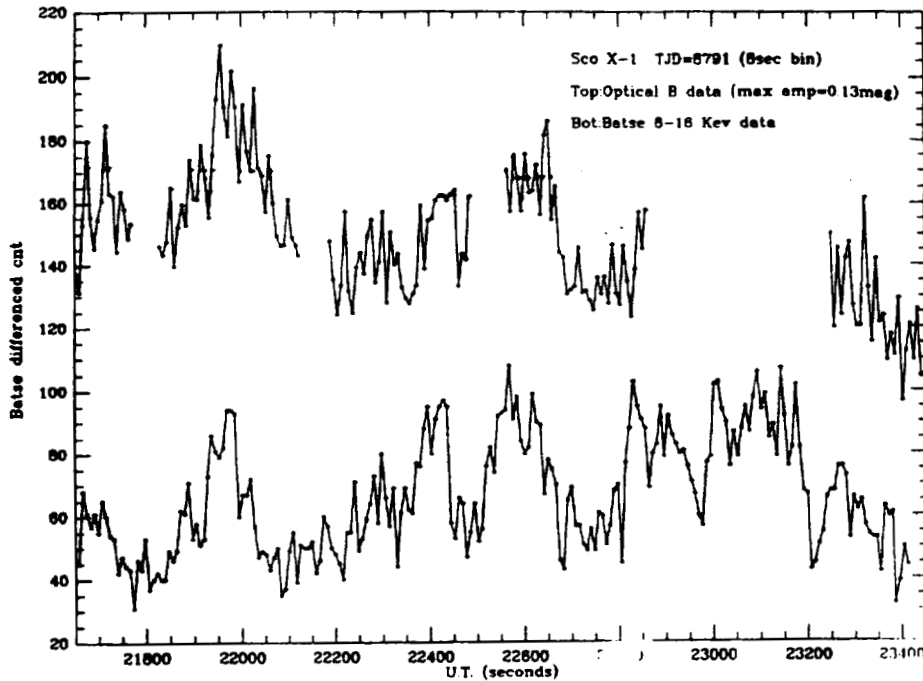
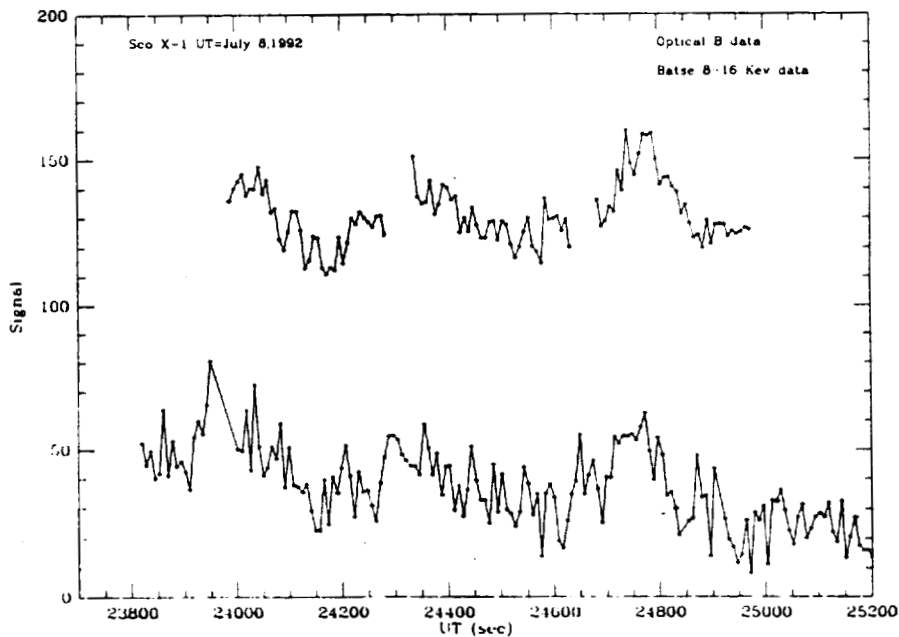


Figure 3



1992

NASA/ASEE Summer Faculty Fellowship Program

Marshall Space Flight Center
The University of Alabama

PROBLEMS INVOLVING COMBINED LOADING

Prepared By:	Lunelle Miller, Ph.D.
Academic Rank:	Academic Division Head
Institution and Department:	Northeast Mississippi Community College Division of Mathematics and Science
NASA/MSFC:	
Office:	Structures and Dynamics Lab
Division:	Structural Analysis
Branch:	Durability Analysis
MSFC Colleague(s):	Henry Lee, M.S.M.E. Cynthia Stewart, B.S.E.S.M.

The first problem was to determine the capability of a ground support equipment (GSE) rack knee bracket for handling a spacelab rack. The geometric center of gravity was calculated for the upper and lower part of the rack and found to be in the center of gravity's allowable envelope (Spacelab Payload Accommodation Handbook, SPAH, Appendix B page B3-154). Using the corners of the center of gravity envelopes, free body diagrams (FBD) were set up to represent each of the four cases. Moments about point P are caused by the force at G and the weight of the upper and lower part located at the respective centers of gravity (figures 1a-b). The greatest moment would occur when the centers of gravity are located at point 1 for the upper part and point 2 or 3 for the lower part (figure 1a). These locations are at the greatest distance from point P thus causing the greatest moment (figure 1b). Using basic static procedures and a safety factor of 5, this case will give $R_{sy} = R_y = 2944$ lbs and $R_z = 7500$ lbs for a maximum upper rack weight of 375 lbs and a maximum lower rack weight 1125 lbs. In the X-Z plane, the center of gravity may be 2 inches off center (figure 1c). This will give $R_y \text{ max} = 1614$ lbs and $R_z \text{ max} = 4112$ lbs.

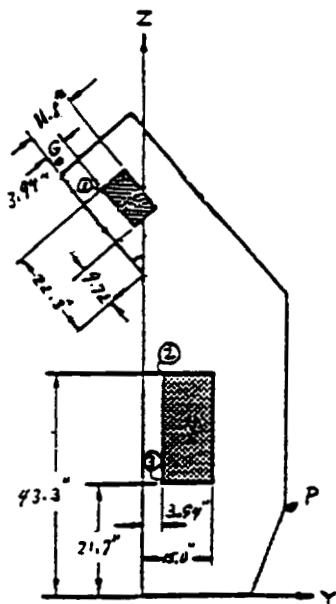


Figure 1a
Side View

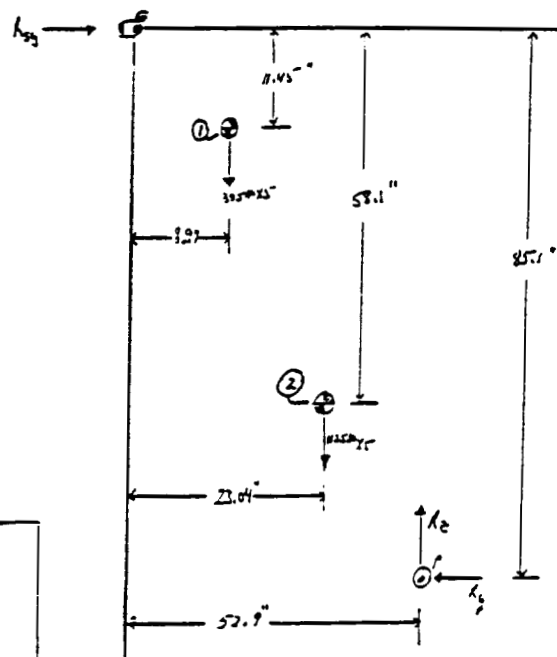


Figure 1b
FBD Side View

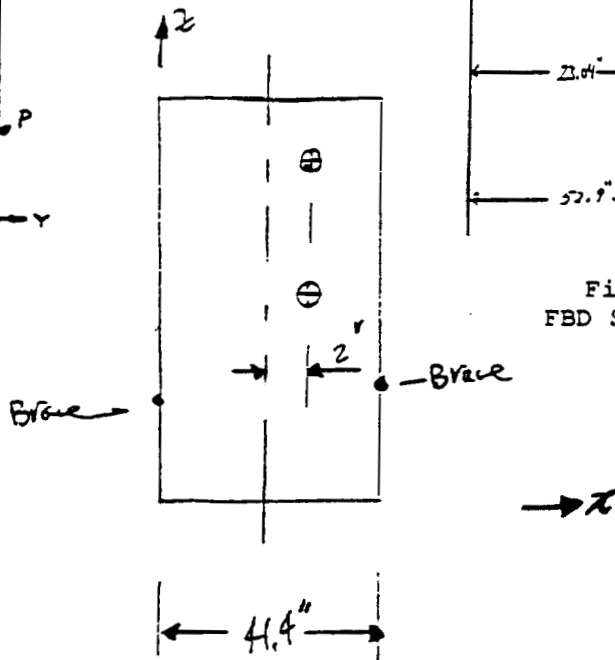


Figure 1c
Front View

The second problem was to determine the exact margin of safety for an axial load and a shear load on a bolt. The equation for failure is axial load squared plus shear load cubed equal one. This gives a curve shaped like the following:

$$a^2 + v^3 = 1$$

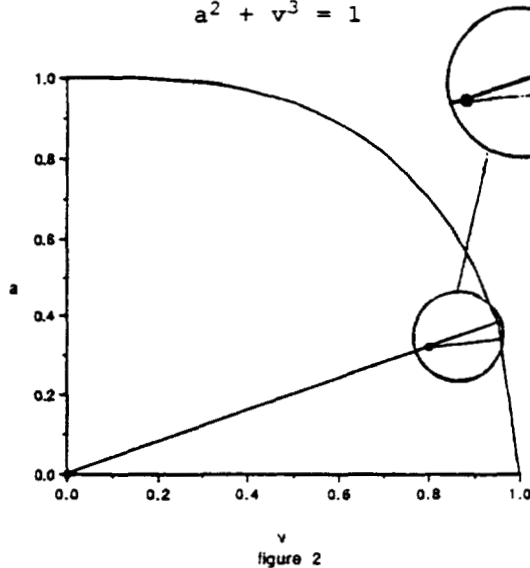


figure 2

With the performance level located under the curve, the margin of safety is the shortest distance to the curve. The traditional method for selecting a margin of safety is the distance from the performance level to the curve located on a straight line through the origin. This is a good enough approximation of the margin of safety except when the bolt is close to failure. Example; close to the curve (figure 2). The shortest distance would always be the minimum distance from the point of performance level to the curve. Using calculus to minimize distance, a seventh degree equation emerges. If specific points of performance are known, it would be

possible to solve. Clearly, additional study is needed.

The third problem was to simplify an expression for stress on a generic non-symmetrical bolt configuration to a form familiar to "bolt people." This form is

$$P_b = PLD + \eta \phi P_{ext} \quad [1]$$

Where P_b is the total load, PLD is the initial bolt preload, η is the loading plane factor, ϕ is the stiffness factor, and P_{ext} is the external load.

$$P_b = PLD + \{P_{ext}\} \frac{\frac{A D k_a k_b}{A D k_a + (A + D) k_b}}{\frac{B C k_a}{B + C} + \frac{A D k_a k_b}{A D k_a + (A + D) k_b}} \quad [2]$$

Using conditions given by the problem, this equation was algebraically reduced to

$$P_b = PLD + \{P_{ext}\} \left(\frac{B + C}{B C} \right) \frac{k_b}{k_a + k_b} \quad [3]$$

which is in the same form as equation [1]. This will be presented in a paper by Henry Lee, MSFC.

The final problem was the structural analysis of the spacelab rack corner posts. The minimum crippling strength of front and rear corner posts (FCP and RCP) was calculated by two methods. The Gerard Method which gives a single value and the Alcoa method which should give values at specific points. The Gerard method equation is

$$\frac{F_{cs}}{F_{cy}} = 0.56 \left[\frac{gt^2}{A} \left(\frac{E}{F_{cy}} \right)^{0.5} \right]^{0.85} \quad [4]$$

(TM-SEAD-85039A page A.3-21) where F_{cs} is minimum crippling strength (ksi), F_{cy} is the minimum allowable compressive yield stress (55 lbs for T73), and E is the modulus of elasticity in compression (10.5×10^3 ksi). The allowable design stress is $0.9F_{cs}$. The Alcoa equations are

$$B_p = F_{cy} \left[1 + \frac{(F_{cy})^{\frac{1}{3}}}{11.4} \right] \quad [5]$$

$$D_p = \frac{B_p}{10} \left(\frac{B_p}{E} \right)^{\frac{1}{2}} \quad [6]$$

$$C_p = 0.409 \frac{B_p}{D_p} \quad [7]$$

$$\lambda_p \frac{t}{b} = 2.89 \text{ no free edge or } 1.24 \text{ one free edge} \quad [8]$$

$$\lambda_p \leq C_p; F_{cs} = B_p - \lambda_p D_p \quad [9]$$

$$\lambda_p > C_p; F_{cs} = \frac{\Pi^2 E}{(\lambda_p)^2} \quad [10]$$

(TM-SEAD-850039A page A.3-23 - a.3-24). These values have been calculated for all rack posts and are ready for the test data correlation.

In order to get crippling values from test data, both axial loads and moment values must be applied. The loads were applied as FPA at the center of gravity, FM_x on the y axis, and FM_y on the x axis. F is the axial load, M_x is the moment in the x direction, M_y is the moment in the y direction, and L is the distance from the center of gravity where FM_x and FM_y are applied. Therefore,

$$M_x = FM_x(L) \quad [11]$$

$$M_y = FM_y(L) \quad [12]$$

$$F = FPA(L) - M_y + M_x \quad [13]$$

(SL-DEV-ED92-012 figure 3 page 10).

A sample test specimen of a FCP of actual flight hardware was used to correlate measured strain gage data with calculated strain values. No measurements were taken of the sample specimen. The strain values were calculated using the following formulas and SPAH B3-195.18 for minimum FCP gross cross section area, I_{x_0} , I_{y_0} , and $I_{x_0 y_0}$ values. Axial stress is

$$\sigma_a = \frac{F}{A} \quad [14]$$

where F is axial load and A is cross section area. Bending stress is

$$\sigma_b = \frac{M_x}{I_x I_y - I_{xy}^2} (I_{xy} X - I_y Y) + \frac{M_y}{I_x I_y - I_{xy}^2} (I_x X - I_{xy} Y) \quad [15]$$

(SPAH B3-195.12)

$$\sigma_{TOT} = \sigma_a + \sigma_b \quad [16]$$

To convert stress to strain: $\epsilon = \frac{\sigma_{TOT}(1-\nu^2)}{E}$ Adjustments of 0.03 inch had to be made in both the X₀ and Y₀ directions to get a good curve shape between the test data and the theory. When the measurements from SPAH B3-195.18 were used, the correlation on the 10,000 lb axial load was very good, but the moment values were off. After a study of the FBD, it was determined the moment was not equally applied over the length of the specimen as originally thought, but decayed in a triangular loading such that the moment at the strain gage locations was approximately .57% of the moment at the top. When this adjustment was made, the correlation between experiment data and theory was excellent (figure 3). Another problem was

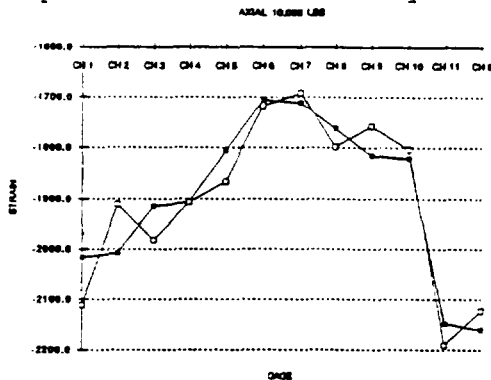


figure 3

the correlation of data at two of the channels. After examining the test specimen, it was discovered that these two channels were next to a bolt hole. This would cause the stress to be concentrated at a higher value (up to 35% more) at that location (Timoshenko, Str. of Mat. Part II page 304). A 10% adjustment in the theory values at these two channels brought them in line with the experimental data.

The testing will continue for some months more. The plans are to correlate the experimental data for the other test specimens using strain gages with the theoretical calculations. The experimental data for crippling values will then be compared with the theoretical crippling data. The goal of the tests is to be able to predict with some accuracy the crippling values of the rack posts.

REFERENCES

1. Spacelab Payload Accommodation Handbook, SLP/2104-2 Appendix B Structure Interface Definition NASA MSFC (1985)154-195.18
2. Spacelab Rack Corner Post Load Characterization Test and Checkout Procedure SL-DEV-ED92-012 (1992) Figure 3, page 10
3. Timoshenko, S., Strength of Materials Part II, third edition D. Van Nostrand Co. Inc., New York (1956) 304
4. TM-SEAD-85039A NASA Contract NAS8-32350, DR SE-12, WBS 4.2.21 (1986) A.3-21 - A.3.24

N 9 3 - 1 7 3 1 5

1992

NASA/ASEE SUMMER FACULTY FELLOWSHIP PROGRAM

MARSHALL SPACE FLIGHT CENTER
THE UNIVERSITY OF ALABAMA

A PROCESS FOR PROTOTYPING ONBOARD PAYLOAD DISPLAYS FOR
SPACE STATION FREEDOM

Prepared By: Loretta A. Moore, Ph.D.
Academic Rank: Assistant Professor
Institution and Department: Auburn University
Department of Computer Science and Engineering
NASA/MSFC:
Laboratory: Mission Operations
Division: Mission Engineering
Branch: Man/Systems Integration
MSFC Colleague: Joseph P. Hale

Introduction

Significant advances have been made in the area of Human-Computer Interface design. However, there is no well-defined process for going from user interface requirements to user interface design. Developing and designing a clear and consistent user interface for medium to large scale systems is a very challenging and complex task. The task becomes increasingly difficult when there is very little guidance and procedures on how the development process should flow from one stage to the next. Without a specific sequence of development steps each design becomes difficult to repeat, to evaluate, to improve, and to articulate to others.

This research contributes a process which identifies the phases of development and products produced as a result of each phase for a rapid prototyping process to be used to develop requirements for the onboard payload displays for *Space Station Freedom*. The functional components of a dynamic prototyping environment in which this process can be carried out is also discussed. Some of the central questions which are answered here include: How does one go from specifications to an actual prototype? How is a prototype evaluated? How is usability defined and thus measured? How do we use the information from evaluation in redesign of an interface? and Are there techniques which allow for convergence on a design?

Benefits of Rapid Prototyping

Rapid prototyping allows a designer to generate effective displays in a short amount of time, to experiment with different approaches to the interface, and to evaluate the displays with end users. Benefits of a prototyping process include the ability to keep development costs down and to maintain a consistent interface for the end user. Rapid prototyping keeps development costs down by iteratively refining the interface during the requirements definition phase, thus minimizing changes that will need to be made during and after flight code development. Rapid prototyping helps to maintain a consistent interface by allowing the designer use a User Interface Management System for the design of displays.

Rapid Prototyping Process

The prototyping process which has been proposed for onboard payload displays consists of five major phases: identification of known requirements, analysis of the requirements, development of a formal design representation and specification, development of the prototype, and evaluation of the prototype. Two additional phases, which are not a part of the prototyping process, are design of an implementation model and programming of the interface. The first five phases are discussed below.

Identify Known Requirements. During this phase the designer gathers all known requirements for the development of the payload displays. There are two categories of requirements. The first category is payload specific and the second category includes those requirements which contain information about the interface design. The list of requirements are as follows:

- Flight Human-Computer Interaction (HCI) Standards
- User Interface Requirements Document
- User Support Environment/Data Management System (USE/DMS) Capabilities/Constraints
- Payload System Capabilities/Constraints
- Functional Objectives
- Functional Flows
- Functional Requirements
- Operations Display Requirements
- Preliminary Procedures
- Displays and Controls Flight Systems Software Requirements (Level B D&C FSSR)

Integrate/Analyze the Requirements. The designer then integrates and analyzes the requirements of the system and ascertains the functions that are needed by the user. The products produced as output of this phase include an User-Centered Functional Analysis, a Task Analysis, an User Analysis, and Operational Flows. During the user-centered functional analysis a functional specification is derived. This specification should not only define the functions of the system and their inputs and outputs, but include human performance requirements for the functions allocated to humans. Human performance requirements should include statements concerning errors, performance speed, training time necessary to ensure the minimum skills,

and job satisfaction, at a minimum. Specific criteria for measuring these requirements should be developed in the next phase.

The goal of the task analysis is to identify what tasks are to be performed while considering the user and the system. The result is a set of specific tasks and concepts the operator will perform and manipulate with the aid of a computer. The task analysis breaks down and evaluates a human function in terms of the abilities, skills, knowledge, and attitudes required to perform these functions.

During the user analysis the designer must attempt to understand the user's mental activities or how the system being designed will influence the user's thoughts, that is, the user's views of a task and the user's view of the functionality and operation of the system. The designer should consider human cognitive processing, such as, limitations on short term memory or processing capability, and the user's model of the system. After analyzing the user the designer must be able to decide training requirements, what form of dialogue is most appropriate, and what level of support the user will require, both semantically and syntactically. The operational flows will specify the simulator requirements.

Develop Formal Design Representation/Specification. During this phase the designer should map concepts to formal representations and specifications. Two representations created should include a behavioral representation and a constructional representation. The behavioral representation is conveyed in the form of a storyboard. This is when a series of sketches (preliminary screen designs) depict the significant changes of actions which will take place during the interaction. It is a design of the appearance and behavior of the user interface. The human interface objects and their relationships augmented with preliminary sketches of screen graphics are depicted here. The constructional representation will consist of a state transition diagram. The state diagram developed at this phase can act as a generator for the system or a mockup to be evaluated. The human interface states with their transitions, triggering conditions for transitions, and side effects are shown here. The usability specification will contain specific measurable criteria for user performance and satisfaction. Convergence on an interface design is achieved by correcting components of the user interface that do not meet the usability specification.

Develop Rapid Prototype. The actual development of the prototype involves prototyping of the displays using the HCI prototyping tool, development of a low fidelity simulator, building of an interface between the displays and the simulator, integration of these components, and testing to ensure that the interface does what the designer expects.

In order to prototype the displays, the look and feel of the window(s) must be defined first. This includes answering questions such as: What will be the initial size and position for the window? What color should the background be? How will the final window work? Should it automatically page to other windows? Should there be help information? Should there be a scroll bar? Once the windows and their characteristics have been developed the types of data to be displayed in each window must be identified. For each dynamic data field the following questions must be answered: How should the dynamic field work? Should it provide online help, menus, pop-up option list, push buttons, or logging? How should the dynamic data be accessed and updated? Should the user be allowed to change the data? Should changes be confirmed and/or logged in an event file? How should the dynamic field look? What is the best way to display this data (e.g., integer, text, bar, gauge, meter, etc.). What should be its size and position in the format? What color should it be? What font should be used for text?

Once the designer has completed the analysis phase, and the content has been designed, the visual design can proceed. This involves determining the best screen layout, the grouping and structuring of information relevant to a task in blocks, the choice of terms and titles, which text symbols and graphics will be used, abbreviations and mnemonics, the distance between blocks, dividing lines, whether there will be left or right justification, design of lists and menus and their placement, and highlighting and labeling. There are guidelines to be followed for all of the areas discussed above. The disadvantage is that there are numerous and sometimes conflicting requirements. In the next section an expert system is proposed which will aid the designer by providing an online and user friendly way to access these guidelines so that they can be followed.

Evaluate Prototype. Evaluation provides a means of objectively assessing a design. It allows the designer/developer to verify user and system performance against requirements, to assess the performance of the User Interface dialogue, and provides data to the iterative design process. During the formal design representation and specification phase, the designer created a usability specification, after each evaluation iteration the user and system evaluation characteristics will be compared against pre-established criteria to determine the degree of correspondence. This allows convergence on a design, by correcting those components of the User Interface that do not meet the pre-established criteria.

During evaluation, the prototype will be shown to the principal investigators of the experiment and typical end users who will provide feedback to the designer and/or developer. The evaluation will consist of a static and dynamic evaluation component. Evaluation of the static displays will involve assessing the displays to determine whether or not they are in compliance with standards such as the Flight Human-Computer (HCI) standards. The dynamic component will consist of evaluation of the interaction between the user and the system.

Evaluation (of the Static Displays). Displays are currently measured against standards by manually inspecting the design and comparing it against what is contained in the requirements document. This process is time consuming and produces errors because of the large volume of requirement standards that exist. An Expert System for Evaluating Static Displays of the HCI is proposed which will evaluate the design, state any problems which are found, provide an explanation for the problem, and offer a suggestion on how to correct it. A good model is Tullis' Display Analysis Program [Tullis, 1988] which takes alphanumeric screen designs (no color, highlighting, separator lines, or graphics) and produces Tullis' display-complexity metrics plus some advice. The only problem with this program is that it only evaluates alphanumeric displays (no color, highlighting, separator lines, or graphics).

Evaluation (of the Human-Computer Interaction). Evaluation of the dynamic component should be accomplished by conducting usability studies. Given a functional prototype and some tasks that can be accomplished on that prototype, the designer should observe how users interact with the prototype to accomplish those tasks in order to identify improvements for the next design iteration. There are two problems that designers should be aware of when conducting these studies: the performance of the users is usually elevated under test conditions and problems created by the artificial environment of testing. Once the evaluation is complete the results should be measured against the pre-established usability criteria and the iteration should continue until there is a match between the output of the evaluation and the usability specification.

Measurable evaluation parameters should include: time to learn to use the system (i.e., training time measurement - how much time it takes to reach a particular level of proficiency), speed of task performance (or time to complete representative tasks), rates and types of errors by users, retention over time, and subjective satisfaction. The load demands of the work situation might also need to be assessed, as well as, whether or not there was effective operator planning. For example, whether or not the user carried out the operation, carried out the operation as efficiently as possible, used wrong commands, used too many keystrokes, or received several help and error messages. The system should also be evaluated to determine which features of the system were used or not used effectively. For example, the number of times a help or explanation screen was requested. This will give the designer or developer some indication of which features of the system should be enhanced and which should be eliminated. Analysis of the errors and types of errors encountered will assist in redesign of the screens and dynamic data objects.

There are several techniques proposed for the collection of this data. They include embedded evaluation techniques, observation, and subjective satisfaction measures. The embedded evaluation techniques includes a capture/playback component and an analysis component. The Capture features captures a user's session and saves this information to a log. This log can later be "played" back or analyzed. Simple reports such as the frequency of each error message, menu-item selection, dialog-box appearance, help invocation, form-field usage, etc., are of benefit in order to redesign the interface. Observation allows a designer to sit down with the users of the system, in order to monitor the interaction, and observe any problems that the user may encounter. This information is used for the next iteration. Subjective satisfaction measures a user's acceptance of a system. This can be done through the use of surveys, questionnaires, and interviews. Shneiderman [1992] developed the Questionnaire for User Interface Satisfaction (QUIS) as a generic user-evaluation questionnaire for interactive systems. This survey could be used in conjunction with an interview.

Interactive Prototyping Environment.

There is no current tool which allows for screen design, simulation, and evaluation. The most advanced tools for rapid prototyping which do not require programming experience are called UIMS (User Interface Management Systems). This term is used to describe software tools that enable designers to create a complete and working user interface without having to program in a traditional programming language. However, the users have to use a programming language to implement additional functions such as database search, network communication, or scientific computation. An environment is presented here which will allow for development, simulation, and evaluation of designs.

There are four components of the HCI prototyping environment: 1. HCI format development tool, 2. Test and evaluation simulator development tool, 3. Dynamic, interactive interface between the HCI prototype and simulator, and 4. Embedded capability to evaluate the adequacy of an HCI based on a user's performance. The HCI format development tool allows the designer to dynamically develop displays. The test and evaluation simulator development tool will allow the functionality of the system to be implemented and will act as a driver for the displays. The dynamic, interactive interface will handle communication between the HCI prototyping environment and the simulation environment. The embedded evaluation tool will perform the evaluation of the Human-Computer Interaction in terms of the measures discussed in the previous sections.

Conclusions

The process presented above provides a means of producing an efficient and effective prototype. Methodologies for gathering and refining operations and end user requirements, approaches to display design, and measures and methods for evaluating designs were presented. An architecture which will enable this process to be carried out was also presented.

References

- Bass, Len and Coutaz, Joelle (1991). *Developing Software for the User Interface*. Reading, Massachusetts: Addison-Wesley Publishing Company.
- Karat, John (Ed.) (1991). *Taking Software Design Seriously: Practical Techniques for Human-Computer Interaction Design*. Boston, MA: Academic Press.
- Shneiderman, Ben. (1992). *Designing the User Interface: Strategies for Effective Human-Computer Interaction (Second Edition)*. Reading, Massachusetts: Addison-Wesley Publishing Company.
- Tullis, T. S. (1988). *Screen Design*. In Helander, Martin (Editor), *Handbook of Human-Computer Interaction* (pp. 377-411), Amsterdam, The Netherlands: Elsevier Science Publishers.

1992

NASA/ASEE SUMMER FACULTY FELLOWSHIP PROGRAM

**MARSHALL SPACE FLIGHT CENTER
THE UNIVERSITY OF ALABAMA**

**DEVELOPMENT OF VENDOR EVALUATION CRITERIA AND
POST-IMPLEMENTATION CONSIDERATIONS FOR
MSFC CENTER-WIDE EXECUTIVE INFORMATION SYSTEM**

Prepared By: Gary P. Moynihan, Ph.D.
Academic Rank: Assistant Professor
Institution and Department: The University of Alabama,
Department of Industrial Engineering
NASA/MSFC:
Office: Information Systems
Division: Systems Engineering and Integration
MSFC Colleague: Alan Forney

In June 1991, the MITRE Corporation submitted a series of recommendations as part of a Marshall Space Flight Center (MSFC) Management Information System Requirements Study, initiated by the Information Systems Office (ISO). A major recommendation of the study was to initiate the development of an Executive Information System (EIS) for MSFC executives. (2) ISO was directed, by center management, to proceed with the development of a Center-Wide Executive Information System. Existing EIS prototypes, developed by the Space Shuttle Projects Office and the Payload Projects Office, were reviewed. These existing MSFC prototypes were considered not to encompass the required functionality needed on a center-wide basis. A follow-up study by MITRE provided top-level system requirements. (4) These were later incorporated into a final requirements specification document by Boeing Computer Support Services. (1)

Another MITRE study addressed the issue of whether to develop the Center-Wide EIS solely using in-house personnel and resources, or the purchase a Commercial Off-The-Shelf (COTS) product. (3). This second alternative was subsequently recommended and accepted by senior center management. A Request For Information (RFI), identifying system requirements, was then published in Commerce Business Daily. Vendor responses to the RFI were then reviewed. It was decided that the expertise of an "8A" contractor (designating a small, disadvantaged firm) would be utilized to evaluate the COTS products under consideration. The appropriate COTS product would then be purchased. The evaluation criteria, developed during this research, are intended to be used as a guide for software selection by the 8A contractor.

An Executive Information System is a computer system designed to support the informational needs of very senior executives. It is intended to provide timely, pertinent information to aid in decision-making, thereby eliminating the need to sift through lengthy reports. The concept of EIS is a relatively recent phenomenon. It was only in 1982 that Rockart and Treacy introduced the term to describe this emerging category of information systems. (7) An EIS may be defined as having the following characteristics:

1. An easy to use and maintainable graphical user interface.
2. Integrated capabilities for data access, security and control.
3. On-request "drill-down" capability to lower levels of detail.
4. Depiction of organizational health indicators.
5. Functionality for decision support, ad-hoc queries and what-if analysis.
6. Sophisticated tools for navigation.
7. Data analysis features.
8. Advanced report generation.
9. Statistical analysis.
10. Access to a variety of external data sources.

EIS may be considered to be a subset of a broader group known as Management Information Systems (MIS). A variety of techniques have been developed to support evaluation of MIS proposals. Relevant published literature on this subject was reviewed, and various methodologies were investigated for their applicability. A weighted scoring technique was selected for the overall evaluation technique. It is considered to be a widely accepted technique by procurement agencies for evaluating "multiple proposals with varying prices and capabilities. (5) The scoring technique focuses on a listing of desired functional characteristics. Weights are assigned to each characteristic based on its perceived desirability. A composite score is then generated. The scoring technique was viewed as a means of fairly prioritizing MSFC requirements and quantifying the resulting vendor responses. It was also considered to be an effective means of countering any potential vendor protest.

The evaluation process analyzes the vendor product alternatives from three perspectives: technical, cost and risk. The overall strategy for the evaluation is to eliminate any vendor alternative that cannot effectively meet the technical requirements. Cost and risk factors are considered only after all alternatives have been functionally reviewed. The composite scores for the technical, cost and risk analyses will be

factored and combined as identified in Equation 1, for any alternative that is deemed functionally acceptable:

$$\text{TOTAL SCORE} = \text{TECHNICAL EVALUATION (50\%)} + \text{COST EVALUATION (30\%)} + \text{RISK EVALUATION (20\%)} \quad [1]$$

The vendor alternative with the highest resulting score will then be purchased by the 8A contractor.

The initial phase of the evaluation process utilizes three types of factors that are applied to each functional line item: requirements qualifier, weighting factor and scoring factor. Technical evaluation criteria were obtained primarily from the requirements specifications documents. (1, 4) Each of the technical criteria have been qualified as to whether they are considered to be mandatory or highly desirable. The scoring factors vary with each designation. Each mandatory line item requires a specific response from the vendor. If a mandatory requirement is not bid by the vendor, it could cause for disqualification. If a highly desirable requirement is not bid, it is not cause for disqualification, however a penalty is assessed via the scoring system for the absence of this functional capability. The weighting factor indicates the relative importance among the requirements. The weighting factors range from 1 (low) to 10 (high). The scoring factor is used to rate each vendor's response. The scoring factors are assigned relative to the following guidelines:

<u>Requirement Qualifier</u>	<u>M</u>	<u>H</u>
Have Capability Now	+1	+1
No Bid	- 3	-1

The product of the scoring factor and the respective weighting factor for each line item is accumulated into the overall technical score for the vendor's proposal.

A series of forms were created in order to document the acceptability of the vendor product functionality, and to thus substantiate the overall technical evaluation. These consisted of a System Test Execution Log, Test Case Form, and a Problem Identification Form. The System Test Execution Log provides a summary of the individual test cases. The Test Case Form provides a standard format for documenting the original evaluation. For each line item requirement of the EIS Technical Evaluation Worksheet, a separate test case is conducted. Upon rejection of a test, a problem identification form is completed. The form provides documentation of system inadequacies.

The cost analysis phase of the evaluation considers not only the price of the individual EIS software package itself, but of additional supporting hardware, annual licensing fees and operational transaction costs. These factors are combined in order to create a total systems cost. The Cost Analysis Summary Worksheet depicts the highest level of detail. Backup should be provided in order to indicate the pricing components of each major category.

The final component of the evaluation involves assigning a confidence factor to each vendor/product. A risk assessment worksheet is used to factor each vendor's response to the RFI. The higher the rating, the higher the perceived credibility. Each vendor's offering is evaluated based on the following general criteria: functionality, compatibility (with existing hardware, software and communications), installation, documentation, total systems cost, and vendor service. Similar to the technical evaluation, the product of the weighting and scoring factors is used to establish a risk assessment score.

Draft versions of analysis worksheets, test case forms and all criteria developed as part of this research, were submitted to personnel from the MSFC Information Systems Office and Boeing Computer

Support Services, for review and comment. Subsequent recommendations for modification were incorporated into the final report to the client.

One of the major barriers to the success of Executive Information Systems has been a failure to consider post-implementation factors regarding these systems. For more traditional information systems applications (e.g. transactions processing, decision support systems), post-implementation issues have been recognized based on years of experience and much trial and error. Unfortunately this experience frequently can not be transferred directly to the EIS environment. "The fragmented nature of executive work, the high degree of environmental uncertainty at this level in the organization, and the political ramifications of providing top management with more and better information, as well as other factors, make implementing (EIS) a special challenge." (6) The subsequent analysis focuses on some critical factors that should be considered following the implementation of the Center-Wide Executive Information System at MSFC.

A post-implementation evaluation of the system should be conducted. This phase consists of two major components: the Development Recap and the Post-Implementation Review. The Development Recap provides an in-depth review of the EIS development activities that have just been completed. Analyses of cost and schedule variances are conducted as part of this recap. It should also identify describe and classify programming errors; suggest any needed revisions to the development methodology used; and provide any other relevant suggestions or insights. The Post-Implementation Review is performed four to six months after the system has been installed. The purpose of the review is to evaluate how well the EIS has performed in meeting the original expectations and projections. It is also intended to identify any further maintenance projects that should be undertaken to enhance or improve the implemented EIS.

The value of any information system depends on the quality of its data; its timeliness, accessibility, accuracy and completeness. This is particularly true of Executive Information Systems. By attempting to provide high-quality data and information, an EIS may often highlight existing data management problems, while at the same time creating new ones. Analysis of the existing MSFC data environment identified a series of issues regarding data availability, ownership, integrity, infrastructure, integration and management. Detailed recommendations were formulated regarding each of these areas.

The primary emphasis of the early post-implementation phase is to isolate and correct any system errors as soon as possible. A series of recommended procedures were suggested regarding this issue. The same overall process is used to address enhancements to the system. These enhancements should be compiled and evaluated after the primary fixes have been made. Because the executive user is particularly sensitive to changes in response time, the implications of any enhancement on this must be carefully considered. It is also important to emphasize that any changes involving the data sources must be communicated to the EIS maintenance group in order to avoid system malfunction. Current procedures regarding information system change control, configuration control, and version control were reviewed and found both adequate and applicable to the EIS.

Consideration should be given to planning the post-implementation migration and evolution of the system. The EIS is likely to spread to additional users. The migration may be both hierarchical and lateral. With hierarchical migration, use of the EIS spreads from the top down in an organization. In lateral migration, use of the EIS moves across organizational units. The system is also likely to evolve to include information that is broader in scope, more detailed and closer to real time. The most effective method of EIS migration appears to utilize a strategic approach. The system is progressively made available to those executives where the need and expected return is the greatest.

Construction of the Center-Wide EIS implies the need for a security system that will control access to sensitive information (e.g. Privacy Act information, long-range plans). In addition to prohibiting

access to the system by unauthorized personnel, the security system must be multi-level in nature, in order to be able to control access within a variety of classifications. According to the literature, there is a wide divergence of strategies in addressing this problem. Aerospace companies tend to use a multi-level security system utilizing the capabilities of the EIS application development software. An alternate approach utilizes a multi-level database to support data having different classifications and users having different clearances. Current plans for the MSFC EIS employ this last approach which is resident in the ORACLE source database. An ORACLE table will be used to identify user access privileges. This table will act in conjunction with queries associated with programmed SELECT statements on an individual field level. This planned security mechanism appears to satisfy the applicable NASA security requirements. Executives will want access to the EIS from remote sites. Security on dial-up access lines should be considered as a priority post-implementation system enhancement. The security system should also be as transparent as possible to the executive user. Multiple levels of passwords should be avoided. Most senior managers prefer "one-button" access to their systems. In the EIS this would be analogous to the WPS (Workstation Presentation Services) password synchronization feature that is currently used.

In order to support the construction of an effective Executive Information System, this research has provided a quantitative method for assessing commercial off-the-shelf EIS development software. An analysis was also conducted which identified important post-implementation considerations. The final judgment concerning the effectiveness of the center-wide EIS will be determined largely by the executive user's expectations and their perceptions of the system's ability to meet their particular support requirements. This highlights the need to obtain agreement from the user community on a clear set of metrics for determining system effectiveness, prior to actual system implementation.

REFERENCES

1. Boeing Computer Support Services, "Final Requirements Specifications for an Enterprise-wide Executive Information System Application Development Environment and Decision Support Tool Set" (prepared for Marshall Space Flight Center) March 18, 1992.
2. MITRE Corp. "Marshall Space Flight Center Management Information System Requirements Study", June 1991, Contract No. NAS9-18057.
3. MITRE Corp. "MSFC Executive Information System Make Versus Buy Analysis Details", March 1992, Contract No. NAS9-18057.
4. MITRE Corp. "Marshall Space Flight Center Executive Information System Requirements Specification", April 1992, Contract NAS9-18057.
5. Powers, Michael J., Adams, David R. and Mills, Harlan D., Computer Information Systems Development: Analysis and Design, Cincinnati: South-Western Publishing Co., 1984.
6. Rockart, John F. and Bullen, Christine V., The Rise of Managerial Computing, Homewood, IL: Dow Jones - Irwin, 1986.
7. Rockart, J.F. and Treacy, M.E., "The CEO Goes On-Line", Harvard Business Review, Vol. 60, No. 1, January - February 1982, pp. 84 - 88.

1992

NASA/ASEE SUMMER FACULTY FELLOWSHIP PROGRAM

MARSHALL SPACE FLIGHT CENTER
THE UNIVERSITY OF ALABAMA

ON THE CONSEQUENCES OF BI-MAXWELLIAN
PLASMA DISTRIBUTIONS FOR PARALLEL ELECTRIC FIELDS

Prepared By: Richard C. Olsen, Ph.D.
Academic Rank: Associate Professor
Institution and Department: Naval Postgraduate School
Department of Physics
NASA/MSFC:
Office: Space Science Laboratory
Division: Solar Terrestrial Division
Branch: Magnetospheric Physics Branch
MSFC Colleagues: Thomas Moore, Ph.D.
Scott Boardsen, NASA/NRC

Plasma observations near the earth's magnetic equator in the outer plasmasphere indicate the presence of core plasma distributions which are often highly anisotropic. The core ion distributions are often 'pancake' like, that is, with enhanced fluxes at 90° pitch angle. These distributions can be modeled with reasonable success as bi-Maxwellian distributions, with perpendicular temperatures as much as an order of magnitude greater than the parallel temperatures. (2)

The anisotropy of the electron distributions will, in general, differ from that found in the ions. In equilibrium, this immediately leads to a requirement for a parallel electric field to maintain charge neutrality. (1) The purpose of the work described here is to investigate the nature of the electric field which is implied by the equatorial measurements of the equatorial plasma measurements near the plasmopause, and the consequences of this electric field for the evolution of the plasma distribution along the field line. The variations in density and perpendicular temperature predicted by kinetic theory will be compared to observations.

Trapped ion (and electron) distributions have been reported for a number of years from the outer plasmasphere, particularly near geosynchronous orbit. Such pitch angle distributions are also typically termed 'pancake' distributions. Data from the electrostatic analyzers on SCATHA showed such trapped distributions, and it was found that the ion (and electron) observations obtained near the magnetic equator, from L ~5.5 to 7, could be described as bi-Maxwellians (2). Ion temperatures of 0.6-0.8 eV were found in the parallel direction, and ~25 eV in the perpendicular direction. (4)

The polar orbiting Dynamics Explorer 1 (DE-1) satellite with provided orbital coverage of the outer plasmasphere which included orbit segments of nearly constant "L", particularly near apogee, at L = 4.5. DE-1 measurements by the Retarding Ion Mass Spectrometer showed that the equatorially trapped plasma was primarily hydrogen ions, and provided latitudinal profiles which clearly showed the trapped nature of these ion distributions. (3)

The DE-1 ion measurements can also be fitted with bi-Maxwellian distributions. Such modeling requires careful consideration of the detector response, with integration in energy and angle. The fitting process uses a model detector response, with the ability to specify an arbitrary ambient distribution function. Fitting data obtained on 5 January 1984, obtained at L = 4.6, 1600 MLT, during a reasonably typical equator crossing, gave the fit parameters: $n = 18 / \text{cm}^3$, $T_{\text{para}} = 2 \text{ eV}$, $T_{\text{perp}} = 33 \text{ eV}$, assuming a spacecraft

potential of +3 V. The density and perpendicular temperature are considered fairly accurate, but there are some indications that the parallel temperature seems is a bit high.

Our objective is to use the measurements of the equatorial particle distributions to obtain the parallel electric field structure and the evolution of the plasma distribution function along the field line. Appropriate use of kinetic theory allows us to use the measured (and inferred) particle distributions to obtain the electric field, and hence the variation in plasma density along the magnetic field line. The approach, here, is to utilize the adiabatic invariants, and assume the plasma distributions are in equilibrium.

Swann set the basis for this work by showing how, in a collisionless plasma, the distribution function remains invariant for motion along a magnetic field line. (5) A useful formalism for studying the problem, is to make use of the invariance of the total energy, and the first adiabatic invariant, μ . (6) If quasi-neutrality is invoked, it is possible to obtain an expression for the electric field. These integrals are relatively straightforward for bi-Maxwellian distributions.

The results of such analysis are that that the distribution function remains the shape of a bi-Maxwellian, even in the presence of a parallel electric field. The parallel temperature remains constant, while the perpendicular temperature drops. The reduced perpendicular temperature is:

$$kT_{\perp\lambda} = \frac{kT_{\perp 0}}{kT_{\perp 0}/kT_{\parallel} + B_0/B_{\lambda}(1 - kT_{\perp 0}/kT_{\parallel})} \quad [1]$$

The new perpendicular temperature is a simple scalar function of the equatorial temperatures, and the change in magnetic field strength. Note that T_{\perp} will approach T_{\parallel} as latitude increases.

The density can be obtained, as well, as a function of the magnetic latitude, and the parallel electric field established by the charge neutrality requirement of the plasma.

$$n_{\lambda} = n_0 (kT_{\perp\lambda}/kT_{\perp 0}) \exp(-q\phi/kT_{\parallel}) \quad [2]$$

The familiar Boltzmann factor appears, along with the temperature ratio, determined in equation 1.

The potential can be obtained by setting the electron and ion densities equal to one another. This requires a specification of the electron and ion distribution. The electric field implied by the SCATHA data described above, and the DE-1 data shown here was evaluated, and found to be ~ 0.1 $\mu\text{V/m}$. The effect on the plasma density is to retard the drop in ion density implied by the local mirroring of the trapped ions.

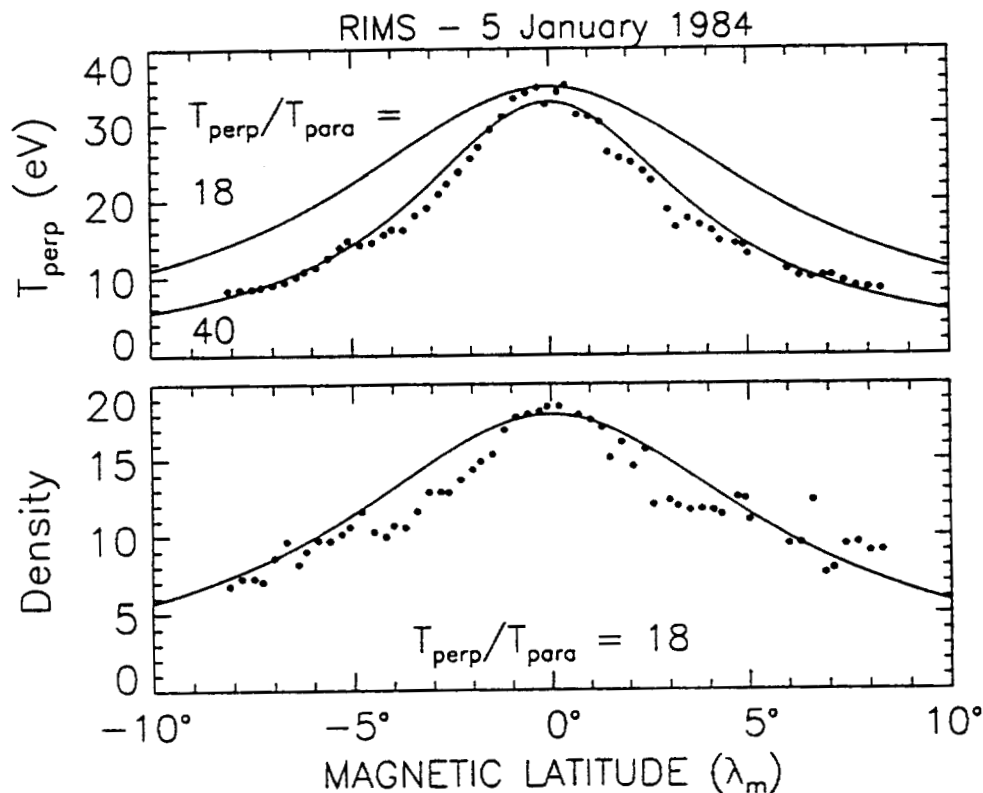
The variation in temperature and density with latitude can be compared with measurements from DE-1. Figure 1 shows how the ion plasma parameters vary with latitude, and compares them to the model. The data analysis showed a drop from ~ 30 eV perpendicular temperature to ~ 10 eV in less than 10° travel away from the equator. The parallel temperature remained constant at ~ 2 eV.

The fitted temperatures and density are overlaid with the curves determined solely by the equatorial measurements. The $T_{\text{perp}}/T_{\text{parallel}}$ ratio of 18 is the value generated by the model; a ratio of 40 appears to more closely match the variation in ion temperature. Note that this aspect of the model does not depend on the electron characteristics (and by implication, the electric field), or on the effects of an isotropic background - only on the temperature ratio at the equator. This comparison of model and data suggests that the parallel ion temperature is closer to ~ 0.8 eV, close to the value found with SCATHA, and a much more typical value for the isotropic plasma of the outer plasmasphere.

The density decrease expected in the absence of an electric field is overlaid on the ion density estimate. It describes the variation in density of the trapped plasma reasonably well - the effects of the electric field are fairly modest close to the equator. The simple kinetic model for the variation in a bi-Maxwellian ion distribution gives a remarkably good agreement with the latitudinal profiles of temperature and density, for this case where there is a maximum in density at the magnetic equator.

The plasma distributions found in the outer plasmasphere can often be described as bi-Maxwellian distributions, at least for the core of the distribution. Specification of the full distribution function at the equator allowed us to develop a kinetic model for the variation in the ion temperature and density with latitude. Comparison of the model with DE data shows that for an isotropic electron background, there will be a local maximum in density at the equator, which is reasonably well described by the model. The potential drop in the equatorial region is only 1-2 V, since the parallel ion temperature is relatively low. Still, such potentials may be adequate to explain the apparent repulsion of low-energy field-aligned ion beams from the equatorial region.

1. Alfvén, H., and C.-G. Fälthammer, *Cosmical Electrodynamics, Fundamental Principles*, p 164, Clarendon, Oxford, 1963.
2. Olsen, R. C., Equatorially trapped plasma populations, *J. Geophys. Res.*, *86*, 11235-11245, 1981.
3. Olsen, R. C. S. D. Shawhan, D. L. Gallagher, J. L. Green, and C. R. Chappell, Plasma observations at the earth's magnetic equator, *J. Geophys. Res.*, *92*, 2385-2407, 1987.
4. Scott, Lewis J., On the consequences of bi-Maxwellian distributions on parallel electric fields, M. S. thesis, Naval Postgraduate School, Monterey, CA, December 1991.
5. Swann, W. F. G., Application of Liouville's theorem to electron orbits in the Earth's magnetic field, *Phys. Rev.*, *44*, 224-227, 1933.
6. Whipple, E. C., The signature of parallel electric fields in a collisionless plasma, *J. Geophys. Res.*, *82*, 1525-1530, 1977.



1992

NASA/ASEE SUMMER FACULTY FELLOWSHIP PROGRAM

MARSHALL SPACE FLIGHT CENTER
THE UNIVERSITY OF ALABAMA

SIMULATION OF CRYOGENIC TURBOPUMP ANNULAR SEALS

Prepared By: Alan B. Palazzolo, Ph.D.

Academic Rank: Associate Professor

Institution and
Department: Texas A&M University
Mechanical Engineering Department

NASA/MSFC:

Office: Structures and Dynamics
Division: Control Systems Division
Branch: Mechanical Systems Control

MSFC Colleague(s): Donald P. Vallely
Steve Ryan
J. Mark Darden

The works of Black(1), von Pragenau(5), Childs(2), and later San Andres(4), have clearly demonstrated the potential that annular seals have for affecting the rotordynamic behavior of pumps. The goal of the current work is to develop software that can accurately predict the dynamic coefficients, forces, leakage and horsepower loss for this type of seal. The fruit of last year's research was the computer code SEALPAL which included capabilities for linear tapered geometry, Moody friction factor and inlet pre-swirl. This code produced results which in most cases compared very well with check cases presented in the literature.

Satya Padavala joined this effort in March 1992 and quickly wrote the code TAMUSEAL I. That code improved SEALPAL by correcting a bug and by adding more accurate integration algorithms and additional capabilities: Moody's and Hir's friction model, and Arbitrary Axial Profile. The reliability of these new features was confirmed by "Hir's", "Wavy Seal" and "Partially Tapered" check cases from the literature, and was reported in;

"Dynamic Coefficients for Incompressible Liquid Annular Seals Including Either Moody's or Hir's Friction Models and Arbitrary Axial Profile," by Palazzolo, A.B. and Padavala, S., June 1992, MSFC Report.

The TAMUSEAL 1 code was then used to predict dynamic coefficients and leakage for the NASA/Pratt and Whitney Alternate Turbopump Development (ATD) LOX Pump's damper seal. The units studied (3-1, 4-1D, 6-1D and 3-1A) had damper seals with converging/diverging axial taper and were modeled with both Hir's and Moody's friction factors. The results showed that the Moody model produced lower stiffnesses than the Hir's, but the difference was small except for extremely divergent seals (4-1D). The results of this study were presented in;

"Simulation Results for Hirs and Moody Models of ATD Units 3-1, 4-1D, 6-1D and 3-1A," by Palazzolo, A., Padavala, S. and Rachamadugu, S., July 13, 1992, MSFC Report.

The theory for eccentric seals was developed during this period following Nguyen and Nelson's(3) work. These authors had employed a Fourier series interpolation in order to implicitly separate out the angular variable from the axial variable, converting the governing steady state partial differential equations (P.D.E.) to ordinary differential equations (O.D.E.). The Fourier interpolation was replaced with a spline based interpolation and the latter approach was significantly more efficient and yielded higher convergence reliability, especially for very eccentric seals. The equations were programmed into

the enhanced code TAMUSEAL II, following an intense derivation verification.

The eccentric capabilities of the TAMUSEAL II code was applied to analyzing the ATD Build 3-1 at 65%, 100% and 115% RPL. The code was run in the prescribed preload mode so that its results yielded the eccentric location of the shaft in the seal due to increasing load along the anticipated side load direction of 290 degrees. The results showed significant changes in most of the dynamic coefficients for side loads greater than 400 lbs. (eccentricity greater than 0.3). A complete summary of results for this study may be found in;

"Results From Study of Eccentric Seal Analysis of ATD Unit 3-1 at 65%, 100% and 115% Power Levels," by Palazzolo, A.B. and Padavala, S., MSFC Report, July 15, 1992.

The capabilities of TAMUSEAL II were next expanded to include variable circumferential profile. This option resulted from the need presented by predicted distortions of the ATD seal obtained from MSFC/Sverdrup finite element results of the entire casing. The following report includes results from a variable circumferential profile simulation of ATD LOX pump unit 3-1 at 115% RPL;

"Simulation of Annular Seals for Cryogenic Turbopumps Including Effects of Arbitrary Profile in the Circumferential and Axial Directions, Eccentricity, Preload an Moody and Hirs Friction Factors," by Palazzolo, A., and Padavala, S., MSFC Report, August 11, 1992.

This report also contains an extensive theoretical manual for TAMUSEAL II, several verification cases for eccentric seals and a complete user's manual for TAMUSEAL II.

Specific conclusions drawn from this work include the following:

TAMUSEAL II results are in good agreement with simulation and test results presented in the literature (see Figure 1)

Eccentricities above approximately 0.4 may have a very significant affect on all dynamic coefficients (see Figure 2)

Variable profile and choice of friction factor models may significantly influence dynamic coefficients, especially at high divergence or eccentricity.

Future work in this area includes variable fluid properties, thermal-elasto-hydrodynamic modeling, transient force determination and friction factor testing.

ACKNOWLEDGEMENTS

The author gratefully acknowledges the technical assistance provided by Donald P. Vallely, Dr. Steve Ryan, J. Mark Darden, Kerry Funston, Eric Earhart, William Walker, Norman Batson and Charles (Chip) Franck of MSFC.

REFERENCES

1. Black, H.F., and Murray, J.L., "The Hydrostatic and Hybrid Bearing Properties of Annular Pressure Seals in Centrifugal Pumps," The British Hydromechanics Research Association (BHRA), October 1969.
2. Childs, D., "Finite Length Solutions for the Rotordynamic Coefficients of Constant Clearance and Convergent-Tapered Annular Seals," IMECH Conference Publication No. C276/84, 1984.
3. Nguyen, D.T., "Analysis of Eccentric Annular Pressure Seals," Ph.D. Dissertation, Texas A&M, May 1988.
4. San Andres, L., et. al, "Thermohydrodynamic Analysis of Cryogenic Liquid Annular Seals," Earth to Orbit Propulsion Conference, MSFC, 1992.
5. von Pragenau, G.L., "Damping Seals for Turbomachinery," NASA TP 1987, 1982.

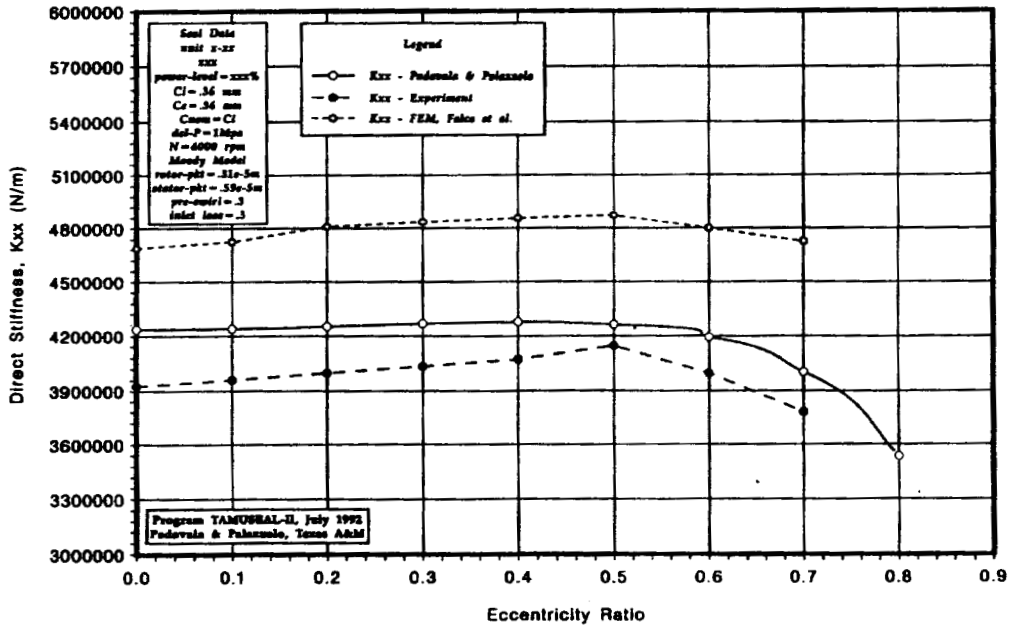


Figure 1 Direct Stiffness vs. Eccentricity Ratio-Comparison Between Methods

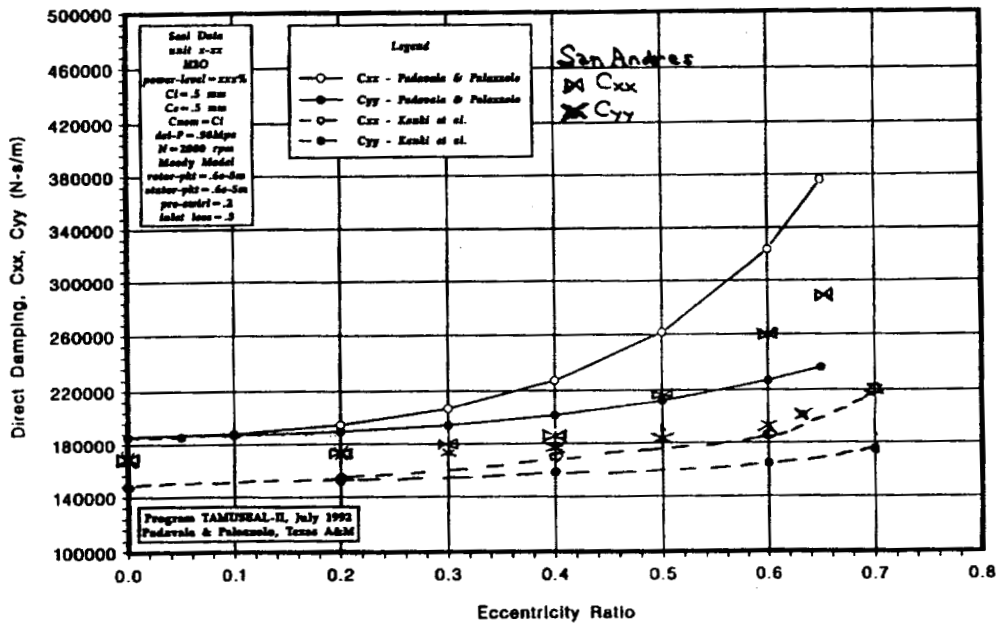


Figure 2 Effects of Eccentricity Ratio on Direct Damping

N 9 3 - 1 7 3 1 9

1992

NASA/ASEE SUMMER FACULTY FELLOWSHIP PROGRAM

MARSHALL SPACE FLIGHT CENTER
THE UNIVERSITY OF ALABAMA

THE KAPPA DISTRIBUTION AS A VARIATIONAL SOLUTION FOR AN
INFINITE PLASMA

Prepared By:

Michael J. Pangia, Ph.D.

Academic Rank:

Assistant Professor

Institution and Department:

Georgia Southwestern College
Department of Geology and Physics

NASA/MSFC:

Office:
Division:
Branch:

Space Science Laboratory
Solar-Terrestrial Physics
Magnetospheric Physics

MSFC Colleagues:

Dennis L. Gallagher, Ph.D.
Craig J. Pollock, Ph.D.
Thomas E. Moore, Ph.D.

The basis for this research is the 1991 Summer Faculty Fellowship work by the present author. In review, *Pangia* [1992] postulated that the preferred state of a single component infinite plasma is the one that will change the least when perturbed. The plasma distribution of such a state would maximize the plasma wave damping rate, or, minimizing γ where negative γ is the damping rate. This explained the tendency for low values of κ , when fitting plasma distributions to a κ -distribution, which is

$$\frac{A_\kappa}{(1 + v^2/(2\kappa v_\kappa^2))^\kappa} \quad [1]$$

where A_κ and v_κ are the overall normalization factor and thermal speed parameter, respectively. A more compelling question is why a κ -distribution works so well in fitting both electron and ion distributions. *Hasegawa et al.* [1985] derived that the electron distribution subject to a superthermal radiation field is given by [1], but that the ion distribution is Maxwellian for speeds less than the electron thermal speed. It is also desirable to calculate κ , which is not readily doable from the result of *Hasegawa et al.* [1985]. The present study continues from the ideas developed by *Pangia* [1991] to determine what distribution function maximizes the damping rate. A κ -distribution will be the outcome for either electrons or ions, with κ tending toward 3/2.

It is necessary to extend the work of the author to include the general case of a multi-component plasma. For the sake of completeness, this presentation will reproduce also the arguments of the previous work. For a 1-dimensional, collisionless plasma with electrostatic field, $E(t,x)$, the Vlasov and Maxwell equations are

$$\frac{\partial f_s}{\partial t} + v \frac{\partial f_s}{\partial x} + \frac{q_s}{m_s} E \frac{\partial f_s}{\partial v} = 0 \quad [2]$$

$$\frac{\partial E}{\partial x} = \sum_s 4\pi q_s \int_{-\infty}^{\infty} dv f_s \quad [3]$$

$$\frac{\partial E}{\partial t} = - \sum_s 4\pi q_s \int_{-\infty}^{\infty} dv v f_s \quad [4]$$

where $f_s(t,x,v)$ is the reduced distribution function for particles of type s . In use is the normalization that the number of particles of type s that are between x and $x+dx$ with velocities ranging from v to $v+dv$ is $f_s dx dv$. Particles of type s have charge q_s and mass m_s .

In the absence of any external field, the steady state solution to the Vlasov-Maxwell equations is $f_s = F_s(v)$ and $E = 0$, where F_s is any positive function normalized to the number density. One might then infer that, in equilibrium, a plasma distribution is virtually likely to be anything. However, the response of the plasma to a perturbation from equilibrium will greatly depend on the function $F_s(v)$. Since plasmas evolve to equilibrium under the influence of plasma waves, a particular steady state could be favored over all the others based on its response to a perturbation. In an actual plasma, waves are usually present, indicating some sort of evolution of the distribution function. Although equilibrium may never be fully obtained, the plasma should be at least tending toward it. Changes in the background distribution function should diminish as equilibrium is approached. Change can possibly be used as the criterion for identifying the preferred steady state of a plasma, because a steady state that appreciably changes after having been perturbed is expected to evolve to a different steady state which is more stationary. Therefore, it will be postulated that the plasma will tend toward the steady state which changes the least when perturbed from equilibrium.

Since the steady state distribution in a plasma where external forces are absent is spatially uniform, each distribution function will be expressed as a sum of a spatially uniform part, $f_s(t,v)$, and the deviation from uniformity, $f'_s(t,x,v)$, with a similar expression for the electric field

$$f_s(t,x,v) = f_s(t,v) + f'_s(t,x,v) \quad [5]$$

$$E(t,x) = E(t) + E'(t,x) \quad [6]$$

The uniform electric field, $E(t)$, may be zero, but, in general, it will exist if a zero wave number mode is part of the perturbation or if it develops in time. A spatial average over all space will be used to formally define the uniform part of any function $Y(x)$; namely,

$$\langle Y \rangle_x = \lim_{L \rightarrow \infty} \int_{-L}^L \frac{dx}{2L} Y(x) \quad [7]$$

The subscript x on the angular bracket is used to identify it as a spatial average. In regard to [5] and [6], $f_s(t, v) = \langle f_s(t, x, v) \rangle_x$ and $E(t) = \langle E(t, x) \rangle_x$. Taking the spatial average, [2] through [4] become

$$\frac{\partial}{\partial t} f_s(t, v) + \frac{q_s}{m_s} \frac{\partial}{\partial v} \left\{ E(t) f_s(t, v) + \langle E' f'_s \rangle_x \right\} = 0 \quad [8]$$

$$0 = \sum_s 4\pi q_s \int_{-\infty}^{\infty} dv f_s(t, v) \quad [9]$$

$$\frac{d}{dt} E(t) = - \sum_s 4\pi q_s \int_{-\infty}^{\infty} dv v f_s(t, v) \quad [10]$$

Subtracting [8] through [10] from [2] through [4], respectively, gives

$$\frac{\partial f'_s}{\partial t} + v \frac{\partial f'_s}{\partial x} + \frac{q_s}{m_s} \frac{\partial}{\partial v} \left\{ E(t) f'_s + E' f_s(t, v) + E' f'_s - \langle E' f'_s \rangle_x \right\} = 0 \quad [11]$$

$$\frac{\partial E'}{\partial x} = \sum_s 4\pi q_s \int_{-\infty}^{\infty} dv f'_s \quad [12]$$

$$\frac{\partial E'}{\partial t} = - \sum_s 4\pi q_s \int_{-\infty}^{\infty} dv v f'_s \quad [13]$$

Equations [8] through [13] are basically the starting equations for quasi-linear theory [see for example, Swanson, 1989], just extended to include a uniform electric field. Derivable from [8] through [13] are the conservation laws for the system, which are written

$$\frac{d}{dt} \int_{-\infty}^{\infty} dv f_s(t, v) = 0 \quad [14]$$

$$\frac{d}{dt} \sum_s m_s \int_{-\infty}^{\infty} dv v f_s(t, v) = 0 \quad [15]$$

$$\frac{d}{dt} \left(\sum_s m_s \int_{-\infty}^{\infty} dv v^2 f_s(t, v) + \frac{1}{4\pi} E^2(t) + \frac{1}{4\pi} \langle E'^2 \rangle_x \right) = 0 \quad [16]$$

Due to the quadratic non-linearity present in the Vlasov equation, an additional simplifying assumption will be made in order to derive a result. Having perturbed a system from equilibrium, it will be assumed that, eventually in its evolution, the predominant wave modes that remain are $k=0$ and k nearly zero, where k is the wave number, all other modes having been depleted. This assumption is made even if an instability exists for some particular range of modes. The rationale is that non-linear effects will channel wave energy to other modes,

most of which damp away. To understand the basic effect of the quadratic non-linearity, consider the spatial dependence of any mode k at some time t . It will have the basic form $e^{ikx} \pm e^{-ikx}$. The product of two modes, k_1 and k_2 , will result in modes $k_1 + k_2$, and $k_1 - k_2$. In particular, if $k_1 = k_2$, there will be mode conversion to $2k_1$ and 0 , and if k_1 and k_2 are nearly equal, the nearly zero wave mode will result. If k_1 is unstable, the process will convert it to stable modes. Modes that find their way to the instability will have been damped beforehand, amplified during the instability, and, finally, converted back to stable modes. Therefore, all wave activity will experience some damping, either directly or indirectly, during some time in the system's evolution except for the $k=0$ mode. Due to the initial perturbation having a small amount of total wave energy distributed over all the modes, it is being assumed that even an unstable mode would be depleted of its field intensity through the eventual conversion of all modes to $k=0$. There comes a stage in the plasma evolution when only the undamped mode, $k=0$, and the least damped mode, k nearly zero, have survived.

When the plasma reaches the stage of predominantly $k=0$ and nearly zero wave modes, further amplification of the $k=0$ mode will be negligible, because only the nearly zero mode, which is decaying, is available to convert to $k=0$. At this point, $E(t)$, which is the $k=0$ mode, is well-approximated as an oscillation at the plasma frequency. From [10], $f_s(t,v)$ will oscillate with opposite phase to $E(t)$. Therefore, on a time average, the effects of the $k=0$ mode on changing the distribution function will be zero. Defining a time average for any function $Y(t)$ by

$$\langle Y \rangle_t = \int_t^{t+T} \frac{dt'}{T} Y(t') \quad [17]$$

where T is the plasma period, the time average of [8] is

$$\frac{\partial}{\partial t} \langle f_s(t,v) \rangle_t = -\frac{q_s}{m_s} \frac{\partial}{\partial v} \langle E' f'_s \rangle_{x,t} \quad [18]$$

where the combined subscript x,t on the angular bracket indicates a double average over space and time.

The nearly zero mode, which is given by $E'(t,x)$, will be in a regime where its evolution and effects are describable by quasi-linear theory. In the quasi-linear approximation, products of E' and f'_s are retained in [8], but neglected in [11]. In search of the distribution that changes the least, a restriction will be made to distributions that change only slightly. Such a subclass of distributions can be insured to exist by making the perturbation small enough. Specifically, based on [16], the initial wave field must satisfy the condition

$$E^2(t) + \langle E'^2 \rangle_x \ll 4\pi \sum_s m_s \int_{-\infty}^{\infty} dv v^2 f_s(t,v) \quad [19]$$

at $t=0$. Then $E(t)$ will be small, and the term $E(t) f'_s$ will be negligible in [11], reducing it to

$$\frac{\partial f'_s}{\partial t} + v \frac{\partial f'_s}{\partial x} + \frac{q_s}{m_s} E' \frac{dF_s}{dv} = 0 \quad [20]$$

where $f_s(t,v)$ was replaced by $F_s(v)$ since it only slightly varies. Equations [12] and [20] are the common linearized equations for electrostatic waves. The solution is that, for a stable mode of wave number k , E' oscillates with frequency ω and exponential decays with damping rate $|\gamma|$ (negative γ corresponds to damping) given by [Nicholson, 1983]

$$\epsilon(\omega+i\gamma,k) = 1 - \sum_s 4\pi q_s^2 / (k^2 m_s) \int_C \frac{dF_s/dv}{v - \frac{\omega+i\gamma}{k}} = 0 \quad [21]$$

where the integration is in the complex v -plane along the Landau contour, and ϵ is the dielectric function. With E' exponentially decaying at a damping of η , [18] says that, on the average, the change in $f_s(t,v)$ decays at least as fast. Consequently, the distribution that changes the least will be the one that damps the nearly zero wave mode the most. From [21], one seeks the F_s that maximizes η , or minimizes γ . Mathematically, the problem at hand is under the classification of Calculus of Variations, where F_s is varied slightly and a minimum in γ is sought.

The functions about which one varies have to be physical. To insure this, constraints must be imposed. The conservation laws, [14] through [16], require that

$$\int_{-\infty}^{\infty} dv F_s = n_s ; \sum_s m_s \int_{-\infty}^{\infty} dv v F_s = n P ; \sum_s m_s \int_{-\infty}^{\infty} dv v^2 F_s = n T \quad [22]$$

where, n_s , n , P , and T are, respectively, the number density of particle type s , the total number density of all particle types, the total plasma momentum, and the total plasma temperature, all of which are constants. The existence of these velocity moments imply that the high speed dependence of F_s must be less than $1/v^3$. This puts a limit on damping rate, because, for small k , γ is proportional to the dF_s/dv evaluated at high velocity ω/k [Nicholson, 1983]. Therefore, the damping is maximized for the function that has the steepest descending slope, which is when the high speed dependence of F_s tends to $1/v^3$. In regard to [1], κ tending to $3/2$ would maximize damping.

To find the function for all velocity, additional constraints must be imposed to keep F_s physical. One condition is that F_s must be positive. Another condition arises from the fact that each distribution function F_s will consist of a definite number of plasma components, Λ_s , which is determined by the origin of the plasma. Therefore, it is a fixed property of the system. Defining $F_{s,c}$ as the distribution function for component c of particle type s , the total distribution for particle type s is

$$F_s = \sum_{c=1}^{\Lambda_s} F_{s,c} \quad [23]$$

The number of components, Λ_s , is determined by counting the humps in F_s . By constraining $F_{s,c}$ to be positive with only one hump, F_s is insured to be physical. This is done by maximizing the following integral

$$\int_{-\infty}^{\infty} dv (F_{s,c})^r \quad [24]$$

where the exponent r has to be determined, where $r \neq 1$, so that maximizing [24] is independent from the first equation in [22]. The problem is now well defined, whereby γ is minimized in [21] subject to the constraints in [22] while maximizing [24]. A solution for arbitrary and small variations in $F_{s,c}$ only exists if k approaches zero. The answer is that each component is given by a κ -distribution with appropriate flow speed, where $\kappa = 1/(1-r)$ with $3/2 < \kappa < \infty$, and κ tending to $3/2$ gives the absolute minimum in γ .

References

- Hasegawa, A., K. Mima, and M. Duong-van, "Plasma distribution function in a superthermal radiation field," *Phys. Rev. Lett.* **54**, 2608, 1985.
 Nicholson, D. R., *Introduction to Plasma Theory*, John Wiley & Sons, New York, 1983.
 Pangia, M. J., "A theoretical study of the steady state of a space plasma," 1991 NASA/ASEE Summer Faculty Fellowship Program, N92-15850, 1991.
 Swanson, D. G., *Plasma Waves*, Academic Press Inc., London, 1989.

1992

NASA/ASEE SUMMER FACULTY FELLOWSHIP PROGRAM

MARSHAL SPACE FLIGHT CENTER
THE UNIVERSITY OF ALABAMA

STUDIES OF THE CHARGING OF A THIN
DUST LAYER IN A PLASMA

Prepared By: Lennart R. Peterson, Ph.D.
Academic Rank: Professor
Institution: University of Florida
Department of Physics

NASA/MSFC:
Laboratory: Space Science Laboratory
Division: Solar-Terrestrial Physics
Branch: Magnetospheric Physics

MSFC Colleague: Craig J. Pollock, Ph.D.

INTRODUCTION

When an infinite plane layer of dust having a number-density profile normal to the plane is exposed to an ambient e^- , p^+ plasma, one can imagine the features of the charging process near the layer boundary. If the e^- , p^+ temperatures are equal, and the B field is normal to the dust layer, the controlling factor is the large electron relative to proton speeds. Since the collision rate between plasma particles of number density n and speed v and an uncharged dust grain of radius a is estimated as the product $n v \pi a^2$, electrons dominate the charging process. The outer edge of the layer charges negatively, setting up an electrical potential that inhibits penetration of electrons into the layer and at the same time accelerates protons inward. Interior to the outer negative region then, one would expect many energetic protons compared to a reduced number of electrons from the ambient plasma. Charge imbalances are bound to arise, but the details are not so easy to deduce from simple arguments. These details are the subject of the present study.

DISCUSSION

Studies of dust charging have been carried out by a number of authors under a variety of assumptions. An important effect pointed out first by Goertz and Ip (1984) is that for interparticle grain separations much smaller than the plasma Debye length, the amount of charge on single grains is much smaller than the value expected when other dust grains are absent. Refinements to the charging model were made by Whipple, et al. (1985) and by Houpis and Whipple (1987). These efforts all involved a linearized form of the Poisson equation. The study by Houpis and Whipple also included a power-law grain-size distribution.

For many problems involving plasmas, neither a fluid approach nor an analytical kinetic approach is practical at present. For this reason, Wilson (1987, 1988) constructed a simulation code to determine the charge and field structure of an optically thin layer of dust in a plasma. Parameters chosen were within the ranges that describe the A and B rings of Saturn. The dust layer was described as a plane sheet of grains with fixed radius, having either Gaussian or square number-density profile and fed by a pool of Maxwellian plasma particles. In addition to the charge structure and the E fields in the layer, the results also gave the phase space distribution of plasma particles in the layer. Photoionization of dust grains was included. Along with collisions between plasma particles and dust grains, p-p collisions were assumed, e-p and e-e collisions were neglected. The primary factor controlling particle trajectories within the dust layer are local E fields.

The present work has been a three-phase process to extend Wilson's code. In phase I, the code was modified to move particles more accurately through the simulation cells so that larger cells and longer time steps can be used. This has resulted in a faster code that still gives reasonable convergence and consistent results, although more testing is needed to further reduce run time. The movement of particles is done by starting with the initial position Z_1 and Z-component of velocity V_1 in a given simulation cell. The particle is then moved to its new position Z_2 with new velocity V_2 by assuming there is an average acceleration and an average velocity that we can deduce by successive approximations. For example, as long as no cell boundary is crossed, then a reasonable starting point is

$$V_2 = V_1 + (e/m) (E_{AVE}) dt \quad (1)$$

and

$$Z_2 = Z_1 + (V_1 + V_2) dt/2. \quad (2)$$

Knowing the fields at the lattice points allows one to write Eq. 1 to first order in a Taylor expansion of the E-field,

$$V_2 = V_1 + (e/m)E_1 dt + (e/m)(\text{Grad } E)(V_{AVE}/2) dt^2 \quad (3)$$

Approximately, one can set $V_{AVE} = V_1$ in Eq. (3) to get V_2 , which is used back in Eq. (2) to get a final value of Z_2 . If a boundary is crossed by a particle during a time step, or if a particle changes direction in a cell, one must of course use special techniques.

Phase II has been to introduce a size distribution by defining a discrete starting distribution of Gaussian form for each dust particle radius a_i

$$n(z, a_i) = c a_i^{-P} \exp\{-[z/z_0(a_i)]^2\} \quad (4)$$

where the central density is described by a power P that normally is expected to lie between 3 and 4. The width of the Gaussian is controlled for each size by making the parameter z_0 a function of particle radius. The optical depth for each particle size is then defined by the integral

$$T_i = \int_{-\infty}^{\infty} n(z, a_i) \pi a_i^2 dz \quad (5)$$

giving

$$T_i = c a_i^{-P} \pi^{3/2} a_i^2 z_0(a_i) \quad (6)$$

By specifying the total optical depth, the constant c is determined for the given parameters P and $z_0(a_i)$.

RESULTS

A single long computer run was made to test code improvements and to track the charging process. Parameters are for a dust layer of total optical depth 1.0 in a 1 eV plasma. Seven grain radii, between 1×10^{-5} to 1×10^{-2} m are included, with $P = 3.5$ in Eq. (4). Grains are assumed as Gaussians with $1/e$ widths of 10.0 m for the smallest grains to 5.0 m for largest grains. The resulting E field after 56,000 iterations, is shown in Fig. 1. In the outer region of the layer, as expected, the negative E field indeed is a barrier for incident electrons. By $z = 23$ m, the integration of the E field leads to a potential of about -2.7 volts, thus boosting proton energies but allowing only those electrons having energy above 2.7 eV to penetrate to the interior of the layer. For z near 23 m, protons outnumber electrons by almost 2 orders of magnitude. Thus, interior to the outer negative layer, a positive E field develops. The process then repeats itself. Figure 2 shows the variations of electrical potential with position. Of particular interest are the consistent oscillations of the potential between zero and almost -3.0 volts. It appears that the well known result for isolated grains, where equilibrium is achieved when the grain potential has the value $2.51 kT/e$ (which equals 2.51 for a 1 eV plasma), has its counterpart for the dust layer.

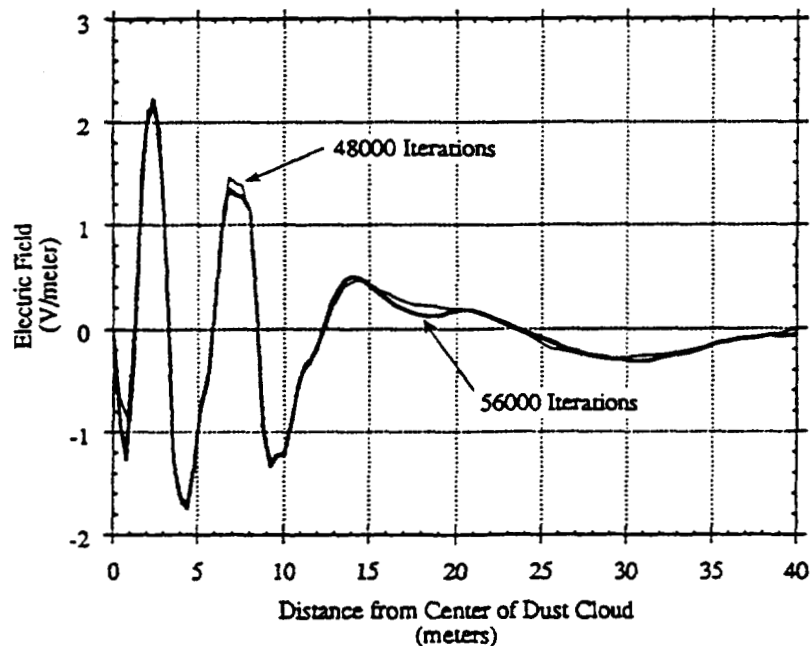


Figure 1. Electric field versus position for 48,000 iterations (light line) and for 56,000 iterations (heavy line)

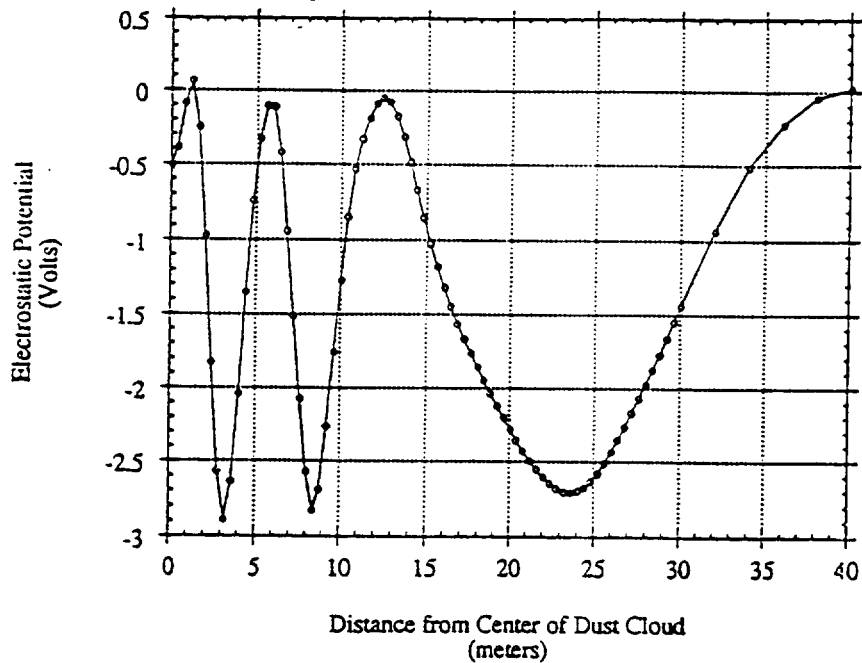


Figure 2. The electrostatic potential versus position in the layer

The result of looking at the average charge on individual grains also suggests the consequence of allowing the dust grains to move in response to the E field. The smallest grains near the layer edge will have relatively large negative e/m values and will be forced outward. Equilibrium will be reached ultimately when the outward electrical force is balanced by the restoring gravitational force. These issues will be explored in the near future.

REFERENCES

1. Goertz, C. K. and W.-H. IP, Limitation of electrostatic charging of dust particles in a plasma, *J. Geophys. Res. Lett.*, 11, No. 4, 349-352, April, 1984.
2. Houppis, H. L. F. and E. C. Whipple, Electrostatic charge on a dust size distribution in a plasma, *J. Geophys. Res.*, 92, No. A11, 12,057-12,068, Nov., 1987.
3. Whipple, E. C., T. G. Northrop, and D. A. Mendis, The electrostatics of a dusty plasma, *J. Geophys. Res.*, 90, No. A8, 7405-7413, Aug., 1985.
4. Wilson, G. R., Simulation of the plasma interaction with thin dust clouds, Ph.D Dissertation, Brigham Young Univ., Dec., 1987.
5. Wilson, G. R., The electrostatic charging of thin dust clouds, *J. Geophys. Res.*, 93, No. A11, 12,771-12,781, Nov., 1988.

1992

NASA/ASEE SUMMER FACULTY FELLOWSHIP PROGRAM

**MARSHALL SPACE FLIGHT CENTER
THE UNIVERSITY OF ALABAMA**

**SEDS1 MISSION SOFTWARE VERIFICATION
USING A SIGNAL SIMULATOR**

Prepared By: William E. Pierson

Academic Rank: Professor

**Institution: West Virginia Institute of Technology
Department of Electrical Engineering**

NASA/MSFC:

Laboratory: Program Development
Division: Payload and Orbital Systems
Branch: Orbital Support Systems Group

MSFC Colleague: Charles Rupp

SEDS1 MISSION SOFTWARE VERIFICATION USING A SIGNAL SIMULATOR

July, 1992

BACKGROUND

The first flight of the Small Expendable Deployer System (SEDS1) is scheduled to fly as the secondary payload of a Delta II in March, 1993. The objective of the SEDS1 mission is to collect data to validate the concept of tethered satellite systems and to verify computer simulations used to predict their behavior. SEDS1 will deploy a 50 lb. instrumented satellite as an end mass using a 20 km tether. Langley Research Center is providing the end mass instrumentation, while the Marshall Space Flight Center is designing and building the deployer. The objective of the experiment is to test the SEDS design concept by demonstrating that the system will satisfactorily deploy the full 20 km tether without stopping prematurely, come to a smooth stop on the application of a brake, and cut the tether at the proper time after it swings to the local vertical. Also, SEDS1 will collect data which will be used to test the accuracy of tether dynamics models used to simulate this type of deployment. The experiment will last about 1.5 hours and complete approximately 1.5 orbits.

Radar tracking of the Delta II and end mass is planned. In addition, the SEDS1 on-board computer will continuously record, store, and transmit mission data over the Delta II S-Band telemetry system. The Data System will count tether windings as the tether unwinds, log the times of each turn and other mission events, monitor tether tension, and record the temperature of system components. A summary of the measurements taken during the SEDS1 shown in Table 1. The Data System will also control the tether brake and cutter mechanisms.

Preliminary versions of two major sections of the flight software, the data telemetry modules and the data collection modules, were developed and tested under the 1990 NASA/ASEE Summer Faculty Fellowship Program. To facilitate the debugging of these software modules, a prototype SEDS Data System was programmed to simulate turn count signals. During the 1991 summer program, the concept of simulating signals produced by the SEDS electronics systems and circuits was expanded and more precisely defined. During the 1992 summer program, the SEDS signal simulator was programmed to test the requirements of the SEDS Mission software, and this simulator will be used in the formal verification of the SEDS Mission Software. The formal test procedures specification was written which incorporates the use of the signal simulator to test the SEDS Mission Software and which incorporates procedures for testing the other major component of the SEDS software, the Monitor Software.

SEDS MISSION SOFTWARE VERIFICATION TEST SPECIFICATION

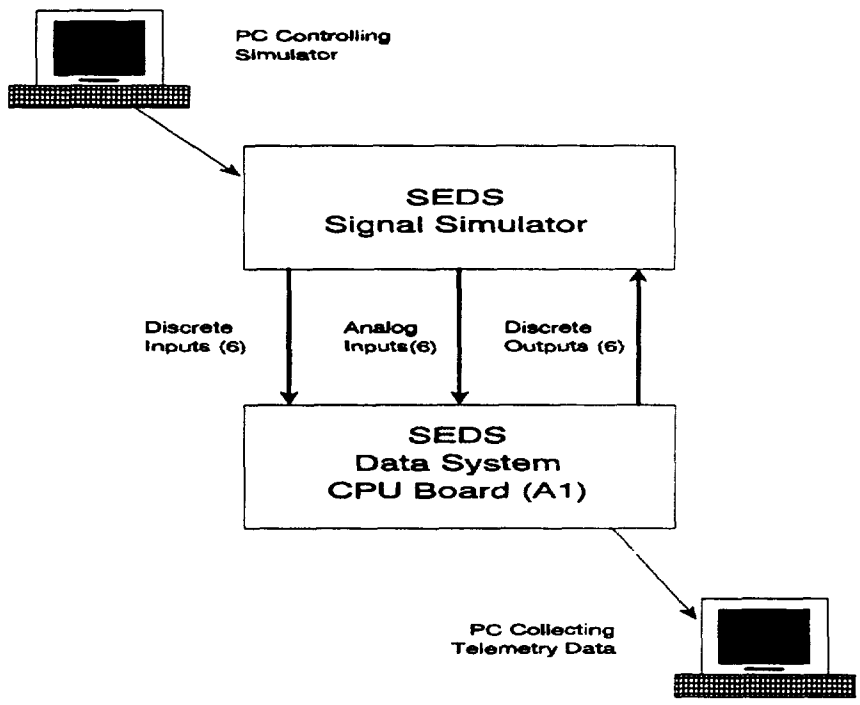
A series of tests will be performed to exercise the software modules which make up the Mission Software of the SEDS Data System. These tests will be performed by using a SEDS Signal Simulator to generate signals which will simulate the inputs normally produced by sensors and circuits in the SEDS system. The test configuration is depicted in Figure 1. A SEDS Data System CPU Card will be modified to construct the SEDS Signal Simulator.

Signals will be generated which simulate both nominal flight conditions and all anticipated anomalies. In addition, the tests provide a means for monitoring and analyzing outputs produced by the SEDS Mission Software for controlling the tether brake and cutter mechanisms.

Table 1. SEDS Measurements

<u>MEASUREMENT</u>	<u>RANGE</u>	<u>SAMPLE RATE</u>
T1 - Tether Temperature	-30 ⁰ to +80 ⁰ F	1 per 10 seconds
T2 - Brake Temperature	-30 ⁰ to +80 ⁰ F	1 per 10 seconds
T3 - Canister Temperature	-30 ⁰ to +80 ⁰ F	1 per 10 seconds
T4 - Electronics Temperature	-30 ⁰ to +80 ⁰ F	1 per 10 seconds
B1 - Turn Counter Beam #1	Discrete	Asynchronous
B2 - Turn Counter Beam #2	Discrete	Asynchronous
B3 - Turn Counter Beam #3	Discrete	Asynchronous
F1 - Tether Tension #1	-0.25 to +0.25 N.	500 per second
F2 - Tether Tension #2	-2.5 to +7.5 N.	500 per second
IN1/IN2- Satellite Deployment	Discrete	Asynchronous

FIGURE 1. SEDS MISSION SOFTWARE TESTING USING A SIGNAL SIMULATOR



With the exception of control signals for the tether brake and cutter, correct operation of the Mission Software can be verified by examining the telemetry data collected and transmitted by the Mission Software over the serial port of the SEDS Data System. An IBM-compatible PC will be

connected to this serial port to collect the mission data. The PC will execute software to display summary data contained in the Master Frames sent by the SEDS Data System. In addition, this software will store the serial data in a disk file to be used in post-test analysis and documentation. The signals generated by the SEDS Data System to control the tether brake and the tether cutter cannot be analyzed by monitoring the serial data stream. Therefore, the PC controlling the SEDS Signal Simulator will monitor, display and store these control signals levels. Specifically, the brake motor and tether cutter signals are sampled once every 1ms and their state is displayed by the PC anytime a change is detected in any one of the signals. The time that the change was detected is also displayed.

Three tests are performed on the SEDS Mission Software using simulated input signals. The first test generates turn count signals at three different rates: fast, nominal, and slow. In addition, signals are generated which simulate false signals which may occur during flight due to vibration of the tether, and which are eliminated by the Mission Software. No turn count failures are introduced during this first test.

The second test simulates a failure on turn count channel-B by intermittently turning signals off and on. A total of 50,000 simulated turn counts are generated on channel-A to verify that the SEDS Mission Software can withstand a failure on channel-B. The third test is similar to test #2 except that a failure is introduced on channel-A.

During each of the SEDS Mission Simulation Tests, the SEDS Simulator will generate independent signals to each analog input of the SEDS unit under test. The analog signals provided by the simulator will be one of three levels: 0v (0.2v, max), half-scale ($2.5v \pm 10\%$), or full-scale ($5.0v \pm 10\%$) and will be applied in regular cycles. The purpose of applying simulated analog inputs to the SEDS Data System is not to gauge the accuracy of the A/D converter circuitry but to assure that the data collection modules in the Mission Software is correctly collecting and transmitting temperature and tension information.

CONCLUSION

The SEDS Signal Simulator will be used in the formal verification of the SEDS1 Mission Software. The Simulator will not only emulate normal flight conditions but also exercise all modules written to handle anticipated anomalous flight conditions, conditions that would be difficult to reproduce and control with actual SEDS hardware. The simulator will apply signals which test the limits of the SEDS Mission Software as defined in the requirements document, thereby increasing the confidence that the Mission Software will perform according to specifications during the actual flight of the SEDS experiment. With little modification, the Simulator can be useful in the software development of future SEDS flights.

REFERENCES

1. "SEDS Data System Functional Requirements", Energy Sciences Laboratories, Inc. and Program Development, MSFC, May 1988.
2. "SEDS Data System Data Collection and Telemetry Software", Final Report, NASA/ASEE 1990 Summer Faculty Fellowship Program, Contract No. NGT-01-002-099, MSFC, Huntsville, AL.
3. "SEDS Mission Software Verification Test Procedures, NASA/ASEE 1991 Summer Faculty Fellowship Program, Contract No. NGT-01-008-021, MSFC, Huntsville, AL.
4. "MSFC Software Management and Development Requirements Manual", Software and Data Management Division, January 1991, MSFC, Huntsville, AL.
5. "SEDS Software Requirements Document (DM06), Vol. II., MSFC-RQMT-1967, February 1992, MSFC, Huntsville, AL.
6. "SEDS Software Verification Test Specification (DM20), MSFC-SPEC-2033, July 1992, MSFC, Huntsville, AL.

1992

NASA/ASEE SUMMER FACULTY FELLOWSHIP PROGRAM

**MARSHALL SPACE FLIGHT CENTER
THE UNIVERSITY OF ALABAMA**

RELIABILITY ANALYSIS OF EXTERNAL TANK ATTACH RING (ETA)

Prepared By: Chandra S. Putcha, Ph.D.

Academic Rank: Professor

Institution and Department: California State University,
Fullerton
Department of Civil Engineering

NASA/MSFC:

Office: Systems Safety and Reliability
Division: Reliability & Maintainability
Engineering

MSFC Colleague: Frank Pizzano

The work in this report is part of an overall study in the area of the evaluation of the performance of the shuttle. Besides the main engines and the Orbiter, the main parts of a shuttle are the Solid Rocket Boosters, External Tank, and the External Tank Attachment Ring (ETA). The present study is restricted to ETA, but the concepts discussed are general in nature and can be applied to any structural component. The strengths of steel, the cross-sectional dimensions of the steel section and, thus, the strength of the model itself and the loads are all variable parameters. In other words, taking the entire structural element under consideration, the resistance and the applied load are random variables. Consequently, the traditionally used deterministic analysis (the so-called margin of safety approach) does not reveal the actual safety reserve in the structure, because it does not include the inherent variability in the material, geometric and load parameters. Such a variability can easily be included in the probabilistic analysis using probabilistic methods which are in use and have been continuously developed for about the last two decades. The objective of this research work is to use some of the existing probabilistic methods to calculate the reliability of ETA Ring at various critical sections for the limit state of stress. This is done both in terms of the traditional probability of failure (P_f) and reliability levels as well as the well known safety indices (β) which have become a commonly accepted measure of safety.

For any probabilistic analysis, a certain deterministic model is needed for which the limit state function can be formulated in terms of the general basic variables of resistance and load. The variability of the materials, cross-sectional properties and load can then be incorporated into the deterministic model which then forms the basis of the probabilistic model and the beta value can then be calculated. The details of the deterministic model and the corresponding deterministic analysis which was done by USBI (2) under contract for NASA and specifically for Marshall Space Flight Center forms a basis for the present probabilistic study.

If R is the resistance variable and S is the load variable, the limit state function g is then $g=R-S=0$ which divides the failure and the survival region. The corresponding safety index (β) which is the shortest distance from the origin to the failure surface can be defined as,

$$\beta = \frac{\bar{g}}{\sigma_g} \quad [1]$$

β can also be considered as the measure of the number of standard deviations that the mean value of the limit state function is from the failure surface. If R and S are normal-normal or lognormal-lognormal, the following relations hold:

$$P_f = \Phi(-\beta) \quad [2]$$

where Φ is the standard cumulative normal distribution function. If R and S are normal, β can be expressed as (1)

$$\beta = \frac{\bar{R} - \bar{S}}{\sqrt{\sigma_R^2 + \sigma_S^2}} = \bar{g} / \sigma_g \quad [3]$$

Knowing P_f from equation [2], which in turn uses β from equation [3], the reliability can be calculated. This would indicate that the higher the value of beta, the higher is the safety reserve in the structure with respect to that limit state. It should be noted that while there exists in the literature a closed form relation similar to equation [3] for R and S both being lognormal, numerical techniques have to be employed for other distributions.

In the present study, as the ETA Ring is complicated, there are no closed form expressions between the output variable of principal stress and the corresponding input variables. Hence, probabilistic study is quite complicated. The deterministic procedure used for the calculation of stresses is the well known finite element method (FEM). The corresponding probabilistic study which will use Monte Carlo techniques, will involve FEM in conjunction with the properties of the probability distributions of all variables involved in the calculation of stresses at critical points. This procedure has been successfully applied before (5) and the details are given in the extended report (4). In the study of ETA Ring the limit state g is defined as

$$g = (\sigma_u)_{ALL} - (\sigma_p)_{ACT} \quad [4]$$

corresponding to $P_f = P((\sigma_u)_{ALL} < (\sigma_p)_{ACT})$. $(\sigma_p)_{ACT}$ stands for actual principal stress and $(\sigma_u)_{ALL}$ is the ultimate allowable stress of the material. In here, both $(\sigma_u)_{ALL}$ and $(\sigma_p)_{ACT}$ are considered as random variables. Using the procedure described in detail in reference 4, P_f , R and β values are calculated for all the critical elements at all critical sections. The critical sections identified were the tunnel splice plate and H-fitting lugs (2). In addition to this a probabilistic

margin of safety (PMS) is calculated which is defined as (3)

$$PMS = \frac{(\bar{\sigma}_u)_{ALL} - (\sigma_p)_{\max}}{S_{\sigma_u}} \quad [5]$$

$$(\sigma_p)_{\max} = \bar{\sigma}_p + \beta S_{\sigma_p} \quad [6]$$

where, a bar over a variable indicates the mean value and s indicates standard deviation of the variable used as a subscript for s . This is done for ready comparison with the corresponding deterministic value of margin of safety calculated in reference 2.

Based on this extensive study discussed in detail(4), it has been found that the probabilistic margin of safety is consistently higher than the deterministic margin of safety indicating higher safety reserve. It has also been found that the reliability of all the critical elements is quite high indicating a good quality control of the work done at NASA.

REFERENCES

1. Ellingwood, B., Galambos, T.V, MacGregor, J. G. and Cornell, C.A., "Development of a Probability Based Load Criterion for American National Standard A58 - Building Code Requirements for Minimum Design Loads in Buildings and Other Structures," NBS Report No. 577, Washington, D.C., June 1980.
2. External Tank Attach 360° Ring Stress Analysis, Revision A, Vol. I, USBI-ANAL-32-88, June 1988.
3. Haugen, E.B, "Probabilistic Approaches to Design," John Wiley & Sons, Inc., New York, 1968.
4. Pizzano, F. and Putcha, C.S., "An In-depth Probabilistic Study of External Tank Attach Ring (ETA)," Internal Report No. CT RPT-02, Reliability and Maintainability Engineering Division, MSFC, August 1992.
5. Putcha, C.S. and Kreiner, J. H., "Reliability Factor Analysis of Shafts," Proceedings of Canadian Conference of Applied Mechanics, Ottawa, Canada, June 1989.

1992

N93-17323

NASA/ASEE SUMMER FACULTY FELLOWSHIP PROGRAM

MARSHALL SPACE FLIGHT CENTER
THE UNIVERSITY OF ALABAMA

EMERGENCY EGRESS REQUIREMENTS
FOR
CAUTION AND WARNING, LOGISTICS, MAINTENANCE,
AND ASSEMBLY STAGE MB-6
OF
SPACE STATION FREEDOM

Prepared By: Paul S. Ray, Ph.D.
Academic Rank: Assistant Professor
Institution and Department: The University of Alabama, Tuscaloosa
Industrial Engineering Department

NASA/MSFC:

Office: Systems Safety and Reliability
Division: Systems Safety Engineering
Branch: Project Safety Engineering

MSFC Colleagues: Richard D. Siler
John M. Livingston

Introduction

The safety and survival of the crewmembers has been the prime concern of NASA. Previous studies have been conducted mainly for emergencies occurring during the operating mode of the fully assembled Station. The present study was conducted to evaluate the emergency requirements for the caution and warning, logistics, maintenance, and assembly stage MB-6 of the Station in space. Effective caution and warning is essential to achieve safe egress in emergencies. In order to survive a long period in space, the safety and emergency requirements for maintenance, logistics, and extravehicular assembly operation in space must be met.

Objectives

The objective of the study was to have an independent evaluation of the safety and emergency egress requirements for caution and warning, logistics, maintenance, and assembly of the Station in space.

Emergency Egress

Emergency egress is defined as the egress from a pressurized element when an event makes the element uninhabitable and ingress into a contiguous pressurized element that is safe.

Caution and Warning Methods

The Data Management System of the Station will provide the caution and warning signals, while EMAD will provide an additional warning for emergency situations. At present, EMAD has limited independent sensors for detecting emergency situations. It is recommended that the sensors located throughout the Station for detecting emergency situations should also be connected to EMAD to improve the effectiveness of the EMAD system. A suggested location for the work stations is the midsection of the modules. According to the current plan, there is no EMAD panel in logistics modules. A drag on EMAD panel is recommended for logistics modules to supplement the auditory alarm in an emergency.

A graphical cum alphanumerical format is recommended for displaying emergency action information (figure 1) at the Multipurpose Application Consoles. The detailed specifications of the graphical model, consistent with the human factors requirements have to be developed. The emergency action depends on the location of the crew members for a particular accident; as such, the action message should be appropriate at each work station for a particular emergency.

EMERGENCY ACTION INFORMATION DISPLAY

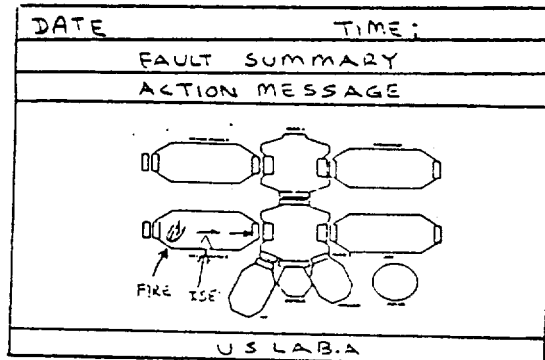


FIGURE 1

Operation of Mini/Pressurized Logistics Modules (MPLM/PLM)

The function of logistics modules is to support cargo transportation in racks from the US LAB, JEM, Columbus modules, and nodes to PLM and vice versa. The major tasks for logistics operation consist of handling racks to and from MPLM/PLM units. The average time required for handling a rack is estimated to be about 30 minutes. Based on the Neutral Buoyancy Simulation conducted recently (1), it is suggested that two persons are required to safely handle a rack as shown in figure 2.

HANDLING A RACK

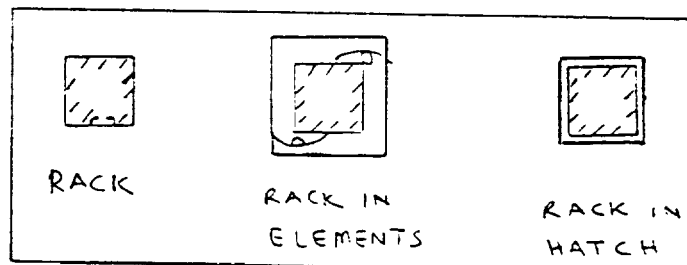


FIGURE - 2

One person at the front and a second person at the rear should hold a rack handgrip by one hand and use the other hand for translation guidance (figure 2). Recessed handgrips located centrally at the front and rear of a rack are recommended for translation purposes. Special care should be exercised while crossing hatch openings as the clearance between a moving rack and a hatch opening is very limited as shown in figure 2. In addition, the speed of translation during rack handling should not exceed 1 foot/second to allow frequent stops required to achieve a controlled movement and avoid accidents.

In an emergency during logistics operation, crew members present in MPLM/PLM should egress to the attached node. There is a probability of a catastrophe in case of a large fire occurring in the attached node (3). A contingency drag on oxygen supply is recommended for the waiting period of trapped crewmembers in this situation.

Maintenance Mode of Major Equipment

A typical Intravehicular Activity (IVA) for maintenance consists of shutdown, safing, gain access, replace or repair, close access, and testing of Orbital Replaceable Units or Orbital Maintainable Items, done sequentially by one person (2). A total of 640 IVA preventive and corrective maintenance tasks were identified. It is estimated that a total of 360 manhours/year will be required to cover all these tasks. During 50 percent of maintenance duration, one or more racks will be tilted on the aisle for access, causing partial blockage of the egress path. Typically, a tilted rack will be flat on an aisle and will reduce the egress path from 80 inches x 80 inches to 80 inches x 40.3 inches, as shown in figure 3. However, the reduced opening is adequate for emergency egress inside a module as illustrated in figure 6.

Although the egress path is blocked during hatch maintenance, the probability of an emergency during hatch maintenance is extremely low. A rigorous preventive maintenance is recommended to minimize the breakdown of hatch mechanism.

Safety and Emergency Egress During Assembly Phase MB-6

A total of 17 stages have been planned for assembling the Station in space. From MB-6, the Station will be occupied by humans at least for short periods. As such, safety and emergency provisions are required beginning this assembly stage.

Most of the assembly operations consist of hazardous Extravehicular Activities (EVA). A catastrophic emergency may arise due to puncture of an EVA suit (4). It is recommended that all sharp edges must be rounded or capped. In case of any emergency situation during this assembly operation, the crewmembers should translate to the docked Orbiter and de-orbit. For safe assembly operation, handholds and attachments are required on all modules and nodes. All EVA tools should also be tethered. A safe EVA operation procedure should be developed and used for training of EVA crewmembers.

During an emergency at MB-6, the worst emergency scenario consists of an accident at Node 2 and all four crewmembers located in the lab cannot translate through the damaged Node 2 to the Orbiter. In this case, crewmembers should close the lab hatch, isolate the lab, and wait for rescue by Orbiter.

Reference:

1. International Standard Payload Rack (ISPR) Neutral Buoyancy Simulation (NBS) Quick Look Report, Boeing Defense and Space Group, Doc: 2-H8W1-LCK-442, June 26, 1992
2. Maintainability Allocations, Predictions and Analyses, Report C, Boeing Defense and Space Group, Doc: D683-10483-1, March 30, 1992
3. MPLM Phase B Safety Analysis, Alenia Spazio SPA, Doc: MPLM-RP-AI-002, January 17, 1992
4. Safety Assessment Report for MB-6, Draft 1, Boeing Defense and Space Group, Doc: D683-46007-1, July 23, 1992

1992

NASA/ASEE SUMMER FACULTY FELLOWSHIP PROGRAM

MARSHALL SPACE FLIGHT CENTER
THE UNIVERSITY OF ALABAMA

ANALYSIS OF WAVES IN SPACE PLASMA (WISP)
NEAR FIELD SIMULATION AND EXPERIMENT

Prepared By: James E. Richie, Ph.D.

Academic Rank: Assistant Professor

Institution and Department: Marquette University
Department of Electrical and Computer Engineering

NASA/MSFC:

Office: Information and Electronic Systems Laboratory
Division: Computers and Communications
Branch: Communication Systems

MSFC Colleagues: David P. Harris
Hubert Gangl

The WISP payload scheduled for a 1995 space transportation system (shuttle flight) will include a large power transmitter on board at a wide range of frequencies. The levels of electromagnetic interference/electromagnetic compatibility (EMI/EMC) must be addressed to insure the safety of the shuttle crew. This report is concerned with the simulation and experimental verification of EMI/EMC for the WISP payload in the shuttle cargo bay. The simulations have been carried out using the method of moments for both thin wires and patches to simulate closed solids (2). Data obtained from simulation is compared with experimental results. An investigation of the accuracy of the modeling approach is also included.

The report begins with a description of the WISP experiment (4). A description of the model used to simulate the cargo bay follows. The results of the simulation are compared to experimental data on the input impedance of the WISP antenna with the cargo bay present. A discussion of the methods used to verify the accuracy of the model is shown to illustrate appropriate methods for obtaining this information. Finally, suggestions for future work are provided.

The WISP Experiment: EMI/EMC Issues

The specifics of the experiment that concern this investigation are as follows. First, a number of antenna lengths will be deployed: 5, 15, and 50 meters. Second, a frequency range from 100 KHz to 30 MHz will be transmitted in both a continuous wave and a pulsed fashion. Finally, the power transmitted will reach a maximum of 500 W (only in pulsed mode). These are the range of values that must be addressed to fully understand the near field strengths present at various components inside the cargo bay. A payload safety specification has not been written for these low frequencies; however, it is expected that 4 V/m will be chosen.

Cargo Bay Model

The cargo bay is modeled as a single, fully enclosed metallic object with infinite conductivity. The model is shown in figure 1. The model was broken into 5 inside panels, 5 outside panels, and a square O ring on the top to close the structure. The thickness of the box, α , is a parameter of the model. Each of the two sets of 5 panels is broken into 5 regions, as shown in figure 2. This was done to allow for a finer sampling of the current near the edges of the model. The value of γ is also a parameter called the corner dimension of the model and will be discussed later. Each of the 5 regions on each of the 5 panels on each of the two sets of open-box surfaces was then broken into rectangular patches that are inputs to the method of moments code NEC (1).

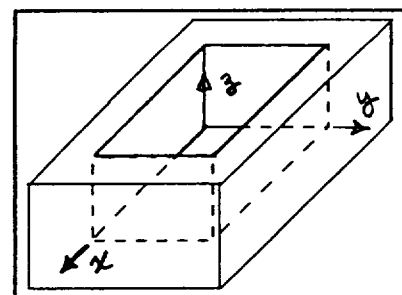


Figure 1

The model was constructed using guidelines concerning the total area of a patch and the aspect ratio of the rectangular patches. The aspect ratio of a single patch is defined to be the ratio of the large dimension divided by the small dimension. In summary, a shuttle cargo bay model has been developed that has four parameters: the thickness, the corner dimension, the maximum patch area, and the maximum aspect ratio.

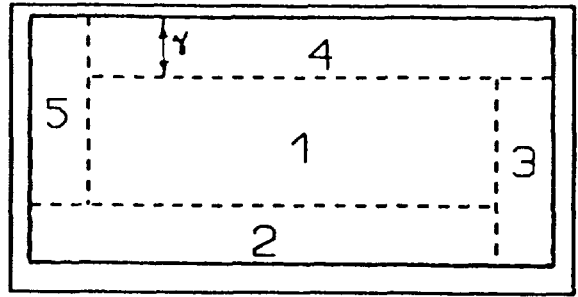


Figure 2

The corner dimension is a parameter of the model that recognizes the fact that the current must be sampled at a higher rate (or density) when compared with the center of a flat plate. This dimension allows the sections 2 through 5 to be broken into finer patches than section 1. Each of the five sections shown in figure 2 will be evenly broken into rectangular patches by specifying the number of patches in the length and the width of the section. Use of the corner dimension as a parameter allows the area near a corner and far from a corner to be different. This will help keep the number of patches (or unknowns) as low as practical.

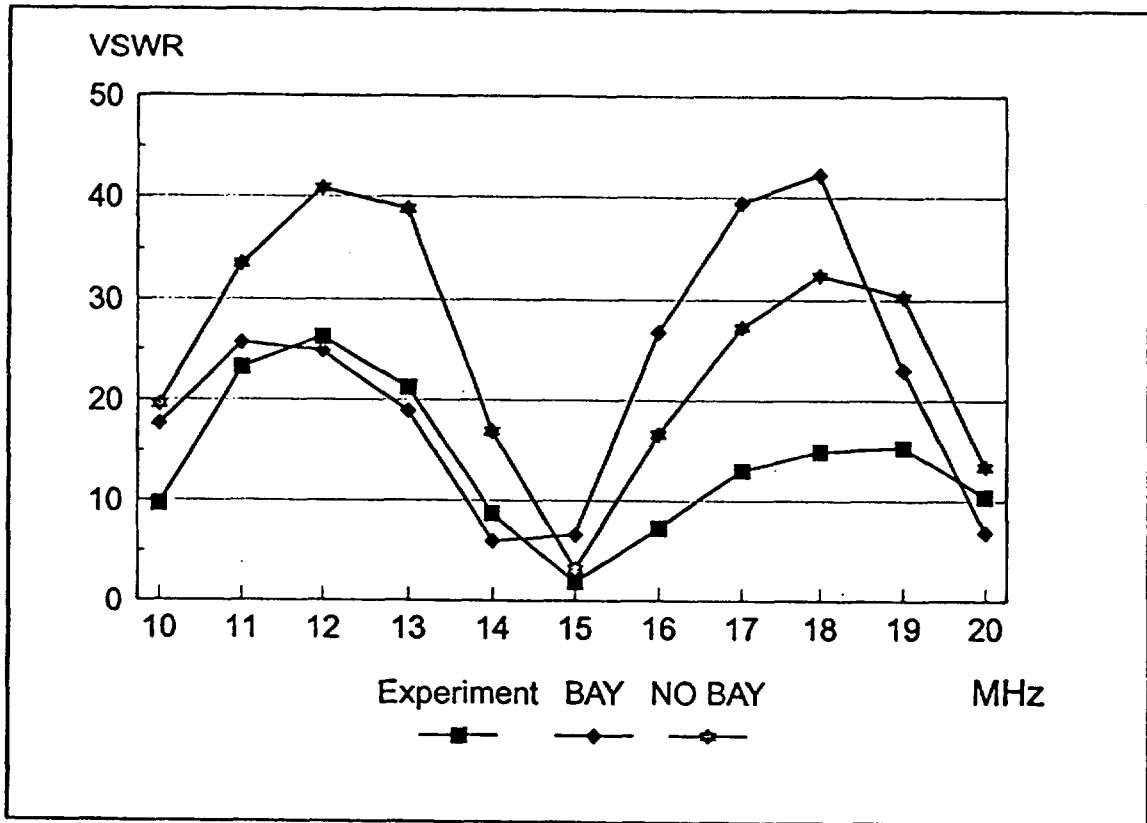


Figure 3

Results

Initial measurements necessary to continue the experiment are to find the antenna impedance and voltage standing wave ratio (VSWR) relative to 50Ω . The VSWR is necessary to find the actual power that is emitted by the antenna. In the laboratory, a balun is used to convert from the unbalanced coaxial line to the balanced requirement of a dipole antenna. The impedance of the balun and the antenna in parallel can be found, and the impedance of the balun can be found alone using a network analyzer. The VSWR of the antenna can then be found by removing the effect of the balun from the impedance data. This has been accomplished for the case of a 50 meter WISP dipole at a set of frequencies ranging from 10 to 20 MHz, in steps of 1 MHz. A plot of the VSWR for the experiment and the NEC model is shown in figure 3. This graph also shows the VSWR for a 50 m antenna in free space to illustrate the effect of the cargo bay.

The simulation appears to accurately model the physical situation at the lower frequency end. Recall that the frequency range of operation is from 100 KHz to 30 MHz and the figure shows results only from 10 to 20 MHz. It is believed that the model would also be suitable at frequencies lower than 10 MHz. As the frequency increases in figure 3, it is apparent that the model is not adequate. A further refinement for the higher frequencies is necessary for accurate modeling of the effect of the cargo bay. These results also are consistent with similar codes (3).

Accuracy of the Model

The hope of any numerical modeling procedure is that it accurately reflect what occurs in the laboratory. More often, however, it is found that a model is only partially acceptable. To quantify the accuracy of any electromagnetic model, it is appropriate to measure the degree that the boundary conditions have been satisfied. In

this work, three lines parallel to the x axis inside the model have been used, as shown in figure 4. The electric and magnetic fields inside any metal box should be zero. Therefore, by requesting the field points inside the box, one can calculate the mean squared error inside the box and use this single number to measure how effectively the boundary conditions have been satisfied. Results for a particular model are given in table 1.

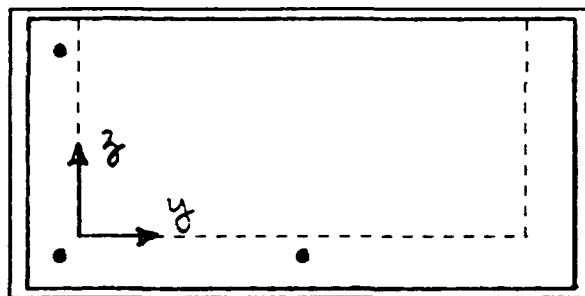


Figure 4

Model Parameters				Mean Squared Errors (Total)			No. Unknowns
α	γ	Area(max)	Aspect Ratio (max)	30 MHz	20 MHz	10 MHz	
1 m	1 m	$0.01 \lambda^2$	1.33	0.154	0.473	0.572	733

Suggestions for Future Work

The extent that the method of moments and in particular the NEC code can model the cargo bay of the space shuttle for the WISP experiment has been investigated. It appears that careful choice of model parameters such as wall thickness, corner dimension, area and aspect ratio will lead to an appropriate model.

The model that accurately reflects the desired characteristics has not been found. The following suggestions for future work have been developed:

1. The NEC model should, of course be compared to other techniques of similar origin.
2. Comparison with near field data would more likely be within the range of the numerical models. It is generally true that the input impedance of an antenna is strongly dependent on higher order effects.
3. A modification of the NEC code could be performed that incorporates a more accurate patch model. This would not only cause the solutions to be more precise, but may significantly reduce the number of degrees of freedom necessary to solve.

Acknowledgment

The author would like to thank the EB33 team for their help and patience over the previous two summers. The many discussions on this and other topics have been very beneficial and greatly appreciated.

References

1. Burke, A.J., and Poggio, A.J., "Numerical Electromagnetics Code (NEC) - Method of Moments," Technical Report NOSC/TD 116, Naval Ocean Systems Center, San Diego, CA July 1977.
2. R. F. Harrington, *Field Computation by Moment Methods*, Krieger, 1982.
3. Hwu, S., "Near Field Predictions for the High Power Dipole Antenna of the Space Shuttle Wisp Payload", IEEE AP-S International Symposium Digest, Chicago, IL, July, 1992.
4. James, H.G., *et al*, "Exploring Space Plasmas - The WISP/HF Experiment," Proceedings of the IEEE, Vol. 75, No. 2, February 1987, pp. 218-235.

N 9 3 - 1 7 3 2 5

1992

NASA/ASEE Summer Faculty Fellowship Program

**Marshall Space Flight Center
The University of Alabama**

**Industry Survey of Space System
Cost Benefits from New Ways of Doing Business**

Prepared By:	Russell L. Rosmait
Academic Rank:	Associate Professor
Institution:	Pittsburg State University, Dept. of Engineering Tech Pittsburg, Kansas 66762
NASA/MSFC:	
Office :	Program Planning Office
Division:	Engineering Cost Group
MSFC Colleague:	Joseph W. Hamaker

Introduction

The cost of designing, building and operating space system hardware has always been expensive. Small quantities of speciality parts escalate engineering design, production and operations cost. Funding cutbacks and shrinking revenues dictate aggressive cost saving programs. NASA's highest priority is providing economical transportation to and from space.

Over the past three decades NASA has seen technological advances that provide greater efficiencies in designing, building and operating of space system hardware. As future programs such as NLS, LUTE and SEI begin, these greater efficiencies and cost savings should be reflected in the cost models. There are several New Ways Of Doing Business (NWODB) which, when fully implemented will reduce space system costs. These philosophies and/or culture changes are integrated in five areas. 1. More Extensive Pre-Phase C/D & E, 2. Multi Year Funding Stability, 3. Improved Quality, Management and Procurement Processes, 4. Advanced Design Methods and 5. Advanced Production Methods. Following is an overview of NWODB and the Cost Quantification Analysis results using an industry survey, one of the four quantification techniques used in the study.

The NWODB Cost Quantification Analysis is a study performed at Marshall Space Flight Center by the Engineering Cost Group, Applied Research Incorporated and Pittsburg State University. This study took place over a period of four months in mid 1992. The purpose of the study was to identify potential NWODB which could lead to improved cost effectiveness within NASA and to quantify potential cost benefits that might accrue if these NWODB were implemented.

NWODB Industrial Survey Cost Savings Summary

A literature survey & historical data analysis, programmatic effects analysis, and parametric cost model analysis were used in the first stages of this study to assist in cost quantification. The final analysis to assist in cost quantification was the use of an industry survey. At the beginning of June 1992 an industry survey was developed using the five NWODB areas. The survey listed the NWODB main topics and gave several examples for each. The survey participants were asked to rate the five general categories of NWODB using a rating scale that ranged from 2.00 (twice as costly) to .25 (25% as costly or 75% savings.) They were asked to rate the five NWODB within the three phases of Development, Production and Operations. In addition these areas were rated twice, first for *structural/mechanical* and second for *Electrical/Electronics*. Thirty people were identified as survey recipients and a survey was sent to them. Of the thirty surveys, nineteen were received and the data tabulated and analyzed. Figure 1 shows the mean scores of combined data for the five areas of NWODB. The aggregate column illustrates cost saving at their highest potential. It should be kept in mind that these maximum cost savings if all NWODB changes are made. Because it is unlikely that any project can fully implement all of the NWODB ideas the team findings reflect the more probable savings range is in the 20% to 30% percent range.

NWODB Industrial Survey Cost Savings Summary

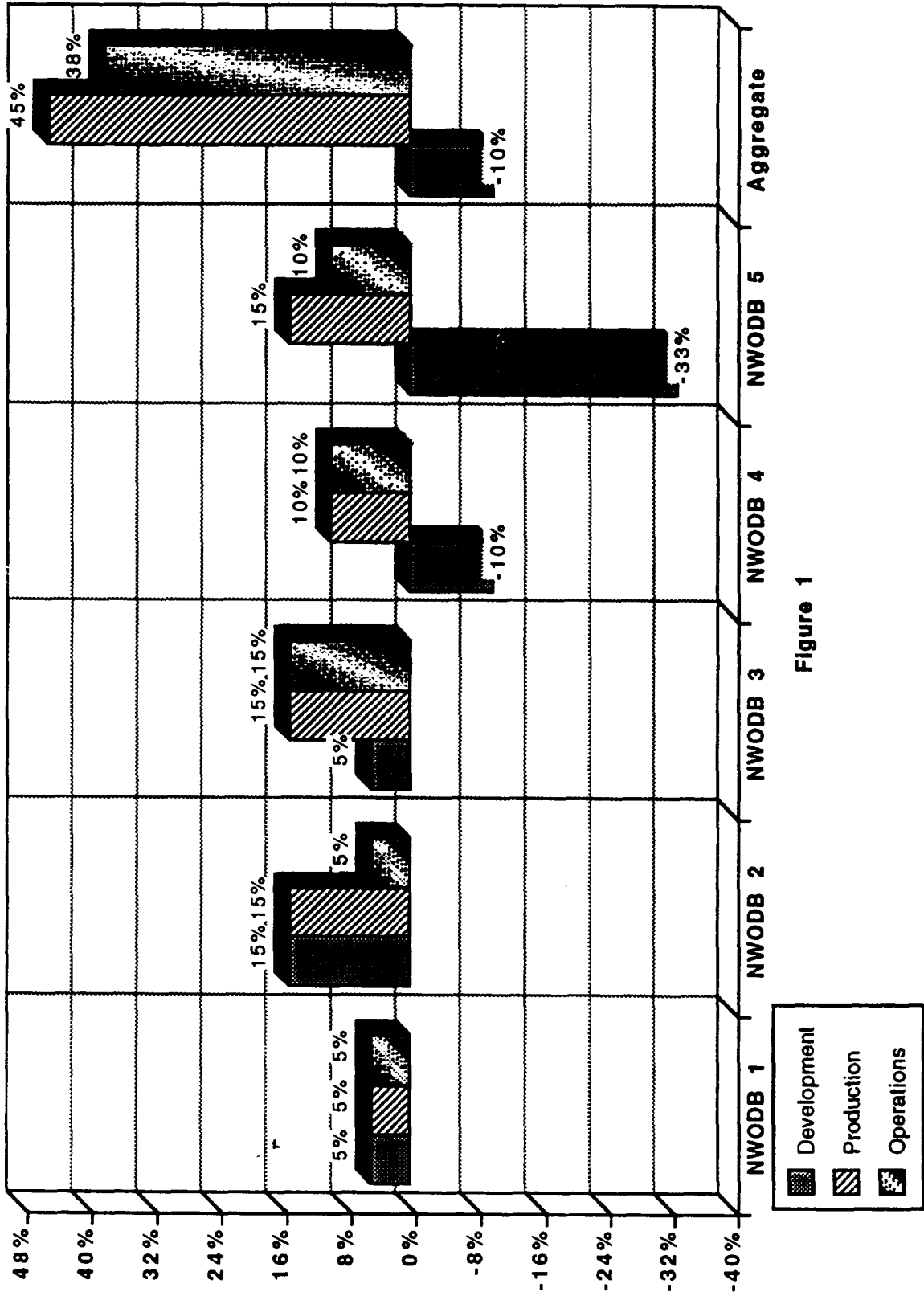


Figure 1

N 9 3 - 1 7 3 2 6

1992

NASA/ASEE SUMMER FACULTY FELLOWSHIP PROGRAM

**MARSHALL SPACE FLIGHT CENTER
THE UNIVERSITY OF ALABAMA**

**DESIGN OF A WELDED JOINT FOR ROBOTIC, ON-ORBIT ASSEMBLY OF SPACE
TRUSSES**

Prepared By: William K. Rule

Academic Rank: Assistant Professor

**Institution and
Department:** The University of Alabama
Department of Engineering Mechanics

NASA/MSFC:

Office: Structures and Dynamics Laboratory
Division: Structures
Branch: Structural Development

MSFC Colleagues: Frank P. Thomas
Pedro I. Rodriguez

INTRODUCTION

In the future, some spacecraft will be so large that they must be assembled on-orbit (1,2,7,13). These spacecraft will be used for such tasks as manned missions to Mars or used as orbiting platforms for monitoring the Earth or observing the universe. Some large spacecraft will probably consist of planar truss structures to which will be attached special purpose, self-contained modules. The modules will most likely be taken to orbit fully outfitted and ready for use in heavy-lift launch vehicles. The truss members will also similarly be taken to orbit, but mostly unassembled. The truss structures will need to be assembled robotically because of the high costs and risks of extra-vehicular activities. Some missions will involve very large loads. For instance, the truss structure supporting an aerobrake heat shield will experience up to 6 g's of deceleration during entry into the Martian atmosphere (4). To date, very few structures of any kind have been constructed in space. Two relatively simple trusses were assembled in the Space Shuttle bay in late 1985 (12).

Here the development of a design of a welded joint for on-orbit, robotic truss assembly is described. An expanded version of this document has been written (10). Mechanical joints for this application have been considered previously (9,14). Welded joints have the advantage of allowing the truss members to carry fluids for active cooling or other purposes. In addition, welded joints can be made more efficient structurally than mechanical joints. Also, welded joints require little maintenance (will not shake loose), and have no slop which would cause the structure to shudder under load reversal. The disadvantages of welded joints are that a more sophisticated assembly robot is required, weld flaws may be difficult to detect on-orbit, the welding process is hazardous, and welding introduces contamination to the environment. In addition, welded joints provide less structural damping than do mechanical joints. Welding on-orbit was first investigated aboard a Soyuz-6 mission in 1969 and then during a Skylab electron beam welding experiment in 1973 (5,15). A hand held electron beam welding apparatus is currently being prepared for use on the MIR space station (8). Presently, Marshall Space Flight Center is evaluating processes appropriate for on-orbit welding (11). A low gravity environment has been found to have very minor effects on the welding processes appropriate for this application. This is based on tests run on-orbit as well as low gravity environments achieved by flying aircraft in parabolic trajectories. In fact, low gravity can make welding easier since the flow of the molten metal is dictated by surface tension effects undisturbed by gravitational forces (11). It appears that a modified form of gas tungsten arc welding (GTAW) will be most appropriate for welding together structures on-orbit (11). The process has been modified to work in a vacuum by providing gas to the arc zone by means of a hollow tungsten electrode with special shielding. A commercial tube welding head has been successfully modified for use on-orbit with a gas leakage rate of approximately 2.5 liters/min (11).

To develop as realistic a joint as possible, a specific truss structure was selected on which to base the design. The structure considered was based on the 120 foot diameter aerobrake tetrahedral truss structure (4,6,9,14). The truss members were assumed to consist of graphite/epoxy tubes. Also, it was assumed that the nodes were constructed of 2219-T87 aluminum alloy. The magnitude of the member load assumed for design purposes was 100 kips.

MEMBER FORCES GENERATED BY RANDOM MEMBER MISFITS

The 660 members of the tetrahedral truss were all 12.56 ft long and consisted of identical graphite/epoxy tubes (elastic modulus = $10.5E6$ psi, shear modulus = $4.0E6$ psi, Poisson's ratio = 0.33, outside diameter = 5 in., wall thickness = 0.375 in.). The truss was 10.25 ft. deep in accordance with the geometric properties of a tetrahedron. No manufacturing or assembly process is absolutely accurate. Thus, after being welded into the truss, the members will tend to be slightly too long or short. These randomly distributed misfits will lock in member forces before service loads are applied and they will also distort the truss to some degree. Before a joint can be designed some measure of an acceptable misfit must be determined which will dictate the accuracy required of the robot and the joint configuration. Member misfits will be randomly distributed so peak member forces can only be determined in a statistical sense. The structure was analyzed 50 times with different randomly generated sets of member misfits, and the mean and standard deviation of the peak member force magnitudes were calculated from these results. The analysis procedure can be summarized as follows. Random member misfits were generated and the associated initial member forces were calculated and stored in a file. Nodal loads due to the initial member forces were calculated and summed up to form a global nodal load vector. The load vector was applied to the structure and the finite

element program was run to calculate a set of intermediate member loads. Finally, the initial member loads were added to the intermediate member loads to produce a set of final member loads.

For a maximum member misfit of 0.02 in. (only 0.013% of the member length), the estimated maximum member force (that will not be exceeded with a 97% level of certainty) was 11.4 kips, which is a significant portion of the design load capacity of 100 kips. Besides generating member forces, random member misfits will distort the structure causing problems for truss structures supporting equipment with fine pointing requirements, and for the heat shield associated with aerobrake structures (3).

NODE SEPARATION INDUCED BY RANDOM MEMBER MISFITS

Here, the effect of member misfits on relative node displacement of a partially assembled truss structure is considered. Misfit induced member forces will cause the truss to distort and thus will force pairs of nodes to move closer together or farther apart from each other. These relative nodal displacements will have to be corrected by the robot during the assembly process. As more members are assembled, relative nodal displacements will tend to increase since there are more member misfits to cause distortion. Thus, the robot will have to make the largest relative nodal displacement corrections while assembling the last few members of the truss.

To correct for these misfit induced relative nodal displacements, the robot will be required to push or pull on pairs of nodes. The magnitude of force required to make these corrections must be estimated because it affects the design of both the robot and the joint. The correction force can only be estimated in a statistical sense since the member misfits are randomly distributed. To be conservative, the correction force required while assembling the last member of the structure was considered. It was assumed that the structure will be assembled from one edge through to a far edge, so the last member would be an edge member. Accordingly, for this relative nodal displacement correction force study, an edge member was removed from the structure described in the previous section. Fifty sets of random member misfits were generated and the robotic force required to reposition the nodes for assembly of the last member was calculated. This analysis indicated that the assembly robot must be capable of pulling or pushing with a force of 3.8 kips (that will not be exceeded with a 97% level of certainty) while attempting to correct for member misfit induced relative node displacements. Here, a maximum possible member length error of 0.02 in. was also assumed.

PRELIMINARY DESIGN OF THE WELDED JOINT

The trusses under consideration here will be robotically assembled on-orbit. This makes it imperative that the truss members and joints be *designed for assembly*. The design should be such that the robot can: transport the member from the storage pallet to the appropriate position on the truss; insert the member between the nodes; correct the node positions for member misfit errors; and weld the member into position. The members and joints must also be light and able to be densely packed together for efficient transport to orbit, a major cost driver. A light design is also necessary to control inertial forces while in service. The joint components must be relatively easy to produce so that manufacturing costs will not be excessive. The joint design must provide a seal so that fluids may be pumped throughout the members of the truss. Based on prior studies (14) it was assumed that the joint must be capable of carrying 100 kips and that the members consist of graphite/epoxy tubes of circular cross section (5 in. outside diameter, 0.375 in. wall thickness).

A major difficulty with the joint design was allowing for the member to be inserted into the nozzles of two nodes that had already been welded into position. This could be handled in two ways. A member could be made precisely the correct length so that it could be positioned between the nozzles (without being inserted) and then welded into place. This approach has two major drawbacks: the joint configuration provides no alignment assistance to the robot; and joint gap control will be difficult. Alternatively, one half of the member could be designed to telescope into the other as shown in Fig. 1. This would allow a member to be shortened (telescoped), placed between the nodes, and then extended so that its ends would fit inside the nozzles of the nodes. This provides for very accurate alignment of the joints and complete control of the weld joint gap. When the joint has been fully made up the joint overlap will be snug against the inside surface of the nozzle of the node and the joint will be temporarily held together by the friction provided by a compressed o-ring. The telescoping action allows for very compact shipment to orbit. A disadvantage of the telescoped member

approach is that three weld joints will now have to be made (at each end and at the sliding joint in the middle) instead of the two required for the nontelescoped design. However, it appears that the telescoped design will make it easier for the robot to assemble and weld up the structure, and so the telescoped design was selected for further study.

A preliminary analysis of the joint using an isotropic finite element model without thermal loading was conducted. The finite element mesh and joint dimensions are displayed in Fig. 2. Axisymmetric elements were used in the analysis. As shown in Fig. 2, the part of the node that the truss member ferrule was welded to was assumed to consist of a nozzle similar to that found in pressure vessels. A design of this nature allows for the easy passage of fluid along the truss member and into the node. This configuration also provides for a very simple and clean design of both the member ferrule, the weld, and the node. However, the nozzle approach is not very efficient structurally since the load path must change abruptly as axial loads run from the member into the node. This produces large bending stresses in the node fitting. Thus, generous fillets and relatively thick components will be required for the design of the node. A GTAW groove weld 0.5 in. deep is required to keep the Von Mises stress level within the heat affected zone to less than the weld metal yield stress of 26 ksi (16).

For many applications, the ideal design of the graphite/epoxy strut will consist of laying up the fibers such that they are oriented at $\pm 10^\circ$ with respect to the axis of the member (4). This layup will provide for high stiffness and strength parallel to the axis of the member, along with a slightly negative axial coefficient of thermal expansion. The slightly negative coefficient of thermal expansion of the struts, coupled with the relatively large positive coefficient of thermal expansion of the aluminum fittings can produce members with a net axial coefficient of thermal expansion of zero. This is highly desirable in spacecraft since it prevents temperature changes from causing structural distortions. However, a $\pm 10^\circ$ layup will create some problems, especially in applications where the composite material must be attached to a metallic component in an environment where there will be large temperature changes, as is the case here. In this study it was assumed that during the mission temperature variations as large as $\pm 250^\circ\text{F}$ could occur. The primary difficulty with this type of joint is that the coefficient of thermal expansion of the composite material in the circumferential direction is five times that of the aluminum. Fig. 2. shows a double scarf joint for the composite strut - aluminum ferrule connection. This scarf joint was subsequently redesigned due to concerns about manufacturability and thermal loading capacity. The redesigned joint is still under development.

CONCLUSIONS

On the basis of this study the following conclusions were reached:

1. Member length errors should be carefully controlled in large truss structures. Member length errors can lock in large stresses and structural distortions before service loads are applied. Distortions may cause problems for instruments with accurate pointing requirements. Distortions may also disturb the flow of hot gases over an aerobrake heat shield.
2. The assembly robot will need to be designed to exert relatively large forces while building the truss structure. The assembly robot will also require an accurate device for ensuring that the member length is correct before welding.
3. The telescoping member and joint overlap with o-ring approach seems to be a workable technique for positioning the truss members before welding. It is important that the joint system be *designed for assembly*.
4. A modified GTAW process appears to be a feasible technique for the automated welding of aluminum components on-orbit.
5. A 0.5 in. thick groove weld will be required to carry the design loads. This weld will be made in three passes.
6. A good design for the graphite/epoxy strut - aluminum end fitting joint is difficult to obtain because of the differential thermal expansion problem. Temperature changes during the mission should be minimized.

REFERENCES

1. Braun, R. D., and Blersch, D. J. "Propulsive Options for a Manned Mars Transportation System," AIAA/ASME/SAE/ASEE 25th Joint Propulsion Conference, Monterey, CA, Paper No. AIAA-89-2950, 1989.

2. Cirillo, W. M., Kaszubowski, M. J., Ayers, J. K., Llewellyn, C. P., Weidman, D. J., and Meredith, B. D. "Manned Mars Mission Accommodation - Sprint Mission," NASA TM-100598, 1988.
3. Dorsey, J. T., and Mikulas, M. M. "Preliminary Design of a Large Tetrahedral Truss/Hexagonal Heatshield Panel Aerobrake," NASA TM 101612, 1989.
4. Dorsey, J. T., and Mikulas, M. M. "Preliminary Design of a Large Tetrahedral Truss/Hexagonal Panel Aerobrake Structural System," 31st Structures, Structural Dynamics, and Materials Conference, Long Beach, CA, AIAA Paper No. 90-1050, 1990.
5. McKannan, E. C., and Poorman, R. M. "Skylab M551 Metal Melting Experiment," Proceedings of the 3rd Space Processing Symposium on Skylab Results, Vol. 1., 1976, pp. 85-100.
6. Mikulas, M. M., Bush, H. G., and Card, M. F. "Structural Stiffness, Strength, and Dynamic Characteristics of Large Tetrahedral Space Truss Structures," NASA TM X-74001, 1977.
7. Mikulas, M. M., and Dorsey, J. T. "An Integrated In-Space Construction Facility for the 21st Century," NASA TM-101515, 1988.
8. Paton, B. "State-of-Art and Prospects of Development of Aerospace Engineering in the USSR," Conference on Welding in Space and the Construction of Space Vehicles, American Welding Society, 1991, pp. 1-11.
9. Rhodes, M. D., Will, R. W., Wise, M. A. "A Telerobotic System for Automated Assembly of Large Space Structures," NASA TM-101518, 1989.
10. Rule, W. K., and Thomas, F. P. "Design of a Welded Joint for Robotic, On-Orbit Assembly of Space Trusses," to be submitted for publication as a NASA Technical Memorandum.
11. Russel, C., Poorman, R., Jones, C., Nunes, A., and Hoffman, D. "Considerations of Metal Joining Processes for Space Fabrication, Construction, and Repair," Proceedings of the 23rd International SAMPE Technical Conference, Kiamesha Lake, NY, 1991.
12. Thomson, M. "Orbital Construction Design Data Book," Astro Aerospace Corporation, Carpinteria, CA, AAC-TN-1160, 1991.
13. Walberg, G. D. "A Review of Aerobraking for Mars Missions," 39th Congress of the International Astronautical Federation, Bangalore, India, Paper No. IAF-88-196, 1988.
14. Williamsen, J., Thomas, F., Finckenor, J., and Spiegel, B. "Definition of Large Components Assembled On-Orbit and Robot Compatible Joints," NASA TM-100395, 1990.
15. "MSFC Skylab Corollary Experiment System, Mission Evaluation," NASA TM x-64820, 1974.
16. Saunders, H. L. "Welding Aluminum: Theory and Practice," the Aluminum Association, 1989, pp. 8.1-8.11.

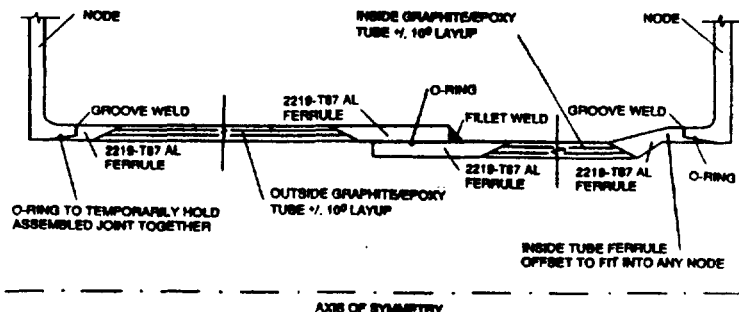


Fig. 1 Truss Member Telescoping Design Concept

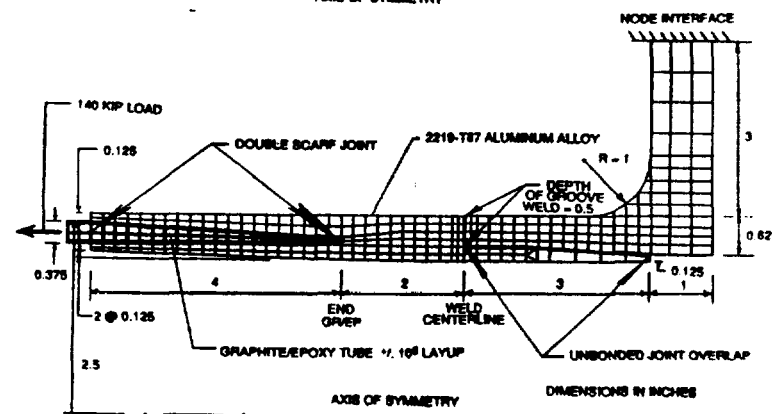


Fig. 2 Finite Element Model of Preliminary Joint Design

1992

NASA / ASEE SUMMER FACULTY FELLOWSHIP PROGRAM

MARSHALL SPACE FLIGHT CENTER
THE UNIVERSITY OF ALABAMA

ELECTROMAGNETIC SCATTERING IN CLOUDS

Prepared by:	Richard Solakiewicz
Academic Rank:	Assistant Professor
Institution and Department:	Chicago State University Department of Mathematics and Computer Science
NASA / MSFC:	
Laboratory:	Space Science
Division:	Earth Sciences / Applications
Branch:	Remote Sensing
MSFC Colleagues:	William Koshak Richard Blakeslee Hugh Christian

Techniques used to explain the nature of the optical effects of clouds on the light produced by lightning include a Monte Carlo simulation (10), an equivalent medium approach (6), and methods based on Boltzmann transport theory (4, 7). A cuboidal cloud has been considered using transform methods (7) and a diffusion approximation (4).

Many simplifying assumptions have been used by authors to make this problem tractable. In this report, the cloud will have a spherical shape and its interior will consist of a uniform distribution of identical spherical water droplets. The source will be modeled as a Hertz dipole, electric or magnetic, inside or outside the cloud. An impulsive source is used. Superposition may be employed to obtain a sinusoid within an envelope which describes a lightning event. The problem is investigated by transforming to the frequency domain, obtaining Green's functions, and then using the Cagniard-DeHoop method (3) to symbolically recover the time domain solution.

The Hertz dipole potential may be derived from a wave equation whose source is proportional to the dipole moment per unit volume,

$$\mathbf{P} = N\mathbf{p}, \quad \mathbf{p} = Q\mathbf{s}, \quad [1]$$

where N is the number of dipoles per unit volume and \mathbf{p} is the dipole moment of a single dipole constructed from equal and opposite charges of magnitude Q separated by a distance s oriented along $\hat{\mathbf{s}}$. From Maxwell's equations, it is possible to show that the electric Hertz vector is the solution to

$$\nabla^2 \mathbf{\Pi} - \mu\epsilon \frac{\partial^2 \mathbf{\Pi}}{\partial t^2} = -\frac{\mathbf{P}}{\epsilon}. \quad [2]$$

The resulting electric and magnetic fields may be written in terms of $\mathbf{\Pi}$ by

$$\mathbf{H} = \epsilon \nabla \wedge \frac{\partial \mathbf{\Pi}}{\partial t}, \quad \mathbf{E} = \nabla \nabla \cdot \mathbf{\Pi} - \mu\epsilon \frac{\partial^2 \mathbf{\Pi}}{\partial t^2}. \quad [3]$$

Similarly, for a magnetic dipole,

$$\nabla^2 \mathbf{\Pi}_m - \mu\epsilon \frac{\partial^2 \mathbf{\Pi}_m}{\partial t^2} = -\mathbf{M}, \quad \mathbf{E} = \mu \nabla \wedge \frac{\partial \mathbf{\Pi}_m}{\partial t}, \quad \mathbf{H} = \nabla \nabla \cdot \mathbf{\Pi}_m - \mu\epsilon \frac{\partial^2 \mathbf{\Pi}_m}{\partial t^2}. \quad [4]$$

The symbols are defined as in (9). Polarizations may be induced in a dielectric by the fields. The dipole moments used above are considered to be controlled only by the source. The sources will be taken to be unit pulses (polarizations per unit time),

$$\mathbf{P} = \delta(\mathbf{r} - \mathbf{r}')\delta(t - t')\hat{\mathbf{p}}, \quad \mathbf{M} = \delta(\mathbf{r} - \mathbf{r}')\delta(t - t')\hat{\mathbf{p}}_m. \quad [5]$$

Superposition may be used to construct fields due to general temporal and spatial dependencies.

In the following, script variables will denote quantities in the frequency domain. They are related to the time domain variables through

$$\mathbf{E}(\mathbf{r}, t) = \int_{-\infty}^{\infty} d\omega \vec{\mathcal{E}}(\mathbf{r}, \omega) e^{-i\omega(t-t')}, \quad \mathbf{H}(\mathbf{r}, t) = \int_{-\infty}^{\infty} d\omega \vec{\mathcal{H}}(\mathbf{r}, \omega) e^{-i\omega(t-t')}. \quad [6]$$

The transforms of the Hertz potentials are given by

$$\bar{\pi} = \frac{iK}{4\pi\epsilon} h_0^{(1)}(KR)\hat{\mathbf{p}}, \quad \bar{\pi}_m = \frac{iK}{4\pi} h_0^{(1)}(KR)\hat{\mathbf{p}}_m, \quad h_0^{(1)}(x) = \frac{e^{ix}}{ix}, \quad K^2 = \omega^2\mu\epsilon, \quad [7]$$

where $R = |\mathbf{r} - \mathbf{r}'|$, \mathbf{r} is an observation point and \mathbf{r}' is a source point. The electric and magnetic fields due to these dipoles are given by

$$\begin{aligned}\vec{\mathcal{E}} &= \frac{iK}{4\pi\epsilon} \left\{ \left(iK - \frac{1}{R} \right) (\hat{\mathbf{p}} \cdot \nabla) \nabla R + \left(-K^2 - \frac{2iK}{R} + \frac{2}{R^2} \right) [(\hat{\mathbf{p}} \cdot \nabla) R] \nabla R + K^2 \hat{\mathbf{p}} \right\} h_0^{(1)}(KR), \\ \vec{\mathcal{H}} &= \frac{K\omega}{4\pi} \left(iK - \frac{1}{R} \right) (\nabla R \wedge \hat{\mathbf{p}}) h_0^{(1)}(KR),\end{aligned}\quad [8]$$

where $\vec{\mathcal{E}}_m$ and $\vec{\mathcal{H}}_m$ are obtained from $\vec{\mathcal{H}}$ and $\vec{\mathcal{E}}$ by replacing $\frac{K\omega}{4\pi}$ by $-\frac{K^3}{4\pi\omega\epsilon}$ and $\frac{iK\omega}{4\pi\epsilon}$ by $\frac{iK}{4\pi}$. The electric and magnetic field vectors may be written in terms of Hansen's functions (5) as

$$\begin{aligned}\vec{\mathcal{E}} &= \frac{iK^3}{4\pi\epsilon} \sum Q_n^m [\mathbf{M}_{mn}^3(K, \mathbf{r}) \mathbf{M}_{-mn}^1(K, \mathbf{r}') + \mathbf{N}_{mn}^3(K, \mathbf{r}) \mathbf{N}_{-mn}^1(K, \mathbf{r}')] \cdot \hat{\mathbf{p}}, \\ \sum &\equiv \sum_{n=1}^{\infty} \sum_{m=-n}^n, \quad Q_n^m = \frac{(2n+1)(-1)^m}{n(n+1)}, \quad r > r'\end{aligned}\quad [9]$$

for an electric dipole source; the magnetic field is obtained from $\vec{\mathcal{E}}$ by replacing $\frac{iK^3}{4\pi\epsilon}$ by $\frac{K^2\omega}{4\pi}$ and interchanging $\mathbf{M}_{-mn}^1(K, \mathbf{r}')$ and $\mathbf{N}_{-mn}^1(K, \mathbf{r}')$. The superscript 1 denotes a Hansen function containing regular (Bessel type) functions; 3 refers to outgoing (Hankel type) functions. Analogous forms for fields due to magnetic sources are obtained by replacing the constants to the left of the summations by $-\frac{K^4}{4\pi\epsilon\omega}$ and $\frac{iK^3}{4\pi}$ respectively and interchanging $\mathbf{M}_{-mn}^1(K, \mathbf{r}')$ and $\mathbf{N}_{-mn}^1(K, \mathbf{r}')$ again. If $r < r'$, the corresponding vectors in [9] are interchanged.

If the medium inside the cloud is specified by $K(\mu, \epsilon)$ and that outside the cloud by $k(\mu_o, \epsilon_o)$ and the cloud is taken to be a sphere of radius a , the fields may be written as $\vec{\mathcal{G}}_e^e = \vec{\mathcal{E}}^s + \vec{\mathcal{E}}^i$, $\vec{\mathcal{G}}_m^e = \vec{\mathcal{E}}_m^s + \vec{\mathcal{E}}_m^i$, $\vec{\mathcal{G}}_e^h = \vec{\mathcal{H}}^s + \vec{\mathcal{H}}^i$, $\vec{\mathcal{G}}_m^h = \vec{\mathcal{H}}_m^s + \vec{\mathcal{H}}_m^i$, where the superscript on the $\vec{\mathcal{G}}$'s indicates whether the Green's function corresponds to the electric or magnetic field and the subscript indicates the type of source. The superscripts i and s refer to the source (i) or the scattered field (s). Green's functions for external excitation (1), which were obtained by enforcing continuity of the tangential components of the fields across the boundary, may be easily modified to work for sources inside a sphere. Explicit results for an electric dipole source are given by

$$\vec{\mathcal{G}}_e^e = \frac{iK^3}{4\pi\epsilon} \left\{ \begin{aligned} &\sum Q_n^m \left\{ \mathbf{M}_{mn}^1(K, \mathbf{r}) [\mathbf{M}_{-mn}^3(K, \mathbf{r}') + a_n \mathbf{M}_{-mn}^1(K, \mathbf{r}')] \right. \\ &\quad \left. + \mathbf{N}_{mn}^1(K, \mathbf{r}) [\mathbf{N}_{-mn}^3(K, \mathbf{r}') + b_n \mathbf{N}_{-mn}^1(K, \mathbf{r}')] \right\}, \quad r < r', \\ &\sum Q_n^m \left\{ [\mathbf{M}_{mn}^3(K, \mathbf{r}) + a_n \mathbf{M}_{mn}^1(K, \mathbf{r}')] \mathbf{M}_{-mn}^1(K, \mathbf{r}') \right. \\ &\quad \left. + [\mathbf{N}_{mn}^3(K, \mathbf{r}) + b_n \mathbf{N}_{mn}^1(K, \mathbf{r}')] \mathbf{N}_{-mn}^1(K, \mathbf{r}') \right\}, \quad r' < r < a, \\ &\sum Q_n^m [c_n \mathbf{M}_{mn}^3(k, \mathbf{r}) \mathbf{M}_{-mn}^1(K, \mathbf{r}') + d_n \mathbf{N}_{mn}^3(k, \mathbf{r}) \mathbf{N}_{-mn}^1(K, \mathbf{r}')] , \quad r > a \end{aligned} \right\} \quad [10]$$

when the source is inside the sphere ($r' < a$) and

$$\vec{\mathcal{G}}_e^e = \frac{ik^3}{4\pi\epsilon_o} \left\{ \begin{aligned} &\sum Q_n^m [a_n \mathbf{M}_{mn}^1(K, \mathbf{r}) \mathbf{M}_{-mn}^3(k, \mathbf{r}') + b_n \mathbf{N}_{mn}^1(K, \mathbf{r}) \mathbf{N}_{-mn}^3(k, \mathbf{r}')] , \quad r < a, \\ &\sum Q_n^m \left\{ [\mathbf{M}_{mn}^1(k, \mathbf{r}) + c_n \mathbf{M}_{mn}^3(k, \mathbf{r}')] \mathbf{M}_{-mn}^3(k, \mathbf{r}') \right. \\ &\quad \left. + [\mathbf{N}_{mn}^1(k, \mathbf{r}) + d_n \mathbf{N}_{mn}^3(k, \mathbf{r}')] \mathbf{N}_{-mn}^3(k, \mathbf{r}') \right\}, \quad a < r < r', \\ &\sum Q_n^m \left\{ \mathbf{M}_{mn}^3(k, \mathbf{r}) [\mathbf{M}_{-mn}^1(k, \mathbf{r}') + c_n \mathbf{M}_{-mn}^3(k, \mathbf{r}')] \right. \\ &\quad \left. + \mathbf{N}_{mn}^3(k, \mathbf{r}) [\mathbf{N}_{-mn}^1(k, \mathbf{r}') + d_n \mathbf{N}_{-mn}^3(k, \mathbf{r}')] \right\}, \quad r > r' \end{aligned} \right\} \quad [11]$$

when the dipole is outside the cloud. The associated magnetic fields are obtained by replacing $\frac{iK^3}{4\pi\epsilon}$ and $\frac{ik^3}{4\pi\epsilon_0}$ by $\frac{K^2\omega}{4\pi}\{1+(\beta-1)H(r-a)\}$ and $\frac{k^2\omega}{4\pi}\left\{1+\left(\frac{1}{\beta}-1\right)H(a-r)\right\}$, $\beta = \sqrt{\frac{\mu\epsilon_0}{\mu_0\epsilon}}$, where H is the Heavyside function, respectively and interchanging those M's and N's which are functions of \mathbf{r} but not those which are functions of \mathbf{r}' . Vector fields are recovered by inner multiplication with the source polarization from the right (i.e., $\vec{\mathcal{G}} = \vec{\mathcal{G}} \cdot \hat{\mathbf{p}}$). If the source is a magnetic dipole, $\vec{\mathcal{G}}_m^e$ and $\vec{\mathcal{G}}_m^h$ are obtained from $\vec{\mathcal{G}}_e^e$ and $\vec{\mathcal{G}}_e^h$ by replacing $\frac{iK^3}{4\pi\epsilon}$, $\frac{K^2\omega}{4\pi}$, $\frac{ik^3}{4\pi\epsilon_0}$, and $\frac{k^2\omega}{4\pi}$ by $-\frac{K^4}{4\pi\epsilon\omega}$, $\frac{iK^3}{4\pi}$, $-\frac{k^4}{4\pi\epsilon_0\omega}$, and $\frac{ik^3}{4\pi}$ respectively and interchanging only those M's and N's which are functions of \mathbf{r}' . The constants are given by

$$\begin{aligned} a_n &= \frac{\beta \frac{h_n}{\mathfrak{r}} (\mathfrak{r} h_n)' - \frac{h_n}{x} (x h_n)'}{\frac{h_n}{x} (x j_n)' - \beta \frac{i a_n}{\mathfrak{r}} (\mathfrak{r} h_n)'}, & b_n &= \frac{\beta \frac{h_n}{x} (x h_n)' - \frac{h_n}{\mathfrak{r}} (\mathfrak{r} h_n)'}{\frac{i a_n}{\mathfrak{r}} (\mathfrak{r} h_n)' - \beta \frac{h_n}{x} (x j_n)'}, \\ c_n &= \frac{\frac{h_n}{x} (x j_n)' - \frac{i a_n}{x} (x h_n)'}{\frac{h_n}{x} (x j_n)' - \beta \frac{i a_n}{\mathfrak{r}} (\mathfrak{r} h_n)'}, & d_n &= \frac{\frac{i a_n}{x} (x h_n)' - \frac{h_n}{x} (x j_n)'}{\frac{i a_n}{\mathfrak{r}} (\mathfrak{r} h_n)' - \beta \frac{h_n}{x} (x j_n)'}, \end{aligned} \quad [12]$$

$$x = ka, \quad \mathfrak{r} = Ka, \quad j_n = j_n(x), \quad \mathcal{J}_n = j_n(\mathfrak{r}), \quad h_n = h_n^{(1)}(x), \quad \mathfrak{h}_n = h_n^{(1)}(\mathfrak{r}).$$

The constants a_n and b_n are obtained from c_n and d_n respectively by multiplying by β and interchanging h_n with \mathcal{J}_n , x with \mathfrak{r} , and j_n with \mathfrak{h}_n ; constants c_n and d_n are obtained from a_n and b_n respectively by multiplying by -1 and interchanging h_n with \mathcal{J}_n and \mathfrak{h}_n with j_n . The abovementioned interchanges apply only to the respective numerators. Allowing $r \sim \infty$ and using asymptotic forms for the Hansen's functions gives explicit forms for the far-field scattering amplitudes \tilde{g} . Obtaining \tilde{g} for external excitation of a water droplet allows calculation of the bulk parameters of the cloud using the methods described in (6).

A dyadic version of Helmholtz's surface integral representation as given in (11) for $\vec{\psi} = \vec{\mathcal{E}}^e$ or $\vec{\mathcal{E}}^h$,

$$\begin{aligned} \vec{\psi}(\mathbf{r}, \mathbf{r}') &= \int_S dS(\hat{\mathbf{r}}_s) \left\{ \left[\nabla_s \wedge \vec{\mathcal{G}}(\mathbf{r}-\mathbf{r}_s) \right]^T \cdot \left[\hat{\mathbf{n}} \wedge \vec{\psi}(\mathbf{r}_s, \mathbf{r}') \right] \right. \\ &\quad \left. - \left[\hat{\mathbf{n}} \wedge \vec{\mathcal{G}}(\mathbf{r}-\mathbf{r}_s) \right]^T \cdot \left[\nabla_s \wedge \vec{\psi}(\mathbf{r}_s, \mathbf{r}') \right] \right\} \equiv \left\{ \vec{\mathcal{G}}, \vec{\psi} \right\}, \\ \vec{\mathcal{G}}(\mathbf{r}-\mathbf{r}_s) &= \frac{3ik}{8\pi} \left(\vec{\mathbb{I}} + \frac{\nabla\nabla}{k^2} \right) h, \quad h = h_o^{(1)}(kR), \quad \mathbf{R} = \mathbf{r} - \mathbf{r}_s, \end{aligned} \quad [13]$$

where ∇_s operates on the variables associated with \mathbf{r}_s on the surface S of the scatterer and T denotes the transpose, may be used with the asymptotic form of h to obtain

$$\vec{\mathcal{G}} = -\frac{3ik}{8\pi} (\vec{\mathbb{I}} - \hat{\mathbf{r}}\hat{\mathbf{r}}) h, \quad \vec{\psi}(\mathbf{r}, \mathbf{r}') = h\tilde{g}(\hat{\mathbf{r}}, \mathbf{r}'), \quad \tilde{g} = \frac{3}{8\pi ik} \left\{ (\vec{\mathbb{I}} - \hat{\mathbf{r}}\hat{\mathbf{r}}) e^{-ik\hat{\mathbf{r}}\cdot\mathbf{r}_s}, \vec{\psi}(\mathbf{r}_s, \mathbf{r}') \right\}. \quad [14]$$

Here, \mathbf{r} , \mathbf{r}_s , and \mathbf{r}' refer to vectors to the observation point, surface point, and source point respectively. Using Sommerfeld's integral representation (12) for h , we write

$$\left(\vec{\mathbb{I}} + \frac{\nabla\nabla}{k^2} \right) h = \frac{1}{2\pi} \int_c d\Omega_c (\vec{\mathbb{I}} - \hat{\mathbf{r}}_c \hat{\mathbf{r}}_c) e^{ik\hat{\mathbf{r}}_c \cdot (\mathbf{r}-\mathbf{r}_s)}, \quad [15]$$

in [13], interchange the order of integration, and recognize \tilde{g} from [14] to obtain

$$\vec{\psi}(\mathbf{r}, \mathbf{r}') = \frac{1}{2\pi} \int_c d\Omega_c e^{ik\hat{\mathbf{r}}_c \cdot \mathbf{r}} [\tilde{g}(\hat{\mathbf{r}}_c, \mathbf{r}')]. \quad [16]$$

This spectral representation is valid for r greater than the scatterer's projection on $\hat{\mathbf{r}}$.

Substituting the form of \tilde{g} obtained from [10, 11] together with asymptotic representations for Hansen's functions in [16] or, equivalently, using Sommerfeld type complex contour integral representations for the M's and N's (5) which are functions of \mathbf{r} gives

$$\tilde{\psi}(\mathbf{r}, \mathbf{r}') = \sum A_n^m(\omega) \bar{\mathbf{R}}_{-mn}(\eta K, \mathbf{r}') \frac{1}{2\pi} \int_c d\Omega_c e^{ik\hat{\mathbf{r}}_c \cdot \mathbf{r}} \bar{\mathbf{S}}_{-mn}(\hat{\mathbf{r}}_c), \quad [17]$$

where $\bar{\mathbf{R}}$ is M or N, $\bar{\mathbf{S}}$ is B or C, and $\eta k = K$; A involves the coefficients in [12]. Rotating the coordinate system so that $\hat{\mathbf{r}}$ is parallel to $\hat{\mathbf{z}}$, we obtain $\hat{\mathbf{r}}_c \cdot \mathbf{r} = r \cos \theta_c$. In this form, the time domain solution may be written in a symbolic form by inspection (3). We obtain, for $ct > R$,

$$\tilde{\psi}(\mathbf{r}, \mathbf{r}', t) = - \sum A_n^m \left(\frac{i}{c} \frac{\partial}{\partial t} \right) \bar{\mathbf{R}}_{-mn} \left[\frac{i\eta}{c} \left(\frac{\partial}{\partial t} \right), \mathbf{r}' \right] \left\{ \frac{\int_0^{2\pi} d\varphi \bar{\mathbf{S}}_{-mn} [P_n^m(\frac{ct}{R})]}{[t^2 - (\frac{R}{c})^2]^{\frac{1}{2}}} \right\}. \quad [18]$$

When $ct < R$, $\tilde{\psi} = 0$. The sum is to be taken over all relevant combinations and the forms containing derivatives are to be expanded in a series and operate from left to right.

ACKNOWLEDGMENT

The author expresses his appreciation to William Koshak, Richard Blakeslee, Hugh Christian, and Dieudonne Phanord for their time, help, and ideas during his appointment as a NASA / ASEE Summer Faculty Fellow. The financial support of the NASA / ASEE Summer Faculty Fellowship Program and the assistance of Gerald F. Karr, Michael Freeman, Director and Frank Six, Administrator, are gratefully acknowledged.

REFERENCES

1. Asvestas, J. S. et al, *Electromagnetic and Acoustic Scattering by Simple Shapes*, Hemisphere Pub., NY (1987).
2. Felsen, L. B., et al, *Transient Electromagnetic Fields*, Springer—Verlag, Berlin (1976).
3. Felsen, L. B., "Transient solutions for a class of scattering problems", *Quart. Appl. Math.*, 23 (1965) 151-169.
4. Koshak, W., et al, "A diffusion model for lightning radiative transfer", To be submitted to *J. Geophys. Res.*
5. Morse, P. M. and Feshbach, H., *Methods of Theoretical Physics*, McGraw Hill, NY (1953).
6. Phanord, D. D., "Analytical optical scattering in clouds", NASA Report NASA CR-184044, (xxxvi) (1990).
7. Solakiewicz, R., "Transport of photons produced by lightning in clouds", NASA Report NASA NGT-01-008-021 (TT) (1991).
8. Sommerfeld, A., *Partial Differential Equations in Physics*, Academic Press, NY (1949).
9. Stratton, J., *Electromagnetic Theory*, McGraw Hill, NY (1941).
10. Thomason, L. W. and Krider, E. P., "The effect of clouds on the light produced by lightning", *J. Atmos. Sci.*, 39 (1982) 2051-2065.
11. Twersky, V., "On a general class of scattering problems", *J. Math. Phys.*, 3 (1962) 716-723.
12. Twersky, V., "Multiple scattering of electromagnetic waves by arbitrary configurations", *J. Math. Phys.*, 8 (1967) 589-610.

1992

NASA/ASEE SUMMER FACULTY FELLOWSHIP PROGRAM

MARSHALL SPACE FLIGHT CENTER
THE UNIVERSITY OF ALABAMA

RELIABILITY EVALUATION METHODOLOGY FOR NASA APPLICATIONS

Prepared By: Vidya S. Taneja, Ph.D.
Academic Rank: Professor
Institution and Department: Western Illinois University
Department of Mathematics
NASA/MSFC:
Office: System Safety and Reliability
Division: Reliability & Maintainability
Engineering
Branch: Analysis Branch
MSFC Colleague(s): Fayssal Safie, Ph.D.
William C. Smith
Frank Pizzano

1. Introduction

Liquid rocket engine technology has been characterized by the development of complex systems containing large number of sybsystems, components, and parts. The trend to ever larger and more complex systems is continuing. The liquid rocket engineers have been focusing mainly on performance driven designs to increase payload delivery of a launch vehicle for a given mission. In otherwords, although the failure of a single inexpensive part or component may cause the failure of the system, reliability in general has not been considered as one of the system parameters like cost or performance. Up till now, quantification of reliability has not been a consideration during system design and development in the liquid rocket industry. Engineers and managers have long been aware of the fact that the reliability of the system increases during development, but no serious attempts has been made to quantify reliability. As a result, a method to quantify reliability during design and development is needed. This includes application of probabilistic models which utilize both engineering analysis and test data.

Classical methods require the use of operating data for reliability demonstration. In contrast, the method described in this paper is based on similarity, analysis, and testing combined with Bayesian statistical analysis.

2. Reliability Evaluation Process

In general, due to the costly testing of a liquid rocket engine, it is not feasible to establish high reliability based on test only. Traditionally, reliability has been incorporated in the design using safety factor information. But, safety factors do not provide adequate assessments of reliability which takes into consideration all of the available information from historcal data, engineering analysis, and test is needed for reliability evaluation. The following is a description of a reliability evaluation process based on the three above mentioned sources of information.

The reliability evaluation process shown in figure 1 consists of two major steps. The two steps are predicting reliability during design and verifying it during development (segment 1) and certification (segment 2).

The reliability prediction begins with defining reliability requirements, followed by a design selection process which involves evaluating alternative designs to obtain a base design. For a given base design, a preliminary failure mode effects analysis (FMEA) is then performed. FMEA is then used to identify all failure modes relevant to predicting the engine design reliability. The failure modes identified are used with historical database and engineering analysis to predict design reliability.

The predicted reliability is checked against the requirements to determine if the targeted design reliability is met. If target is not met, feasibility of design changes are investigated. If design changes are not feasible, a formal management decision is required.

After the completion of the reliability prediction phase, the process goes into development phase (segment 1) which is the first part of the reliability verification step. The development phase, in general, consists of lower level testing, which includes part and component testing. Some system testing is also done to a limited extent in the development phase. The testing during this phase is mainly intended to verify assumptions and resolve concerns identified during the design reliability prediction phase. Also, a reliability growth and management system is established during this phase to continually evaluate reliability as more testing data becomes available.

Following the development phase, the certification phase (segment 2) emphasize system level testing. The test data obtained during this phase is used to update system reliability predicted earlier. The updated reliability is then compared to the reliability requirement. If reliability requirement is not met, a formal management decision is required. Otherwise, the reliability evaluation process is considered complete with respect to the readiness for flight.

3. Reliability Prediction

The reliability prediction is part of the overall reliability assessment process shown in figure 2. The assessment process consist of predicting reliability using FMEA in conjunction with historical databases and other engineering analyses such as structural analysis. The predicted reliability is then compared to the target value. Failure to meet the target requires management action to reallocate reliability, change the design, change the process, perform additional tests, or simply to accept system reliability as is.

4. Reliability Verification

The reliability verification process discussed in this report is based on predicting reliability during design and verifying reliability during testing (development and certification) as shown in figure 3. During the design phase of the STME, information relevant to the estimation of reliability will be available from different sources at different levels. This information is combined in computing an estimate of the STME reliability. This estimated reliability is updated as test data on the engine become available using Bayesian method as described in figure 4.

Specifically, the reliability verification process uses information from similarity and analysis in the form of a prior and combines this information with the test via the Bayesian analysis to estimate reliability as shown in figure 4.

Referring back to figure 3, other reliability verification is done using DOE and other tools at part and the component level. This includes verifying prediction assumptions and resolving concerns raised during prediction. It should be noted that the prediction process just described also provide a reliability audit trail. This includes complete history of various assumptions used, concerns noted, and data sources.

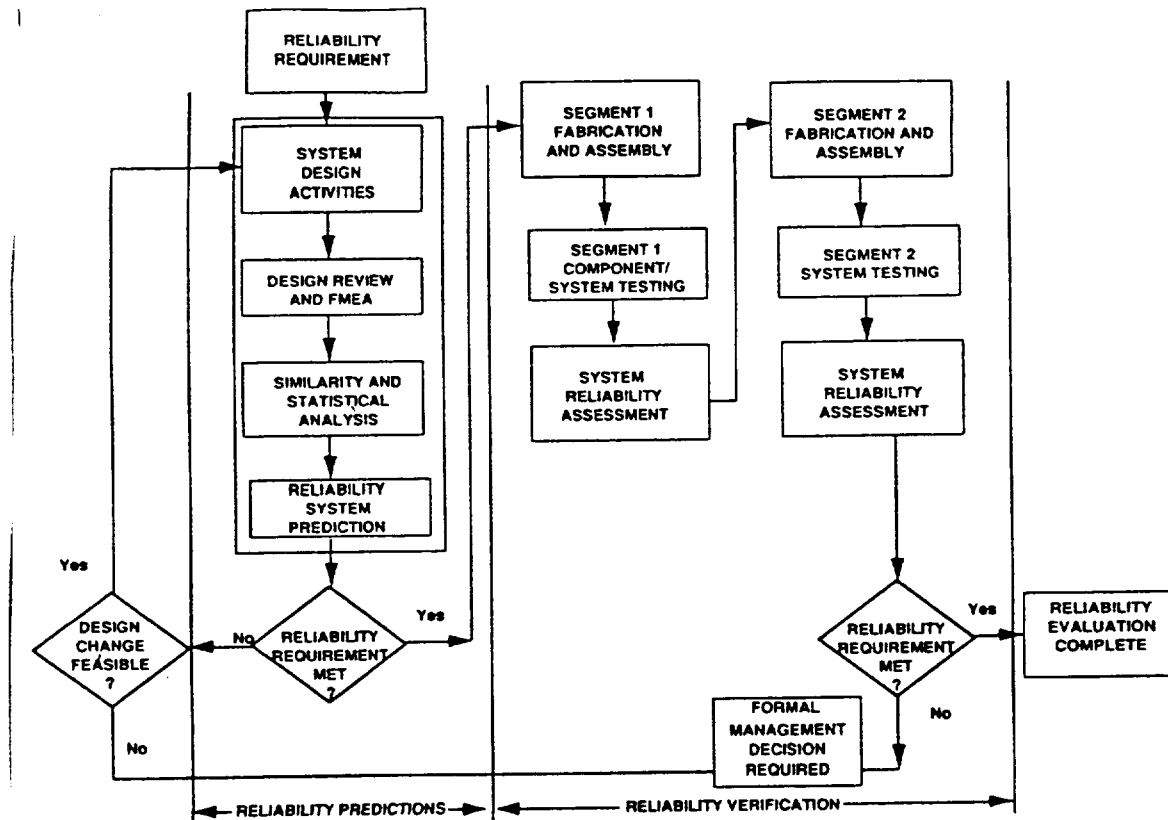


FIGURE 1: RELIABILITY EVALUATION PROCESS

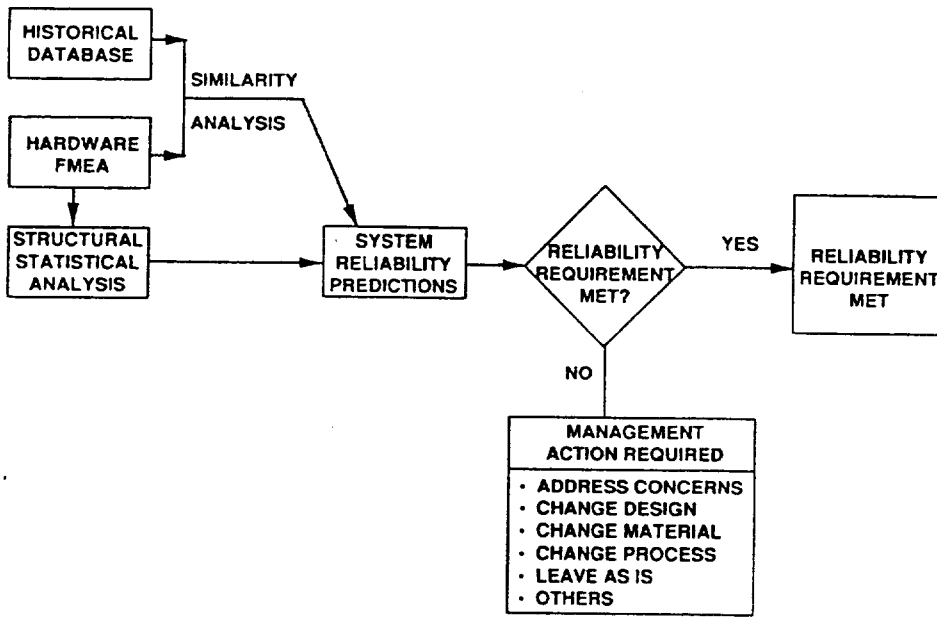


FIGURE 2: RELIABILITY ASSESSMENT PROCESS

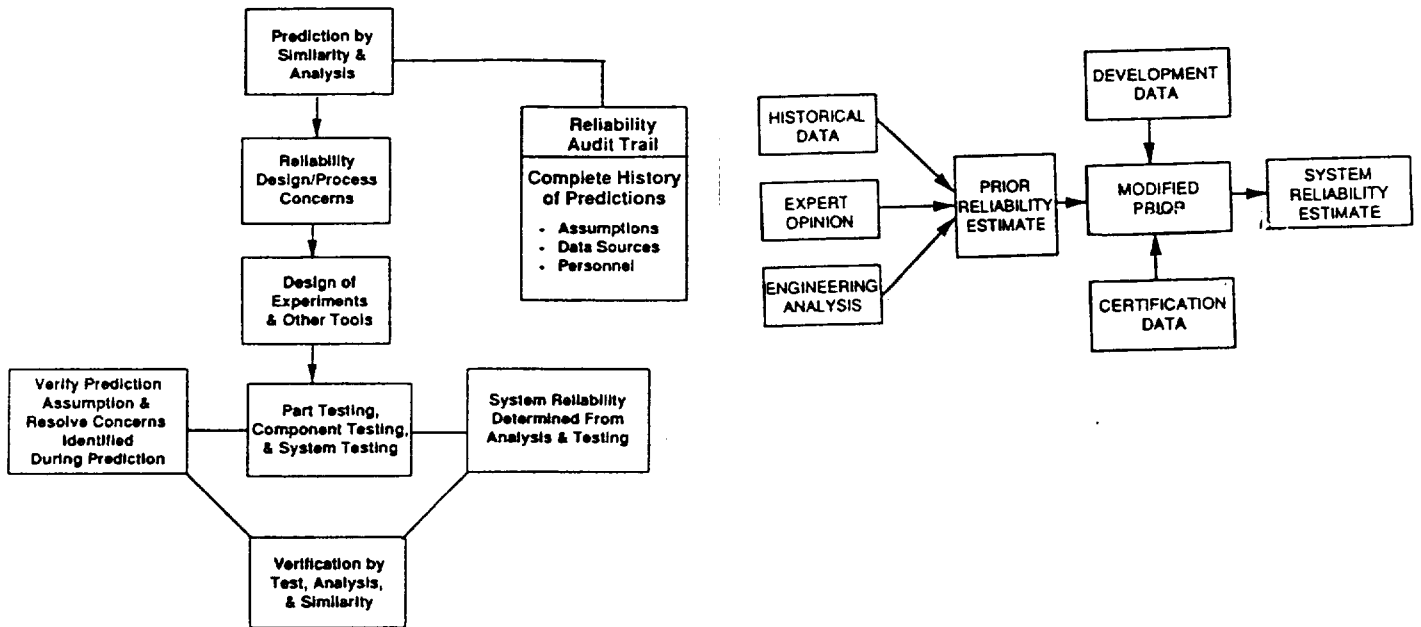


FIGURE 3: RELIABILITY VERIFICATION PROCESS

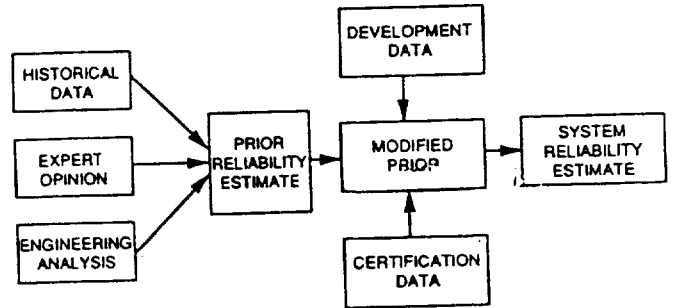


FIGURE 4: BAYESIAN RELIABILITY PROCESS

1992

NASA/ASEE SUMMER FACULTY FELLOWSHIP PROGRAM

MARSHALL SPACE FLIGHT CENTER
THE UNIVERSITY OF ALABAMA

ACCELERATION OF FDNS FLOW SIMULATIONS
USING INITIAL FLOWFIELDS GENERATED
WITH A PARABOLIZED NAVIER-STOKES METHOD

Prepared By: Peter W. TenPas, Ph.D.

Academic Rank: Assistant Professor

Institution and
Department: The University of Kansas
Department of Mechanical Engineering

NASA/MSFC:

Office: Structures & Dynamics Laboratory
Division: Aerophysics
Branch: Computational Fluid Dynamics

MSFC Colleagues: Ten-See Wang, Ph.D.
Paul K. McConnaughey, Ph.D.

INTRODUCTION

The capability of computational fluid dynamics (CFD) analysis to predict complex flowfields has been greatly advanced by the widespread use of flow simulation programs based on the Navier-Stokes (NS) equations. The flow physics are theoretically well represented, and with proper care the numerical solution should not introduce appreciable uncertainties. However, the computational cost of a typical simulation in terms of both memory and execution time are large by current standards. Therefore, the efficiency of the numerical algorithm in solving the set of model equations is one factor determining the usefulness of CFD tools. The objective of the present study is to reduce the execution time of the FDNS flow simulation code by using the parabolized Navier-Stokes (PNS) equations to provide a "good" starting condition. The technique is not universal, however the PNS model can be applied to convection dominated flows with moderate deflection in geometries that are free of large obstructions.

The FDNS computer code developed by Chen *et al.* (1990) is a general-purpose CFD program for solving the Navier-Stokes equations in finite-difference form. The method is widely used at the Marshall Space Flight Center for modeling flows in propulsion systems. CFD analysis of a given problem involves a sequence of steps, including: generation of a mesh to represent the physical geometry, specification of the boundary conditions on the flowfield, estimation of an initial flowfield from which to start the simulation, calculation of a converged solution to the model equations, analysis of the solution by graphical as well as numerical techniques, revision of the numerical model if necessary, and finally presentation of the results. The calculation stage of the analysis requires the greatest computational resources. Additionally, considerable human effort is invested in all other phases of the analysis. Effective computer tools can relieve some of the burden in performing these pre- and post-processing tasks. A "front end" code to aid the analyst in estimating an initial flowfield may reduce the engineering time needed to set up an FDNS case.

NUMERICAL METHOD

The FDNS code uses an iterative method to solve a large set of non-linear equations. The total execution time is the product of the number of nodes, the calculation time per node, and the number of iterations. The number of nodes is primarily determined by the complexity of the given problem. The calculation time per node depends upon the computer hardware and the details of the FDNS coding. Finally, the number of iterations is a function of the nature of the errors present in the starting field and the error reduction properties of the FDNS solver. Since a large effort is needed to validate modifications to the FDNS code, it is not practical to make internal changes without good cause. But, the starting field is an arbitrary program input prepared by the user, and the converged solution is independent of the starting condition. Thus, by providing a starting condition with low initial error, the execution time may be reduced without altering the end results.

A procedure for generation of the starting flowfield is constrained by several factors, primarily quick execution time, generality and ease of use. Since parabolic equations may be solved at a much lower computational cost than elliptic equations, the PNS equations have been chosen to generate the initial

flowfield. Furthermore, the PNS equations apply to a wide range of flow conditions and geometries without introducing many physical approximations. The decomposition of the pressure field is the most significant approximation for the cases studied. To facilitate use of the code, the standard FDNS input is utilized.

The PNS equations are a sub-set of the full Navier-Stokes (NS) equations derived by the following steps, which isolate the solution from the influence of downstream flow conditions.

- 1) Neglect streamwise diffusion terms.
- 2) Neglect streamwise convection in regions of reversed flow.
- 3) For subsonic flow, assume a mean streamwise pressure gradient applies at all points across any given flow cross-section.
- 4) For supersonic flow, solve for the pressure field in supersonic regions and impose this pressure on the subsonic boundary layer.
- 5) Apply boundary conditions for a well-posed parabolic problem.

The numerical solution is obtained by approximating the PNS equations by finite-differences in transformed coordinates in a manner similar to the FDNS program. First-order approximations for streamwise derivatives are used in the present code since high accuracy is not needed. The set is solved by a single space-marching sweep through the grid. The kernel of the solver is the coupled space-marching method of TenPas and Pletcher (1991), which advances the solution one grid step in the primary flow direction based on the known values upstream. A distinguishing feature of the algorithm is the coupled solution of the momentum and continuity equations, with Newton linearization of the non-linear convective terms. This formulation permits the velocity components and pressure to be solved for directly. With the velocity field known at a given marching step, parabolized transport equations are independently solved for the enthalpy and turbulence properties as necessary. Local iteration is used to converge the coefficients of the linearization and to update large changes in properties. The space-marching calculation proceeds step-by-step until the exit boundary is reached. In the course of this study it was found useful to perform a final smoothing procedure on the pressure field. A pressure Poisson equation formulated as a linear combination of the momentum equations is solved by line iterative method to distribute sharp pressure changes among surrounding nodes.

To evaluate the potential benefit of this procedure a flow initialization computer code has been developed for incompressible two-dimensional flow. The FDNS source code is used as the basis for the PNS code. The FDNS input and initialization modules are used to input data defining the geometry and flow conditions. One additional file is read to define the PNS solution parameters. The solver portion of FDNS is replaced by the space-marching solver, and the modules that evaluate the finite-difference equations have been modified to permit access by the new solver. The non-linear terms are reworked to implement the Newton linearization. The output routines from FDNS are kept intact. The PNS code is executed starting from FDNS input files, and produces a flowfield output file containing the PNS solution. Depending upon the convergence limits for the Newton and local property iteration loops, the entire PNS flow initialization solution is executed in the time required for between one and ten FDNS iterations. The FDNS program is then executed using the PNS output file as the starting condition.

RESULTS

The PNS flow initialization method was tested on two flow geometries for incompressible flow. Both laminar and turbulent flows were simulated. Tables 1 and 2 present comparisons of the iterations required to converge the FDNS solution based on a simple starting condition versus the PNS estimate. The convergence rate of the FDNS program is dependent upon several factors. The input values used for various constants are: REC=0.5, BETAP=1.0, PSMO=0.005, and ICOUP=2. The convergence rate is also sensitive to the time step. The time step shown for the baseline FDNS calculations was determined by trial and error to minimize the number of iterations. The same time step was then used for the PNS initialized cases. The study time was not sufficient to evaluate the time step sensitivity using the PNS initialization. The convergence tolerance was selected to represent a compromise between accuracy and total execution time. The fine grid cases in particular are difficult to converge to a high level of precision, and the laminar flows may also be unsteady to a small degree. Therefore, the iteration count comparison is rather arbitrary as the value depends upon the convergence tolerance. However, since the iteration counts are roughly proportional for various levels of convergence, the percentage of the baseline execution time is not strongly related to the magnitude of the convergence tolerance.

The first geometry is a 180 degree turn-around-duct (TAD) similar to that studied by Monson *et al.* (1990). A fully developed laminar or turbulent profile is specified upstream. Uniform grids are used for the laminar flow runs. For the turbulent cases the mesh is compressed near the channel walls to grid sizes of 0.01 and 0.002, to yield y^+ values of 50 and 75 for Reynolds numbers of 10^5 and 10^6 , respectively. In each case the 180 degree turn is subdivided into 40 marching steps with equally spaced grids in the straight sections upstream and downstream. To test the range of application of the PNS approximation the tightness of the turn was varied from a gentle bend with outer to inner radius ratio of 5/4 to a very tight ratio of 3/1. The PNS approximation for the gentle turn is relatively good and significant reductions in the FDNS execution time are obtained for both the laminar and turbulent case. For a tighter turn the PNS approximation does not model the actual flow well, and the change in FDNS execution time diminishes.

The second case is flow over a backward-facing step as simulated by Chen (1988). A parabolic inlet profile is specified for laminar flow, and a plug flow profile with turbulent kinetic energy of 0.005 and dissipation rate of 0.0002 is specified for the turbulent case. In both cases the flow inlet plane is at the sudden expansion and the grid spacing is uniform across the channel. The laminar flow case is a 2/1 expansion at a Reynolds number of 400, which is the upper limit of steady laminar flow for this geometry. The numerical grid extends 20 channel heights downstream to allow for the near approach to separation on the straight wall and subsequent flow redevelopment. Comparisons are made for a uniformly spaced coarse grid and a refined grid with grid compression near the expansion. Large reductions are achieved for the coarse grid case, with the FDNS convergence deteriorating for the refined mesh. A 3/2 expansion is used for the turbulent case, with a variable grid extending 10 channel heights downstream. As with the TAD case, the PNS initialization is less effective for the turbulent conditions. Even though the PNS flowfield looks reasonable for this case, the fine grids and the coupling between the velocity field and turbulence properties slows convergence. Under these conditions the FDNS code is slow to eliminate even relatively small errors in the solution.

Table 1. Comparison of FDNS iteration counts for TAD cases.

Re	R ₂ /R ₁	Grid	Δt	Poiseuille V, Uniform P			PNS V & P fields			CPU %
				UΔt/Δx	ε	N	UΔt/Δx	ε	N	
500	5/4	101x21	0.72	2	10 ⁻⁴	943	2	10 ⁻⁴	250	27
500	2/1	101x21	0.08	3/4	"	513	3/4	"	390	76
500	3/1	201x21	0.08	1	"	767	1	"	715	93
10 ⁵	5/4	101x21	0.18	1/2	10 ⁻³	1000	1/2	10 ⁻³	487	49
10 ⁵	3/1	201x21	0.02	1/4	"	1019	1/4	"	988	97
10 ⁶	3/1	201x41	0.01	1/8	8x10 ⁻³	3000	1/8	8x10 ⁻³	3000	100

Table 2. Comparison of FDNS iteration counts for backward-facing step cases.

Re	H ₂ /H ₁	Grid	Δt	Static V, Uniform P			PNS V & P fields			CPU %
				UΔt/Δx	ε	N	UΔt/Δx	ε	N	
400	2/1	81x41	0.25	1	10 ⁻⁴	1028	1	10 ⁻⁴	197	19
400	2/1	121x81	0.25	3/2	10 ⁻³	1000	3/2	10 ⁻³	500	50
10 ⁵	3/2	61x49	0.32	2	10 ⁻⁴	2370	2	10 ⁻⁴	1861	79

CONCLUSIONS

While the results obtained for laminar flow are encouraging, much smaller reductions were achieved for the turbulent flow cases. For fine grids or complicated flows the FDNS convergence history is most strongly determined by the slow decay of low frequency errors. In contrast, the flow initialization procedure is most likely to reduce high frequency errors. And, the influence of the starting condition diminishes as the iteration count becomes large. To achieve significant reduction in the iteration count for complex problems the specific properties of the finite-difference equations (e.g. truncation error properties, amount of damping) or the algebraic solver (e.g. matrix structure, limits on inner iterations) must be examined. Finally, the PNS solver may have some practical use, by saving engineering time in setting up an FDNS case.

REFERENCES

1. Chen, Y.S., "Viscous Flow Computations Using a Second-Order Upwind Differencing Scheme," AIAA Paper 88-0417, Jan. 1988.
2. Chen, Y.-S., Farmer, R.C. and Freeman, J.A., FDNS User's Manual (Version 1.0), SECA-TR-90-10, SECA, Inc., Huntsville, Alabama, Contract NAS8-37408, June 1990.
3. Monson, D.J., Seegmiller, H.L., McConnaughey, P.K. and Chen, Y.-S., "Comparison of Experiment with Calculations Using Curvature-Corrected Zero and Two-Equation Turbulence Models for a Two-Dimensional U-Duct," AIAA Paper 90-1484, June 1990.
4. TenPas, P.W. and Pletcher, R.H., "Solution of the Navier-Stokes Equations for Subsonic Flows using a Coupled Space-Marching Method," *AIAA Journal*, Vol. 29, no. 2, Feb. 1991, pp. 219-226.

V93-17330

1992

NASA/ASEE SUMMER FACULTY FELLOWSHIP PROGRAM

**MARSHALL SPACE FLIGHT CENTER
THE UNIVERSITY OF ALABAMA**

**CONTROL-STRUCTURE-THERMAL INTERACTIONS
IN ANALYSIS OF LUNAR TELESCOPES**

Prepared by: Roger C. Thomspson, Ph.D.

Academic Rank: Assistant Professor

Institution and
Department: The Pennsylvania State University
Department of Aerospace Engineering

NASA/MSFC:

Office: Program Development
Division: Subsystems Design
Branch: Guidance, Navigation, and Control

MSFC Colleague: Connie Carrington, Ph.D.

The Program Development Office is studying the process of concurrent engineering as it applies to the design and development of space vehicles. The research program is specifically charged with developing a process in which the structural, thermal, and active control systems are designed and simulated simultaneously because these subsystems will have a direct effect on mission performance. A small, lunar-based telescope was chosen as a design project about which the Controls-Structures-Thermal Interaction (CSTI) study could formulate the concurrent engineering process and analyze the results. The lunar telescope project was an excellent model for the CSTI study because a telescope is a very sensitive instrument, and thermal expansion or mechanical vibration of the mirror assemblies will rapidly degrade the resolution of the device. Consequently, the interactions are strongly coupled. The lunar surface experiences very large temperature variations that range from approximately -180°C to over 100°C . Although the optical assemblies of the telescopes will be well insulated, the temperature of the mirrors will inevitably fluctuate in a similar cycle, but of much smaller magnitude. In order to obtain images of high quality and clarity, allowable thermal deformations of any point on a mirror must be less than $1\ \mu\text{m}$. Initial estimates (2) indicate that this corresponds to a temperature variation of much less than 1° through the thickness of the mirror. Therefore, a lunar telescope design will most probably include active thermal control, a means of controlling the shape of the mirrors, or a combination of both systems.

Historically, the design of a complex vehicle was primarily a sequential process in which the basic structure was defined without concurrent detailed analyses of other subsystems. The basic configuration was then passed to the different teams responsible for each subsystem, and their task was to produce a workable solution without requiring major alterations to any principal components or subsystems. Consequently, the final design of the vehicle was not always the most efficient, owing to the fact that each subsystem design was partially constrained by the previous work. This procedure was necessary at the time because the analysis process was extremely time-consuming and had to be started over with each significant alteration of the vehicle. With recent advances in the power and capacity of small computers, and the parallel development of powerful software in structural, thermal, and control system analysis, it is now possible to produce very detailed analyses of intermediate designs in a much shorter period of time. The subsystems can thus be designed concurrently, and alterations in the overall design can be quickly adopted into each analysis; the design becomes an iterative process in which it is much easier to experiment with new ideas, configurations, and components. Concurrent engineering has the potential to produce efficient, highly capable designs because the effect of one subsystem on another can be assessed in much more detail at a very early point in the program.

The research program consisted of several tasks: scale a prototype telescope assembly to a 1 m aperture, develop a model of the telescope assembly by using finite element (FEM) codes that are available on site, determine structural deflections of the mirror surfaces due to the temperature variations, develop a prototype control system to maintain the proper shape of the optical elements, and most important of all, demonstrate the concurrent engineering approach with this example. In addition, the software used for the finite element models and thermal analysis was relatively new within the Program Development Office and had yet to be applied to systems this large or complex; understanding the software and modifying it for use with this project was also required. The I-DEAS software by Structural Dynamics Research Corporation (SDRC) was used to build the finite element models, and TMG developed by Maya Heat Transfer Technologies, Ltd. (which runs as an I-DEAS module) was used for the thermal model calculations. All control system development was accomplished with MATRIX_X by Integrated Systems, Inc.

It was decided that the best approach would be to start with very simple models of low order so that understanding the FEM code and developing the individual elements of the analysis technique would not be hampered with large data files and long computation times. After evaluating the results for each model, additional components would be added to the structure and the cycle would be repeated. Before proceeding to develop simplified telescope models, two test cases were used to establish the operational characteristics of the computer codes for finite element modeling and heat transfer calculations. The first model was a simple cantilevered beam with 20 degrees-of-freedom (DOF), and the second was a planar truss structure with 11 DOFs. The beam model was used to exercise the dynamic analysis modules of the FEM code, and the truss structure was used as a simple example for evaluating the results of the heat transfer codes. These two models were chosen because the dynamics of beam vibration and thermal expansion of truss structures are well known, and solutions for these problems using similar techniques were readily available.

Several problems with the software and its operational peculiarities were clarified. It was discovered that the FEM program was not set up to write the reduced mass and stiffness matrices that are required in the development of the control system. Full-order mass and stiffness matrices were available, but complex post-processing would have been required to eliminate the constrained coordinates. Part of the code actually solved the reduced-order dynamic equations, but the software developers apparently never considered that any users would want to preserve the system equations for future evaluation. Further, the software has a "hard-coded" limit of 500 DOFs. This may be considered adequate for many applications, but when trying to model deflections on the order of a few μm on a large, flexible, thin-shelled structure, more than 500 DOFs will be needed. To fix these problems, several program files were revised and stored for later use; however, working around the DOF limit remains a cumbersome process. In addition, the terminology used in defining boundary condition specifications and DOF definitions was not straightforward to new users of the program. The proper use of these functions was resolved by using the simple beam model and comparing the solutions to known results. The only problem encountered with the TMG solver was its inability to handle higher-order finite elements; parabolic quadrilateral (8-node) elements were used for the mirrors because of the improved accuracy that they can provide. The thermal model, however, simply ignores the mid-side nodes and calculates the temperatures of the corner nodes for each element. A post-processor (included in the TMG module) must then be executed to produce nodal temperatures for the mid-side nodes by linearly interpolating the nodal temperature data at adjacent nodes.

The I-DEAS and TMG software always retains full-order coordinate sets but the control system must use a reduced-order set corresponding to the actual DOFs (i.e. the constraints are eliminated). Therefore, a computer program was needed to transfer the data from one code to the other. Data generated in the I-DEAS format (which includes the TMG results) is stored in no specific order, but the information that must be passed to MATRIX_X has to be processed, and the calculations must be made in a very specific order. For example, it is impossible to reduce the nodal displacements to the reduced DOF set unless the data containing the relationship between the reduced-order and the full-order coordinates is known prior to the operation. Further, investigators have the option of choosing which coordinate set to use for evaluating the results, so the program must be able to accommodate the coordinate set that is chosen. A Fortran code was written to search the I-DEAS data files, select and process the data as specified by the user, and write the data in a format acceptable to the MATRIX_X software.

The next task of the CSTI project was to develop a prototype controller to be used to simulate the mirror shape control. A Linear Quadratic Regulator (LQR) with Integral control (1) was selected because it is a very stable feedback control system, and steady-state errors due to constant inputs or disturbances can be driven to zero. When fully developed, the control system will also include a Kalman Filter to simulate a network of sensors. This type of control system has good response characteristics, and the control and observer gains can be adjusted to simulate different conditions. A control system with these features was written and debugged in MATRIX_X because the software has preprogrammed functions that determine the control and observer gains from the dynamic equations of motion, and a simulation was performed using the truss model as a test case. At that point in the CSTI study, all of the elements required to perform a complete analysis were in place; the next phase was to begin the analysis of the telescope structure.

The initial model that was tested was a free-floating mirror of the correct size and shape but without any additional supporting structure. With this model, the vibrational frequencies would be incorrect, but the thermal loads are quasi-static, and the purpose of this exercise was to proceed through each step in the analysis technique with a representative example. By studying the response of the free mirror, some insight into the placement of sensors and actuators could be gained. Although the mirror was not connected to the structure in any way, a sun shade and lander model, provided by the LUTE project (4), was used to provide more realistic temperature profiles to result from the thermal analysis. A thorough analysis of the thermal loads on the mirror could not be completed prior to the conclusion of the summer program because of the long computation times required to simulate a lunar cycle. Normally, the analysis should cover at least 2 cycles to eliminate any effect of the assumed initial temperatures. Nevertheless, an abbreviated analysis was performed, and it was found that the mirror temperatures can be expected to cycle from -100°C to 52°C during the course of a lunar day (Fig. 1). The data appears to have some errors, particularly near the peak temperatures, but the results should be indicative of the response that can be expected.

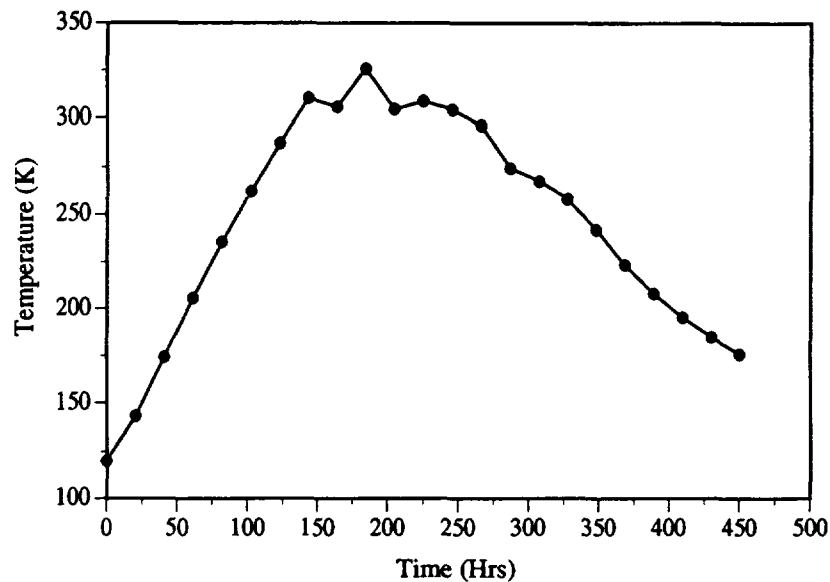


Figure 1. Nodal Temperature Profile

Maximum nodal displacements due to the thermal loads were found to be approximately $550 \mu\text{m}$. This is far beyond the allowable deformations, and some form of active thermal control and active shape control will probably be necessary. To test the control system, the thermal loads were applied as step functions; this loading is far worse than would normally be encountered on the lunar surface because of the sudden application of the external loads rather than a smooth, continuous change in conditions. The step disturbance profile could be representative of the thermal loading on the Hubble Space Telescope as it passes through the terminator. Initially, the control system was ineffective, but that was traced to an insufficient number and placement of actuators. Because finding actuator placements that guarantee controllability can be a time-consuming process, the control system was simplified such that actuator placement was not a factor. The observer was eliminated and the actuators, one for each mode, were simulated in "modal space" where each one can operate independently on an individual mode (3). It should be noted that the simplified controller is essentially the same as the LQR/Integral Controller with an observer; instead of an observer providing an estimated state vector for feedback, the "actual" state vector was used. The use of independent modal controllers, however, is a more serious departure from simulating an actual structure, but any set of actuators which yields a fully controllable system is capable of producing similar results. The control system simulation, shown in Fig. 2, shows that all deformations were eliminated in less than two seconds and the overshoot was very small. These results could be improved by "tuning" the control gains to obtain a more desirable response.

The CSTI study advanced considerably during the ten week period of the 1992 Summer Faculty Fellowship Program. The software used to analyze the control-structure-thermal interactions was tested with representative examples, and some serious problems were resolved. In addition, a computer code was written to interpret the data needed for the control simulations and put the appropriate data in a format that was readable by the MATRIX_X software. Therefore, all of the components necessary for the concurrent engineering approach were developed during the summer program. A simple truss structure was then used as a test case and the CSTI procedure was applied. Finally, an accurate representation of the primary mirror of a proposed lunar telescope was analyzed using the procedure developed during the CSTI study.

Although the description of the procedure may be very succinct, there is a considerable amount of work that goes into each step of the process. The tools are there, but the analysts must determine how a procedure is applied and what accuracy is warranted by the project. Finite element modeling, particularly when highly accurate but low DOF systems are desirable, is a complex field that requires an analyst familiar with the problems that

must be addressed. Similarly, the thermal modeling will require personnel familiar with the thermal environment and the structural configuration. The third component of the CSTI program, controls, also requires a researcher familiar with the trade-offs that must be made and who has some insight into the effect of the performance parameters that must be chosen. Consequently, the CSTI study was developed as a technique by which experts in the very different fields could share results and iteratively refine the design of the subsystems by working more interactively. The software and methods used in the CSTI study can accomplish this goal; for example, the mirror model was constructed and analyzed through one "cycle" of the iterative process in less than one week.

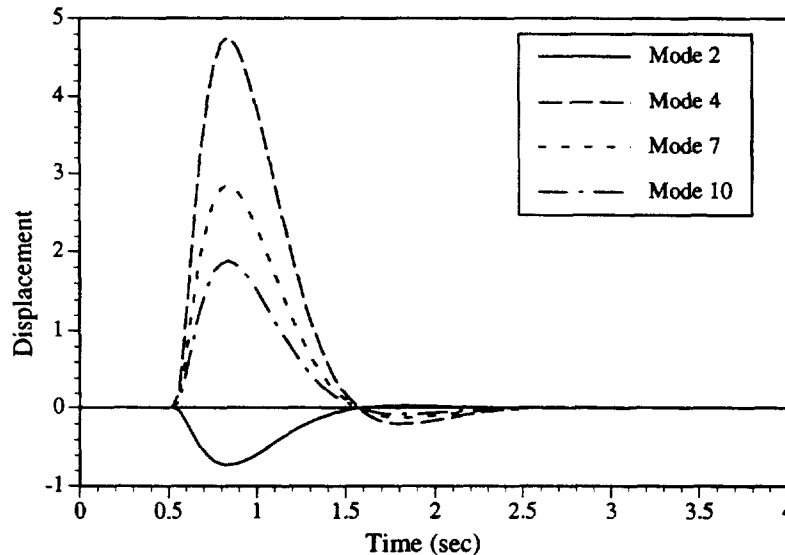


Figure 2. Control System Simulation

The lunar telescope project of the CSTI study has much more work to be done in the future. The foremost task is to develop a more detailed structure. The secondary and tertiary mirrors have to be added to the analytical model and a structure to support all three mirrors must be added. In addition, components such as baffles, optical instrumentation, and support for other subsystems such as power, communications, and command and data handling must be included. The results from this research will be useful in future activities because some knowledge of the displacement patterns was gained from the work completed during the summer program. Additional components of the telescope structure can be added as necessary and the analysis technique can be used to measure the effectiveness of the modifications. Actuator and sensor placement is perhaps the most crucial of the structural issues that must be addressed; actuators produce heat sources, and sensors must be capable of measuring the minute distortions that are to be controlled. Finally, a method of evaluating the optical performance of the structure, and hence the performance of the control system, needs to be included in the simulations. A computer code created specifically for the evaluation of optical systems will be used to determine the telescope's optical aberrations due to mirror deformations, and it should be possible to couple the optical analysis to the control software such that an "instantaneous" evaluation of the telescope performance can be determined.

REFERENCES

1. Kuo, B. C., *Automatic Control Systems*, 6th Edition, Prentice-Hall, 1991.
2. Luz, Paul, Unpublished notes on the Lunar Ultraviolet Telescope Experiment, August 1992.
3. Meirovitch, L. and Baruh, H., "Control of Self-Adjoint Distributed Parameter Systems," *Journal of Guidance, Control, and Dynamics*, Vol. 5, No. 1, JAN-FEB 1982, pp. 60-66.
4. Walker, Sherry and Alexander, Reggie, "Preliminary Design of the Lunar Ultraviolet Telescope Experiment," to be published December 1992.

1992

NASA/ASEE SUMMER FACULTY FELLOWSHIP PROGRAM

**MARSHALL SPACE FLIGHT CENTER
THE UNIVERSITY OF ALABAMA**

STIFNESSES BY (TtN) ENSEMBLE MOLECULAR DYNAMICS

Prepared By: Patrick Tibbits, Ph.D.
Academic Rank: Assistant Professor
Institution: Indiana Institute of Technology
Department: Mechanical Engineering
NASA/MSFC:

Office: Science and Engineering
Division: Materials and Processes

MSFC Colleague: Ilmars Dalins, Ph.D.

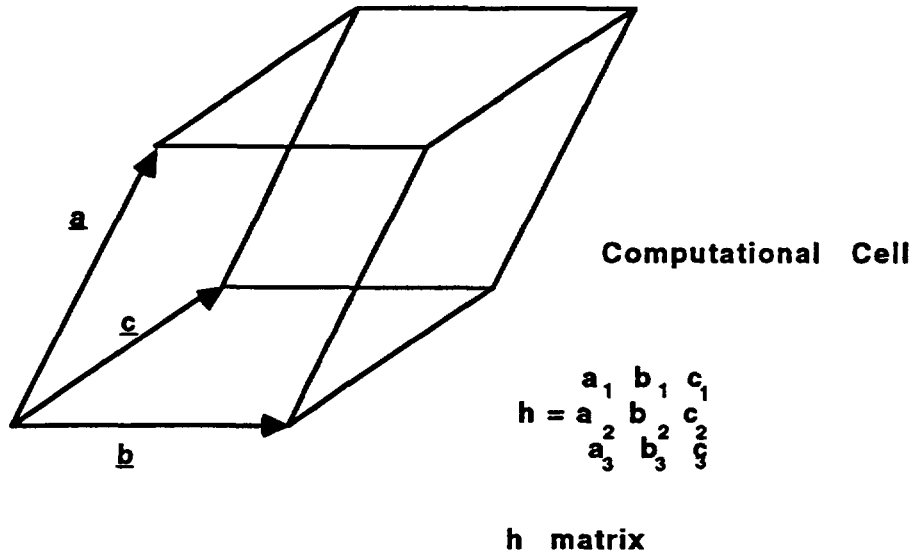


Figure 1. Computational Cell and h Matrix

The position vector of atom i , \underline{r}_i , is in the Cartesian basis

$$\underline{r}_i = x_i \underline{e}_1 + y_i \underline{e}_2 + z_i \underline{e}_3. \quad [1]$$

The underlines denote vectors. Figure 1 shows the molecular dynamics computational cell. The position vector of atom i can be written in terms of the \underline{a} , \underline{b} , and \underline{c} vectors spanning the computational cell edges as

$$\underline{s}_i = \xi_i \underline{a} + \eta_i \underline{b} + \zeta_i \underline{c} \quad [2]$$

where $\xi, \eta, \zeta \in [0, 1]$ for all atoms in the computational cell. This representation is useful in applying periodic boundary conditions, where an atom leaving the computational cell on the right is considered to reenter the cell on the left. Scaling, the change of basis from the Cartesian orthogonal unit vectors to the \underline{a} , \underline{b} , \underline{c} basis is accomplished through

$$\underline{s}_i = h^{-1} \underline{r}_i, \quad [3]$$

and the reverse transformation through

$$\underline{r}_i = h \underline{s}_i. \quad [4]$$

The h matrix defines the metric tensor G through

$$G = h^T h \quad [5]$$

and G modifies the dot product through

$$\underline{s}_i \cdot \underline{s}_j = \underline{s}_i^T G \underline{s}_j. \quad [6]$$

Also, G defines the strain tensor through

$$\epsilon = \frac{1}{2} [(h_0)^T G h_0]^{-1} \quad [7]$$

where h_0 is the h matrix for the reference state.

Newton's equations of motion are, in the Cartesian basis,

$$\ddot{r}_i = \frac{f_i}{m_i} \quad [8]$$

Integration of this set of coupled ordinary differential equations, the molecular dynamics method, provides the position of each atom as a function of time. In the scaled basis,

$$\ddot{u}_i = \frac{f_i}{m_i} - G^{-1} G \ddot{u}_i, \quad [9]$$

and an additional matrix equation tracks changes in the size and shape of the computational cell through

$$\dot{h} = \frac{1}{W} [(\pi - P) \sigma - h \Sigma], \quad [10]$$

where W is a pseudo-mass assigned to each element of the h matrix, p is related to the internal stress tensor, P is applied pressure, S is related to applied stress, and s is the inverse of the transpose of h .

The fluctuation of two stress or strain tensor components is just their covariance²

$$\delta(xy) \equiv \langle (x - \langle x \rangle)(y - \langle y \rangle) \rangle = \langle xy \rangle - \langle x \rangle \langle y \rangle, \quad [11]$$

where $\langle \rangle$ denotes a time averaged quantity. The usual formula for the mean,

$$\langle x \rangle = \frac{1}{N} \sum_{k=1}^N x_k, \quad [12]$$

risks inaccuracy through cancellation when the sum becomes large. A better formula,

$$\langle x \rangle_k = \frac{k-1}{k} \langle x \rangle_{k-1} + \frac{1}{k} x_k \quad [13]$$

updates the average at each timestep k .

The elastic constants² of a material are the tensor components C_{ijkl} , the stiffnesses, or the components of the inverse tensor, S_{ijkl} , the compliances. The relation

$$S_{ijkl} = \frac{V_0}{k_B T} \delta(\epsilon_{ij} \epsilon_{kl}) \quad [14]$$

provides values of the compliances from the fluctuations of the strain components, the reference state volume, and the temperature. Stress fluctuations are related to the elastic constants by a similar formula.

Calculation of elastic constants requires initializing a lattice of atoms, an h matrix defining the computational cell boundaries, and the parameters defining the interatomic potentials, then numerically integrating the equations of motion for the atoms and the computational cell boundaries, calculating strains and stresses at each timestep, and updating at each timestep the average quantities required for calculation of fluctuations.

Applications of interest to NASA include calculation of elastic constants near lattice defects such as dislocations and grain boundaries, and investigation of the effect of changes in elastic constants, caused by core ionization in XPS, on asymmetries in spectral peaks³.

Enhancements of the DYNAMO⁴ FORTRAN code included addition of documentation, improved memory management and data flow, and enabling use of several interatomic potentials.

Documentation included headers for each subroutine which document the parameters input to the routine, algorithms employed, and output. Numerous comments were added to the body of each routine as well.

Improvements to memory management consisted of removing all common blocks, replacing them with dimension statements, thus eliminating many variables and arrays from the specification section of subroutines in which they were not referenced. Passing all parameters explicitly through argument lists clarified data flow.

Enabling the use of all available interatomic potentials required inclusion of data structures for each type of potential. Setting an input variable selects the potential, obviating maintenance of a separate version of the code for each potential.

1 Parinello and Rahman, *Journal of Applied Physics*, December 1981

2 Ray, J.R., *Computer Physics Reports* 8 (1988) 109-152

3 Beamson, G., Clark, D.T., et al., *Journal of Electron Spectroscopy and Related Phenomena*, 57 (1991) 79-90

4 Daw, M.S., and Baskes M.I., *Phys. Rev. Lett.* 50, 1285 (1983)

N 9 3 - 1 7 5 3 2

1992

NASA/ASEE SUMMER FACULTY FELLOWSHIP PROGRAM

MARSHALL SPACE FLIGHT CENTER
THE UNIVERSITY OF ALABAMA

UPT SCENARIOS - IMPLICATIONS FOR SYSTEM RELIABILITY

Prepared By: Daniel W. Walsh, Ph.D.

Academic Rank: Professor

Institution/Department: California Polytechnic State University,
San Luis Obispo, Materials Engineering
Department

NASA/MSFC:
Laboratory: Materials and Processes
Division: Metallic Materials
Branch: Corrosion

MSFC Colleague: Merlin D. Danford, Ph.D.

Contract Number: NGT-0-002-099
The University of Alabama

OBJECTIVE

The objective of this project was to examine the corrosion resistance of 316L stainless steel in several urine pre-treat solutions. Four solutions were examined - untreated urine (control), urine pretreated with oxone (potassium peroxydisulfate sulfate), urine pretreated with sodium hypochlorite (NaOCl) and urine pretreated with ozone (O₃). In accordance with current procedures, all solutions but the control were acidified to a pH of 2.5 using sulfuric acid - this suppresses the generation of ammonia in the solutions and is intended to limit microbial growth. Welded and unwelded coupons were exposed to each solution. In addition, Titanium coupons (welded and unwelded) were exposed to biologically active environmental control and life support system (ECLSS) water. Microbial attachment and biofilm growth were monitored. Ozone was examined as a biocide/oxidizer/corrosion preventative (simultaneous addition) and as a remediation method (added one week after exposure).

In an unrelated effort, HP 9-4-30 coupons were exposed to biologically active solutions. Corrosion rates for welded and unwelded samples were determined - results were correlated to the ongoing HP 9-4-30 weldment stress corrosion study.

INTRODUCTION

Microbiologically influenced corrosion (MIC) is ubiquitous - all alloy systems exhibit susceptibility to microbiological attack. Stainless steels are not thermodynamically resistant to corrosion - they resist corrosive attack in oxidizing solutions because they "passivate". This is a kinetic phenomena, based on a critical Cr content in the alloy system and the development of a tightly adherent surface layer that forms a barrier to further corrosive attack. In many environments, including biologically active environments, these alloys are subject to local breakdown of the of the passive layer and localized attack - pitting.

A number of investigators have reported MIC of austenitic stainless steels. In some cases investigators attribute MIC to macroscopic features (suckback, undercut, excessive reinforcement) associated with the weld. Though these features can produce stagnant water conditions which foster MIC, the more critical association is between the microbe and microscopic metallurgical features. A "typical" microbe is on the order of 2u long - undercut is typically 1 to 2mm deep, a weld crown 20mm across. Thus, the undercut is typically 500 to 1000 times the dimension of the microbe and the crown 10,000 times the dimension of the microbe! In human terms this is equivalent to a typical adult looking into a canyon 2,000 meters deep and 18 km wide from its' lip to choose a camping site - clearly there is interaction on a finer scale.

Metal oxidizing and sulfate reducing bacteria have been reported

to cause corrosion in stainless steels. Several investigators have reported MIC associated with welds in fabricated components. Even stainless steels containing molybdenum, which effectively resist crevice corrosion in sea water, have been found susceptible to MIC. The case of a stainless steel tank that was not completely drained after hydrotest has been reported - subsequent through wall (8mm) pitting occurred in four weeks. Even high purity water systems are not immune. The case of a stainless steel tank storing demineralized water that failed by stress corrosion cracking - initiating at pits beneath bacterial deposits - has been reported.

The study of MIC is an inherently interdisciplinary endeavor - involving microbiology, metallurgy and electrochemistry. Though many have studied environments that promote MIC, catalogued materials that are subject to MIC, described methods of detecting MIC and found treatments to mitigate MIC problems - investigators have not yet completely correlated MIC to microstructural features. Surfaces of any kind are attractive to bacteria in aqueous environments. Surfaces, particularly metal surfaces, concentrate organic molecules crucial to microbial development. Furthermore, metal surfaces are extremely heterogeneous. Regional differences (on all scales, from submicron to macroscopic) are so well defined that local anodes and cathodes form and corrosion progresses on monolithic pieces of material. Surface condition, stress state, microstructure, chemistry and inclusion size and distribution affect local electrochemistry and MIC susceptibility. Fabrication procedure can also change MIC sensitivity. The thermal wave associated with the passage of a welding arc changes surface texture and produces local stress fields. More importantly, it alters the size, shape, amount and distribution of microstructural constituents in the fusion zone and the heat affected zone (HAZ).

PROCEDURE

Discs (15mm Diameter) of 316L stainless steel, in the as welded and as received conditions were degreased in trichloroethylene and washed with alcohol to remove surface films. Discs were used for polarization resistance studies in an EG&G Model 273 potentiostat / galvanostat. The program POLCUR, as modified by Danford, was used to estimate Tafel constants and calculate corrosion rates:

$$I_{corr} = B_a B_c / [2.3 (B_a + B_c) R_p] \quad (1)$$

Samples were exposed to raw urine as a control, and to urine with three different pretreatments - each pretreatment was acidified to a pH of 2.5 using sulfuric acid, standard practice for the Vapor Compression Distillation (VCD) subsystem. Three different oxidants were studied - oxone, hypochlorite and ozone. Oxone and hypochlorite were added to the respective test cells to concentrations specified in VCD pretreatment protocols. Ozone was produced from pure oxygen by UV irradiation and was introduced into the solution through a glass frit. The ozone was supplied to the solution for a two day period and reached a peak concentration of 60ppm. Solutions were continually stirred, corrosion rates were monitored over a three week period.

After the corrosion tests, samples were removed, fixed with

formalin and dried in methanol and freon. Prior to examination by scanning electron microscopy, samples were sputter-coated with Au-Pd. Ti discs, exposed to untreated and ozonated ECLSS water, were fixed, dried and sputter-coated in a similar fashion. The effectiveness of ozone in removing established biofilms was also studied.

RESULTS AND DISCUSSION

Figure 1 shows the results of corrosion testing. The corrosion rates found in the control samples are much higher than any of the treated solutions. Corrosion rates in the treated solutions are low, however, the corrosion rates of the as welded samples are five to ten times as great as their unwelded counterparts. High corrosion rates measured early in testing are indicative of the passivation of the stainless steel in an oxidizing environment. Figure 2a-d are SEM photomicrographs of coupon surfaces. Figure 2a shows the ozone treated sample, no biofilm or microbes are present. Figure 2b shows the partially melted region of the hypochlorite treated coupon. Note the localization of microbes in the remelted grain boundaries. Figure 2c is an enlargement of this region. The surface of the weld region in the oxone treated sample, 2d, was covered with a more extensive biofilm that also showed localization at structural features produced by welding. All pretreatments limited the attachment of bacteria to the base metal surfaces. The number of colony forming units per milliliter found in the various solutions ranges from 10^9 /ml in the control solutions to near zero in the ozone. Oxone and hypochlorite have reduce the number of microbes in solution by a factor of 10^5 , although figures 2a through 2d indicate they are less effective at the metal surface. The localization of the microbial colonies - and the potential for localized corrosive attack at/near these colonies pose a particularly insidious problem for the VCD system, even at low corrosion rates.

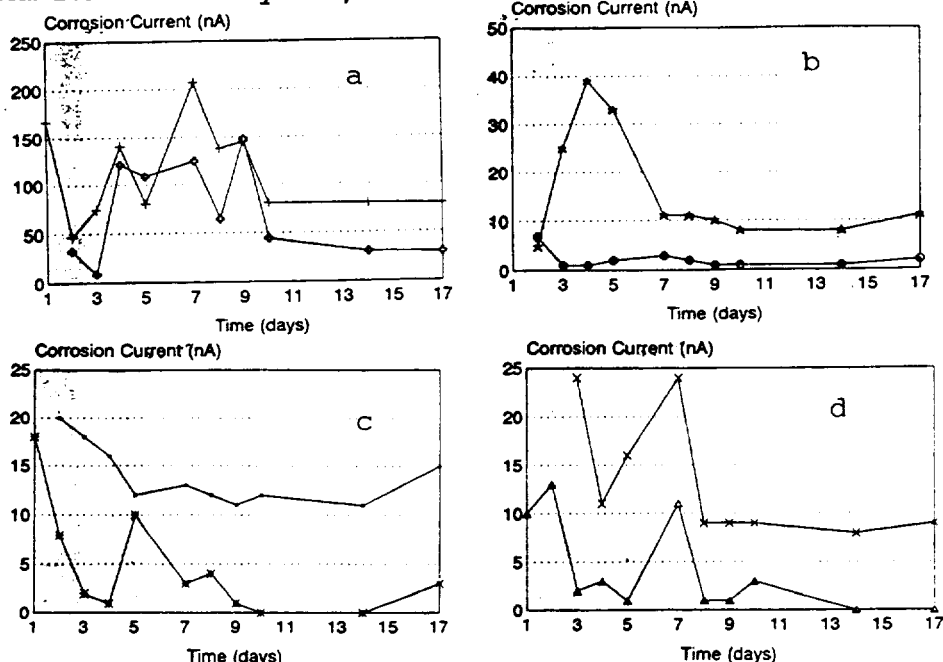


Figure 1. Corrosion rates measured over a three week period. a) control, b) ozone, c) hypochlorite, d) oxone.

The results of the film remediation study on Ti indicate that ozone is also capable of removing established biofilms - even after long term exposure.

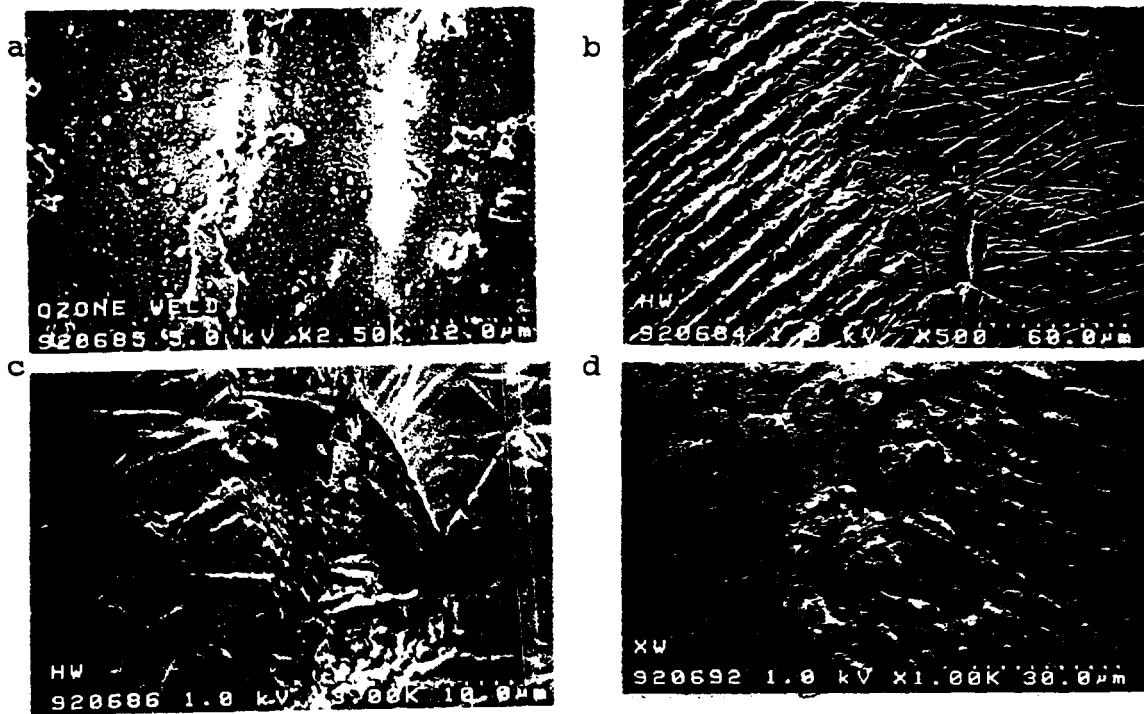


Figure 2. SEM photomicrographs of the surface of 316L coupons exposed to UPT fluid. a) ozone treated, b) hypochlorite, c) region b, higher magnification, d) oxone.

CONCLUSIONS

The results of this investigation indicate that:

- urine pretreatment diminishes the corrosion rate in 316L
- the corrosion rates in welded samples are an order of magnitude greater than corresponding base metal samples
- localized colonies of bacteria are associated with weld fusion zone and HAZ structures in all pretreatments but ozone
- localized corrosion could be damaging, even at low overall corrosion rates
- ozone removed established biofilms on Ti surfaces

ACKNOWLEDGEMENTS

I thank all the people at the M&P lab, and the Corrosion, Failure Analysis and Microbiology groups in particular - who make every trip to MSFC enjoyable and fruitful. In particular I would like to thank Merlin Danford for his patient help and interest, Tim Huff for sharing excitement and stealing coffee, Joe Montano for putting up with a paradox(c)s, Barry Moody, Mitch Mendrick, Larry Foreman, Kevin Buford, Dave Hedgepeth, Carla Hooper, Pablo Torres, Liz Rogers and Don Oberhuber. Special thanks to Jim Coston, Wendell Deweese and Jim Holly who took the time to give me help whenever needed.

198-17883

1992
NASA/ASEE SUMMER FACULTY FELLOWSHIP PROGRAM

MARSHALL SPACE FLIGHT CENTER
THE UNIVERSITY OF ALABAMA

THERMOSTRUCTURAL RESPONSES OF CARBON PHENOLICS
IN A RESTRAINED THERMAL GROWTH TEST

Prepared By: C. Jeff Wang, Ph.D.
Academic Rank: Assistant Professor
Institution and Department: Tuskegee University, AL
Department of Chemical Engineering
NASA/MSFC:
Office: Materials and Processes Laboratory
Division: Non-Metallic Materials
Branch: Ceramics & Coatings
MSFC Colleague: Ann N. Puckett

I. INTRODUCTION

The thermostructural response of carbon phenolic components in a solid rocket motor (SRM) is a complex process. It involves simultaneous heat and mass transfer along with chemical reactions in a multiphase system with time-dependent material properties and boundary conditions.

In contrast to metals, the fracture of fiber-reinforced composites is characterized by the initiation and progression of multiple failures of different modes such as matrix cracks, interfacial debonding, fiber breaks, and delamination. The investigation of thermostructural responses of SRM carbon phenolics is further complicated by different failure modes under static and dynamic load applications.

Historically, there have been several types of post-firing anomalies found in the carbon phenolic composites of the Space Shuttle SRM nozzle. Three major failure modes which have been observed on SRM nozzles are pocketing (spallation), ply-lift, and wedge-out. In order to efficiently control these anomalous phenomena, an investigation of fracture mechanisms under NASA/MSFC RSRM (Redesigned Solid Rocket Motor) and SPIP (Solid Propulsion Integrity Program) programs have been conducted following each anomaly.

This report reviews the current progress in understanding the effects of the thermostructural behavior of carbon phenolics on the failure mechanisms of the SRM nozzle. A literature search was conducted and a technical bibliography was developed to support consolidation and assimilation of learning from the RSRM and SPIP investigation efforts. Another important objective of this report is to present a knowledge-based design basis for carbon phenolics that combines the analyses of thermochemical decomposition, pore pressure stresses, and thermostructural properties. Possible areas of application of the knowledge-based design basis include critical material properties development, nozzle component design, and SRM materials control.

II. LITERATURE SEARCH ON CARBON PHENOLICS FOR SRM NOZZLE

A. Carbon Phenolics

There are four groups of test data available for different SRM carbon phenolic materials:

- 1) Avtex preshutdown rayon, before 1988 initial shutdown,
- 2) Avtex postshutdown rayon, after 1988 initial shutdown,
- 3) NARC (North American Rayon Corporation), rayon selected to develop an Avtex clone, and
- 4) PAN (polyacrylonitrile), an alternative to rayon.

B. Anomalies on SRM nozzle

Pocketing is referred to the tensile failure of fill fiber yarn in the resin pyrolysis zone. It is caused by the across-ply expansion of pyrolysis gases in a restrained environment. Another failure phenomenon, "ply-lift", is considered to be caused by the across-ply tensile or interlaminar shear stresses, driven by across-ply thermal expansion, during resin volatilization or pyrolysis. "Wedge-out" is hypothesized as an interlaminar failure of the outer charred material as a result of the small interlaminar surface area at the corners of adjacent rings.

C. Technical Reports

Five groups of test report on thermal and mechanical properties of SRM carbon phenolics, as well as two failure mechanism related test programs are listed below.

1. AVTEX PRESHUTDOWN/NTA: 1986 - 1989.
2. AVTEX PRESHUTDOWN/SPIP/NIP: 1988 - 1991.
3. AVTEX POSTSHUTDOWN: August 1990.
4. NARC: 1990 - present.
5. PAN: 1989 - present.
6. Permeability: 1988 - present.
7. Ply-lift: 1988 - present.

In addition, research papers in the study of thermochemical expansion of polymer composites during matrix decomposition were also searched and reviewed. Science and engineering fundamentals of thermochemical response of polymer composites, simultaneously decomposing and thermal expanding during the rapid heating, were discussed in these papers.

III. THERMOSTRUCTURAL ANALYSIS PROPERTIES OF COMPOSITES

A. Critical Material Properties

The thermostructural response of carbon phenolics exposed to the severe SRM exhaust environment have been observed to occur in three distinct temperature regions. Thus, the critical material property parameters needed for thermostructural analysis of SRM carbon phenolics have to be related to the phase changes occurring in these temperature regions. The evaluation and qualification efforts of carbon phenolics have been aimed at correlating these thermostructural properties with the failure modes observed in flight and static rocket motors.

Pocketing is induced by excess fiber tensile strains and subsequent fracture of fiber. Therefore, fill tensile strength is a critical property. Ply-lift is referred to the inter-ply failure and subsequent lifting between plies. Wedge-out is associated with ply angle and adjacent ring interactions across bondlines.

Therefore, across-ply coefficient of thermal expansion, across-ply tensile strength, and interlaminar shear strength are identified as the critical material properties for these two anomalies.

B. Restrained Thermal Growth (RTG) Tests

To include the pore-pressure stress, which is generated by pyrolysis gases, into the analysis of stress-strain curves, a combined effect of temperature increase on internal gas pressure and thermal expansion of composites has to be considered in investigating the thermostructural response. The Restrained Thermal Growth test represents this type of test where stiffness, thermal expansion, thermal decomposition, and strength characteristics interact as functions of temperature and heating rate. By simulating the flight environment of a SRM nozzle, the effect of internal gases on the thermostructural response as well as the resistance to pocketing failure can be measured.

In the restrained-strain environment, the internal gases will escape through the pores and microcracks of the material. Since the stress fields affect the extent of microcracking, stress fields also affect the permeability of gases, which in turn affects the stress fields via the variation of pore pressure.

By correlating the lateral strain measured from a RTG test to the fill tensile stress-strain curves, after subtracting out the free thermal expansion, the fill tensile stress on fill fiber can be calculated. Assuming that the fiber yarn is a homogeneous material, the maximum transverse shear stress on the fiber can be estimated by an in-plane tensile stress (pulling the yarns) due to lateral strain and an across-ply compressive stress (crushing the yarns) due to compressive load. Therefore, from the lateral strain and compressive stress, the in-plane fiber failure stress and the temperature at which pocketing occurs can be determined.

Other important material properties revealed from RTG tests are the first peak temperature (T_g), stress at T_g , saddle stress, second peak stress (the ultimate stress), and failure/explosive blowout temperature.

Comparison between the RTG responses of several Avtex-Preshutdown specimens at 1°F/sec and 10°F/sec heating rates indicated that at the higher heating rate, the gases had less time to migrate to the free surface and the internal pressure increased faster. Consequently, the stresses at both peaks are much higher than those at lower heating rate. RTG responses of two PAN-based specimens, Amoco 23 and FM5834, are shown in Figures 1 and 2, respectively. In-plane permeability of Amoco 23 has been shown to be extremely low, lower than any other measured PAN-based material. The single high peak stress (>30 kpsi) of this RTG response revealed the effect of low permeability on RTG response. Visual inspection of the tested specimen indicated that the specimen

failed by explosive blowout with both fill and warp yarn failures. On the contrary, the FM5834 RTG response shows a well-defined two peaks and low peak stresses. Another important feature of this PAN-based RTG response is that following the second peak, the stress declines gradually, indicating that, with a completely developed pathway for internal pyrolysis gases, the gases readily bled off to the free surface and the compressive stress decreased to zero without an explosive blowout.

From RTG data, it is clear that carbon phenolic permeability and pyrolysis/volatilization gases are two important variables affecting the failure mechanism. Therefore, material permeability is considered as a critical variable which can be used to control the pocketing anomaly.

V. SUMMARY AND RECOMMENDATIONS

Thermostructural responses and failure mechanisms of a series of carbon phenolics, including rayon- and PAN-based, have been investigated. The result indicated that there is a close relationship between these two materials behaviors. Three critical property parameters in the thermostructural responses of carbon phenolics in a RTG test have been reviewed. Possible explanation of the difference in RTG responses, based on the effect of gas permeability on the internal gas pressure, has been explored. It is recommended that more testing of these three critical properties, having a capability to elucidate their combined effects on controlling the failure mechanism, be conducted at different temperatures. It was founded from the test results of PAN based specimens that resin to fiber bonding plays an important role in determining the thermostructural properties of the composites. An investigation into its effect on gas permeability and failure mechanisms is recommended.

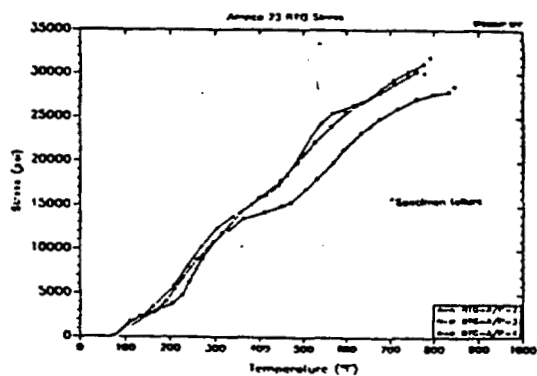


Figure 1 Amoco 23 Phase II RTG A/P Compressive Stress vs. Temperature Response

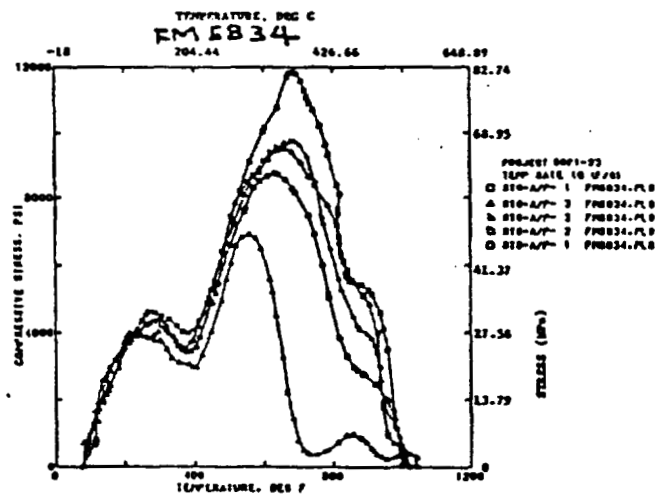


Figure 2 Stress as a Function of Temperature (STC Constant Strain Rate)

1992

NASA/ASEE SUMMER FACULTY FELLOWSHIP PROGRAM

**MARSHALL SPACE FLIGHT CENTER
THE UNIVERSITY OF ALABAMA**

**NATURE OF FLUID FLOWS IN DIFFERENTIALLY HEATED
CYLINDRICAL CONTAINER FILLED WITH A STRATIFIED SOLUTION**

Prepared By: Jai-Ching Wang, Ph.D.

Academic Rank: Associate Professor

**Institution and
Department:** Alabama A&M University
Department of Physics

NASA/MSFC

Lab: Space Science Laboratory
Division: Microgravity Science & Application Division/ES 71
Branch: Electronic & Photonic Materials Branch/ES 75

MSFC Colleague(s): Sandor L. Lehoczky, Ph.D.
Frank Szofran, Ph.D.

Semiconductor crystals such as $Hg_{1-x}Cd_xTe$ grown by unidirectional solidification Bridgmann method have shown compositional segregations in both the axial and radial directions (Lehoczký et al. 1980, 1981, 1983). Due to the wide separation between the liquidus and the solidus of its pseudobinary phase diagram (Lehoczký and Szofran 1981), there is a diffusion layer of higher HgTe content built up in the melt near the melt-solid interface which gives a solute concentration gradient in the axial direction. Because of the higher thermal conductivity in the melt than that in the crystal there is a thermal leakage through the fused silica crucible wall near the melt-solid interface. This gives a thermal gradient in the radial direction. Hart (1971), Thorpe, Hutt and Soulsby (1969) have shown that under such condition a fluid will become convectively unstable as a result of different diffusivities of temperature and solute. It is quite important to understand the effects of this thermosolute convection on the compositional segregation in the unidirectionally solidified crystals. To reach this goal, we start with a simplified problem. We study the nature of fluid flows of a stratified solution in a cylindrical container with a radial temperature gradient. The cylindrical container wall is considered to be maintained at a higher temperature than that at the center of the solution and the solution in the lower gravitational direction has higher solute concentration which decrease linearly to a lower concentration and then remain constant to the top of the solution (see Fig. 1). The sample solution is taken to be salt water with its properties listed in table 1.

Table 1. Material Properties for 3.5% salt water

Mass diffusivity for salt water	$\alpha_C = 1.3E-9 \text{ m}^2/\text{s}$
Thermal diffusivity	$\alpha_T = 1.5E-7 \text{ m}^2/\text{s}$
Density of salt water	$\rho = 920 \text{ Kg}/\text{m}^3$
Viscosity of salt water	$\mu = 7.6E-4 \text{ Kg}/\text{m}\cdot\text{s}$
Kinematic viscosity	$\nu = 8.26E-7 \text{ m}^2/\text{s}$
Prandtl number	$Pr = \nu/\alpha_T = 5.65$
Schmidt number	$Sc = \nu/\alpha_C = 635.4$
Volume expansion coefficient (thermal)	$\beta_T = 2.75E-4$
Diameter of the cylinder	$R = 0.005 \text{ m}$
Grashof number for temperature	$Gr_T = 22.23^2$

Under the Boussinesq approximation, the vector form of the governing equations for incompressible fluid flow of the system are:

Momentum Conservation

$$\frac{\partial \vec{u}}{\partial t} + \vec{u} \cdot \nabla \vec{u} = -\frac{1}{\rho} \nabla p - g(\beta_T(T-T_0) + \beta_C(C-C_0)) \hat{e}_z + \nu \nabla^2 \vec{u} \quad [1]$$

Continuity Equation

$$\nabla \cdot \vec{u} = 0 \quad [2]$$

Energy Conservation

$$\frac{\partial T}{\partial t} + \vec{u} \cdot \nabla T = \alpha_T \nabla^2 T \quad [3]$$

Solute Conservation

$$\frac{\partial C}{\partial t} + \vec{u} \cdot \nabla C = \alpha_C \nabla^2 C \quad [4]$$

Where \vec{u} is fluid flow velocity, T and C are the temperature and the solute concentration of the fluid, respectively, and α_T and α_C are the diffusivity for temperature and solute, respectively.

For axial symmetric boundary conditions, the governing equations in cylindrical coordinates are:

$$\frac{\partial u}{\partial t} + u \frac{\partial u}{\partial r} + \omega \frac{\partial u}{\partial z} = -\frac{1}{\rho} \frac{\partial p}{\partial r} + \nu \left(\frac{\partial^2 u}{\partial r^2} + \frac{1}{r} \frac{\partial u}{\partial r} + \frac{\partial^2 u}{\partial z^2} - \frac{u}{r^2} \right) \quad [5]$$

$$\begin{aligned} \frac{\partial \omega}{\partial t} + u \frac{\partial \omega}{\partial r} + \omega \frac{\partial \omega}{\partial z} = -\frac{1}{\rho} \frac{\partial p}{\partial z} + \nu \left(\frac{\partial^2 \omega}{\partial r^2} + \frac{1}{r} \frac{\partial \omega}{\partial r} + \frac{\partial^2 \omega}{\partial z^2} \right) \\ + g(\beta_T(T - T_0) + \beta_C(C - C_0)), \end{aligned} \quad [6]$$

$$\frac{u}{r} + \frac{\partial u}{\partial r} + \frac{\partial \omega}{\partial z} = 0 \quad [7]$$

$$\frac{\partial T}{\partial t} + u \frac{\partial T}{\partial r} + \omega \frac{\partial T}{\partial z} = +\alpha_T \left(\frac{\partial^2 T}{\partial r^2} + \frac{1}{r} \frac{\partial T}{\partial r} + \frac{\partial^2 T}{\partial z^2} \right), \text{ and} \quad [8]$$

$$\frac{\partial C}{\partial t} + u \frac{\partial C}{\partial r} + \omega \frac{\partial C}{\partial z} = \alpha_C \left(\frac{\partial^2 C}{\partial r^2} + \frac{1}{r} \frac{\partial C}{\partial r} + \frac{\partial^2 C}{\partial z^2} \right) \quad [9]$$

The equations can be nondimensionalized by setting the temperature and solute concentration as

$$T = T_0 + \Delta T T^* \quad \text{and} \quad C = C_0 + \Delta C C^*, \text{ and}$$

scaling the variables by a factor F; i. e. $V = F V^*$. Scaling length by R, velocity by $\sqrt{g\beta_T \Delta T R}$, time by $R/\sqrt{g\beta_T \Delta T R}$, pressure by $\rho g\beta_T \Delta T R$, temperature by ΔT and solute by ΔC . After the scaling and dropping all the *, the dimensionless equations become:

$$Gr_T^{1/2} \left(\frac{\partial u}{\partial t} + u \frac{\partial u}{\partial r} + \omega \frac{\partial u}{\partial z} \right) = -\frac{\partial p}{\partial r} + \left(\frac{\partial^2 u}{\partial r^2} + \frac{1}{r} \frac{\partial u}{\partial r} + \frac{\partial^2 u}{\partial z^2} - \frac{u}{r^2} \right) \quad [10]$$

$$\begin{aligned} Gr_T^{1/2} \left(\frac{\partial \omega}{\partial t} + u \frac{\partial \omega}{\partial r} + \omega \frac{\partial \omega}{\partial z} \right) = -\frac{\partial p}{\partial z} + \left(\frac{\partial^2 \omega}{\partial r^2} + \frac{1}{r} \frac{\partial \omega}{\partial r} + \frac{\partial^2 \omega}{\partial z^2} \right) \\ + Gr_T^{1/2} (T + (Gr_C/Gr_T) C), \end{aligned} \quad [11]$$

$$Pr Gr_T^{1/2} \left(\frac{\partial T}{\partial t} + u \frac{\partial T}{\partial r} + \omega \frac{\partial T}{\partial z} \right) = \frac{\partial^2 T}{\partial r^2} + \frac{1}{r} \frac{\partial T}{\partial r} + \frac{\partial^2 T}{\partial z^2}, \text{ and} \quad [12]$$

$$Sc Gr_T^{1/2} \left(\frac{\partial C}{\partial t} + u \frac{\partial C}{\partial r} + \omega \frac{\partial C}{\partial z} \right) = \frac{\partial^2 C}{\partial r^2} + \frac{1}{r} \frac{\partial C}{\partial r} + \frac{\partial^2 C}{\partial z^2}. \quad [13]$$

Where the thermal and solutal Grashof numbers respectively, Gr_T , Gr_C are defined by:

$$Gr_T = \frac{g \beta_T \Delta T R^3}{\nu^2} \quad \text{and} \quad Gr_C = \frac{g \beta_C \Delta C R^3}{\nu^2}.$$

The Prandtl number, Pr , and Schmidt number, Sc , are defined by:

$$Sc = \nu / \alpha_C \quad \text{and} \quad Pr = \nu / \alpha_T.$$

These governing equations show that the flow characteristic are determined uniquely by Gr_T , Gr_C , Pr and Sc . These equations have been solved by the FIDAP program developed by Fluid Dynamics International, Inc. Preliminary results reveal that any convection influences the solute field much more than it does the temperature field. Since the Prandtl and Schmidt numbers are properties of the particular fluid, the variations with Gr_T and Gr_C were primarily studied. Figure 1 through 4 depict the computational domain and some of the results obtained.

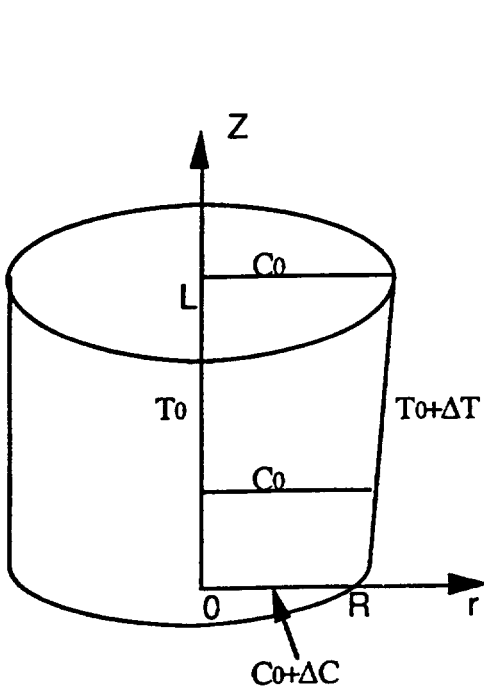


Fig1. Problem set up

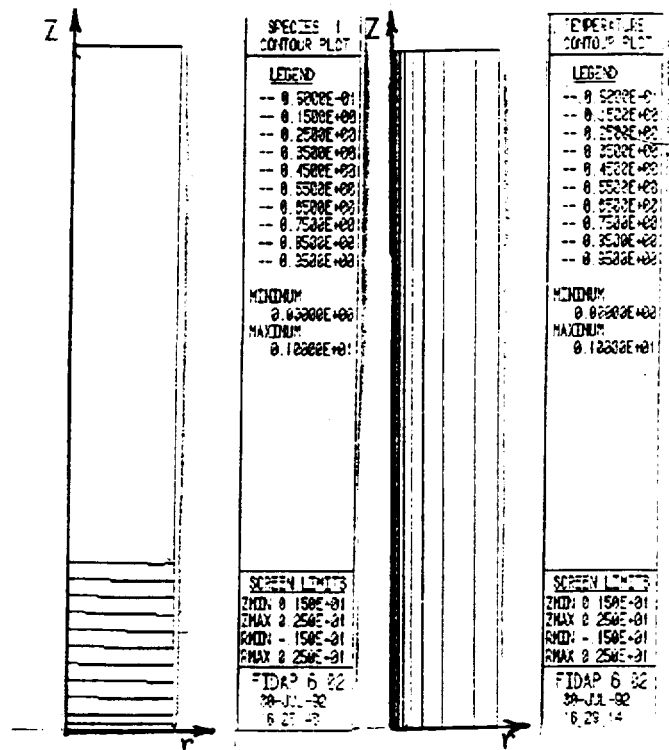


Fig. 2. Concentration and temperature fields for $Gr_T = 0.04$ and $Gr_C/Gr_T = 1.0$

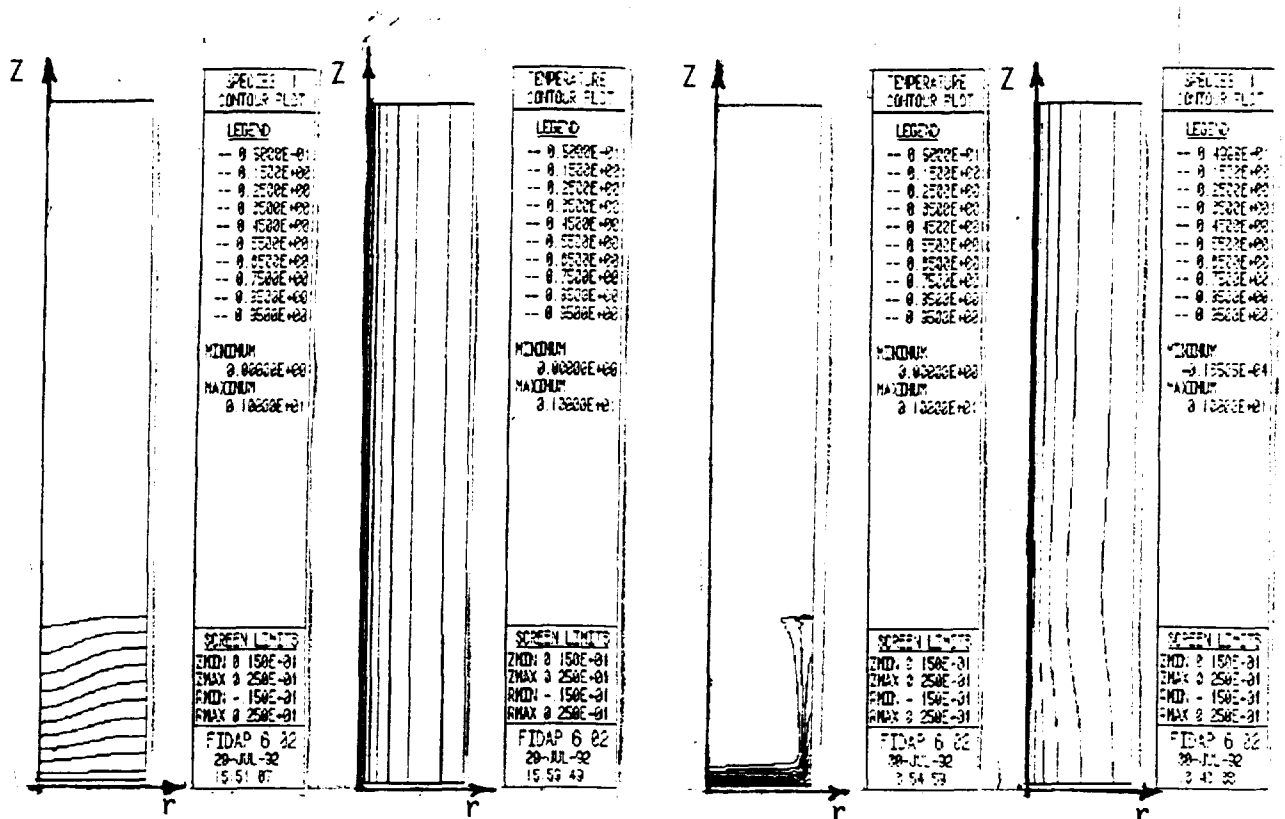


Fig. 3. Concentration and temperature fields for $Gr_T = 0.49$ and $Gr_C/Gr_T = 1.0$

Fig. 4. Concentration and temperature fields for $Gr_T = 0.49$ and $Gr_C/Gr_T = 1000$

ACKNOWLEDGMENT

I would like to express my sincere appreciation to the NASA/ASEE Summer Faculty Fellowship Program Administrators Drs. Michael Freeman and Frank Six for providing me the opportunity to participate in this program. The seminars and the Education Retreat are very helpful. Special thanks go to my NASA counterparts Drs. Sandor L. Lehoczky and Frank Szofran for their suggestions and guidance. I would also like to extend my sincere appreciation to Dale Waring for providing me technical consultations on the use of the FIDAP program and Dr. Ching-Hua Su for his valuable discussions. The hospitality and friendships of all the members in the Electronic & Photonic Materials Branch has made this summer very enjoyable for me.

REFERENCES

1. Lehoczky, S. L. and F. R. Szofran, "Directional Solidification and Characterization of $Hg_{1-x}Cd_xTe$ Alloys", in Materials Research Society Symposium Proceeding--Material Processing in the Reduced Gravity Environment of Space, ed., Guy E. Rindone (Elsevier, New York), 409 (1983).
2. Lehoczky, S. L. and F. R. Szofran, "Advanced Methods for preparation and Characterization of Infrared Detector Materials", NASA report, NAS8-33107 (September 1981).
3. Lehoczky, S. L., F. R. Szofran, and B. G. Martin, "Advanced Methods for preparation and Characterization of Infrared Detector Materials", NASA report, NAS8-33107.(July 1980).
4. Hart, J. E., "On sideways diffusive instability", J. Fluid Mech. 49 (1971), pp 279-298.
5. Thorpe, S. A., P. K. Hutt and R. Soulsby, J. Fluid Mech. 38 (1969), 375-400.

1992

NASA/ASEE SUMMER FACULTY FELLOWSHIP PROGRAM

MARSHALL SPACE FLIGHT CENTER
THE UNIVERSITY OF ALABAMA

AN EXPERIMENT TO STUDY FULLERENE
FORMATION UNDER REDUCED GRAVITY

Prepared By: Thomas J. Wdowiak, Ph.D.

Academic Rank: Associate Professor

Institution and Department: The University of Alabama at Birmingham
Department of Physics

NASA/MSFC:

Office: Space Science Laboratory
Division: Microgravity Science and Applications
Branch: Electronic and Photonic Materials

MSFC Colleague: Peter Curreri, Ph.D.

The study of the carbon molecular species known as fullerenes represented by the molecules of C₆₀ and C₇₀ is at today's frontier of molecular physics and materials science. Research in this area was initiated by the astrophysical considerations of the nature of complex molecules of the interstellar environment and their probable formation in the outer atmospheres of highly evolved stars (Kroto et al. 1985). The ability to produce C₆₀ and C₇₀ in gram amounts is also the consequence of researchers having astrophysical intent (Kratschmer et al. 1990a). This has resulted in a technique for a gram amount production of fullerenes incorporating an electric carbon arc with inert gas atmospheres at reduced pressure (Kratschmer et al. 1990b, Haufler et al. 1990, Curl and Smalley 1991). A high current electric arc is struck between two carbon rods or a carbon rod and carbon plate in an inert gas such as helium at pressure of ~100 torr. The material produced is vigorously convected upward from the arc and collected in a chimney for later solvent extraction of the fullerene component. Other techniques such as flames have also yielded fullerenes (Howard et al. 1991).

While gram amounts of fullerenes are produced in arcs in inert atmospheres, the initial experiments involving laser ablation and yielding amounts detectable only by mass spectrometry (Kroto et al. 1985), provides insight into the role of the inert gas. In that experiment a pulse of helium applied after laser ablation, swept the vaporized carbon out into a vacuum chamber. This supersonic expansion cooled the vaporized carbon atoms condensing them into clusters including substantial fractions of C₆₀ and C₇₀. In the arc process a similar thing occurs except in a continuous fashion as carbon atoms move out from the arc region and into the inert gas atmosphere. However, the process is continuous and extensive convection occurs. Convective transport out of the arc region is a significant parameter in the process therefore it is of obvious interest to control it by carrying out the process under microgravity conditions, and determining the effect of doing so on fullerene production. As buoyancy-driven convection is governed by the Rayleigh number $Ra \propto gL^3$ reduction of gravity to 10⁻³ suggests scale length changes of ~10x.

Since the electric arc/inert gas atmosphere process for fullerene production is technically simple, experimenting with it under reduced gravity offered by drop towers, aircraft trajectories, and space flight ought to be an easy task. These experiments would allow sampling of the material produced for fullerene assay afterwards, and study of the arc and plume during reduced gravity by imaging, interferometry, spectroscopy, and inserted probes. Because fullerene production is a rapid process compared to the duration of reduced gravity for aircraft trajectories and even that of a drop towers (Appendix B of NRA-91-OSSA-17), the development of technique and acquisition of usable data should be possible with those methods. Space flight offers an even more attractive environment. Indeed the integration of fullerene research with microgravity appears to as desirable situation one can ask for research into a new field.

The activity of the summer focused on the design and construction of key components of a carbon arc/inert gas reactor for fullerene production, that is suitable for reduced gravity experiments onboard the KC-135 aircraft. The apparatus will be configured for both floor-mount and free-floating operation providing access to reduction to 10⁻² and 10⁻³ of normal respectively. It is planned to incorporate "seat belt" restraints that will allow a safe transition from reduced gravity free-float to full gravity, at the end of the parabolic.

A spherical chamber housing two carbon rods will be the core of the reactor. The drive mechanism that will maintain a constant current arc through feedback has been constructed.

After initial laboratory measurements of the performance of a bread board version of the arc control system it will be configured for flight experiments. The chamber to be constructed at UAB this fall will be fitted with ports for view and sample extraction. The view ports will be used for a shadowgraph system will incorporate a diode laser with a CCD camcorder having an interference filter with a band pass at the laser wavelength. The filter will reject most of the light emitted by the arc allowing recording of the shadows induced by density variations in the plume. Because operations of an arc at reduced gravity will be a new experience, shadowgraph imaging will be interesting to say the least. Experiments at reduced gravity involving flames can provide some suggestions of what to expect, however, the energy densities of the arc and low pressures of ~100 torr are quite different from those involved in flames. A laser interferometer could be constructed for follow on experiments in the second and third years, and for use in spaceflight.

The extraction of samples for assay of fullerene production and its correlation with plume imagery and other parameters, will be accomplished by offset carousel rotation of circular substrates over sample extraction port (Figure 1). This apparatus with stepping motor circuitry was completed prior to fabrication of the arc mechanism. The circular substrate materials will include silicon allowing FTIR transmission spectroscopy of the soot deposited from the plume (Kratschmer et al. 1990a). Substitution of quartz allows UV/VIS transmission spectroscopy and a reflective metal substrate makes possible reflection spectroscopy of the deposited plume soot over the entire UV-IR range. Because only a portion of the substrate will be over the extraction port, the sampling will be time-resolved. Raman spectroscopy, electron microscopy, and x-ray diffraction of the deposited material will be carried out. the ~100 torr pressures involved allow rapid removal of coated substrates, replacement with fresh substrate surfaces, pump-down and gas replenishment permitting many "shots" per KC-135 flight. Extraction and concentration of fullerenes with solvents will be carried out after spectral and physical measurements have been made of the neat plume deposits.

In addition to imagery and sample extraction/analysis, determination of temperature gradients will be accomplished by placement of thermocouple strings at various geometries in the reactor chamber. The ability to correlate fullerene production with plume density images and thermal gradients under reduced gravity (10^{-2} - 10^{-3} "gee") and normal gravity will provide important information for assessing the role of convection in an arc/inert atmosphere reactor.

Curl, R.F. and Smalley, R.E. 1991, *Sci. Am.* 265, No. 4, 54.

Hauffer, R.E. et al. 1990, *J. Phys. Chem.* 94, 8634.

Howard, J.B., McKinnon, J.T., Makarovsky, Y., Lafleur, A.L., and Johnson, M.E. 1991, *Nature* 352, 139.

Kratschmer, W., Fostiropoulos, K., and Huffman, D.R., 1990a, in "Dusty Objects in the Universe," eds. E. Bussoletti and A.A. Vitone (Kluwer), 89.

Kratschmer, W., Lamb, L.D., Fostiropoulos, K., and Huffman, D.R., 1990b, *Nature* 347, 354.

Kroto, A.W., Heath J.R., O'Brien, S.C., Curl, R.F., and Smalley, R.E. 1985, *Nature* 318, 162.

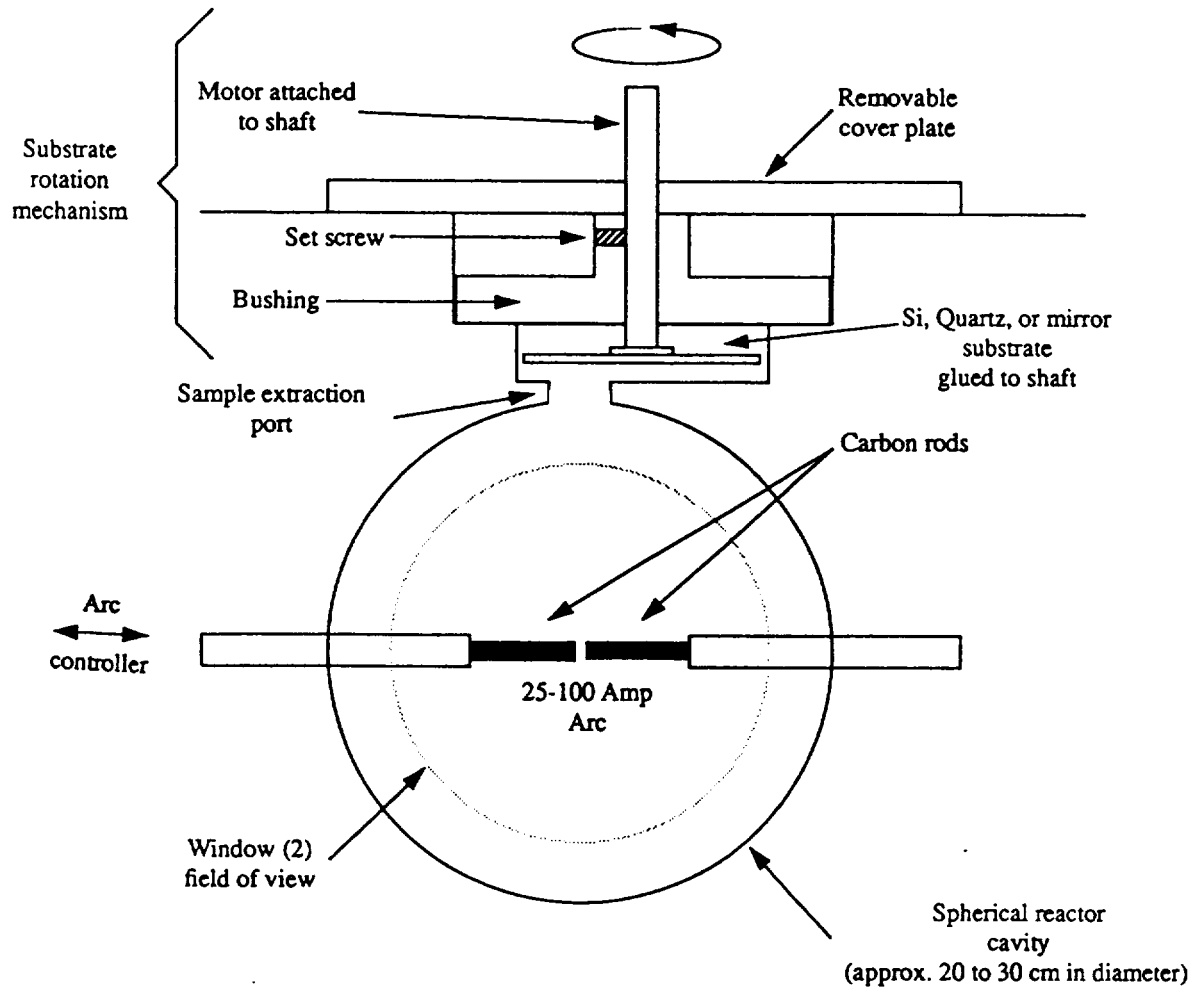
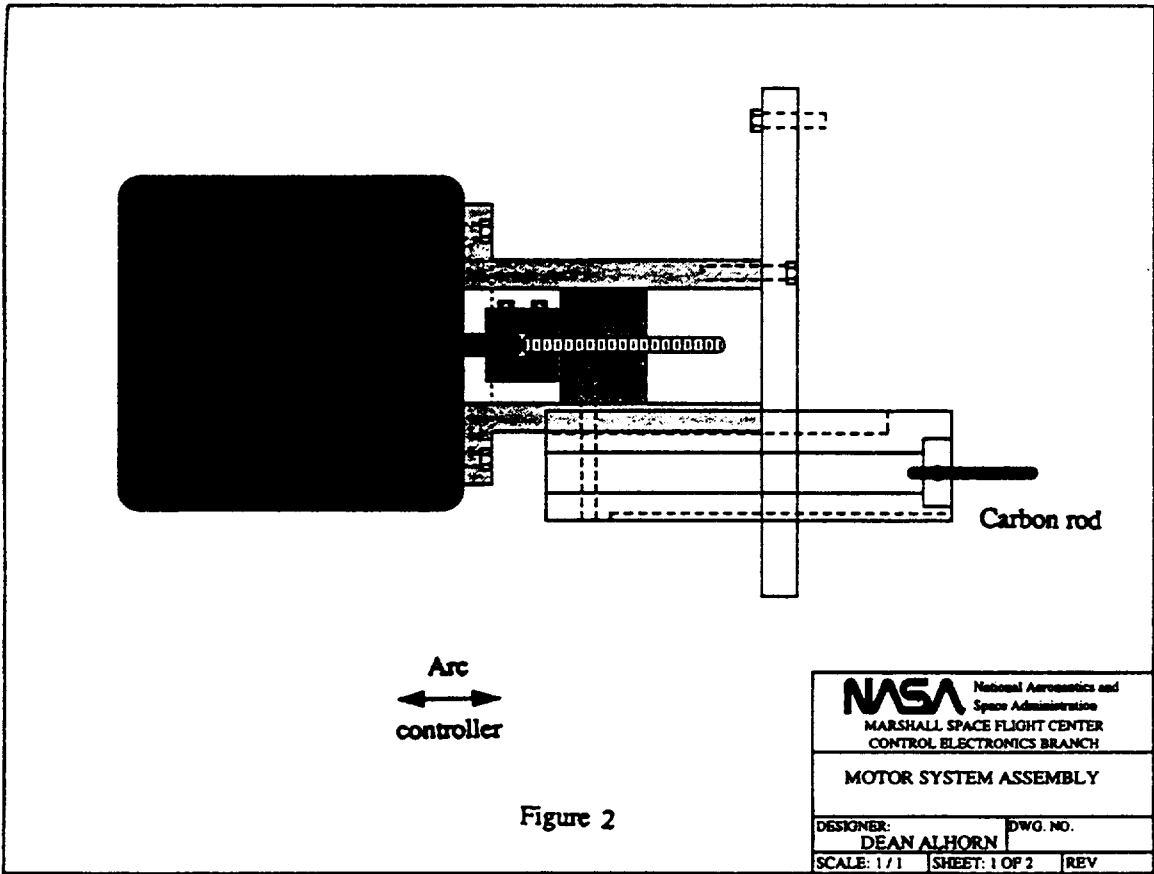


Figure 1. Conceptual configuration (not to scale) of fullerene production reactor for reduced gravity operation. Power for the arc (25-100 amp) to be provided by aircraft supply



N93-17888

1992

NASA/ASEE SUMMER FACULTY FELLOWSHIP PROGRAM

**MARSHALL SPACE FLIGHT CENTER
THE UNIVERSITY OF ALABAMA**

NEURAL NETWORK ARCHITECTURES TO ANALYZE OPAD DATA

Prepared By: Kevin W. Whitaker, Ph.D.
Academic Rank: Assistant Professor
Institution and Department: The University of Alabama
Department of Aerospace Engineering

NASA/MSFC:
Laboratory: Information and Electronic Systems
Division: Guidance, Control, and Optical Systems
Branch: Sensors

MSFC Colleagues: W. T. Powers
Anita E. Cooper

INTRODUCTION

Plume emission spectroscopy (PES) can be applied to rocket engine testing by treating the engine plume as a precisely-controlled laboratory flame for chemical analysis. Test stand or remotely-mounted telescopes can collect engine plume emissions and direct the light, via a grating spectrometer system, onto a linear array of silicon photodetectors. In a quantitative manner, light from many wavelengths of interest can be compared to identify elements, ratioed to recognize alloys, or monitored as a function of time to establish trends and the onset of significant material erosion.

The space shuttle main engine (SSME) became the subject of plume emission spectroscopy in 1986 when researchers from NASA-Marshall Space Flight Center (MSFC), Arnold Engineering Development Center (AEDC), and Rocketdyne went to the SSME test stands at the NASA-Stennis Space Center and at Rocketdyne's Santa Susana Field Laboratory to optically observe the plume. Since then, plume spectral acquisitions have recorded many nominal tests and the qualitative spectral features of the SSME plume are now well established. Significant discoveries made with both wide-band and narrow-band PES systems led MSFC to promote the Optical Plume Anomaly Detection (OPAD) program with a goal of instrumenting all SSME test stands with customized spectrometer systems.

A prototype OPAD system is now installed on the SSME Technology Test Bed (TTB) at MSFC. The OPAD system instrumentation consists of a broad-band, optical multiple-channel analyzer (OMA) and a narrow-band device called a polychrometer. The OMA is a high-resolution (1.5-2.0 Angstroms) "super-spectrometer" covering the near-ultraviolet to near-infrared waveband (2800-7400 Angstroms), providing two scans per second. The polychrometer consists of sixteen narrow-band radiometers: fourteen monitoring discrete wavelengths of health and condition monitoring species and two dedicated to monitoring background emissions. All 16 channels are capable of providing 500 samples per second. To date, the prototype OPAD system has been used during 35 SSME firings on the TTB, collecting well over 200 megabytes of plume spectral data.

The plume spectral data analysis and database correlation efforts to determine how much of a specie (or element) is present and where it came from require the handling and processing of a massive database. The data analysis is an incredibly labor intensive task and not one to be performed by hand. In the case of engine monitoring for flight operations, which is the ultimate goal of the OPAD technology program, PES contributions to a condition monitoring system must be made in real-time or near real-time in addition to processing a large database. These OPAD system requirements dictate the need for fast, efficient data processing techniques.

To address this need of the OPAD system, a study was conducted into how artificial neural networks could be used to assist in the analysis of plume spectral data.

WHY NEURAL NETWORKS?

The latest trend in artificial intelligence (AI) research is the resurrection of artificial neural networks (often simply called neural networks). Inspired by the working of the human brain and nervous system, neural networks have recently offered breakthroughs in vision and speech processing technology. Additionally, the systems have contributed to the practice of operations research providing insight to decision-making methodology. Neural network research was originally conducted in the 1960's but the research became dormant for almost the next two decades, primarily due to the inability to train a multiple-layered network. This was overcome in the late 1980's and neural network research has started to flourish once again with many successes.

A fundamental difference between the philosophies underlying conventional artificial intelligence techniques (such as expert systems or rule-based systems) and neural networks involves the emphasis on logical versus perceptive abilities. For example, AI in the form of expert systems employs logic to drive its

intelligence using rules and their logical combinations. Neural networks, on the other hand, are based on the ability to recognize patterns through experience, rather than the deduction or recollection of rules. In fact, neural networks can also be referred to as adaptive pattern recognition devices but, because of their flexibility and ability to generalize, their applicability typically extends well outside the established realm of pattern recognition. Since neural networks excel at tasks requiring the identification of relationships among large amounts of data, such as is the case with the OPAD data, they are a superior alternative to the conventional expert system approach.

WHAT TYPE OF NEURAL NETWORK?

All neural networks have some type of structure associated with them. In fact, much research has been conducted into the orientation of neuron layers, neuron interconnections, and the interconnection weights. Unfortunately, parameters such as the number of neurons, the interconnection schemes, and the network learning-rate strategy elude *a priori* assignment and require something of a "black art" to determine them. Thus most neural network research centers around finding these network parameters.

Many neural network architectures exist. However, only a few are suited for analyzing OPAD data and these are discussed below.

Traditional Neural Networks

A traditional neural network is based on the concept of the adaptive linear element first studied in detail by Widrow and Angell¹ in the early 1960's. The network consists of simple, highly-interconnected processing elements called neurons. Each input signal to a processing element is amplified or dampened by a weighting factor associated with the path from the signal source to the processing element. The processing element collects all the weighted inputs and sums them to form a total weighted input. This weighted input is passed to an activation threshold function, typically the mathematical function called the sigmoid. If the weighted input exceeds a certain threshold, the neuron fires sending a signal along its output path to another processing element.

Neural systems solve problems by adapting to the nature of the data they receive. This is done primarily through supervised training. In supervised training, a network is told whether its answer (output) to a given input is correct or, if incorrect, what the magnitude of the error is. If the network's answer is not correct, the network begins to adjust the weights along each and every signal path to reduce the error between the predicted output and the actual output. The most popular supervised training method is called backpropagation, which was initially described by Werbos² in 1974, and later by Rumelhart et al.³ in 1987. In short, backpropagation dictates how error at the output layer is fed backwards through the network, adjusting the path-weights along the way. Through repeated applications of a set of training data and subsequent backpropagation of error, the weights eventually converge to an optimal configuration which allows the neural network structure to identify patterns in any new data presented to it. (It is tacitly assumed that the new data lies within or near a domain spanned by the training data.)

Probabilistic Neural Networks

The structure of a probabilistic neural network (PNN) is similar to a traditional network built using a backpropagation training algorithm. The primary difference is that the sigmoidal activation function is replaced by a *class* of functions which includes, in particular, the exponential. Probability is then used to select which function in the class is used to determine whether or not the neuron fires. Theoretically, this allows data patterns to be quickly imbedded in the network structure. It has been demonstrated^{4,5} that training a PNN is several orders-of-magnitude faster than training a traditional backpropagation network of comparable size.

Fuzzy Neural Networks

In practice there exists a close relationship between neural networks and fuzzy logic systems since they both work with degrees of imprecision in a space that is not defined by sharp, deterministic boundaries. Fuzzy and neural technologies can be fused into a unified methodology known as fuzzy neural networks in which the conventional control parameters in the neuron and the connection weights are replaced by fuzzy regions⁶.

A fuzzy neuron has an architecture that approximates the classical McCulloch-Pitts neuron⁷. The differences between a traditional neuron and a fuzzy neuron are evident when examining their respective control properties. In place of scalar weights, fuzzy neurons use fuzzy sets as strength mediators of input signals. When a signal is received by a fuzzy neuron, it is summed along with all the other active input signals to generate a cumulative signal. This cumulative signal is then mapped to a fuzzy set region containing possible activation levels. Using a defuzzification methodology, such as centroid or minimum entropy, the fuzzy region is collapsed to a scalar value representing the expected value of the fuzzy region under the signal conditions. A conventional fuzzy alpha-cut threshold is used by the neuron to decide whether or not the cumulative signal strength lies above a minimal gain boundary. If it is, the output of the fuzzy neuron is roughly proportional to the fuzzy compatibility state, mapping the input signal strength to the topology of the fuzzy threshold space. If the cumulative signal strength is below the threshold, the output is zero.

Entropy Networks

As has been repeatedly discussed, a multiple-layer artificial neural network structure is capable of recognizing patterns, or stated more formally, implementing arbitrary input-output mappings. Similarly, hierarchical classifier systems, more commonly known as decision trees, possess the capability to generate arbitrarily complex decision boundaries in an n -dimensional space. Exploiting this similarity, it is possible to restructure a given decision-tree as a multiple-layered neural network. This mapping of decision-trees into multiple-layered neural network structures can be used for the systematic design of a class of layered neural networks called entropy nets⁹ which have far fewer interconnections than a traditional neural network. This means that the number of weights contained in the network is minimized while still maintaining the generalizability of the network.

WHAT SHOULD BE DONE?

The raw spectral data obtained by the OPAD system is voluminous, approaching seven megabytes per SSME test-firing. That is the primary difficulty to be tackled by any AI system which hopes to analyze (or help analyze) the data. Much hidden information is contained in each set of data. Patterns which exist may be functions of many variables such as time, engine age, or operating conditions. Also, there is an interplay between species data meaning that spectral signals must be looked at in unison rather than separately. This is a classic problem of complex pattern recognition for which neural networks are well suited.

The task at hand is to identify what type of neural network architecture should be utilized to analyze OPAD data. Unfortunately, even with all the neural network research being conducted there are no reliable rules for selecting neural network architectures for a given problem. Network selection and design is still very much an art rather than a science. To that end, specific recommendations are put forth as how to select, design, and apply neural network technology to the OPAD system.

Recommendation #1

All of the network architectures discussed have advantages and disadvantages when considering them for use with the OPAD system. With no basis for eliminating any of the network types, what should be

done is evaluate each type with a systematic approach. An investigation should be undertaken to first construct neural networks of the various architecture types discussed in this report and then train each one on a *simplified subset* of OPAD (or OPAD-like) data to learn how network behavior and architecture interact. Items to be looked at should be ease of training, final size of the trained network, generalizability, and accuracy and speed of predictions.

Recommendation #2

Once each of the network types has been studied using a simplified set of data, they should be designed and trained using full sets of OPAD data. Again, each network will be evaluated on its ease of training, size, and generalizability. It is anticipated that at least one of the network architectures will prove to be superior but until they are all trained and exercised with real OPAD data it is unknown which one that will be.

Recommendation #3

Conduct a parallel research effort into developing new network architectures. It is conceivable that the neural network architectures discussed may not be entirely appropriate for the OPAD system. However, by combining some of the architectures it may be possible to develop a neural network which is, in essence, customized for OPAD data analysis. For example, it may be possible to combine fuzzy set theory with entropy nets to produce a network with an optimum number of nodes and the entropy net aspect will allow existing decision-tree structures from expert systems currently in use at Stennis Space Center to be converted into a neural network.

REFERENCES

1. Widrow, B., and Angell, J. B., "Reliable, Trainable Networks for Computing and Control," *Aerospace Engineering*, Vol. 21, pp. 78-123, 1962.
2. Werbos, P., "Beyond Regression: New tools for Prediction and Analysis in the Behavioral Sciences," Ph.D. Dissertation, Committee on Applied Mathematics, Harvard University, Nov. 1974.
3. Rumelhart, D. E., Hinton, G. E., and Williams, R. J., "Learning Internal Representations by Error Propagation," *Nature*, Vol. 323, pp. 318-362, 1986.
4. Specht, D. F., "Probabilistic Neural Networks," *Neural Networks*, Vol. 3, pp. 109-118, 1990.
5. Specht, D. F., "Probabilistic Neural Networks and the Polynomial Adaline as Complementary Techniques for Classification," *IEEE Transactions on Neural Networks*, Vol. 1, No. 1, pp. 111-121, 1990.
6. Cox, E., "Integrating Fuzzy Logic into Neural Nets," *AI Expert*, pp. 43-47, June 1992.
7. McCulloch, W. W., and Pitts, W., "A Logical Calculus of the Ideas Imminent in Nervous Activity," *Bulletin of Mathematical Biophysics*, Vol. 5, pp. 115-133, 1943.
8. Rumelhart, D. E., "Learning Internal Representations by Error Propagation," *Parallel Distributed Processing*, Vol. 1, pp. 318-362, 1986.
9. Sethi, I. K., "Entropy Nets: From Decision Trees to Neural Networks," *Proceedings of the IEEE*, Vol. 78, No. 10, pp. 1605-1613, 1990.

192-10887

1992

NASA/ASEE SUMMER FACULTY FELLOWSHIP PROGRAM

MARSHALL SPACE FLIGHT CENTER
THE UNIVERSITY OF ALABAMA

COMPUTERIZED REDUCTION OF ELEMENTARY REACTION
SETS FOR CFD COMBUSTION MODELING

Prepared by:	Carl V. Wikstrom, Ph.D.
Academic Rank:	Assistant Professor
Institution:	University of Arkansas Mechanical Engr. Dept. Fayetteville, AR
NASA/MSFC:	
Laboratory:	Propulsion
Division:	Propulsion Systems
Branch:	Performance Analysis
MSFC Colleague:	Charles F. Schafer, Ph.D.

1. Introduction

Modeling of chemistry in Computational Fluid Dynamics can be the most time-consuming aspect of many applications. If the entire set of elementary reactions is to be solved, a set of stiff ordinary differential equations must be integrated. Some of the reactions take place at very high rates, requiring short time steps, while others take place more slowly and make little progress in the short time step integration.

Historically, the problem has been approached in several ways:

1) Single Step - Instantaneous Reaction: While computationally simple, this technique will over-predict conversion since the equilibrium point will be surpassed.

2) Total Equilibrium: This is the assumption used in ODE and TDE at MSFC. The assumption may be adequate in describing the overall performance of an engine, but may fail to provide the detail required for the spatial resolution which CFD analysis is to provide. That is, the assumption may not be valid for the local conditions resulting from the CFD calculations.

3) Reduced Mechanism - Finite Rate: The choice of the appropriate reduced set is difficult, since the local conditions are not constant throughout the CFD calculations. Since the importance of the elementary reactions may change within the computational space, the global set chosen may not be appropriate for the local conditions.

4) Partial Equilibrium - Finite Rate: A portion of the reactants are assumed to be in equilibrium, while the remainder are integrated in finite rate kinetics. This approach removes the very short time step calculations and allows integration of fewer equations at longer time steps. Since there is an interaction between the equilibrated and non-equilibrated species, an equilibrium calculation is performed at each time step. KIVA (Los Alamos) utilizes this approach. However, the proper choice of equilibrated and non-equilibrated reactions may change with the local conditions.

The goal of this work is to develop a procedure to automatically obtain sets of finite rate equations, consistent with a partial equilibrium assumption, from an elementary set appropriate to local conditions. The sets can be applied to the appropriate regions within the CFD space where the total equilibrium assumption is inappropriate.

2. Approach

A program was successfully run using the entire combustion chamber as a single cell in the summer of 1991. (Wikstrom, 1991) While the reduced reaction set should be adequate to predict the overall performance of the combustion chamber, the test of applicability requires variation within the combustion space. The conditions for the reduction were to be chosen from a CFD solution in which the local temperature and mixture ratio varied with the combustion solution. In order to find such a solution, a two phase model of the combustion was used, and in order to demonstrate the value of the technique, hydrocarbon fuel, with its more complicated chemistry was selected.

Coinciding with this work was a renewed interest in the F1 engine as a "predeveloped" low-cost engine. Since the F1 met the above criteria, it was chosen as the CFD test case. The remainder of the period spent at MSFC was spent in producing a two phase CFD solution to the F1. Cells are to be chosen as input to the reaction reduction scheme from the solution.

3. F1 Solution

The physical parameters for the F1 were obtained from a recent review of the F1 testing. (Oefeleein and Yang, 1992) A two phase version(2.07) of Reflegs (CFDRC) was used. The code used allowed droplets to be introduced in up to 100 cells in the computational grid.

The grid chosen was 110 by 30, with the densest portion in the combustion chamber. (See figure 1.)

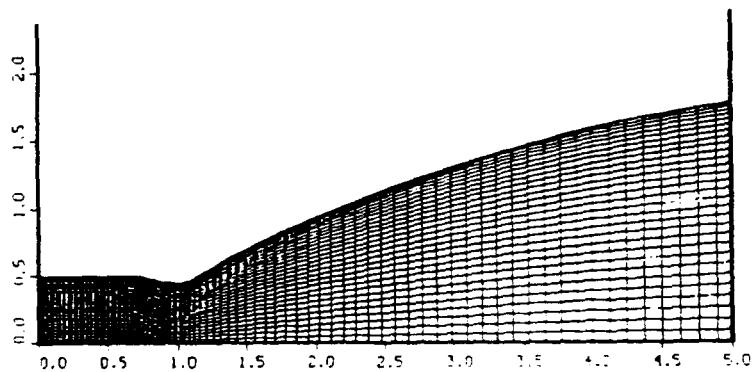


Figure 1. Computational grid used for the F1 engine.

Since the variation in mixture ratio needed to be modeled for testing of the reaction reduction scheme, an approximation of the complicated injector element location (Figure 2.) was included in the input file. Since the LOx had a 20 degree impingement angle and the RP-1 had a 15 degree impingement angle, the droplets were introduced into cells 2 and 3 respectively. Also the variation in orifice are per ring was also modeled to a certain extent, although the grid was not dense enough for a one-to-one correspondence with the injector rings. The presence of the baffles was ignored. A 3D solution would be required to take the presence of the radial baffles into account.

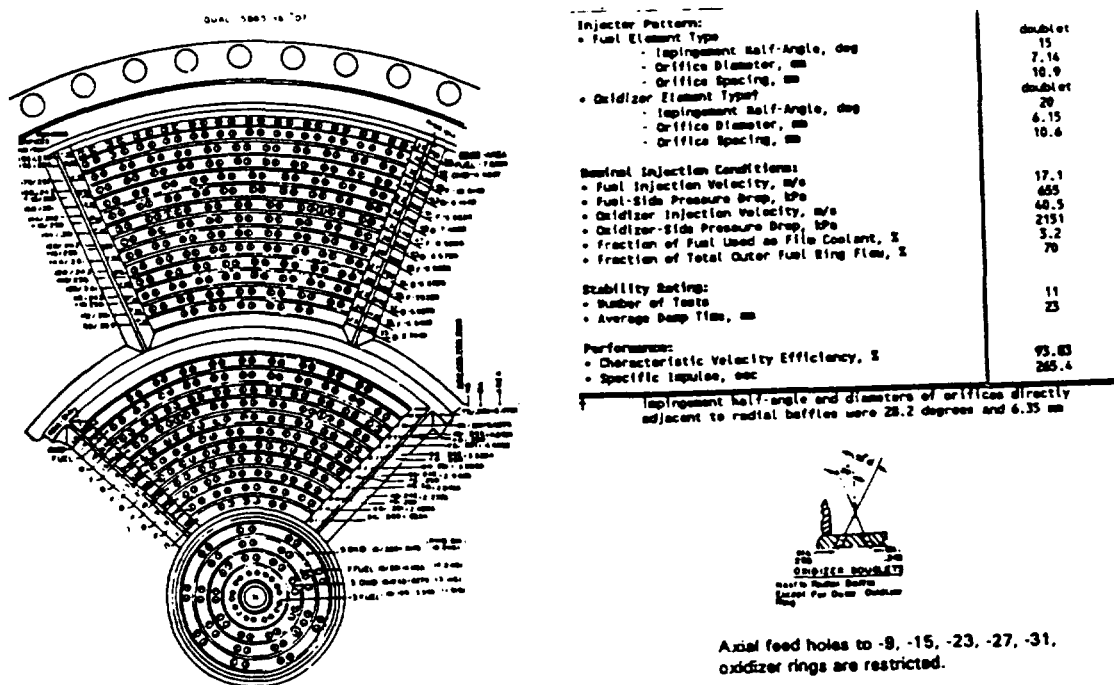


Figure 2. Injector configuration used in the CFD solution. (From Oefelein and Yang, 1992)

The inclusion of the variation of mixture ratio resulted in variation within the solution necessary to test the reaction reduction scheme. (Figure 3) However the actual test of the reduction procedure has yet to be performed due to time constraints.

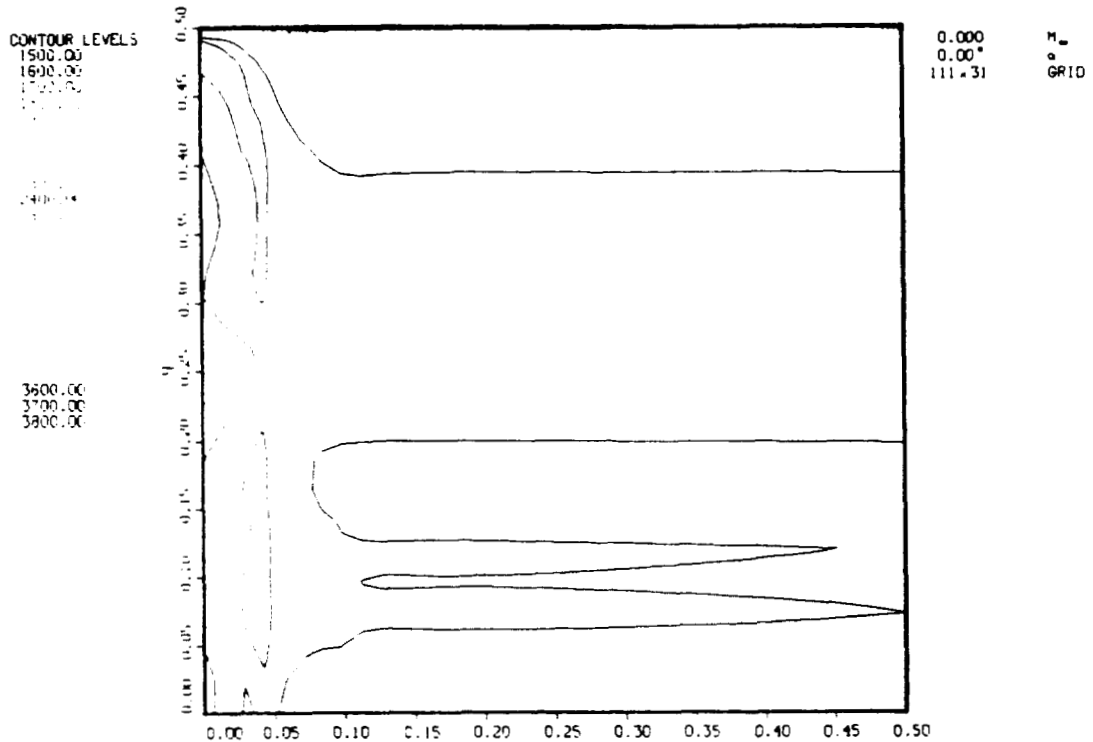


Figure 3. Temperature predictions near the injector.

4. Conclusions and Future Work

A two-phase solution of the FL engine with equilibrium in the vapor phase was found which showed enough variation within the combustion field to expect reduced reaction sets produced with the scheme previously outlined (Wikstrom, 1991) to vary with the computational grid.

The above conclusion has yet to be confirmed by implementation of the final CFD solution in the reaction reduction scheme. Selection of representative cells with the predicted inlet conditions is the next step in furthering this work.

A two-phase CFD code (Refleqs, CFDR) can provide new insight as to the combustion within the F-1 engine. Better modeling of the impinging injectors should yield more meaningful results.

5. References

Oefelein, J.C. and Yang, V, "A Comprehensive Review of Liquid-Propellant Combustion Instabilities in F-1 Engines", Interim Version, July 23, 1992.

Wikstrom, C.V., "Computerized Reduction of Elementary Reaction Sets for Combustion Modeling", Final Report, ASEE/NASA Summer Faculty Fellowship Program, 1991.

1992

NASA/ASEE SUMMER FACULTY FELLOWSHIP PROGRAM

MARSHALL SPACE FLIGHT CENTER
THE UNIVERSITY OF ALABAMA

THE INNER MAGNETOSPHERIC IMAGER (IMI):
INSTRUMENT HERITAGE AND ORBIT VIEWING ANALYSIS

Prepared By:	Gordon R. Wilson, Ph.D.
Academic Rank:	Senior Research Associate
Institution and Department:	The University of Alabama in Huntsville Department of Physics, and Center for Space Plasma and Aeronomic Research
NASA/MSFC:	
Office:	Program Development
Division:	Payload & Orbital Systems
Branch:	SP Science and Applications
MSFC Colleagues:	Les Johnson Dennis Gallagher, Ph.D.

Introduction

For the last two years an engineering team in the Program Development office at MSFC has been doing design studies for the proposed Inner Magnetospheric Imager (IMI) mission. This team had a need for more information about the instruments that this mission would carry so that they could get a better handle on instrument volume, mass, power, and telemetry needs as well as information to help assess the possible cost of such instruments and what technology development they would need. To get this information an extensive literature search was conducted as well as interviews with several members of the IMI science working group. The results of this heritage survey are summarized below.

There was also a need to evaluate the orbits proposed for this mission from the stand point of their suitability for viewing the various magnetospheric features that are planned for this mission. This was accomplished by first, identifying the factors which need to be considered in selecting an orbit, second, translating these considerations into specific criteria, and third, evaluating the proposed orbits against these criteria. The specifics of these criteria and the results of the orbit analysis are contained in the last section of this report.

Heritage Summaries for the IMI Instruments

FUV Auroral Imagers

Of all of the proposed IMI instruments the FUV auroral imager has the greatest amount of heritage. Instruments designed to image the aurora have been flown for over 20 years. They have been designed to operate from low altitude (500-1000 km) and high altitude (6000 km-3.5 Re), and to image the aurora at wavelengths from the vacuum ultraviolet through the near infrared. These instruments have flown at low altitude on a series of air force weather service satellites (DMSP) during the late sixties and seventies and on their air force descendents (HILAT and Polar Bear) during the eighties. A series of Japanese satellites (Exos A-Exos D) also carried FUV auroral tv cameras. The instruments with the closest applicable heritage to IMI are the V5 auroral imager flown on the Swedish Viking satellite in 1986 (*Anger et al.*, 1987), the Scanning Auroral Imager (SAI) launched on Dynamics Explorer 1 in 1981 (*Frank et al.*, 1981), and the Ultraviolet Imager (UVI) scheduled for launch on the ISTP POLAR spacecraft in June of 1983 (*Torr et al.*, 1992). Of these last three UVI comes closest to meeting the IMI requirements; its main drawback is that its field of view (8° full cone) is too small to meet the IMI requirement of $30^\circ \times 30^\circ$.

Geocoronal Imagers

In the last 20 years two instruments have been flown which had the capability to image the hydrogen geocorona. The first, in 1972, was a electronographic Schmidt f/1 system operated from the moon's surface by the Apollo 16 astronauts. The second was the SAI instrument carried on DE 1. In addition to its ability to image the aurora SAI also had the capacity to image the geocorona. Of these two instruments the SAI instrument is the closest to meeting the IMI requirements. In fact, a simplified version of SAI would probably be adequate to the task.

He⁺ 304 Å Imager

This instrument has no direct heritage; no He⁺ 304 Å imagers have flown in the past. The signal that it would measure (solar 304 Å light scattered by plasmaspheric He⁺ ions) has been detected by photometer and spectrometer instruments flown in the past so we know that there is a signal to measure and what its intensity is. We also know from these previous measurements that this signal contains information on the structure of the plasmasphere. The question then is: Can an imaging instrument be built to take pictures of the plasmasphere given the intensity of the 304 Å scattered sunlight coming from it? A compact telescope (ALEXIS) designed to do an all sky survey in several soft x-ray bands (133 Å, 171 Å, 186 Å) has many of the features needed for a He⁺ imager (*Bloch et al.*, 1990). To modify ALEXIS so that it could operate at 304 Å would require a redesigned multilayer mirror and transmission filter. Such modifications have been made and a He⁺ imager called WIDGET will fly this fall (Sept. 1992) to test the instrument (*Cotton et al.*, 1992).

O⁺ 834 Å Imager

Like the 304 Å imager, this instrument has no direct heritage. Furthermore, it is not clear that the 834 Å emission levels from O⁺ ions in the magnetosphere are large enough to be detected, especially since

these emissions would often need to be seen against the dayside ionosphere which is a strong producer of 834 Å emissions. The filtering system for this instrument would also need sufficient out of band rejection to eliminate the strong Lyman- α signal coming from the geocorona. A conceptual design for a self-filtering 834 Å camera, which has in theory sufficient out of band rejection, was recently proposed by *Zukic et al.* (1991), but has not yet been tested. Some limited work has been done on fabricating and testing filters for this instrument, but the work is still in its early stages. Before IMI could fly a O⁺ imager a great deal of work needs to be done to demonstrate that a working 834 Å imager can be built and that a strong enough signal exists to be detected above the background.

Electron Precipitation Imager

Spacecraft instruments detected bremsstrahlung x-rays coming from the auroral ionosphere, in regions of energetic electron precipitation, as early as 1972. Since then a series of satellites have carried x-ray detectors whose data have furthered our knowledge about these emissions and permitted a limited amount of imaging, all from low altitude. For IMI, an x-ray auroral imager capable of simultaneously imaging the whole auroral oval from altitudes as high as 7 Re, has been proposed. No previous instrument with capabilities even close to these has been flown. An x-ray imager to be carried on the ISTP POLAR spacecraft (called PIXIE-Polar Ionosphere X-ray Imaging Experiment) (*Imhof et al.*, 1991) will attempt to do many of the things that are expected of the IMI electron precipitation imager. Several though, have expressed their doubts about how well it will work and if the x-ray fluxes will be high enough for it to make useful measurements from the higher altitude portions of the POLAR orbit. Even if PIXIE works perfectly it will still fall short of meeting the IMI requirements of angular resolution and energy detection range for this instrument. Much work needs to be done to demonstrate an x-ray imaging instrument capable of meeting the IMI requirements.

Proton Aurora Imager

The first detection of doppler shifted Lyman- α coming from precipitating protons (charge exchanged into precipitating hydrogen atoms) was made by a spectrometer flown on the S3-4 satellite in 1978 (*Ishimoto et al.*, 1989). No instrument however, has ever imaged these emissions so the proton auroral imager has no direct heritage. Such an instrument would need to spectrally separate Lyman- α emissions coming from the proton aurora and Lyman- α emissions coming from the geocorona. To do so would require good spectral resolution near 1216 Å (≤ 1 Å), which also gives the instrument the capability to determine the energy distribution of the precipitating protons as well. An instrument designed to do high spatial and spectral resolution (0.04 Å) imaging of Jupiter, in order to study proton aurora there, was flown on a sounding rocket in 1991 (*Harris et al.*, 1992). The imaging portion of this instrument was a telescope with a small field of view, appropriate for imaging a distant target. To adapt it to the task of imaging terrestrial proton aurora at close range would require a front end telescope with a wider field of view and good angular resolution.

Neutral Atom Imagers

The use of neutral atoms for imaging the magnetosphere involves a concept totally different from that used by the instruments discussed above. Here the medium of information are streams of neutral atoms originating from energetic ring current ions which have charge exchanged with hydrogen in the geocorona. The instrument must focus this stream onto an imaging surface capable of detecting it. The only direct heritage for this instrument was a charge particle detector (MEPI) which flew on the ISEE-1 spacecraft. It was only realized some time after the initial measurements were made that the persistent fluxes seen when the spacecraft was outside the region containing the energetic ions were really neutral atoms that the detector was able to see. From this data a crude image of the ring current was made (*Roelof*, 1987). Since then much work has been done defining ENA camera concepts and testing the various components and processes needed for such a camera (*McEntire and Mitchell*, 1989). Much work remains to be done testing full engineering models to see if the techniques needed to reject ions, electrons and photons will work. An instrument with neutral atom imaging capability (SEPS) will be carried on the POLAR despun platform, and a dedicated ENA imager (ISENA) will fly on the SAC-B satellite in 1994.

In addition to an instrument capable of imaging energetic neutral atoms (20–100 keV) as discussed above, IMI will carry a Low Energy Neutral Atom imager (LENA) for the ~ 1 –50 keV energy range.

This instrument is still in the early conceptual stage and a detailed candidate instrument design has yet to be proposed (McComas *et al.*, 1992). Work is currently underway to test the interaction of LENA with thin foils and crystalline surfaces. These processes may play important roles in the operation of any LENA camera.

Magnetospheric Viewing Considerations for IMI

Since the primary aim of the IMI mission will be to obtain global images of the inner magnetosphere and the aurora, viewing considerations should play a major role in the orbit selection process. By viewing considerations we refer to those factors which determine whether or not the particular magnetospheric feature can be seen from the spacecraft, what kind of quantitative information can be obtained from the given viewing location, what fluxes will be available at the viewing location, when other sources will interfere with viewing, etc. Listed here, in order of priority, are the image target regions along with the wavelengths or means of imaging. The means of imaging following each target are listed in order of feasibility and/or importance.

1. Auroral zone (1304 Å, 1356 Å, LBH; Lyman- α ; x-rays)
2. Ring current and ion injection region (ENA; LENA; O⁺-834 Å)
3. Plasmasphere (He⁺-304 Å; O⁺-834 Å)
4. Atomic hydrogen geocorona (Lyman- α)
5. Inner plasma sheet (LENA; O⁺-834 Å)
6. Polar cap low energy ions (≤ 40 eV) (O⁺-834 Å; He⁺-304 Å)
7. Ionosphere (O⁺-834 Å)

Targets 1-3 are absolutely necessary to the success of the mission and are all of about equal importance. Target 4 is also important, at least for analysis of ENA images. Targets 5 and 6 are important from the perspective of understanding the magnetosphere but are of lower priority because of technical difficulties associated with their imaging. Target 7 is of low importance to the magnetospheric investigation role of the mission, but is something which could be easily seen if an 834 Å camera flies on IMI.

Because of the high priority for imaging the auroral zone, the ring current and the plasmasphere considerations affecting their imaging are also of high priority. These considerations are:

1. An unobstructed view of the whole auroral oval.
2. Dwell times at high altitude and latitude that are comparable to auroral evolution time scales.
3. Keeping the sun out of the field of view of those instruments which could see it (FUV, electron aurora imager, proton aurora imager).
4. Whether magnetic local time versus radial distance, or latitude versus radial distance information is desired for the ring current and plasmasphere.
5. The ease of understanding a ring current and plasmasphere images when viewed from outside versus the inside.
6. Higher ENA and 304 Å fluxes (by a factor of at least 2) are available when the ring current and plasmasphere are viewed from outside rather than inside.
7. Orbital period compared to ring current and plasmasphere evolution time scales.

Because of the ease of imaging the geocorona, no specific viewing considerations other than an orbit with an apogee above 3 Re are needed. The plasma sheet, polar cap low energy ions, and the ionosphere require a viewing location at high altitude and low altitude. Because of the lower priority of these features this consideration was not added to the list used to analyze the following orbits.

These viewing considerations were translated into the following specific criteria by which the candidate orbits (see table) were evaluated.

1. The length of time per orbit when the spacecraft is within the auroral oval viewing region.
2. The length of time per orbit when the angle between the spacecraft-sun line and the spacecraft-earth line is less than 20° and the spacecraft altitude is less than 2 Re. (These are times when auroral imaging would not be possible.)
3. The length of time per orbit that the spacecraft is within the plasmasphere and ring current.
4. The length of time per orbit that the spacecraft is within the three latitude bins of 0°-30°, 30°-60°, and 60°-90°.

Candidate Orbits

<u>Orbit</u>	<u>Perigee</u>	<u>Apogee</u>	<u>i</u>	<u>ω_n</u>	<u>d_n</u>	<u>Launch Date</u>	<u>Period(hrs)</u>
#1	4844 km	7 Re	90°	290°	0°	20 Sept.	15.179
#2	4844	7	90°	335°	0°	20 Sept.	15.179
#3	1000	7	90°	270°	0°	20 Sept.	13.795

Each of these orbits have periods long enough to follow auroral substorms, plasmasphere depletions, and ring current injection events. They do not however, offer long enough continuous coverage to follow plasmasphere refilling and ring current decay. Orbit #1 provides the best auroral viewing over the two years of the mission, while orbit #3 allows the viewing of the ring current and plasmasphere from a variety of latitudes. The amount of time spent inside the plasmasphere and ring current is about the same for each orbit so that this criteria does little to discriminate between these orbits. Non of these orbits have times when criteria 2 is met.

It turns out that the requirement for good auroral viewing is in conflict with low latitude viewing. Therefore, if it is decided that having a variety of latitudes from which to view the plasmasphere and ring current is less important than having good auroral viewing, orbit #1 would be most desirable. In this case it would be possible to chose an initial orbit so that during a extended mission, beyond two years, low latitude coverage is provided. If it is decided that latitude coverage is as important as auroral viewing then orbit #2 might be an option. Viewing of several of the secondary targets (polar cap ions, inner plasma sheet, and ionosphere) all require long dwell times at low latitudes, which taken together might tip the balance in favor of an orbit like #3 which spends significant time at low latitudes. Of the three orbits, orbit #1 provides the most time over the life of the mission where the full auroral oval, ring current and plasmasphere can be imaged simultaneously.

References

1. Anger, C. D., et al., An ultraviolet imager for the Viking spacecraft, *Geophys. Res. Lett.*, **14** (1987) 387-391.
2. Bloch, J. J., et al., Design, performance, and calibration of the ALEXIS ultrasoft x-ray telescope, *SPIE Proceedings*, **1344** (1990) 154-164.
3. Cotton, D., Conant, R., and Chakrabarti, S., The WIDe-angle GEocoronal Telescope (WIDGET), *SPIE Proceedings*, **1744**, (1992) 110-116.
4. Frank, L. A., Craven, J. D., Ackerson, K. L., English, M. R., Eather, R. H., and Carovillano, R. L., Global auroral imaging instrumentation for the dynamics explorer mission, *Space Sci. Instr.*, **5**, (1981) 369-393.
5. Harris, W., Clarke, J., Caldwell, J. R., Bush, B., Cotton, D., Chakrabarti, S., and Feldman, P., A high resolution UV spectrograph for a sounding rocket observation of the Jovian H Ly- α profile, *SPIE Proceedings*, **1745**, (1992) 251-267.
6. Imhof, W. L., et al., The Polar Ionospheric X-ray Imaging Experiment (PIXIE), *GGI Polar PI Instrument Manual* (1991).
7. Ishimoto, M., Meng, C.-I., Romick, G. R., and Huffman, R. E., Doppler shift of auroral Lyman α observed from a satellite, *Geophys. Res. Lett.*, **16**, (1989) 143-146.
8. McComas, D. J., Funsten, H. O., Gosling, J. T., Moore, K. R., and Thomsen, M. F., Low-energy neutral-atom imaging, *SPIE Proceedings*, **1744**, (1992) 40-50.
9. McEntire, R. W., and Mitchell, D. G., Instrumentation for global magnetospheric imaging via energetic neutral atoms, in *Solar System Plasma Physics*, eds. Burch, Waite and Moore, AGU, Washington DC (1989) 69-80.
10. Roelof, E. C., Energetic neutral atom images of a storm-time ring current, *Geophys. Res. Lett.*, **14**, (1987) 652-655.
11. Torr, D. G., Torr, M. R., Zukic, M., Spann, J., and Johnson, R. B., The ultraviolet imager (UVI) for ISTP, *SPIE Proceedings*, **1745** (1992) 61-74.
12. Zukic, M., Torr, D. G., Torr, M. R., High throughput narrowband 83.4 nm self-filtering camera, *SPIE Proceedings*, **1549** (1991) 234-244.

1992

NASA/ASEE SUMMER FACULTY FELLOWSHIP PROGRAM

**MARSHALL SPACE FLIGHT CENTER
THE UNIVERSITY OF ALABAMA**

**ANALYSIS OF FILM COOLING
IN ROCKET NOZZLES**

Prepared By: Keith A. Woodbury, Ph.D., P.E.
Academic Rank: Assistant Professor
Institution and Department: The University of Alabama
Mechanical Engineering Department
NASA/MSFC:
Office: Combustion Devices Group
Division: Component Development Division
Branch: Turbomachinery and
Combustion Devices Branch
MSFC Colleague: Dave Sparks

Introduction. Computational Fluid Dynamics (CFD) programs are customarily used to compute details of a flow field, such as velocity fields or species concentrations. Generally they are not used to determine the resulting conditions at a solid boundary such as wall shear stress or heat flux. However, determination of this information should be within the capability of a CFD code, as the code supposedly contains appropriate models for these wall conditions. Before such predictions from CFD analyses can be accepted, the credibility of the CFD codes upon which they are based must be established.

This report details the progress made in constructing a CFD model to predict the heat transfer to the wall in a film cooled rocket nozzle. Specifically, the objective of this work is to use the NASA code FDNS to predict the heat transfer which will occur during the upcoming hot-firing of the Pratt & Whitney 40K subscale nozzle (1Q93). Toward this end, an $M = 3$ wall jet is considered, and the resulting heat transfer to the wall is computed. These values are compared against experimental data available in Reference [1]. Also, FDNS's ability to compute heat flux in a reacting flow will be determined by comparing the code's predictions against calorimeter data from the hot firing of a 40K combustor. The process of modeling the flow of combusting gases through the Pratt & Whitney 40K subscale combustor and nozzle is outlined.

What follows in this report is a brief description of the FDNS code, with special emphasis on how it handles solid wall boundary conditions. The test cases and some FDNS solution are presented next, along with comparison to experimental data. The process of modeling the flow through a chamber and a nozzle using the FDNS code will also be outlined.

FDNS. The computer code name, FDNS, stands for **F**inite **D**ifference **N**avier-**S**tokes. The code, written by SECA, Inc. in 1988 [2], was completely rewritten by ESI, Inc. in 1992. It is a pressure-based finite-difference solver. The code implements artificial viscosity in order to capture shocks in high-speed flows. It solves the continuity, u -, v -, w -momentum, energy, k - ϵ , and specie conservation equations. The k - ϵ turbulence models available in the code are both the "standard" and "extended" versions. Chemistry capability is provided by finite-rate chemical reactions.

Implementation of solid wall boundary conditions in FDNS is by use of *wall functions*. Wall functions are analytically motivated and empirically formulated relationships which are designed to enforce the no-slip and no temperature jump boundary conditions in a turbulent flow. A previous investigation [3] revealed that the earlier version of the code, FDNS2D, employed wall functions which grossly underestimated the heat flux to the wall in compressible flows. However, in the current formulation of the code, the wall function for the energy equation has a form

$$q_w = (h_w - h_p - Pr_t(u_p - u_w)^2/2)(\tau_w/u_p) \quad (1)$$

where h_w and h_p are the enthalpies of the wall and the adjacent point away from the wall, respectively; u_w and u_p are the velocities, τ_w is the wall shear stress, and Pr_t is the turbulent Prandtl number, taken to be $Pr_t = 0.90$.

Note that this wall function is similar to the Reynold's Analogy model proposed in Reference [3]. That function follows from the definition of the heat transfer coefficient for a compressible boundary layer (Shapiro [4], page 1100)

$$q_w = h(T_{aw} - T_w) \quad (2)$$

where T_{aw} is the *adiabatic wall temperature*, and T_w is the actual wall temperature. If the adiabatic wall temperature (given by Shapiro [4], page 1099) is

$$T_{aw} = T_\infty + RU_\infty^2/2c_p \quad (3)$$

which defines the *recovery factor*, R . ($R \approx 0.89$ for air.) Then, with the *Reynolds Analogy* (as suggested by Shapiro ([4], page 1100), and verified experimentally by Holden ([5], Figure 12a), expressed as

$$\frac{C_f}{2} = \frac{\tau_w}{\rho U_\infty^2} \approx C_H = \frac{h}{c_p \rho U_\infty} \quad (4)$$

the heat transfer may be inferred based on the wall friction as

$$q_w = \frac{\tau_w c_p}{U_\infty} (T_\infty - T_w) + \frac{\tau_w}{2} U_\infty R. \quad (5)$$

Or,

$$q_w = \frac{\tau_w}{U_\infty} (h_\infty + R \frac{U_\infty^2}{2} - h_w) \quad (6)$$

where here h is the *enthalpy*, not the heat transfer coefficient. Comparing Equation 1 with Equation 6, and recognizing that Pr_t is numerically equal to R , it can be seen that the expressions are substantially the same.

The wall functions are implemented using a dimensionless distance y^+ . This distance is defined in terms of the resulting shear stress at the wall as $y^+ = y \sqrt{\tau_w / \rho \nu}$. The wall functions implemented in this version are claimed to be accurate over a range of $60 < y^+ < 700$.

Test Cases. Two test cases are used in the present effort to gauge the usefulness of the FDNS code for predicting wall heat flux. The first is specific for an injected film, and the second is more appropriate for a reacting flow.

The test case for film injection is a flow of Mach 6.4 air over a bank of Mach 3.0 Helium wall jets. The helium is injected parallel to the wall. The specific case being studied is "Run 45" from a set of data collected at Calspan and published by Michael Holden [1]. To model his wind tunnel condition, the wall was treated as two isothermal plates; the entry region (up to the wall jets) was taken as 550 R, and the second section (after the wall jets) was taken as 535 R.

Computational meshes were generated using the GENIE++ program (developed by Mississippi State University) on RS/6000 workstations at the University of Alabama. The meshes are coarse, with 121 nodes in the lengthwise direction (x -direction) covering a distance of 4.333 feet, and 41 nodes in the cross-stream direction (y -direction) over a range of 0.5 feet. The mesh in the y -direction was graded using a hyperbolic tangent stretching scheme. Several meshes were used with differing distances to the first node away from the wall (y_p) which resulted in different values of y^+ .

The results from the executions with three different grids are shown in Figure 1 along with Holden's experimental data. The wide variation in results with different grids is evident. The serious disagreement between computed results and the experimental data led to discussions with MSFC personnel in ED32 and ultimately with the author of the code Y. S. Chen of ESI, Inc. This prompted Dr. Chen to examine the code, and he determined that *there was in fact a bug in the code*. The version used up to that point was taken from the Convex computer in ED32 known as tyrell.msfc.nasa.gov on June 6, 1992, from the directory /u/te/ychen/fdnsy. Dr. Chen issued a corrected version of the code on August 3, 1992 from the EADS system.

Preliminary results from the most recent version of the code are shown in Figure 2. Note that agreement over the larger portion of the entrance plate is generally good. However, questions remain about the leading edge results ($-30 < x < -28$) and in the slot region ($0 < x < 16$). It is believed that the discrepancy in the slot region is due to improper gridding ($y^+ < 60$) and this problem is still being worked.

The second test case, involving a combustor flow through a chamber, is based on experimental data gathered in September 1990 on a Pratt & Whitney 40K chamber [6]. Incidentally, the chamber used in that sequence of tests is the same as the one which will be used on the subscale nozzle firing 1Q93. The test case chosen is designated 027C, and had a O/F ratio of 6.00 and a chamber pressure of 1775 lb_f/in². The data gathered during that test is shown in Figure 3.

FDNS results for this test case are not yet available. However, the next section describes the modelling procedure that is being used to analyze this flow.

Modelling Combustor/Nozzle Flows. Ideally, the flow from the injector face to the nozzle

exit should be modelled, including the effect of atomization and mixing of the liquid propellents. However, this degree of computational complexity is expensive, and the FDNS code does not have this ability. An alternative is to remove the injector face-plate from the model and instead of liquid propellant, "inject" the equivalent products of combustion. These products of combustion are obtained from the NASA ODE deck, which determines the products of combustion assuming equilibrium reactions at the specified chamber pressure. Also, the gas velocity is obtained from the ODE deck, which is based on isentropic flow through the chamber/throat.

From the ODE deck, the following results are obtained. The first column corresponds to the test conditions from September 1990 [6], while the second and third columns are the core and wall conditions corresponding to the planned firing of the 40K nozzle in 1Q93.

O/F	6.00	7.5	4.0
P_c (PSIA)	1775	1750	1750
T (R)	6422	6629	5392
ρ (slug/ft ³)	0.01055	0.01164	0.00918
γ	1.1442	1.1336	1.1929
Mach No.	0.203	0.203	0.203
U (ft/sec)	1055.8	993.4	1147.3
H ₂ O (α_1)	0.6723	0.7213	0.4970
O ₂ (α_2)	0.0032	0.0223	0.0000
H ₂ (α_3)	0.2483	0.1327	0.4894
O (α_4)	0.0030	0.0105	0.0000
H (α_5)	0.0313	0.0294	0.0100
OH (α_6)	0.0418	0.0835	0.0035

In the analysis of the combined chamber and nozzle, the chamber will be analyzed separately from the nozzle. This is because the gross details only are required in the chamber, but more detail, including modelling of the film injection region, are required for the nozzle. The table conditions are used as inlet conditions to the chamber. The resulting exit conditions from the chamber section will be used in a more detailed analysis of the nozzle.

Conclusions. The following conclusions can be drawn from this investigation:

- FDNS code from June 1992 contained defects which rendered it useless for modeling thermal effects near solid boundaries.
- The most recent FDNS shows promise for predicting q_w for high speed boundary layer flows.
- The most recent FDNS still must be proven for predicting q_w for film injections.

References

- [1] M. S. Holden, "A data base of experimental studies of shock wave/wall jet interaction in hypersonic flow," Tech. Rep., Calspan-UB Research Center, Buffalo, NY, April 1990.
- [2] Y. Chen, R. Farmer, and J. A. Freeman, "The use of variational principles in improving computational fluid dynamics methodology," Tech. Rep. SECA-TR-90-05, SECA, May 1990. prepared for NASA/MSFC, Contract NAS8-37408.
- [3] K. A. Woodbury, "Assessment of nasa code fdns2d for computation of film cooling effectiveness," Tech. Rep. ZZ, NASA/ASEE SFFP, August 1991. prepared for NASA/MSFC, Contract NGT-01-008-021.

- [4] A. H. Shapiro, *The Dynamics and Thermodynamics of Compressible Flow*. Brown, 1954.
- [5] M. S. Holden, "Shock wave-turbulent boundary layer interaction in hypersonic flow," Tech. Rep. 77-45, AIAA, January 24-26 1977. presented at AIAA 15th Aerospace Sciences Meeting.
- [6] C. Dexter, "Private communication," August 1992.

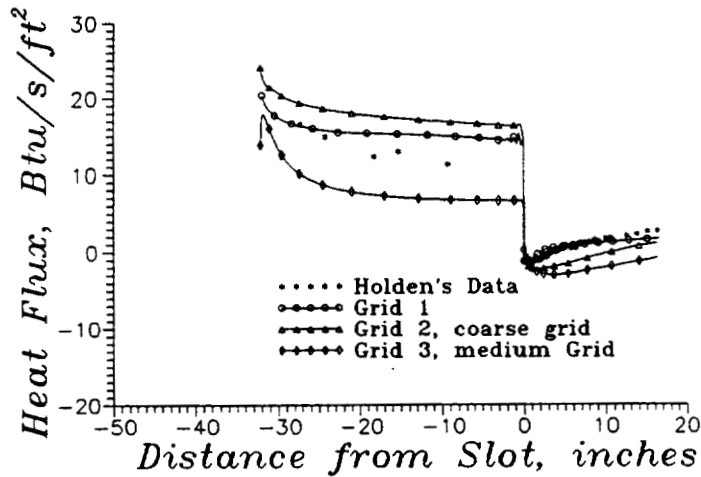
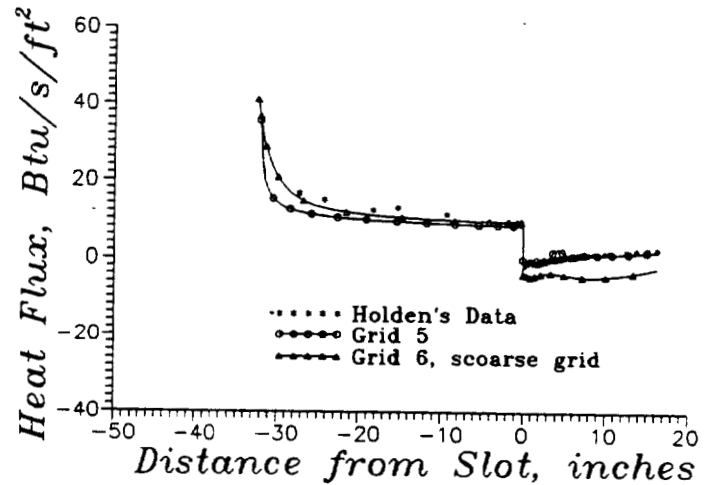


Figure 1: Results from Older FDNS
Version for Different Grids

Figure 2: Preliminary Results from
Newest FDNS Version



P242-027 HEAT FLUX

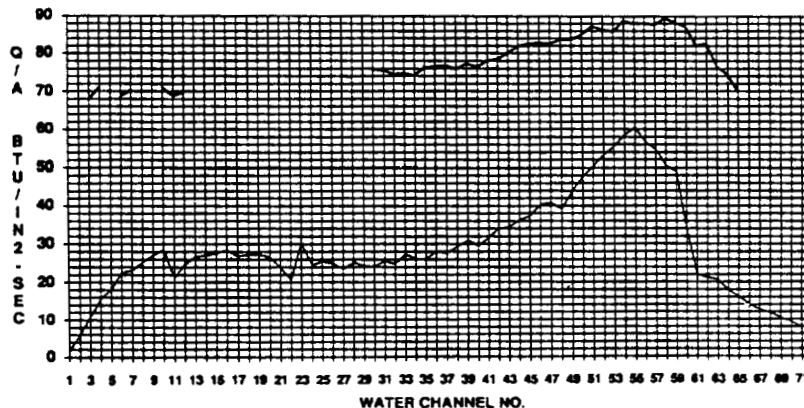


Figure 3: Experimental Data for
40K Calorimeter Chamber

1992

NASA/ASEE SUMMER FACULTY FELLOWSHIP PROGRAM

**MARSHALL SPACE FLIGHT CENTER
THE UNIVERSITY OF ALABAMA**

**STRESS ANALYSIS AND DAMAGE EVALUATION OF FLAWED
COMPOSITE LAMINATES BY HYBRID-NUMERICAL METHODS**

Prepared By: Yii-Ching Yang, Ph.D.
Academic Rank: Assistant Professor
**Institution and
Department:** Tuskegee University
Aerospace Science Engineering
NASA/MSFC:
Laboratory: Material Processes
Division: Engineering Physics
Branch: Non-Destructive Evaluation
MSFC Colleague: Samuel Russell, Ph.D.

INTRODUCTION

Structural components in flight vehicles is often inherited flaws, such as microcracks, voids, holes, and delamination. These defects will degrade structures the same as that due to damages in service, such as impact, corrosion, and erosion. It is very important to know how a structural component can be useful and survive after these flaws and damages.

To understand the behavior and limitation of these structural components researchers usually do experimental tests or theoretical analyses on structures with simulated flaws. However, neither approach has been completely successful. As Durelli states that "Seldom does one method give a complete solution, with the most efficiency."(1) Examples of this principle is seen in photomechanics which additional strain-gage testing can only average stresses at locations of high concentration. On the other hand, theoretical analyses including numerical analyses are implemented with simplified assumptions which may not reflect actual boundary conditions.

Hybrid-Numerical methods which combine photomechanics and numerical analysis have been used to correct this inefficiency since 1950's. But its application is limited until 1970's when modern computer codes became available. In recent years, researchers(2-5) have enhanced the data obtained from photoelasticity, laser speckle, holography and moire' interferometry for input of finite element analysis on metals. Nevertheless, there is only few of literature being done on composite laminates. Therefore, this research is dedicated to this highly anisotropic materials.

CLASSIC LAMINATE THEORY

Composite laminate is made of a stack of laminae in which each lamina may be laid out in a different designated orientation to take advantage of the strength of fibers. It is relatively less understood compare to metal materials. The main differences between composites and metals include non-uniformity through thickness and anisotropic constitutive law. So that the stiffness matrix of a laminate element must be built from every lamina (layer) and assembled according to some basic assumption of elasticity.

In each lamina its unidirectional reinforced fibers may be laid in a direction different from loading axes, structural axes. As it is known the mechanical properties are usually tested and given along or perpendicular to fiber orientation, material axes. Therefore, the stiffness of every lamina must be transformed into unified structural coordinates system for assembly. Consequently, its normal and shear stress-strain relation is coupled after the transformation. This special characteristic is not seen in isotropic materials.

Once the stiffness of all laminae are calculated, the loading-deformation relation of a laminate element can be obtained. In which loading includes in-plane normal/shear forces and bending/twist moments per unit length; deformation includes normal/shear strains at middle plane and bending/twist curvatures. This provides the fundamental constitutive law of composite laminates for finite element analysis.

FINITE ELEMENT ANALYSIS

Finite element method which appreciates the speed and memory size of modern supercomputer becomes very powerful in stress analysis. It use admissible approximate displacement function to estimate strain field in an element. And then stresses field is calculated with the constitutive relation of materials. So the mechanical behavior of whole structure can be defined by minimizing the potential energy and expressed as follow:

$$[K] \{q\} = \{F\} \dots\dots\dots [1]$$

where $\{q\}$ is a column matrix of all nodal displacements and rotations; $\{F\}$ is a column matrix of all input nodal forces and moments; and $[K]$ is a square symmetric stiffness matrix which is assembled with the stiffness of all elements.

Finite element method is very useful specially for structures with complex or singular boundary which can not be solved by analytical methods. Flaws in a composite laminate structure is an example of singular boundary. At those singular areas, stresses are highly concentrated and its displacements vary drastically. So that it requires much finer element to express the variation of stress and strain fields.

DIGITAL IMAGE TECHNIQUE

As it being stated early, displacement fields which can be measured accurately away from stress concentration areas, has been used as input data for finite element analysis to avoid the unknown and difficult boundary conditions in experiments or services. Displacement is measured by a digital image technique developed at the University of South Carolina(6-8). It is done by comparing two digitized images to determine the deformation between images. The system uses a standard video camera attached to a video digitizer. The digitizer transforms an image to a 512 x 512 set of numbers representing the image. Each number represents the intensity of light impinging on a small area of the camera sensor, which is referred to as a pixel. The value of each pixel ranges from 0 to 255 representing from black, different shades of gray, to white respectively. Anyway, these values are then processed by a correlation code in a computer to obtain the deformation field.

FAILURE ANALYSIS

Failure is measured with failure criteria which depend on materials. Because composite materials is interested in this study, the failure modes and failing procedure of a laminate must be understood. And then a criterion can be chosen to predict the failure of composite laminates. As it is known that a lamina can be degraded and failed under following modes: (a) matrix failure with cracks; (b) fibers failure by being broken, buckled, or kinked as a group; (c) debonding between fiber and matrix; (d) delamination between layers. These failure modes interact and occur simultaneously as well as sequentially.

With above understanding researchers have proposed some criteria to assess the failure of composite laminates. Among them, the Tsai-Wu Tensor Theory is mostly adopted for a polymer composite lamina. According to this theory a lamina will have initial crack and start to degrade if its stress state can not satisfy the following inequality:

$$F_{ij}\sigma_i\sigma_j + F_i\sigma_i < 1 \quad \dots\dots\dots [2]$$

It works nicely when delamination and buckling are not concerned. Since linear elasticity has been assumed the Strength Ratio (R), ratio of stresses at failure to the tested stresses, can be estimated by the following equation:

$$(F_{ij}\sigma_i\sigma_j) R^2 + (F_i\sigma_i) R = 1 \quad \dots\dots\dots [3]$$

This Strength Ratio can be interpreted as how many times of current loading the lamina would be started to degrade. If every laminae are degraded the loading level is referred as Last Ply Failure of laminates. In experiments acoustic events may be heard at this moment.

EXAMPLES AND RESULTS

Specimens of quasi-isotropic, [0/45/-45/90],, and cross-ply, [0₂/90₂],, laminates made of T300/F934 prepregs with 1/8 inch diameter central hole are tested with uniaxial tension. Images are taken during the tests for deformation evaluation. The area of images is about 0.77 inch long by 0.91 inch wide. Results of digital image correlation show that the values of displacement along boundary are staggering due to the inevitable error in the process. So that displacements along the boundary of this area are smoothed with the Least Square method before input in the finite element analysis. A computer code, ABAQUS, has been employed for this stress analysis(9).

For quasi-isotropic laminates an eight nodes quadrilateral shell element is used. The edge of hole is divided into 128 elements to catch the stress concentration. Stresses at

concentrate locations is then used to estimate the loading level of first lamina failure and Last Ply Failure. The result predicts that the specimen is totally degraded and its fibers may start to break when loading reaches 980 pound. It agrees very well with the observation in the test while acoustic events has been clearly heard at about 950 pound level. For the cross-ply laminates a 20-nodes solid element is used to reflect the delamination between 0 and 90 degrees laminae which has been observed in the tests. This current work will be done soon in the future, and results will be shown in the next report.

REMARK AND FUTURE WORK

The preliminary results of Hybrid-Numerical Methods has demonstrated an excellent agreement with that in the experiments. It is found that the loading capacity predicted is about an half of the value estimated by a conventional analysis. Because this more realistic approach can enhance structural designs and has the potential to predict the capacity of structures with flaws and after initial damages. It should be studied further on the composite laminates with damages such as impact, delamination, corrosion and erosion.

REFERENCES

1. Durelli, A.J., Applied Stress Analysis, Prentice-Hall Inc., Englewood Clifffs, NJ, 6 (1967)
2. Segalman, D.J., Woyak, D.B. and Rowlands, R.E., "Smooth Spline-like Finite-element Differentiation of Full-Field Experimental Data Over Arbitrary Geometry," EXPERIMENTAL MECHANICS, 19 (1979) 429-439
3. Kobayashi, A.S., "Hybrid Experimental-Numerical Stress Analysis," EXPERIMENTAL MECHANICS, 23 (1983) 338-347
4. Weathers, J.M., Foster, W.A., Swinson, W.F. and Turner, J.L., "Integration of Laser-speckle and Finite-element Techniques of Stress Analysis," EXPERIMENTAL MECHANICS, 25 (1985) 60-65
5. Morton, J., Post, D., Han, B. and Tsai, M.Y., "A Localized Hybrid Method of Stress Analysis: A Combination of Moire' Interferometry and FEM," EXPERIMENTAL MECHANICS, 30 (1990) 195-200
6. Peters W.H. and Ranson, W.F., "Digital Imaging Techniques in Experimental Stress Analysis," Opt. Eng., 21 (1982) 427-431
7. Sutton, M.A., Cheng, M., Peter, W.H., Chao, Y.J. and McNeill, S.R., "Application of an Optimized Digital Correlation Method to Planar Deformation Analysis," Image and Vision Computing, 4 (1986) 143-150
8. Bruck, H.A., McNeill, S.R., Sutton, M.A. and Peters, W.H., "Digital Image Correlation Using Newton-Raphson Method of Partial Differential Correction," EXPERIMENTAL MECHANICS, 29 (1989) 261-267
9. ABAQUS version 4.9, Hibbitt, Karlsson & Sorensen, Inc. (1991)